UNIVERSITA' DELLA CALABRIA

Dipartimento di Fisica

Dottorato di Ricerca in

Scienze e Tecnologie Fisiche, Chimiche e dei Materiali

Con il contributo di (Ente finanziatore)

POR Calabria FESR-FSE 2014/2020

CICLO

XXXV

TITOLO TESI

Extreme events: from geophysics to astrophysics

Settore Scientifico Disciplinare FIS/05

Coordinatore: Ch.ma Prof. Gabriella Cipparrone

Firma _____ Firma oscurata in base alle linee guida del Garante della privacy _____

Supervisore/Tutor: Ch.mo Prof. Vincenzo Carbone

Firma_____ [redacted] Firma oscurata in base alle linee guida del Garante della privacy [redacted]

Dottorando: Dott. Giuseppe Prete

Firma ___ Firma oscurata in base alle linee guida del Garante della privacy

“La borsa di dottorato è stata cofinanziata con risorse del Programma Operativo Regionale Calabria FSE/FESR 2014 – 2020 (CCI 2014IT16M2OP006)”

Contents

Abstract

The aim of this thesis work is the study of extreme event phenomena. Extreme events are well known in nature and they present different characteristics. They are often related to the climate effects, as extreme temperature or rainfall, but it is also possible to define them in the Heliosphere environment, such as slow or fast Coronal Mass Ejection speed events or intense Flares eruptions. Another class of phenomena that can be classified as extreme events are the explosion of Supernova. In this work these different will be analyzed types of phenomena with the help of statistical models, numerical simulations and data analysis.
In the first part we will focus on the extreme events that influence the climate. In particular, we study how these phenomena characterize different world regions. In particular we will concentrate on three regions: the Antarctica continent, the Basilicata and the Calabria regions. The study will be made with the help of a statistical analysis applied on the stations data. This will allow us to make a foresting analysis on the examined regions, identifying what are the zones most affected by extreme phenomena, in order to prevent possible disasters such as floods, landslides, droughts.
In the second part we will explore the nature of Heliosphere extreme events. In particular we will study a particular class of Coronal Mass Ejections defined as extreme, namely the low speed ones. We will study this category of extreme events with the help of spacecraft data and numerical simulations. Numerical simulations help to do predictions on the Space Weather extreme events, because they are able to reproduce a particular event and study how damaging it can be if it has some particular characteristics. Then we will make a comparison between satellite data and numerical results in order to see if the simulation developed is able to reproduce what the spacecraft detects. We will also study the transport properties of energetic particles at the interplanetary shock, analyzing the possible acceleration mechanisms that can influence the particles energization.
In the last part of the thesis, we will concentrate on Galactic and extra Galactic extreme events, called Supernova explosions. We will use numerical simulations in order to reproduce the evolution of the Supernova from early stage to the final time of its evolution. We will set a turbulent and dense environment in which it can develop and we will study its evolution with different configurations. Finally we will try to make a visual comparison between numerical results and spacecraft data obtained for the Supernova Remnant SN1006.

Introduction

The term "extreme event" was first minted in the 1950s and from then it was applied to different scientific disciplines, that span from physics to economics and to psychology and so on (Stewart, Carleton, and Groucutt, 2022). Extreme events are high impact unanticipated events. They are identified in nature as floods, temperature anomalies, tsunamis, earthquakes. It is also possible to define them in the Space Weather, as for example in terms of high or low speed Coronal Mass Ejections (CMEs) or Solar Flares.
From a statistical point of view, we can define an event as extreme when it largely deviates from the statistical mean. In physical terms these events are generated by complex and non-linear systems (Chavez, Ghil, and Urrutia-Fucugauchi, 2015). This poses a serious problem in the study of this kind of phenomena also because they are rare in terms of occurrence. Another problem related to the infrequent occurrence of extreme events is the capability to predict them. Motivated by these reasons, scientists developed different models and tecniques in order to study and to predict extreme events. Extreme value theory (EVT) (Fisher and Tippett, 1928; Gnedenko, 1943; Gumbel, 1958) is one of the statistical approaches often applied to climate (Naveau et al., 2005; Shen, Mickley, and Gilleland, 2016; Pangaluru et al., 2018a; Iyamuremye, Wanyonyi, and Mbete, 2019; Artha and Sofro, 2019; Reis et al., 2022; Rivoire et al., 2022; Moghaddasi, Anvari, and Mohammadi, 2022) and space weather science (Tsubouchi and Omura, 2007; Nakamura et al., 2015; Elvidge and Angling, 2018; Elvidge, 2020; Larrodera, Nikitina, and Cid, 2021) . The EVT is a branch of statistics dedicated to the study of the extreme deviations from the median of the probability. It allows us to extrapolate, from a given ordered sample of a given random variable, the probability of events that are more extreme than any previously observed. In this scenario, the extreme weather events that are characterizing global climate change, can be well described by the EVT.
In the last 20 years a huge number of disaster events have been recorded in all over the world. It was estimated that the 90% of them are associated to extreme weather events. The number of people affected by climate-related disasters and the associated economic damage are growing, as a clear evidence that the frequency of extreme weather events is increasing in parallel with the rise of the global average temperature (Seneviratne et al., 2012).
Figure 1 shows the disasters related to 2 different kinds of extreme events that took place respectively in the South of Italy (Figure 1a) and in the USA (Figure 1b). This growing number of extreme events over the years is also related to anthropogenic

(A)

(B)

FIGURE 1: Extreme events occurred in 2022 (a) extreme rainfall that took place at the beginning of December in the South of Italy(Sicily) (b) the storm near peak intensity that caused the extreme snowfall occurred in December 2022 in the USA.

effetcts. Indeed, the rate of extreme thermal events, related to anthropogenic climate change, overtook historical temperature records at an unprecedented rate (Meehl and Tebaldi, 2004; Power and Delage, 2019; Fischer, Sippel, and Knutti, 2021; Murali et al., 2023). The effects related to the increase of these extreme phenomena have a greater impact in the poorest and warmest regions of the Earth, as the tropical regions (Mahlstein et al., 2011; King et al., 2015; Harrington et al., 2016). Many species have experienced a population extirpation because of episodes of extremly hot temperatures (Vasseur et al., 2014; Till et al., 2019; Román-Palacios and Wiens, 2020; Soroye, Newbold, and Kerr, 2020): extreme temperature events had negative impacts on marine fisheries (Cheung et al., 2021), an important part of the global food system; temperature extremes affect indigenous populations in the Australian continent, increasing the risk of mortality and ill health (Longden et al., 2022); extreme temperatures also have effects on the economic growth, namely that the increase of heat waves that are related to anthropogenic effects has depressed economic output, especially in the world's poorest regions, as the tropical ones (Callahan and Mankin, 2022).

In the last century, the whole Europe and in particular the Mediterranean area was affected by an increase in frequency and intensity of rainfall extremes at daily and sub-daily scale (Brunetti et al., 2001; Brunetti et al., 2004b; Brunetti et al., 2004a; Alpert et al., 2002; Bonaccorso and Aronica, 2016), also in spite of a decrease in total (e.g. annual) rainfall values. It is also known that the increase of the intensity in the extreme rainfall events is related to the increase of the global warming (Scoccimarro et al., 2015; Fischer and Knutti, 2016; Myhre et al., 2019; Huo et al., 2021; Hawcroft et al., 2018). As a consequence, many regions of the Mediterranean basin, characterized by a huge spatial and temporal rainfall variability, have experienced several catastrophic geo-hydrological events (Lionello, Malanotte-Rizzoli, and Boscolo, 2006). Similar considerations can be done for temperature extremes, that are

more linked to the expected global warming. The Mediterranean basin has experienced in the last decade an increase in the heatwave frequency, and different studies predicted a continuous increase of them in the following years (Alpert et al., 2002; Molina, Sánchez, and Gutiérrez, 2020). The same results were obtained in the scenario of future greenhouse gas emissions, in which authors predicted an increase of heatwaves over the Mediterranean for the next years. In such a context, a rigorous analysis and a reliable estimation of the occurrence of extreme events is a relevant and crucial problem in many fields of geosciences, particularly in the analysis of past and projected temperature and rainfall regimes.

As already mentioned, extreme events on Earth are associated to global warming, but it is also possible to define them in our Heliosphere (Cliver et al., 2022). It is possible to classify as extreme events the eruptive events that often happen on the Sun surface as Flares or CMEs. Coronal Mass Ejections (CMEs) are extreme large scale eruptions of plasma and magnetic field from the Sun and they are considered as one of the main drivers of space weather disturbances (Scolini, C. et al., 2019; Kilpua, Koskinen, and Pulkkinen, 2017; Webb, D. F. and Howard, T. A., 2012). Their occurrence can exceed a number greater than ten per days, and this depends on the number of active regions (ARs) present on the Sun's surface related to the solar activity. In these regions the magnetic field has a particular geometric configuration: the magnetic field lines are closed and the energy is stored inside them. When these structures become unstable they erupt, releasing plasma and magnetic field into the heliosphere in the form of CMEs. Once erupted, the CME can propagate throughout the heliosphere and in some cases it can hit the Earth. In Figure 2 there is a schematic view of a CME eruption. A Space Weather event such a flares, or a CME can be defined as extreme if and only if it satisfies some conditions. A CME can be considered as an extreme event if it has an extreme speed such that its frequency of occurrence is extremely rare. Following this idea, we can classify the CMEs as extreme if they have $V_{CME} \geq 3000\, km/s$ or $V_{CME} \leq 400\, km/s$. It is extremely rare to detect a CME with a speed of about $\simeq 3000\, km/s$. Ideeed, from 1996 until 2022, a low number of CMEs with this speed was observed by the Solar and Heliospheric Observatory (SOHO). CMEs with extremely low velocities are more frequent than those with higher speed values. A catalogue of CMEs with low speed is reported in Al-Haddad et al., 2018. When a CME is injected inside the solar wind it is called Interplanetary Coronal Mass Ejection (ICME). From in situ measurements it is possible to observe the classical signature of the passage of an ICME with a sharp enhancement of the total magnetic field, that corresponds to the shock passage generated by the ICME itself (Richardson, I. G. and Cane, H. V., 2010; Kilpua, Koskinen, and Pulkkinen, 2017). This region is followed by the sheath region, in which it is possible to observe important plasma phenomena as magnetic reconnection and turbulence. The last region of an ICME is the region in which it is possible to identify the presence of the magnetic cloud (MC) characterzied by the enhancement of the magnetic field strenght, by a smooth rotation of the magnetic field vector and by low proton

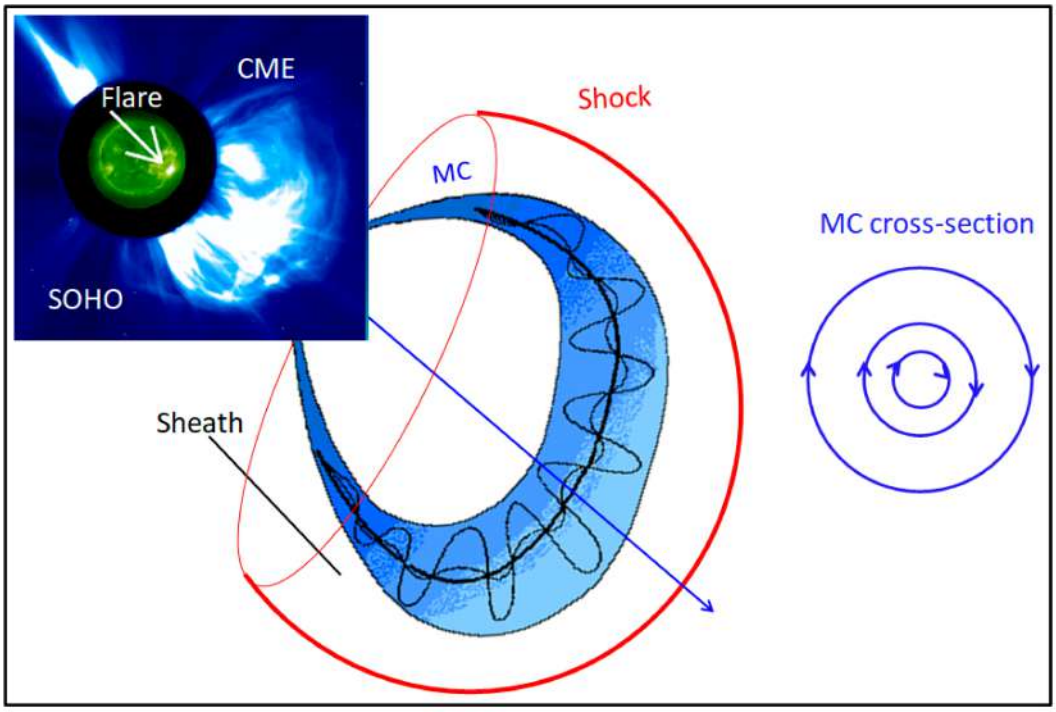

FIGURE 2: Illustration of a CME structure. The SOHO/LASCO image of a CME in the upper left of the figure with the flare location obtained from SOHO/EIT. The shaded blue area represents the magnetic cloud (MC) and it is how the CME is seen in the heliosphere. The MC drives the shock (red line). The blue arrow represents the direction of propagation of the MC. For more details see Figure 11 in Gopalswamy, 2022.

density and temperature. In Figure 3 it is possible to observe the spatial structure of an ICME.

The shock driven by the ICME can accelerate particles from keV up to MeV energies. The main mechanisms invoked to explain the particles' acceleration and energization is the diffusive shock acceleration (DSA) (Bell, 1978; Lee and Fisk, 1982). It is based on the Fermi first order mechanism and on the diffusive motion of energetic particles upstream and downstream of the shock front, owing to the interaction of particles with magnetic field fluctuations. Such an interaction favours particle shock crossings, speeding up the acceleration process. This theory predicts also that the particles fluxes have an exponential decay in the upstream region of an interplanetary shock and a constant behaviour in the downstream region. But this is not often observed in the Heliosphere. Moving from this, scientists tried to explain the particle energization with the help of other different theories as the Superdiffusive Shock acceleration (SSA). This theory asserts that energetic particle motion can be faster than normal diffusive, namely superdiffusive, in the upstream region, thus questioning the validity of DSA (Zumofen and Klafter, 1993; Ragot and Kirk, 1997). In order to better understand and reproduce the phenomena associated to the evolution of CMEs, scientists make use of numerical simulations. In particular, the

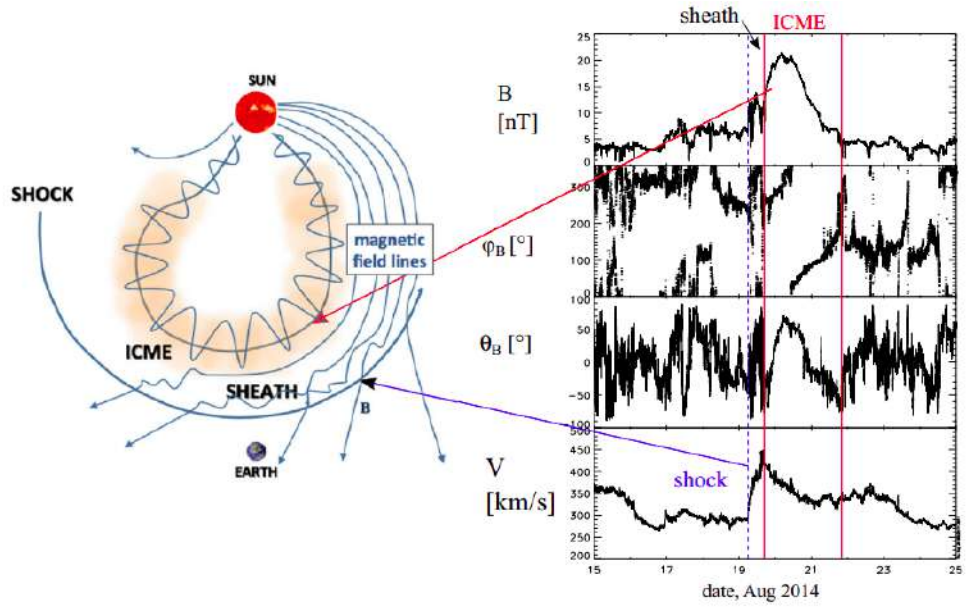

FIGURE 3: **(Left)** Schematic image of the propagation of an ICME. The yellow shaded area is the region associated to the ICME that corresponds to MC; the sheath region is in between the shock region and the ICME region. **(Right)** Solar wind observations during an ICME from the ACE spacecraft. From the top panel to the bottom: the magnetic field magnitude, the longitude and latitude angles of the magnetic field in the Geocentric Solar Magnetospheric (GSM) coordinate system, and the solar wind speed. The blue dashed line marks the shock and the ICME is bounded by the pair of red lines. For more details see Kilpua, Koskinen, and Pulkkinen, 2017.

description of a big scale event, such as a CME, requires the usage of magnetohydrodynamic (MHD) simulations (Parsons et al., 2011; Pomoell, Jens and Poedts, S., 2018; Poedts, Stefaan et al., 2020). These simulations allow us to understand and also forecast the evolution of the big event, such as an extreme event like faster or slower CME. It is also possible to study the transport mechanism of charged particles with the coupling between MHD-simulations and test-particle simulations (Wijsen et al., 2021; Wijsen, N. et al., 2022), Particle In Cell (PIC) and Hybrid simulations (Giacalone et al., 1992; Giacalone and Ellison, 2000; Amano and Hoshino, 2007; Amano and Hoshino, 2009; Caprioli and Spitkovsky, 2014), MHD-PIC (Mignone et al., 2007; Mignone et al., 2011a; Mignone et al., 2018b) simulations, and so on.

Another physical phenomenon that can be included in the category of extreme events is the explosion of a massive star that turns into a Supernova. A Supernova explosion (SNe) is an instantaneous release of energy of about $\simeq 10^{51}\,erg$, associated to the catastrophic collapse of a massive star or due to a runaway nuclear burning on the surface of a white dwarf. SNe are classified on observational basis. Basically SNe are divided in two groups depending on the presence or absence of Hydrogen Balmer lines in their spectra at maximum brightness. SNe in which the Hydrogen Balmer lines are absent in the spectra are called Type I SNe, while the SNe with spectra containing the Hydrogen Balmer lines are called Type II SNe. These two categories of

SNe can be divided in different subcategories, depending on the presence of particular types of elements in the spectrum. Type I SNe can be divided in three subgroups: SNe Ia with strong SiII lines, Type Ib SNe with strong HeI lines and without SiII lines and Type Ic SNe if the spectra are lacking both strong SiII and HeI lines. Supernova of type II can be diveded in a similar way: Type IIP with a plateau in its light curve, Type IIL with a linear phase, Type IIb with a weak hydrogen line after the explosion and SNe Type IIn with narrow emission lines in their spectra, probably due to the interaction between the ejecta and the interstellar dense medium around the explosion (Minkowski, 1941; Barbon, Ciatti, and Rosino, 1979; Filippenko, 1988; Krause et al., 2008; Helder et al., 2012). It is known that about 24% of SNe are type Ia, 10% are type Ib and Ic and 57% are type II (Li and Chen, 2012).

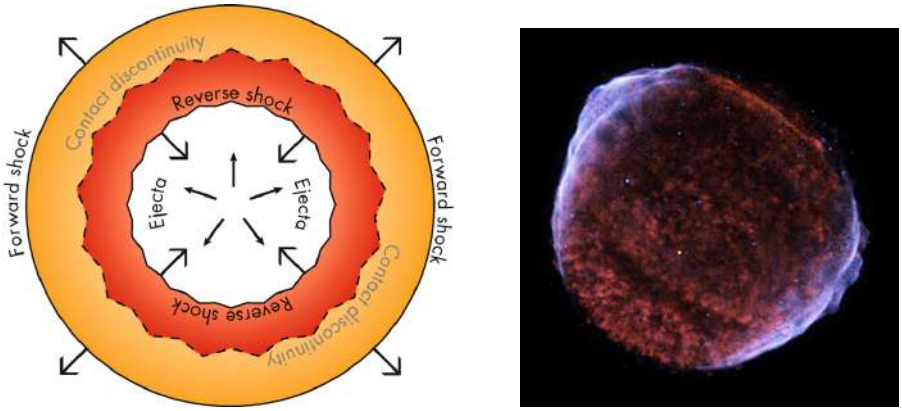

(A) (B)

FIGURE 4: SNR evolution (a) schematic representation of the evolution of a SNe into the interstellar medium (b) SN1006 images in the X-ray from Chandra.

After a star turns into a supernova, the stellar ejecta will expand into the interstellar medium. The stellar material will be accelerated to speeds greater than the speed of sound creating a shock front, called forward shock (FS). This shock will slow down due to interaction with the interstellar medium. As a reaction, a second shock, called reverse shock (RS), will develop moving away from the forward shock, into the ejecta. The expanding material, that the blast collects during its evolution through the interstellar medium, forms the Supernova Remnant (SNR). The SNR evolution is characterized by three phases: free expansion, in which the FS speed is almost constant as long as the swept mass is smaller than the ejecta mass; Sedov-Taylor phase in which most of the energy is transferred from free expanding ejecta to the shock-heated shell and the SNR expands adiabatically; radiative cooling in which the shock slows down to velocities below 200 km/s and the temperature of the post shock will be less than $\simeq 10^5$ K causing the radiation of H, He, C, O lines to increase drastically (Helder et al., 2012; Raymond, 1979).

This thesis work is focused on the analysis of the different typologies of extreme

events described above. With the help of models, numerical simulations and statistical theory we tried to better understand, forecast and reproduce this kind of phenomena. The thesis is organised as follow: in the first chapter will be studied Earth's extreme events with the help of statical and reanalysis models; in the second chapter will be explored the extreme events that characterize the Heliosphere, using both spacecraft data and numerical simulations; in the third chapter the last category of extreme events will be analyzed, i.e. the Supernova explosions and their evolution throught the interstellar medium (ISM), with the help of MHD simulations.

Chapter 1

Extreme events on Earth

Over the 20-year period 2000–2019, 7348 disaster events were recorded worldwide by the EM-DAT database (www.emdat.be), claiming approximately 1.23 million lives and affecting over 4 billion people. Among those, 6681 climate-related disasters – more than two times if compared with the previous 20-year period – affected 3.9 billion people (UNDRR, 2020). The number of people affected by climate-related disasters and the associated economic damage are growing, as a clear evidence that the frequency of extreme weather events is increasing in parallel with the rise of the global average temperature (Seneviratne et al., 2012).
The latest IPCC (Intergovernmental Panel on Climatic Change) report published in 2022 (IPCC Sixth Assessment Report (AR6))(IPCC, 2022) describes an unequivocal increase of the Earth's surface temperature for the next decades. These climatic changes can lead to significant implications for further related environmental phenomena since, for instance, extreme weather events and rainfall are becoming more common and heat waves and droughts are expected to be more extreme. Therefore, the study of extreme events is a key scientific challenge and represents an opportunity to understand the dynamics of natural hazards possibly related to climate variability.
Polar regions are the most sensitive world's zone to ongoing impacts of climate change, showing the most rapid rates of warming in recent years (Anisimov et al., 2007). Given the actual trend of climate change, the global impact involves not only ice melting but it has effects also on terrestrial and freshwater species, communities and ecosystems. As a consequence, the last event of abnormal temperature recorded near the Antarctic Marambio base (Watts, 2013) represents a further reminder for the future, not only for the Antarctic but for the whole planet. In addition to the 20.75 $^{\circ}C$ temperature value, previous extreme temperatures have been registered at other sites in the vicinity, such as 19.8 °C observed on 30 January 1982 at Signy Research Station, Borge Bay on Signy Island and 17.5 °C recorded on 24 March 2015 at the Argentine Research Base Esperanza located near the northern tip of the Antarctic Peninsula (Skansi et al., 2017). A crucial question is the acceleration of the global warming process, in order to understand and, if possible, mitigate potential causes. In the context of climate changes, probability distribution functions (PDFs) of events, as for example land surface temperature extremes, are either shifted to higher values or display enhancements of both tails (see Figure 1.1). In both cases, extreme events

acquire a greater probability of occurrence, and this is observable locally on relatively short time scales. The warming in the Antarctic does not appear in the same way for the entire continent. The warming is happening on longer time scales in the Antarctic Peninsula and West Antarctica but is mostly absent in East Antarctica (Nicolas and Bromwich, 2014; Jones et al., 2019; Turner et al., 2020). Moreover, the average summer temperatures in the Antarctic Peninsula have been cooling since 1998 (Turner et al., 2016). This implies that the maximum temperatures are increasing, while the averages are slowly decreasing.

Overall, in the whole Europe and particularly in the Mediterranean area, an increase in frequency and in the intensity of rainfall extremes at a daily and sub-daily scale was observed in the last century (e.g., Brunetti et al. 2001; Brunetti et al. 2004b; Brunetti et al. 2004a; Alpert et al. 2002; Bonaccorso and Aronica 2016), also in spite of a decrease in total (e.g. annual) rainfall values. In addition, the intensity of the heaviest extreme rainfall events is known to increase with global warming in the current century (e.g., Scoccimarro et al. 2015; Fischer and Knutti 2016; Myhre et al. 2019; Huo et al. 2021; Hawcroft et al. 2018). As a consequence, many regions belonging to the Mediterranean Basin - which is characterized by a huge spatial and temporal rainfall variability (Lionello, Malanotte-Rizzoli, and Boscolo 2006) - have experienced several rainfall-induced catastrophic geo-hydrological events, with high economic and social impacts.

The intensification of the hydrological cycle due to global warming in the Mediterranean area (Zittis et al., 2019) raised the need to carry out several studies based on future climate projections. These studies mainly reveal that the occurrence of extreme precipitation in a (future) warmer climate can possibly increase (Zittis, Bruggeman, and Lelieveld, 2021), even if the mean (light/medium) precipitation amount is predicted to decrease in various zones (Lionello and Scarascia, 2018; Giorgi, Raffaele, and Coppola, 2019). Similar considerations can be done for temperature extremes, clearly more linked to the expected global warming. Heatwaves in the Mediterranean Basin have been assessed to occur more frequently in the last decades (Cramer et al., 2018; Molina, Sánchez, and Gutiérrez, 2020); based on regional climate model simulations, under the more pessimistic greenhouse gas emission scenario (RCP8.5), authors found an increase of heatwaves over the Mediterranean for the future, and that the intensity of these events will be stronger in the southern and eastern part of the Basin.

Although climatological studies are mainly performed using global or regional climate models, a common approach to study extreme weather events is the adoption of statistical procedures, such as the statistical extreme value theory (EVT), on different datasets. The EVT has emerged as one of the most important statistical theories for climate observations and for understanding the outputs of numerical models. A challenge already anticipated by Wigley (Wigley, 1988) and later taken up in a commentary by Coley (Cooley, 2009), who points out the great potential for applications of extreme value theory on climate change. One of the most important results of

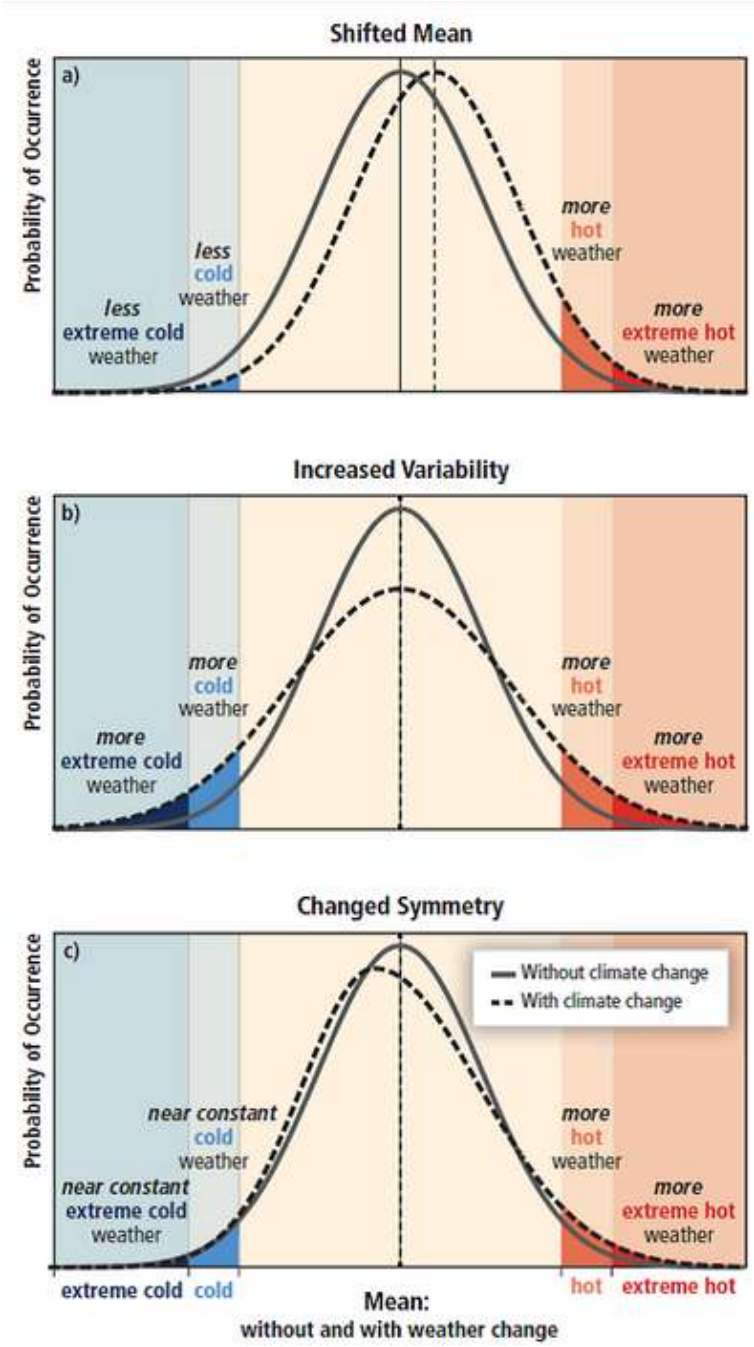

FIGURE 1.1: Probability of occurence for extreme temperatures. From the top to the bottom panel three different types of PDF that indicate an increase of occurence in extreme events are shown. In panel (a) we have a simple shift of the PDF towards higher values of temperature; in panel (b) an increases of temperature variability which leads to an increase in temperature extremes is shown; in panel(c) the increasing of extreme temperature results in a simmetric change of the PDF with a corresponding increase of the tails (IPCC, 2012).

EVT, which differentiates it from other statistical approaches, is its ability to estimate the distribution of extreme values using the asymptotic argument. The origins of the asymptotic characterisation of the maximum sample go back to Fisher and Tippett (Fisher and Tippett, 1928). The first formalisation of a model of extreme

events was proposed by Jenkinson (Jenkinson, 1955; Jenkinson, 1969), showing that there are only three families of possible limit laws for the distribution of extremes, namely the Gumbel, Frechet and Weibull distributions. These three distributions can be expressed in a single distribution function known as "Generalized Extreme Values" distribution (GEV) (Coles et al., 2001a). EVT is currently used in several fields and especially in the analysis of environmental extreme events. For example extreme value theory provides a solid theoretical basis for statistical modelling of extreme hydrological events thanks to its many applications on floods (Canfield et al., 1980; Morrison and Smith, 2002; Tabari, 2021). Several works have used EVT to investigate atmospheric phenomena in order to understand climate extremes (Hanson et al., 2007; Marty and Blanchet, 2012; Rypkema and Tuljapurkar, 2021), hydrology (Burke, Perry, and Brown, 2010; Cannon, 2010) and oceanography (Ruggiero, Komar, and Allan, 2010; Young et al., 2012). There are also several works using EVT on rainfall datasets (Katz, 2010; Mishra and Singh, 2010; Besselaar, Klein Tank, and Buishand, 2013; Bhatia and Ganguly, 2019) and on temperature extremes (Wang et al., 2013; Huang et al., 2016; Pangaluru et al., 2018b).
In this chapter we will use these techniques on three different regional dataset: Antarctic continent, Basilicata region and Calabria region. These regions are characterized by different types of climate and by extreme events. We analyzed these datasets with the EVT approach, with the aim to understand what are the zones more affected by extreme events and also with the purpose to make a forecast study.

1.1 Methods

1.1.1 EVT theory

Extreme value theory (EVT) is one of the statistical approaches often applied to climate science (Fisher and Tippett, 1928; Gnedenko, 1943; Gumbel, 1958; Katz and Brown, 1992; Cooley, 2009; Chavez, Ghil, and Urrutia-Fucugauchi, 2015; Onwuegbuche F. and M., 2019). It has emerged about 70 years ago and it started to be used in many different fields. The statistical approach of EVT has been used to study many phenomena: ocean wave modeling, memory cell failure, wind engineering, managment strategy, biomedical data processing, thermodynamic earthquakes, meterological changes, food science and non-linear beam vibrations (Dawson, 2000; McNulty et al., 2000; Lavenda and Cipollone, 2000; Harris, 2001; Dahan and Mendelson, 2001; Dunne, 2001; Kawas and Moreira, 2001). The main objetive of an extreme value analysis is to quantify the stochastic behavior of a process that assumes larger or smaller values than what is expected from the mean values. Indeed, the analysis of extreme values usually requires the probability estimation of events more extreme than those already observed. There are two approaches that can be followed to apply this method: the Peak Over Threshold approach (POT) and the block maxima approach (BM).
The POT approach is defined as follows: if we consider a set of data of a certain

length, this method consists in choosing a threshold and selecting the data that are greater than the threshold. The statistic is build up only by the values located above the threshold and it is described by

$$G(x) = 1 - \left(1 + \frac{\xi x}{\hat{\sigma}}\right)^{-\frac{1}{\xi}} , \tag{1.1}$$

defined on $\{x : x > 0 \text{ and } (1 + \xi x/\hat{\sigma}) > 0\}$, where

$$\hat{\sigma} = \sigma + \xi(u - \mu) .$$

In the above definitions, u is the chosen threshold. The distribution belongs to the Generalized Pareto family (GPD). The dominant parameter of both distributions is the shape parameter ξ. It determines the qualitative behaviour of the distributions: in the case of GPD, if $\xi < 0$ the distribution of excesses has an upper limit of $u - \hat{\sigma}/\xi$, while if $\xi > 0$ the distribution has no upper bound.
The POT method presents an issue in the determination of the threshold itself. It varies from dataset to dataset and there is no automatic way to uniquely determine it. Let $x_1, ..., x_n$ be a sequence of identically distributed and indipendent measurements. Extreme events will be identified by choosing a threshold u, for which the exceedances will be $\{x_i : x_i > u\}$. The threshold excesses are defined as $y_j = x_{(j)} - u$, for $j = 1, ..., k$, where the exceedances are labelled as $x_{(1)}, ..., x_{(k)}$. The y_j may be deemed as indipendent realizations of a random variable whose distribution can be fitted by a member of the Generalized Pareto family. It is important to pay attention to the threshold choice, because it should be neither too low nor too high. There are two methods that allow us to estimate the threshold.
The first one consists in an exploratory technique applied before the model estimation. It is based on the mean of GPD. If a random variable Y has a generalized Pareto distribution with parameters σ and ξ, the expectation value will be

$$E(Y) = \frac{\sigma}{1 - \xi} ,$$

provided $\xi < 0$. If $\xi > 0$ the mean is infinite. If we now suppose to have a series $X_1, ..., X_n$ that generates excesses of a threshold u_0, we can assume that it can be described by the GPD. If we denote an arbitrary term as X, the expectation will be

$$E(X - u_0 | X > u_0) = \frac{\sigma_{u_0}}{1 - \xi} ,$$

provided $\xi < 0$. If the GPD is valid for the excesses of the threshold u_0, it will be valid for all thresholds $u > u_0$. Therefore, for $u > u_0$

$$E(X - u | X > u) = \frac{\sigma_u}{1 - \xi} . \tag{1.2}$$

$E(X - u|X > u)$ is simply the mean of the excesses of the threshold u. If we now consider n_u observations that exceed u, we can define the mean residual life plot as

$$\left\{ \left(u, \frac{1}{n_u} \sum_{i=1}^{n_u} (x_{(i)} - u) : u < x_{max} \right) \right\} ,$$

where x_{max} is the largest of the X_i. The mean residual life plot should be linear above the threshold u_0. The interpretation of the mean residual life plot is often not easy.

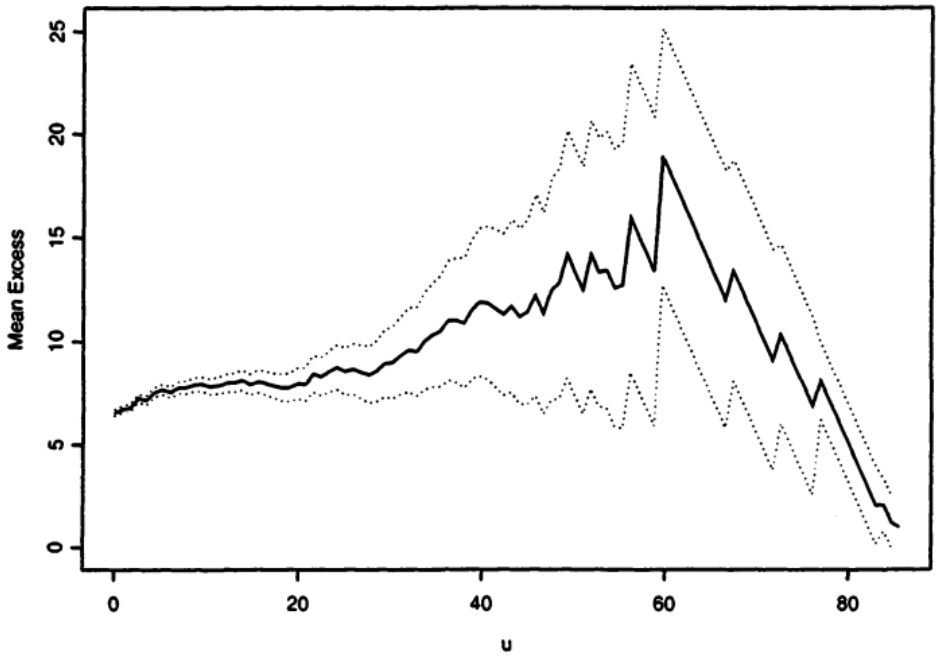

FIGURE 1.2: Mean residual life plot for daily rainfall data (Coles et al., 2001b).

Figure 1.2 shows the mean residual life plot calculated for daily rainfall data from (Coles et al., 2001b). The dotted area is the 95% confidence interval. It seems from the Figure that there is a non-linearity for thresholds from $u = 0$ to $u \approx 20$, and, after a little increase of the mean excesses around a threshold $u \approx 20$, it seems that starting from $u \approx 30$ the linearity is kept up to $u \approx 60$. So we could conclude that the threshold is $u_0 = 60$, but this implies that we have too low exceedances above the threshold. So for this reason we choose the threshold value as $u_0 = 30$.
The second method used for the estimation of the threshold is related to the parameters of the distribution. If a GPD is used for the excesses of a threshold u_0, then also the excesses of a different threshold u can be described by a GPD. The shape parameters of the two distributions are the same. If σ_u is the scale parameter for a threshold $u > u_0$, then

$$\sigma_u = \sigma_{u_0} + \xi(u - u_0) .$$

The scale parameter changes with u unless $\xi = 0$. To avoid this problem the scale parameter is reparameterized as

$$\sigma^* = \sigma_u - \xi u \ .$$

This implies that σ^* is constant with respect to u. Consequently, also ξ should be constant with respect to u, and indeed they should be constant above u_0, if u_0 is a valid threshold for the excesses that follows the GPD . Therefore, plotting σ^* and ξ against u allows us to choose the threshold u_0 as the lowest value of u for which their estimates remain nearly constant.
We report the plot of the scale parameter and of the shape parameter in Figure 1.3 from Coles et al. (2001b).

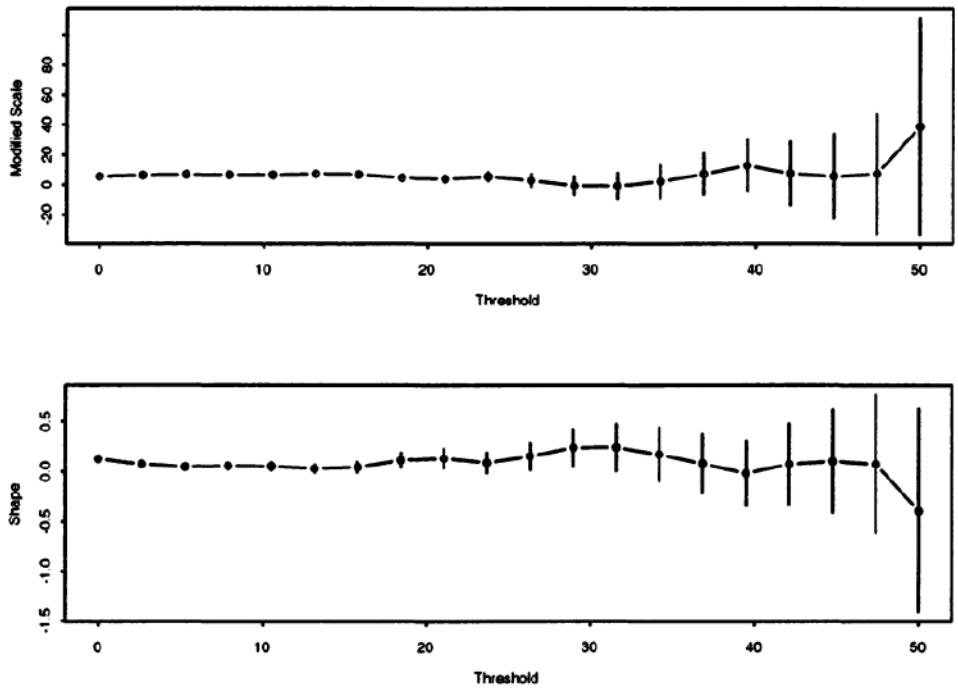

FIGURE 1.3: Scale parameter (**Top panel**) and Shape parameter (**Bottom panel**) against threshold for daily rainfall data Coles et al. (2001b).

As it can be seen from these two plots, in both cases the parameters are near-constant up to $u \approx 30$ and the perturbations are smaller than the sampling errors. Then the choice of $u_0 = 30$ as the threshold value is the most appropriate for the daily rainfall dataset.
Once the threshold is determined, it is possible to estimate the parameters of the GPD through the maximum likelihood estimation (see Prescott and Walden, 1983). If we consider the k values $x_1, ..., x_k$ of the excesses of a threshold u_0, the log-likelihood estimation derived from Eq. (1.1) will be

$$\ell(\sigma, \xi) = -k \log \sigma - (1 + 1/\xi) \sum_{i=1}^{k} \log(1 + \xi x_i/\sigma) \ ,$$

provided $(1+\xi x_i/\sigma) > 0$ for $i = 1,..,k$ and $\ell(\sigma,\xi) = -\infty$ otherwise. Since the analytical maximization of the log-likelihood is not feasible, a numerical technique is used to determine the maximization and to extrapolate the parameters (Lemos, Lima, and Duarte, 2020a).

To asses the quality of a fitted generalized Pareto model four plots, named diagnistic plots, are being built. The four plots are: density plot, probability plot, quantile plot and return level plot. Assuming a threshold u and a sequence of excesses $x_{(1)} \leq ... \leq x_{(k)}$, the probability plot will be

$$\left\{(i/(k+1), \hat{G}(x_{(i)})), \quad i = 1,...,k\right\} ,$$

where $\hat{G}(x_{(i)})$ is the same as in Eq. (1.1), but in this case the parameters have been maximized (the$\hat{}$indicates the maximized parameter)

$$\hat{G}(x) = 1 - \left(1 + \frac{\hat{\xi}x}{\hat{\sigma}}\right)^{-\frac{1}{\hat{\xi}}} .$$

The quantile plot contains the same information as the probability plot, but they are expressed on a different scale. The quantile plot consists of the pairs

$$\left\{(\hat{G}^{-1}(i/k+1), x_{(i)}), \quad i = 1,...,k\right\} ,$$

where

$$\hat{G}^{-1}(i/k+1) = u + \frac{\hat{\sigma}}{\hat{\xi}}\left[x^{-\hat{\xi}} - 1\right] .$$

If the probability plot and the quantile plot lie close to the diagonal, the data are well described by the model. The last plot is the return level plot, made by return level values, i.e., the expected values $\hat{x}_m$ to be exceeded on average once every $1/p$ years and by the return period m. The plot is composed by the pairs $\{(m, \hat{x}_m)\}$ where

$$x_m = u + \frac{\hat{\sigma}}{\hat{\xi}}\left[(m\hat{\zeta}_u)^{-\hat{\xi}} - 1\right] ,$$

$\hat{\zeta}_u$ being the probability for an individual observation to exceed the threshold u. An example of diagnostic plot is presented in Figure 1.4 from Coles et al. (2001b).

The block maxima (BM) approach consists in dividing a set of data, corresponding to observations, into sequences (blocks) of a given length which include n observations, generating a series of block maxima. The block maxima can be fitted with the GEV (Generalized Extreme Value) distribution:

$$G(x) = \exp\left\{-\left[1 + \xi\left(\frac{x-\mu}{\sigma}\right)\right]^{-1/\xi}\right\} , \tag{1.3}$$

where $-\infty < \mu < \infty$, $\sigma > 0$ and $-\infty < \xi < \infty$ are the free parameters of the distribution that are constrained by $1 + \xi(x-\mu)/\sigma > 0$. It is also possible to define,

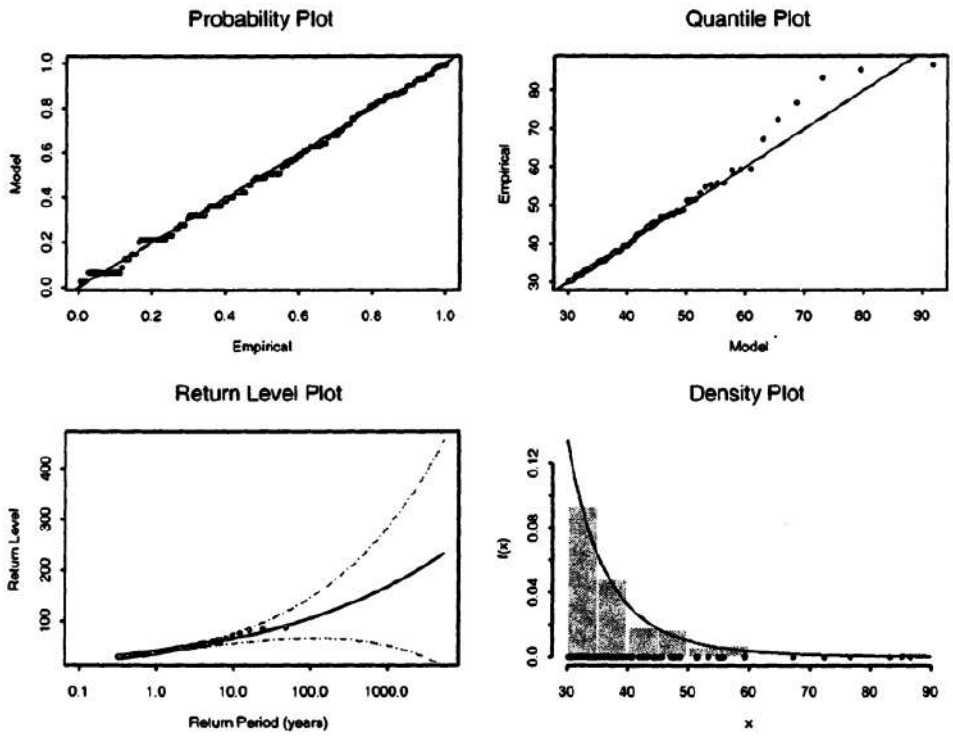

FIGURE 1.4: Diagnostic Plot for the threshold exceedence for the daily precipitations (Coles et al., 2001b). In Figure we can see the Probability Plot (**Top Left**), the Quantile Plot (**Top Right**), the Return Level Plot (**Bottom Left**) and the Density Plot (**Bottom Right**).

in the case of the BM approach, the return level plot as

$$T_p(z) = \mu - \frac{\sigma}{\xi}\left\{1 - [-\log z]^{-\xi}\right\} \tag{1.4}$$

where $z = 1 - p$, and log refers to log to base e . A plot of T_p against $-\log(1-p)$ gives the expectation values of a quantity, with a given accuracy, according to EVT. Return level values are taken in the 95% confidence interval for each station. The Diagnostic Plot in the case of BM approach is shown in Figure 1.5 from Coles et al. (2001b).

1.1.2 Empirical Mode Decomposition

In the method known as "block maxima" (BM), extremes are created by dividing the analysis period into non-overlapping periods of the same size and then choosing the maximum observation of each new period. The choice of the block size is crucial because a very small block could create distortions, while from too large blocks only certain extreme values could be selected (Coles et al., 2001b). The choice of the block length is subject to several considerations. Choosing a time period of one year, then extrapolating the annual maximum, eliminates the problem of seasonal periodicity that strongly influences maximum temperatures. This choice, however,

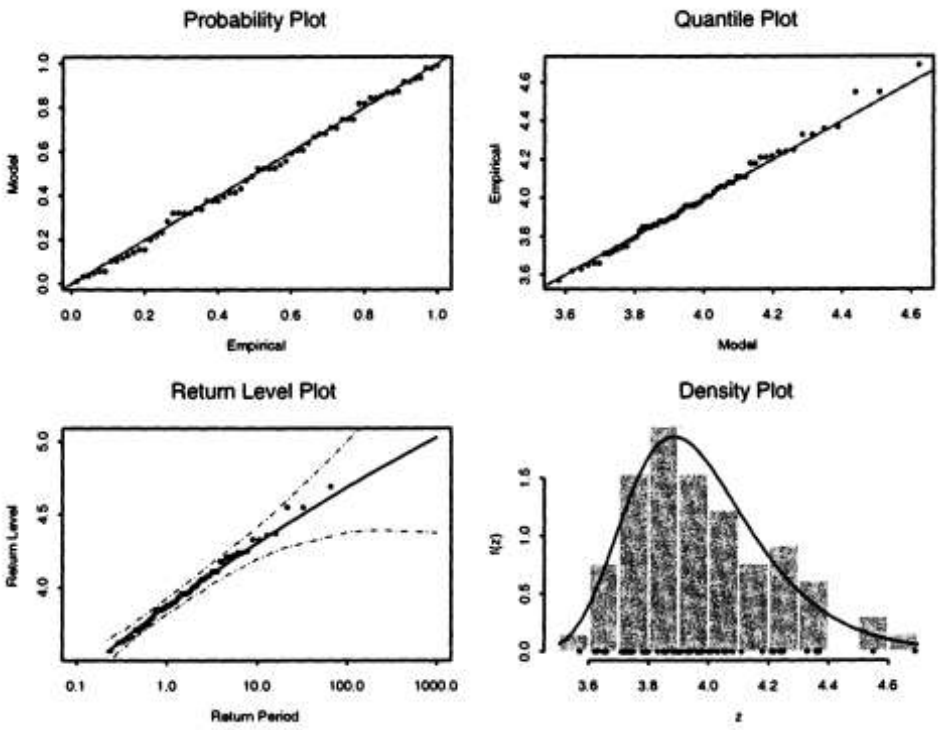

FIGURE 1.5: Diagnostic Plot for the BM fit to the Port Pirie sea level data (Coles et al., 2001b). The Figure has the same composition as Figure 1.4.

greatly reduces the number of extreme events, e.g. in a 30-year dataset there will only be 30 values. On the other hand, selecting monthly maxima allows for many more points but does not eliminate the seasonal contribution, clearly changing the distribution of extreme events. For example, the temperature block maximum in the spring season (defined as March to May) in the upper Midwest will most likely be the same as the May maximum, so the three-month block maximum may not be better approximated than the only May maximum. A block length of 1 year or one season has been used in several number of studies (Fowler et al., 2005; Papalexiou and Koutsoyiannis, 2013; Craigmile and Guttorp, 2013). In other works, in an attempt to use as many points as possible and overcome the effect of seasonality, temperature anomalies were used (Lim and Schubert, 2011; Brown, Caesar, and Ferro, 2008). Daily anomalies are calculated as the difference between each daily temperature and an average value. This value varies depending on the day of the year and is calculated as the average of the daily temperatures recorded over the time interval analysed, namely $\Delta T_i = T_i - \langle T_i \rangle$, where $\langle T_i \rangle$ represents the temperature mean value for the ith calendar day. This definition implicitly assumes the annual seasonal cycle to be constant and generated by a set of stationary processes. The validity of this assumption is often questionable due to the non-linear response of the Sun-Earth system. Irregularities in the seasonal cycle have been observed as both amplitude (Wallace and Osborn, 2002) and phase variations (Thomson, 1995; Stine, Huybers, and Fung, 2009; Vecchio, Capparelli, and Carbone, 2010). Therefore,

following the idea of Vecchio and Carbone (2010), it is possible to use a new definition of temperature anomalies based on the Empirical Mode Decomposition (EMD) (Huang et al., 1998). The EMD has been successfully used in many fields (Echeverria et al., 2001; Battista et al., 2007; Yu, Cheng, and Yang, 2005) including geophysical systems (Salisbury and Wimbush, 2002; Vecchio et al., 2012; Capparelli et al., 2013). The EMD decomposes the temperature signal into a finite number of intrinsic mode functions (IMF) and a residual, which describes the trend, using an adaptive basis derived from each dataset (Huang et al., 1998), i.e.

$$T(t) = \sum_{j=0}^{m} IMF_j(t) + r_m(t) \tag{1.5}$$

Each IMF represents a zero mean oscillation with amplitude and frequency modulations that both depend on time (Huang et al., 1998). For each temperature signal, therefore, it is possible to identify the IMF representing the seasonal oscillation and subtract it from the original signal, so the new definition of temperature anomaly is: $\Delta T_j = T_j - S_j$, where S_j is the IMF that describes the seasonal oscillation, which in a generic dataset can be identified for all stations available by the index j=1 and for simplicity it is indicated by IMF 1. Using this definition, the monthly maximum temperatures used in the EVT analysis maintain a satisfactory number of points and at the same time do not lose useful information from the subtraction of a value set by a simple average. In Figure 1.6 we show an example of the application of the EMD on a sample of temperature data from the United States Historical Climatology Network (HCN) (https://www.ncei.noaa.gov/products/land-based-station/us-historical-climatology-network). In this work Capparelli, Vecchio, and Carbone (2011) applied the EMD model to United States stations located all over the country. Figure 1.6 shows the application of the EMD to two stations: Holly, CO and Covington, LA. They found that both stations are characterized by regular and anomalous seasonal oscillations from the time behaviour of the mode $\theta_1(t)$ (corresponding to our IMF 1). These anomalous oscillations do not occur randomly in time but with some frequency over time. This time, corrisponding to 18.6 years, is related to the nutation motion of the Moon. Therefore, with the application of the EMD to the temperature data of USA's stations, they found a relationship between the temperature seasonal oscillation and the inclination of Moon's orbit with respect to the equatorial plane.

1.2 Accelerated climate changes in Weddell Sea region of Antarctica detected by extreme values theory

On 13 February 2020 The Guardian, followed by many other newspapers and websites, published the news that on 9 February 2020, Antarctic air temperatures rose to about 20.75 °C in a base logged at Seymour Island. This value is not yet validated by the WMO (World Meteorological Organization), but it is not the first time that an

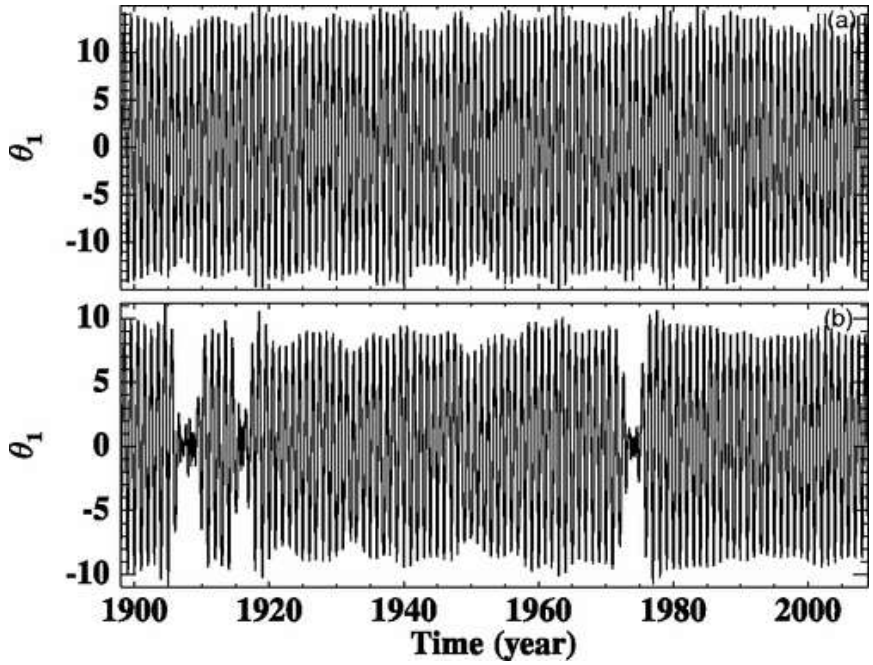

FIGURE 1.6: EMD modes times evolution j=1 for the temperature recorded by (a) Holly, CO. and (b) Covington, LA (Capparelli, Vecchio, and Carbone, 2011).

extreme temperature was registered in these locations. The recorded temperatures have often been described as "abnormal and anomalous", according to a statement made by scientists working at the Antarctic bases. Since polar regions showed the most rapid rates of climate change in recent years, this abnormality is of primary interest in the context of vulnerability of the Antarctic to climate changes. Using data detected at different Antarctic bases, we investigate yearly maxima and minima of recorded temperatures, in order to establish whether they can be considered as usual extreme events or really abnormal, with the help of the Extreme Values Theory (EVT). We aim to establish up to date possible acceleration of regional climate changes (Giorgi et al., 2001; Vaughan et al., 2003), and we try to provide an unbiased measure of the claimed "abnormality" of recent observed events.

1.2.1 Data and Results

We investigated daily temperatures, available on `http://basmet.nerc-bas.ac.uk/sos/`, detected at two different Antarctic bases, whose characteristics and positions are reported in Table 1.1 and Figure 1.7, respectively. In order to ensure good accuracy of the statistical model, a time series of at least 30 years and a low number of data gaps are required. For this reason, only two stations of the dataset have been chosen. An augmented Dickey-Fuller test shows that the data are stationary, the p-value for significance being of the order of 0.05 (Fuller, 1976). For each dataset we split the data into sequences of observations of one year length, and we collected the discrete time series $T_i^{(max)}$ and $T_i^{(min)}$, for $i = 1 \dots, N$, which represent the annual maxima and minima of temperatures (N being the number

of years of each dataset). For the selection of the data we made sure that they were not affected by anomalous effects. High incoming solar flux and high surface albedo result in radiation biases that can occasionally exceed 10°C in summer in cases with low wind speed (Genthon et al., 2011). The early records from all stations were made using a Stevenson screen and then later using aspirated radiation shields, overcoming the effects of anomalous solar heating. Another effect could be related to low speed winds that could lead to a spurious heat up. To bypass the problem of low wind we chose the maximum value of the year considering days with wind speed greater than 2 m/s. It is worth reporting that the whole Halley dataset may be affected by some heterogeneity, because the station has been sometimes moved inland from the relatively warm ocean (Turner et al., 2020). We think that the extreme yearly temperatures we used here should be poorly affected by the heterogeneity, if any. The information about the quality of data is available at `https://legacy.bas.ac.uk/met/READER/metadata/metadata.html`. The time series obtained through annual maxima and minima are reported in Figure 1.18.

TABLE 1.1: Information about the used dataset, namely the names of Antarctic bases, the date from which temperatures are available, latitude and longitude of the bases, the date of the maximum registered temperature and the maximum registered temperature over the considered period. Data are available at `http://basmet.nerc-bas.ac.uk/sos/`.

Base	Record	Latitude	Longitude	Date of T_{max}	$T_{max}(^\circ C)$
Halley Met	1960/01/24	75°36′45″ S	26°11′52″ W	1991/12/23	6.13
Rothera Met	1976/04/01	67°34′06″ S	68°07′33″W	2003/01/20	8.7

We maximize the log-likelihood function, for T_i corresponding to either $T_i^{(max)}$ or $T_i^{(min)}$, subject to variations of GEV free parameters. The log-likelihood is given by

$$\ell(\mu,\sigma,\xi) = -N\log\sigma - (1+1/\xi)\sum_{i=1}^{N}\left[1+\xi\left(\frac{T_i-\mu}{\sigma}\right)\right] - \sum_{i=1}^{N}\left[1+\xi\left(\frac{T_i-\mu}{\sigma}\right)\right]^{-1/\xi} \tag{1.6}$$

for $\xi \neq 0$, and

$$\ell(\mu,\sigma) = -N\log\sigma - \sum_{i=1}^{N}\left(\frac{T_i-\mu}{\sigma}\right) - \sum_{i=1}^{N}\exp\left[-\left(\frac{T_i-\mu}{\sigma}\right)\right] \tag{1.7}$$

for $\xi = 0$.

The maximization provides the best-fit parameters $\hat{\xi}$, $\hat{\sigma}$ and $\hat{\mu}$ for both temperature maxima and temperature minima, reported in Tables 1.2 and 1.3, respectively.

For the Halley-Met dataset, the plot of the GEV function for annual temperature maxima, derived using the free parameters obtained through the maximization of

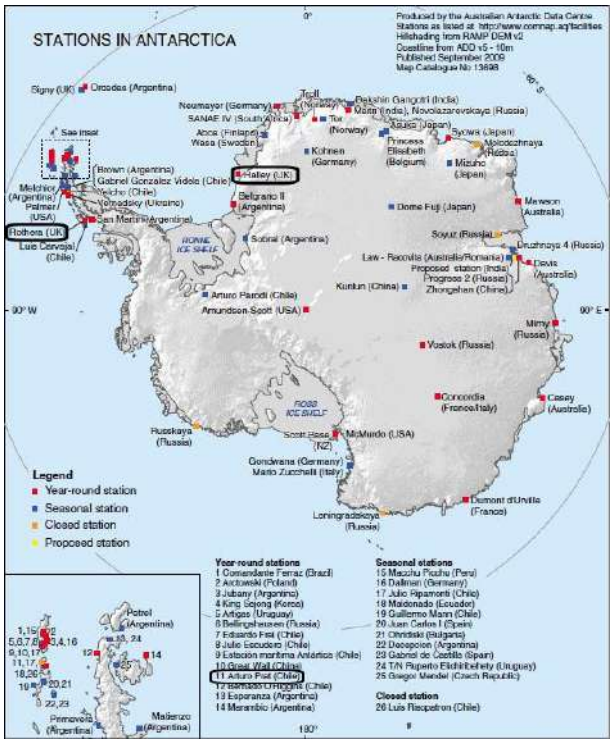

FIGURE 1.7: Map of Antarctic Peninsula and position of the analyzed stations (positions are indicated by the boxes).

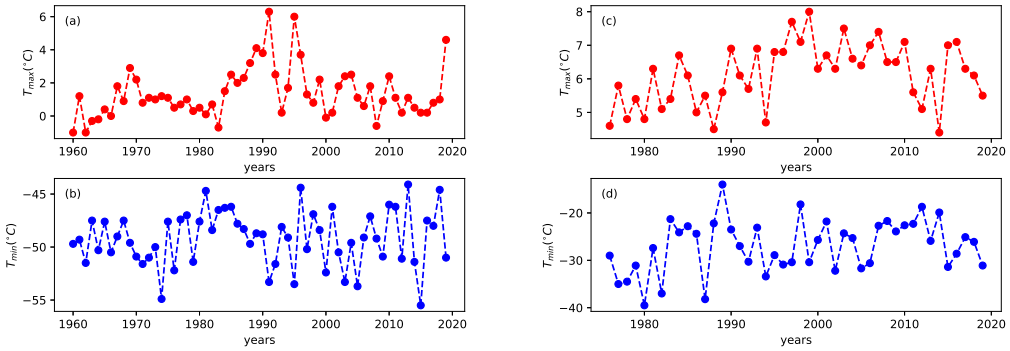

(A) (B)

FIGURE 1.8: (a) - (b) Annual maximum and minimum temperatures at Halley Met Station. (c) - (d) Annual maximum and minimum temperatures at Rothera Met Station.

TABLE 1.2: Values of the three parameters, with their errors, obtained from the maximum likelihood estimation method for maximum temperature events. The distribution type is also indicated.

Station	$\hat{\mu} \pm \Delta\hat{\mu}$	$\hat{\sigma} \pm \Delta\hat{\sigma}$	$\hat{\xi} \pm \Delta\hat{\xi}$	Type of distribution
Halley Met	0.6851 ± 0.1614	1.1191 ± 0.1172	-0.0307 ± 0.0901	Weibull
Rothera Met	5.8517 ± 0.1572	0.9475 ± 0.1157	0.3721 ± 0.1003	Frechèt

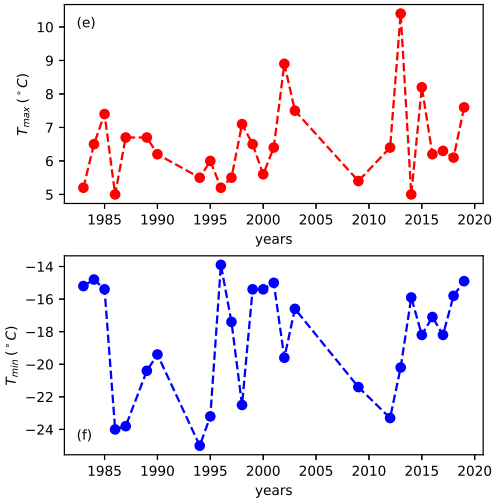

FIGURE 1.9: e) - (f) Annual maximum and minimum temperatures at Arturo Prat Station.

TABLE 1.3: Same information as in Table 1.2, but for minimum temperature events.

Station	$\hat{\mu} \pm \Delta\hat{\mu}$	$\hat{\sigma} \pm \Delta\hat{\sigma}$	$\hat{\xi} \pm \Delta\hat{\xi}$	Type of distribution
Halley Met	-49.9956 $\pm$ 0.3817	2.6866 $\pm$ 0.2765	0.3789 $\pm$ 0.0862	Frechèt
Rothera Met	-28.8881 $\pm$ 0.9259	5.6488 $\pm$ 0.6472	0.1538 $\pm$ 0.0805	Frechèt

log-likelihood, is reported in Figure 1.10. In the same figure, we report the probability plot obtained through the ordered sequence $T_{(1)} \leq T_{(2)}, \cdots \leq T_{(N)}$ by plotting the empirical GEV, namely $G^{(e)}(T_{(i)}) = i/(N+1)$, against the model-based GEV, namely $G(T_{(i)})$, obtained from (1.3). The linear scaling suggests that data are globally in agreement with EVT, although small departures from the linear relation indicate small disagreement with the theory. However, the probability plot is bounded to unity except for few points that do not follow the linear scaling.

To overcome the weakness of the probability plot and highlight possible departures from the GEV model, the quantile plot is particularly useful. It is obtained by plotting $T_{(i)}$ against the inverse GEV function $T_p(i/(N+1))$. Departures of the quantile plot from the reference linear relation indicate real extreme values which are not described through EVT. Looking at Figure 1.10, panel (c), it can be seen that high values of G_{model} are not well reproduced by the linear model, thus indicating a departure from EVT. This implies the occurrence of abnormally high temperatures with respect to the expected values of linear climate changes. Even with the limited datasets at our disposal, the observed change of the linear slope of the data, with respect to the expected model, is a strong indication that the increase in temperatures can be considered as really abnormal, even in the presence of little change.

As far as the return level plot is concerned, through eq. (1.4) we can get μ as a function of T_p, such that the log-likelihood function reads $\ell(T_p, \sigma, \zeta)$, that is, T_p becomes a

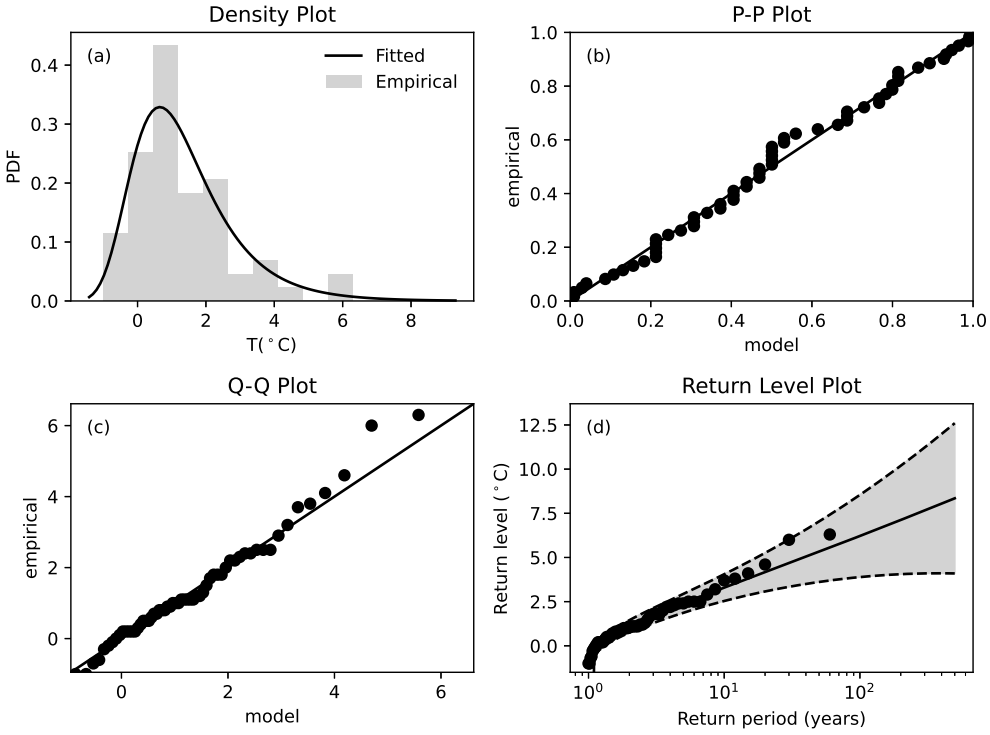

FIGURE 1.10: The four diagnostic plots for maximum temperatures at the Halley Met Station, as described in the text. Panel a) represents the density plot, the data are represented by histogram bars and the solid line corresponds to the fit with the GEV function. The probability plot and the quantile plot are reported in panels b) and c), respectively (the full line is the theoretical model). The return level plot is reported in panel d). The grey area between the dashed lines represents the 95% confidence interval for the probability of occurrence.

parameter which can be obtained through the maximization procedure for each period $1/p$. The return level plot is reported in Figure 1.10, panel d), where the dashed lines represent the 95% confidence interval for the probability of occurrence. According to this plot, we can see that extremes with a theoretical return level (full line) of hundreds of years, namely extreme events possibly described by EVT, could instead occur every tens of years according to the real trends (bullets). Moreover, note that the maximum temperature registered so far $T_M^{(max)} = \max\left[T_i^{(max)}\right]$, can have a high probability of being overcome in a few years. This indicates that a model of linear global warming in Antarctic does not take into account the abnormally high temperatures registered in the last years.

In Figure 1.11 we report the same plots as in Figure 1.10, but obtained for the yearly temperature minima at Halley-Met. The departure from EVT is less evident than for the temperature maxima. The quantile plot shows very small departures from the linear expected values. This means that extreme events for temperature minima cannot be considered as abnormal with respect to EVT. However, the return level plot shows, as before, an increase of the return probability of the warmest minima of yearly temperatures, which have a probability of occurrence anticipated with respect

to the EVT estimate. Also in this case local warming is evident, perhaps anticipating extreme events in the near future. Moreover, we observe that the temperature minima are expected to overcome the maximum value of temperature minima, namely $T_M^{(min)} = \max\left[T_i^{(min)}\right]$, in a few years.

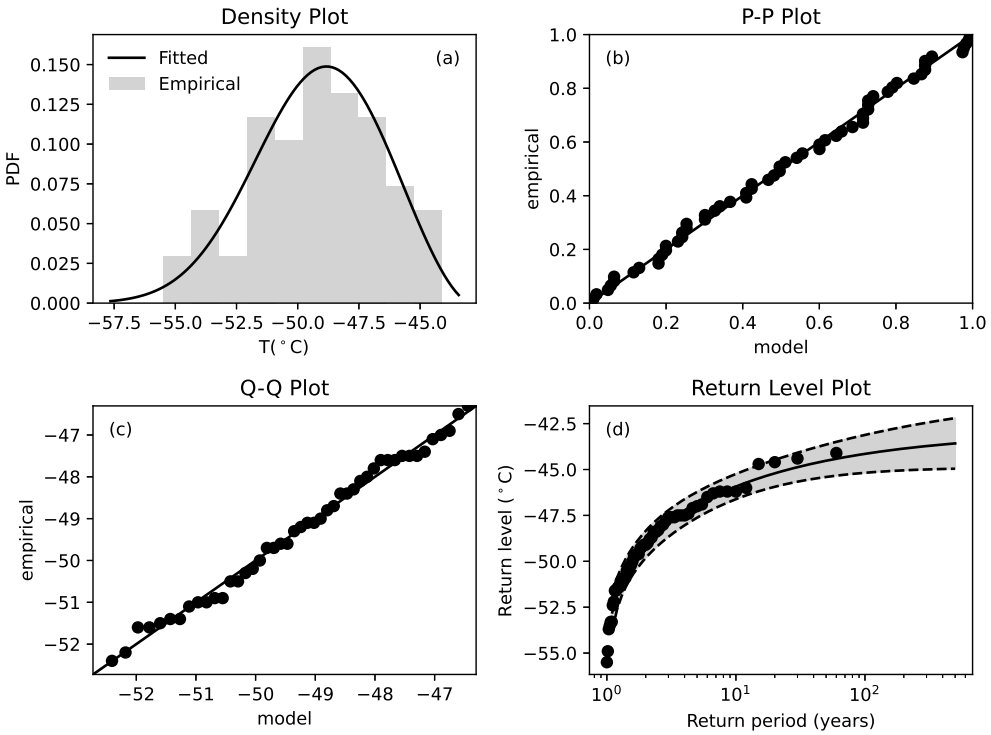

FIGURE 1.11: Same plots as in Fig. 1.10, but for the annual minimum temperature values at Halley Met.

We analyzed also the dataset obtained from Rothera Met. In Figures 1.12 and 1.13 we show the same plots as before for the annual maximum and minimum temperatures, respectively.

We found results which are similar to the previous station. The quantile plot evidences, also in this case, a departure from the linear theory for temperature maxima, even though to a lesser extent with respect to Halley Met.

As we discussed before, the highest temperature reported by the media was found near Marambio station, in the Antarctic Peninsula. We analyzed available data from a station close to Marambio, the Arturo Prat station (see Figure 1.7). In this case, at variance with the previous analysis, for which the temperature maxima were recorded up to 2019, we add the $T_N^{(max)}$ for 2020, under the hypothesis that the February registered value should probably represent the maximum extreme value for 2020. Although the length of the dataset is smaller than for the previous stations, the results shown in Figure 1.14 are very interesting. In fact, the quantile plot shows a strong departure from the linear model and the theoretical return level plot changes slope with respect to the previous cases. This suggests that in the Seymour Island climate changes and local warming are extremely accelerated. The recorded

maximum temperature in February is anticipated with respect to EVT, which would have predicted temperatures like that recorded shifted forward by almost fifty years.

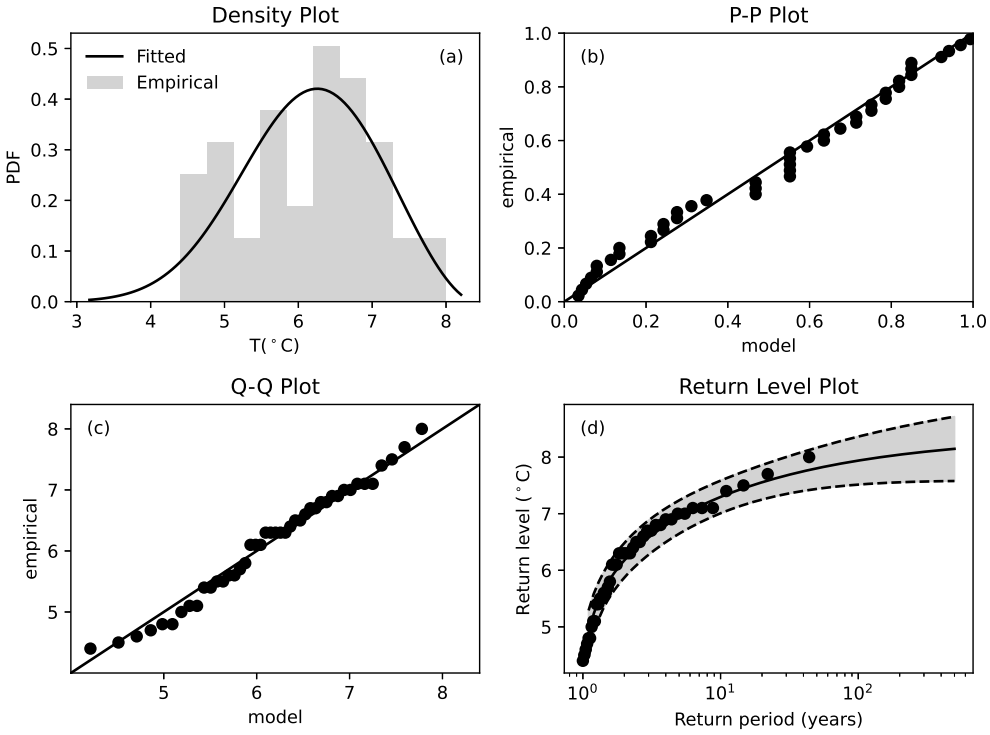

FIGURE 1.12: Same plots as in Fig. 1.10, but for annual maximum temperatures at Rothera station.

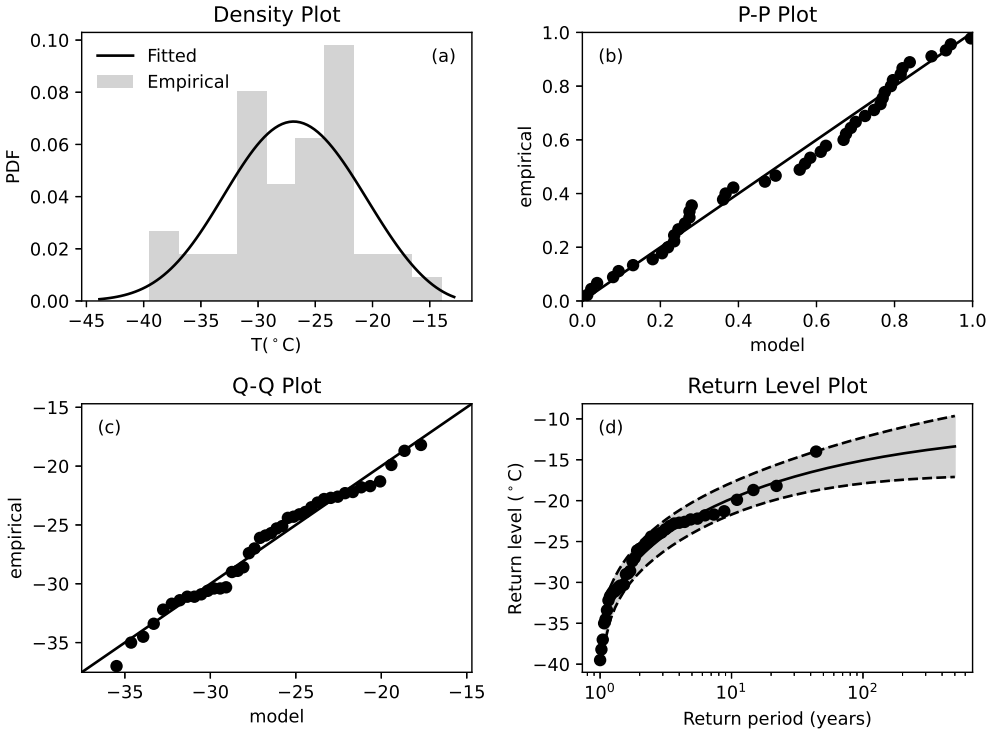

FIGURE 1.13: Same plots as in the previous figures, but for annual minimum temperatures at Rothera station.

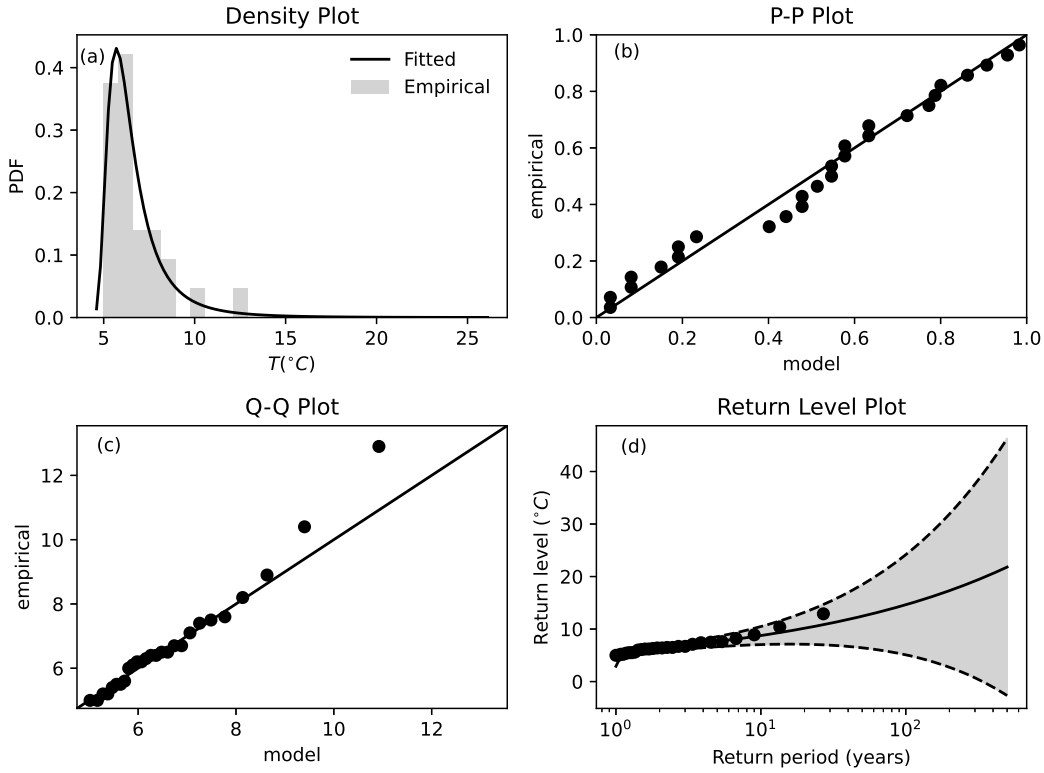

FIGURE 1.14: The four diagnostic plots for maximum temperatures of the Arturo Prat Station.

1.3 Extreme value theory approach for daily rainfall data of Basilicata, southern Italy

The occurrence of extreme rainfall events has increased dramatically in recent years, causing ecological, economic and social disasters. It is now well known that the intensity of the heaviest extreme precipitation events increases with global warming. How often such events arise in a warmer world is, however, less well defined. Using the Extreme Value Theory (EVT), daily data of accumulated rainfall in the Basilicata region - southern Italy - were analysed over a 30-year period. With the help of the EVT a forecasting analysis can be done, in order to better understand what are the zones of the region in which there is a higher occurrence of extreme rainfall and what are the regions affected by the absence of extreme events.

1.3.1 Data

Our analysis is carried out using a historical rainfall dataset of the Basilicata region, located in southern Italy. Data are provided by the multi-risk centre of the regional civil protection office of Basilicata (http://centrofunzionalebasilicata.it/it/scaricaDati.php). The dataset contains information from about 50 stations and for each station the daily rainfall measurements are recorded from different starting times. The dataset starting times vary from station to station, going from 1928 to 2015. Indeed, some series present data gaps that cover, in many cases, periods longer than 10 years. The signal of daily rainfall data for the Potenza station is shown in Figure 1.15(a). This is the most complete dataset at our disposal, with data starting from 1928 and with a lack of data for only a few years after 1940, a very common gap in Italy due to the Second World War. In Figure 1.15(b) the Sinni station data are shown. In this case data start from 2002 and there is no lack of data.

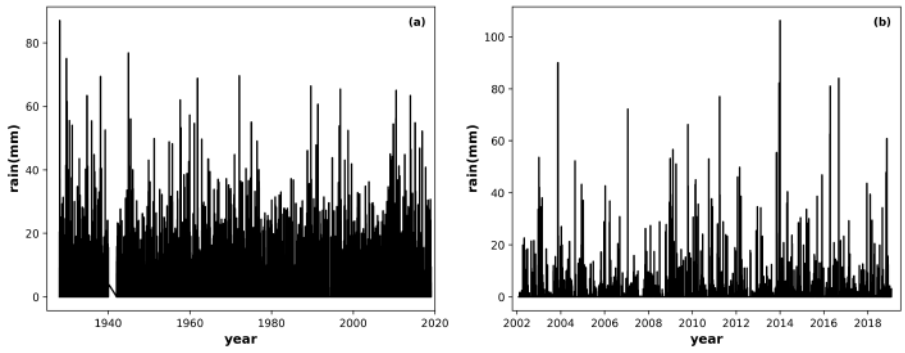

FIGURE 1.15: Daily rainfall data for (a) Potenza station and (b) Sinni station.

Since the aim of our work is to carry out a spatio-temporal statistical analysis of rainfall data, it is necessary an attempt to uniform the dataset in order to make the analysis as meaningful as possible and to use as many stations as possible. To this aim we select the maximum number of stations with at least 30 years of continuous

data in the same time interval, following the indications of the World Meteorological Organization, which read: "a 30-year period is long enough to filter out any inter annual variation or anomalies, but also short enough to be able to show longer climatic trends". This reduces the analysed dataset from 50 to 12 stations covering the time interval from 1950 to 1980. The stations cover quite uniformly the whole Basilicata region. Figure 1.16 shows the locations of the 12 stations over the Basilicata region.

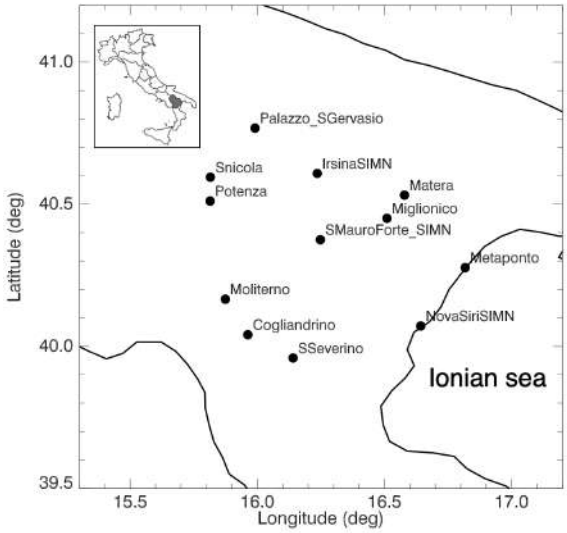

FIGURE 1.16: Geographic distribution of the 12 stations.

1.3.2 Results

The EVT method was applied to the 12 stations using the GPD approach, producing, for all of them, the so called "diagnostic plots", namely the Probability Density Function (PDF), the P-P Plot, the Q-Q Plot, and the Return Level Plot. As already mentioned in Section 1.1.1, when the GPD is used it is necessary to choose a threshold, in order to select the values that will represent the "extreme values" of the sample available. As discussed in Section 1.1.1, there are two methods that can help us to make this choice. The first one is via the Mean Residual Life Plot (MRL). In Figure 1.17 we show the MRL for the Potenza station.

The colored area represents the 95% confidence interval. From Figure 1.17 it is possible to see a linear behaviour of the curve from $u = 0$ to $u \approx 20$ and, after a small increase of the mean excesses around a threshold $u \approx 20$, it seems that the curve has also a linear behaviour up to $u \approx 40$. For the same reasons discussed in Section 1.1.1, we can choose the threshold value as $u_0 = 20$.

In order to have a more precise determination of the threshold for the Potenza station, we can use second the method mentioned in Setion 1.1.1, which uses the parameters of the distribution for the estimation of the treshold. We report the plot of the scale parameter and of the shape parameter in Figures 1.18a and 1.18b.

From the two plots, it seems that the parameters are near-constant up to $u \approx 15$. So we choose $u_0 = 15$ as the threshold value for the Potenza station. We made the same

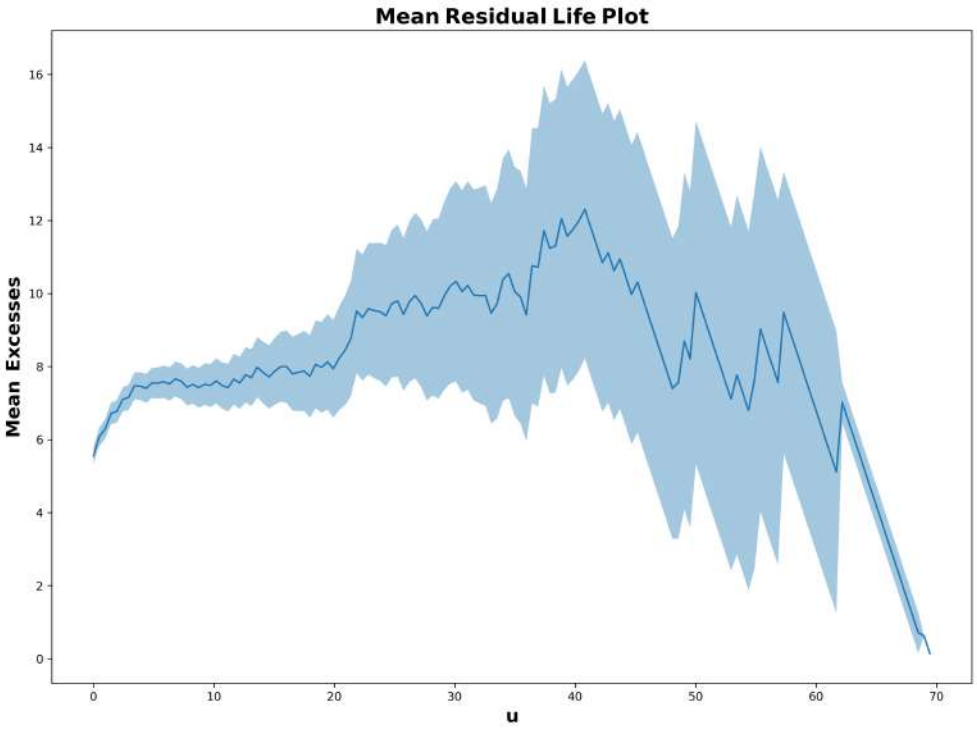

FIGURE 1.17: Mean residual life plot for Potenza station.

assumption for all the stations we analyze in this work.
Figure 1.19 shows the results for the Potenza station, where the selected threshold is $u_0 = 15$ mm. The diagnostic plots indicate that the model appears to be in agreement with the data, although some points in the q-q plot deviates from the diagonal, that is, the largest extreme rainfall values recorded (except for the last point) show a greater increase than the expected extreme value. The same behaviour can be observed in the return level plot, although all the empirical points (blue dots) are within the 95% confidence interval represented by the red dashed lines. It is important to emphasise that, while the empirical values cannot exceed a return time greater than the temporal length of our dataset (30 years), an important property of EVT is that of being able to estimate a return value (with a certain probability) for times greater than 30 years.
Through a spatial interpolation, using the Inverse Distance Weight method (IDW), it was possible to use the return values for all the stations to build up maps of the return levels on a $1.5° \times 1.5°$ grid with a resolution of $0.1°$. THE IDW method is one of the common used method for spatial interpolation, but it presents several limitations: it is sensitive to the anomalous values in the datasets and this can lead to inaccurate predictions; a sparse sampling or a clustering of the sample points can results in inaccurate predictions; the choice of the weighted parameter can highly affect the resulting estimates leading in some cases to an overfitting or an underfitting of the data; the lack of statistical rigore since there is non way to quantify the level of confidence in the estimated values ot to evaluate the accurracy of the predictions; it is limited to small-scale applications because of its computational complexity and

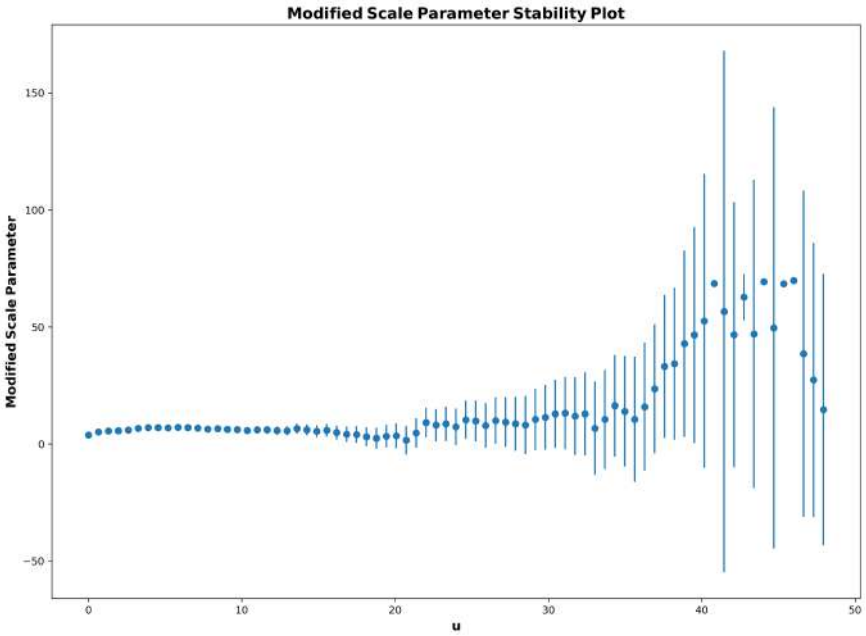

(A)

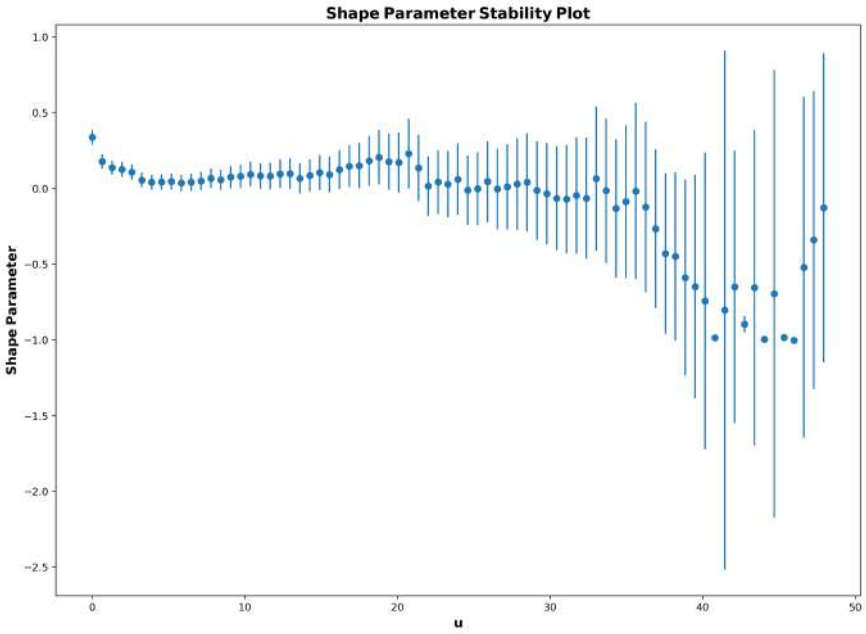

(B)

FIGURE 1.18: (A) Scale parameter against threshold for the Potenza station. (B) Shape parameter against threshold for the Potenza station.

sensitivity to sample distribution. Figure 1.20 shows the return level maps obtained from the empirical data at different return times (RT), namely 5, 8, 15, and 30 years. Figure 1.20 reveals a north-western area where the magnitude of the extreme events is smaller - for each time scale - than in the south-eastern side, in particular for the stations facing the Ionian Sea. Observing Figure 1.20, it can be seen that the Nova Siri station, located on the Ionian Sea, has the highest daily rainfall value at every return time except for RT=30 years, where the maximum value is reached by the

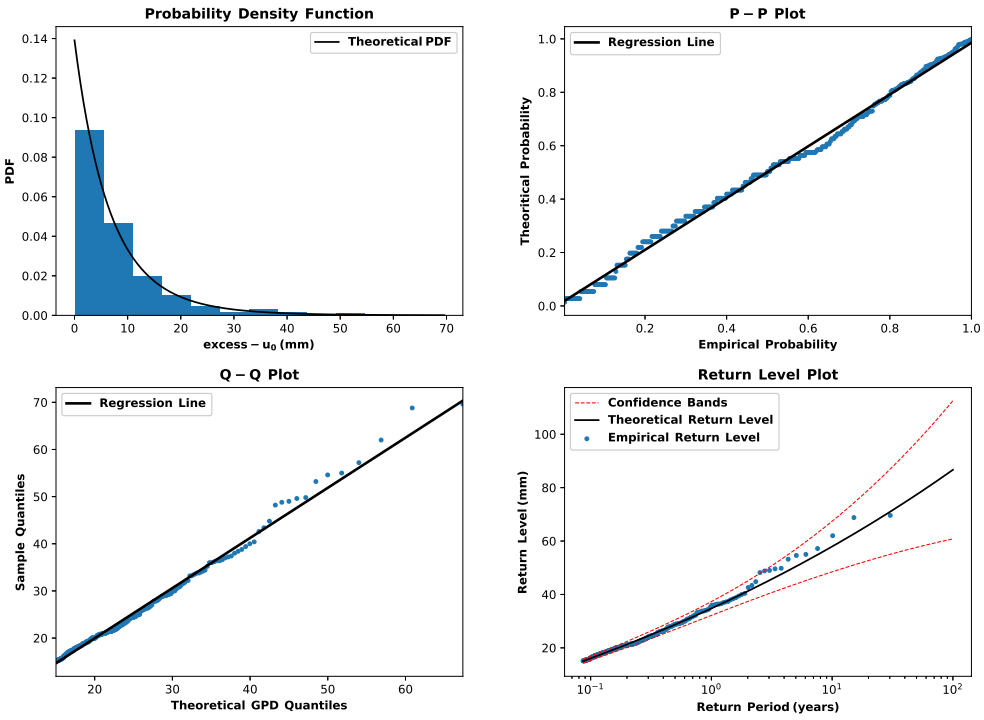

FIGURE 1.19: The Diagnostic Plots for the Potenza station.

Miglionico station, located inland and in a central position. This value, the absolute maximum, corresponds to 249 mm of rainfall accumulated in a single day.

It is important to note that the empirical return values are not known for all the stations, especially for larger return times (see the last panels in Figure 1.20). This is because, being an empirical value, it is not always possible to detect it at the same return time for all the stations. Moreover, since the return time associated to the empirical data is related to the block size of the sample, not all the stations present the same values for the last return period. This implies that, for higher return times, the spatial interpolation was calculated with fewer points. This problem does not arise for the theoretical return value, since extreme events are estimated theoretically and for each return time chosen by the numerical procedure (in our case with a variation of 0.1 years). The theoretical return level maps are reported in Figure 1.21 for return times of 5, 8, 15, and 30 years.

Comparison of the empirical and theoretical return values does not show any strong differences, except for RT = 30 years. Although with lower rainfall values, the theoretical maps confirm the division between the north-western and south-eastern areas. The comparison between the empirical and theoretical maps highlights the anomaly of the Miglionico station, located, as already mentioned, in the central part of the region. For this station, the extreme rainfall recorded is significantly higher

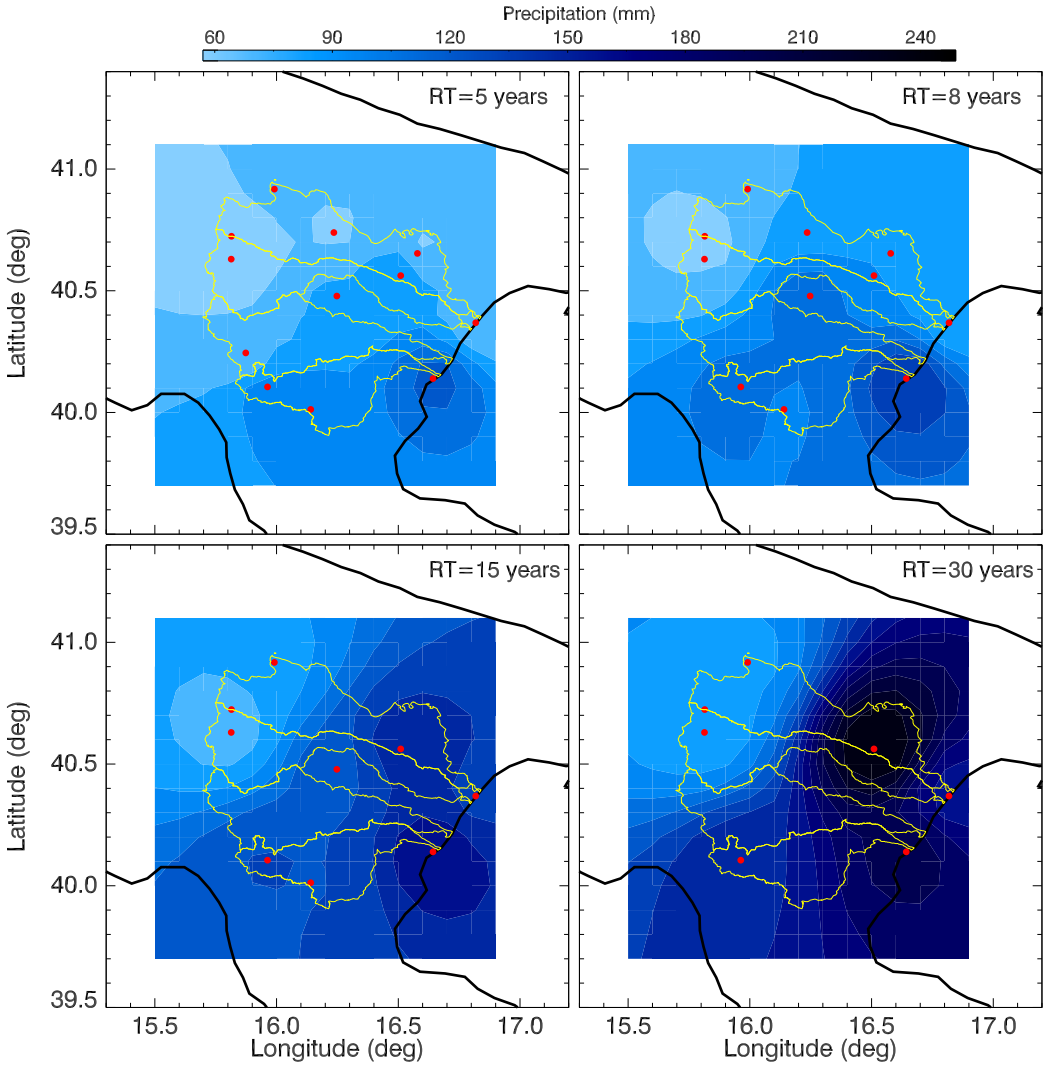

FIGURE 1.20: Empirical return level maps at different return times (RT). The red dots indicate the positions of the stations, while the yellow lines show the main hydrographic basins, namely: Agri, Basento, Bradano e Sinni.

than that predicted by the model, as can be seen in Figure 1.22(a), where the empirical values are higher than expected, even exceeding the limits of the 95% confidence interval. The same behaviour as for Miglionico can be observed in other stations, all located in the central area, in particular Cogliandrino, Moliterno and San Mauro Forte (see Figure 1.22 panels (b), (c) and (d) respectively).

This statement is confirmed and well illustrated in Figure 1.23, which shows the map of the variation between the empirical and theoretical return levels calculated for the same return period, $\Delta P = RL_{emp} - RL_{theo}$. It is evident that for shorter return periods there are areas where the recorded data is lower than expected, while for longer return periods the central area near the Miglionico station presents the maximum variation (approximately 80 mm) with the empirical value being considerably higher than the theoretical one.

The results illustrated in Figures 1.22 and 1.23 indicate that for some stations the

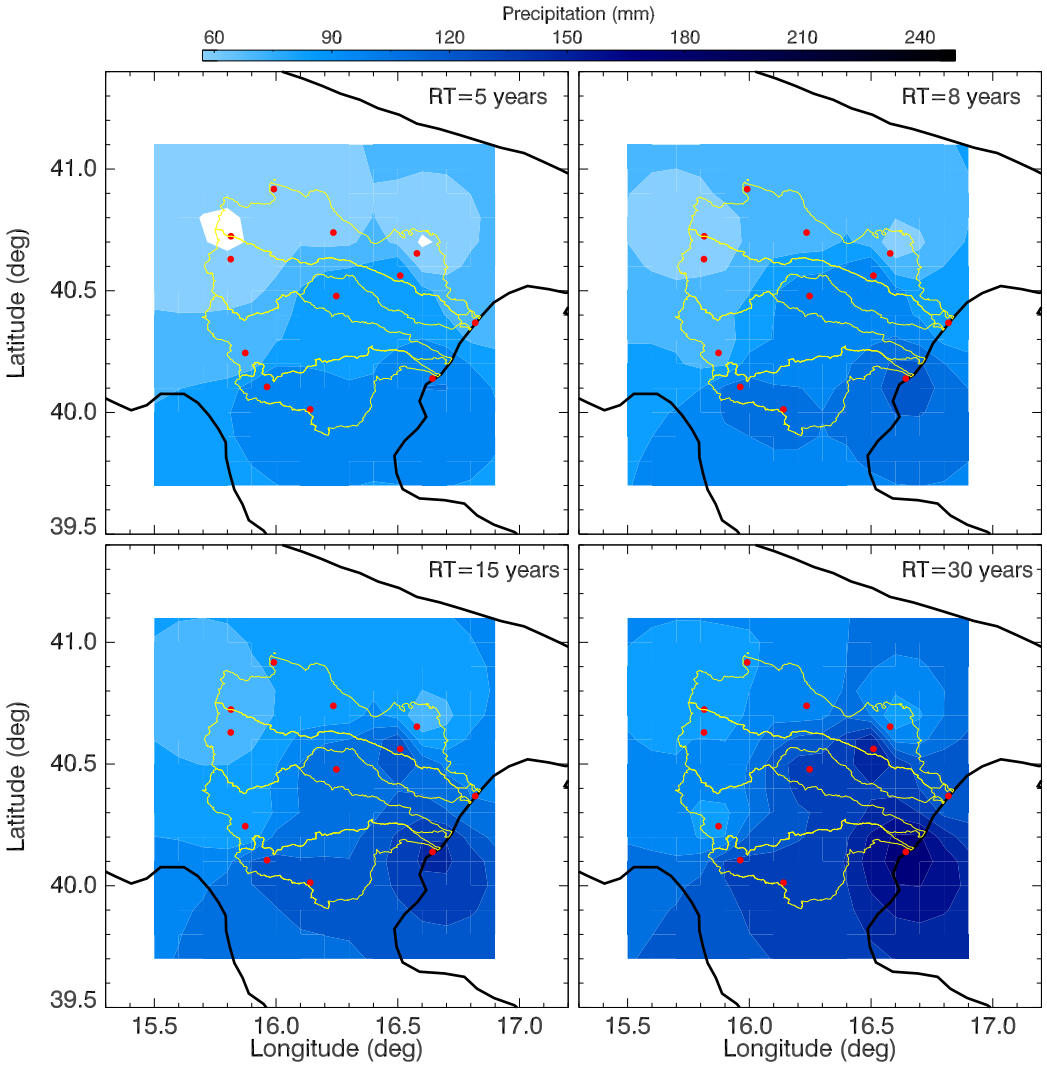

FIGURE 1.21: Theoretical return level maps at different return times (RT). The red dots indicate the positions of the stations while the yellow lines show the main hydrographic basins, namely: Agri, Basento, Bradano e Sinni.

amount of rainfall accumulated in a single day is significantly greater than that expected from the theory of extreme values. These values can be referred to as "anomalous rainfall" occurring in some areas of Basilicata and specifically in the central part of the region.

As previously mentioned, one of the advantages of EVT theory is to be able to predict the return value exceeding the time scale imposed by the dataset. For example, Figure 1.24 shows the forecast for a return time of 50 years. The highest value is reached at the Nova Siri station with a daily rainfall exceeding 200 mm and where there is always a clear separation between the north-western and south-eastern zones.

For the sake of completeness, Figure 1.25 presents a boxplot showing the values of the theoretical return level and the corresponding error obtained for RT=50 years. The stations on the x-axis are shown in descending order of height in the basins. The graph indicates an almost constant trend with altitude, but with two anomalies

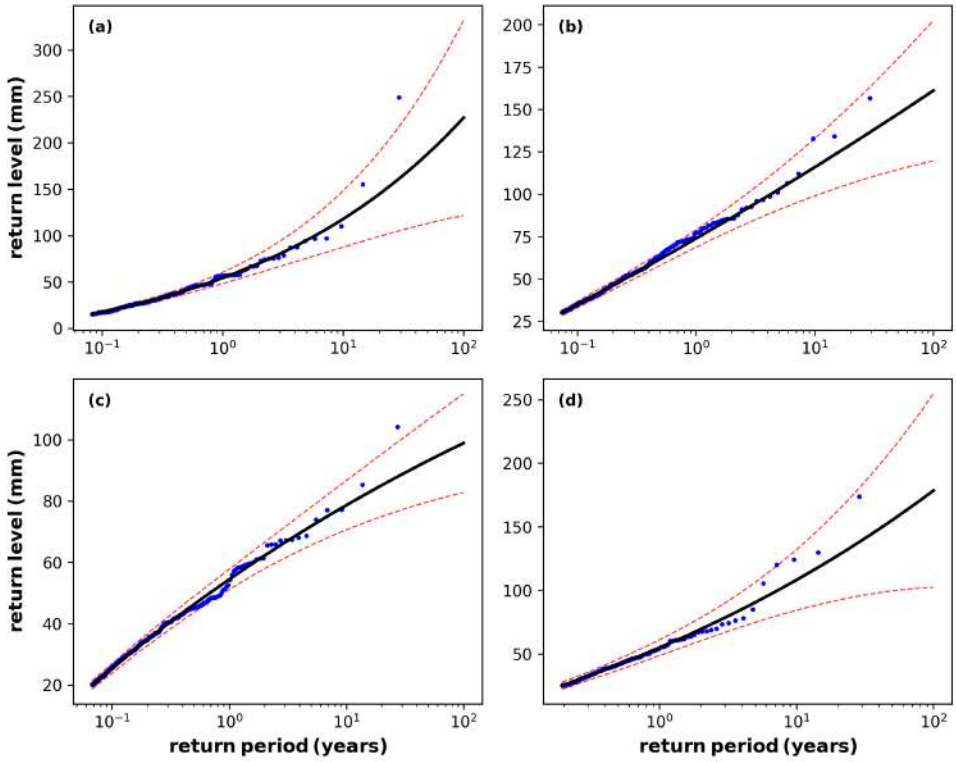

FIGURE 1.22: Return level plots: Miglionico (a), Cogliandrino (b), Moliterno (c) and San Mauro Forte (d) station.

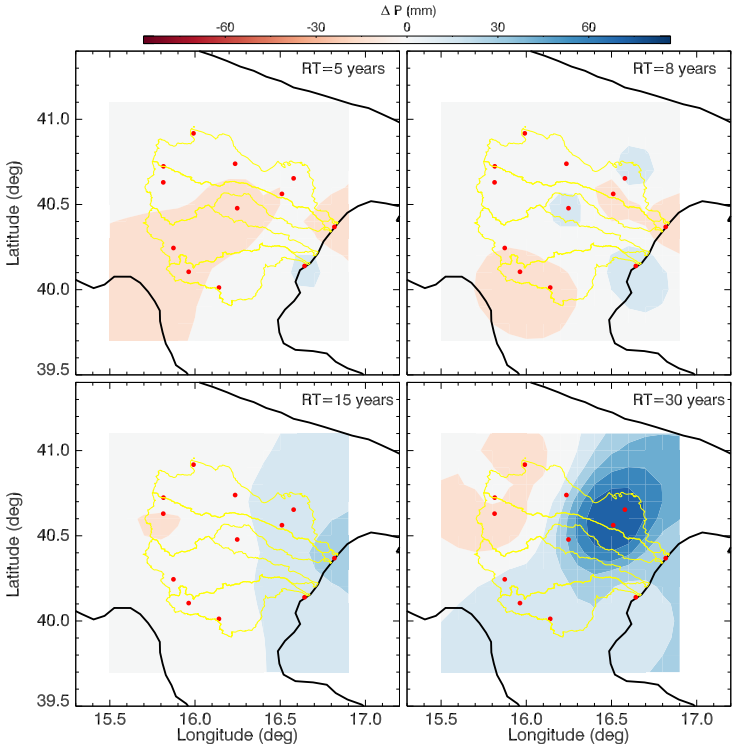

FIGURE 1.23: Maps of the difference between the empirical and theoretical return level at different return times (RT).

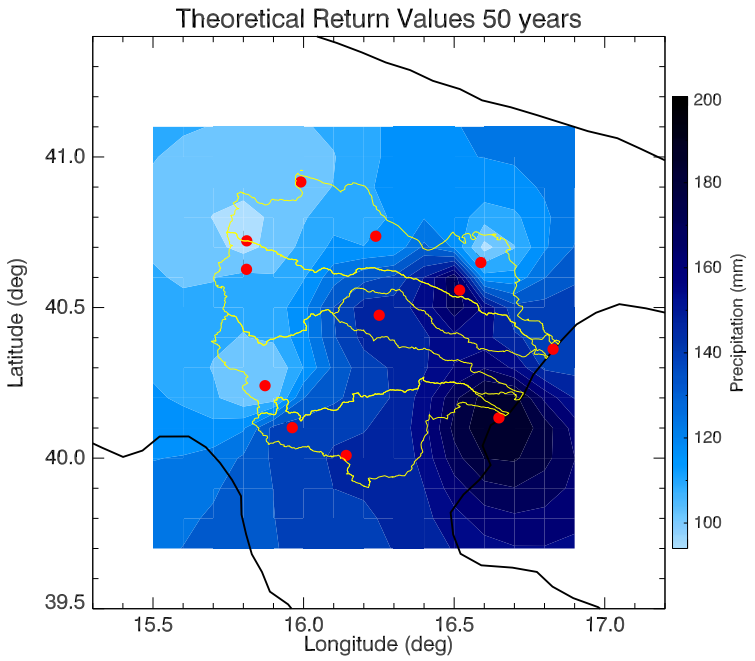

FIGURE 1.24: Theoretical return level map at return time, RT=50 years. The red dots indicate the spatial position of the stations while the yellow lines draw the main hydrographic basins, namely: Agri, Basento, Bradano e Sinni

in the central area, i.e. in the stations of Miglionico and San Mauro Forte, which, together with Nova Siri, present the highest return values associated with a wider confidence interval (see Figure 1.25).

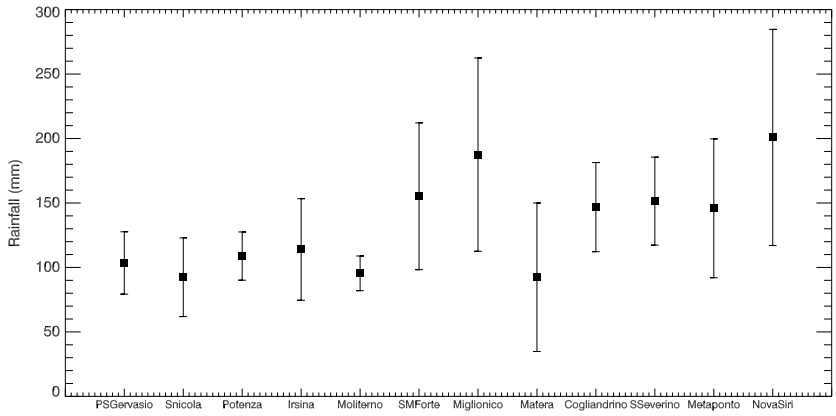

FIGURE 1.25: Box-plot of the return value forecast with its corresponding error for RT=50 years.

1.4 Daily precipitation and temperature extremes in southern Italy (Calabria region)

The application of extreme value theory (EVT) to study daily precipitation and temperature extremes in Calabria region (southern Italy) is performed, mainly considering a long-term observational dataset (1990-2020), and also investigating the possible use of the ERA5 (ECMWF Reanalysis v5) fields. The Calabria region (southern Italy), in the central Mediterranean, is an area particularly prone to heavy rain events and heatwaves. The region has a complex orography with several mountain chains and a marked land–sea contrast that leads to the coexistence of different local atmospheric circulation regimes. Several papers dealt with the topic of severe weather events in the Calabria region, in particular heavy rains, both adopting statistical/climatological approaches (Federico et al., 2009; Federico et al., 2010; Greco, De Luca, and Avolio, 2020), and through in-depth analyses of remarkable extreme episodes (Avolio and Federico, 2018; Federico, Bellecci, and Colacino, 2003; Federico et al., 2008b; Avolio et al., 2019) in order to study their characteristics and dynamic. Federico et al. (2009), in particular, showed a first exploratory analysis on a 30-year (1978–2007) homogeneous precipitation database for the Calabria region (daily precipitation / 88 rain gauges), permitting to assess the key roles of the orography and the sea, as well as the seasonal dependence of rainfall unequivocally linked to the synoptic scale conditions. As a general deduction, despite yearly precipitation being larger on the west side of the region, the most intense rainstorms are more frequent on the east side. In continuation of a work (Federico et al., 2008a) that provided a first classification of atmospheric patterns for the Calabria region, a recent study (Greco, De Luca, and Avolio, 2020) classified the main precipitation systems through the analysis of selected heavy rainfall events, taking into account a high resolution raingauge network. This work also assessed the relationships between the selected events and the main synoptic atmospheric patterns derived by the ERA5 Reanalysis dataset.

The works that have dealt with (extreme) temperatures in Calabria are fewer. Among them, considering a long-time period of monthly mean values and extreme daily temperatures in southern Italy, Caloiero et al. (2014) and Caloiero et al. (2017) revealed a positive trend in spring and summer and a negative trend in the autumn-winter period; specifically, regarding the extreme temperatures, authors observed an increase in the frequency and intensity of the highest temperatures and some negative trends for the lowest ones, i.e., a major (minor) probability of heatwaves (cold extremes) throughout the years.

Observational datasets represent the best data source for carrying out reliable statistical studies; at the same time, the availability of long-term data series is often a problem in several zones, as there are still large areas not sufficiently covered by measurements. In this context, the use of regularly gridded data as those derived

from modelling products (reanalysis) would help, as they are not affected by problems of spatial/temporal availability. Despite this, previous works demonstrated the limited skill of the reanalysis in correctly reproducing extreme values, if compared with other datasets (observations in particular). Reder et al. (2022) considered ERA5 hourly precipitation over Europe to study extreme values and found that reanalysis represents a good reference for general mean statistics (e.g., spatial pattern of annual precipitation, multi-year cycle of monthly precipitation), but the coarser resolution of the dataset tends to generate a smoothing of extreme precipitation, confirming the need of adopting highly localised data and/or dynamical downscaling procedures. A similar study, focusing on Germany (Hu and Franzke, 2020) and considering the precipitation field, assessed a general underestimation of precipitation of various gridded data with respect to observations; the reanalysis datasets (ERA5 in this case) give generally worse extreme value statistics of daily precipitation, in particular failing in reproducing the accurate timing of observed daily precipitation extremes. Concerning extreme temperatures over Europe, Velikou et al. (2022) also considered ERA5 fields; although the reanalyses captured the mean temperatures very well, the results over some European sub-regions (e.g., the Alps and the Mediterranean, in particular) revealed that ERA5 underestimates temperatures. The main differences with observations can be mainly attributed, according to the authors, to the altitude differences between ERA5 grid points and stations. This work presents the first use of the EVT extreme value theory to study temperature and heavy rain in Calabria region, considering a long-term observational dataset and also investigating the possible use of gridded reanalysis data.

1.4.1 Data and study area

The study area is the Calabria Peninsula, in southern Italy. The region is surrounded by the Tyrrhenian Sea (west) and by the Ionian Sea (east and south). The Apennines Mountains ideally separate the region into two sectors, crossing it from north to south more or less symmetrically; a maximum elevation of about 2000 m is reached. Daily extremes are computed taking into account a wide (regional) network of rain-gauges and temperature sensors (see next paragraph). State-of-the-art atmospheric reanalyses are also considered, to evaluate the ability of modelled gridded data in reproducing extreme daily values over Calabria.

1.4.2 Observational dataset

We used the network of the "Regional Functional Center" of the Calabrian Regional Agency for environmental protection (http://www.cfd.calabria.it). The whole dataset of daily temperature and precipitation data from 1990 to 2020 (31 years), distributed quite uniformly over the whole region, was initially considered. Although the data are quality-controlled by the center before being granted for research activities, we also adopted further selection criteria that permitted to retain 38 points/stations,

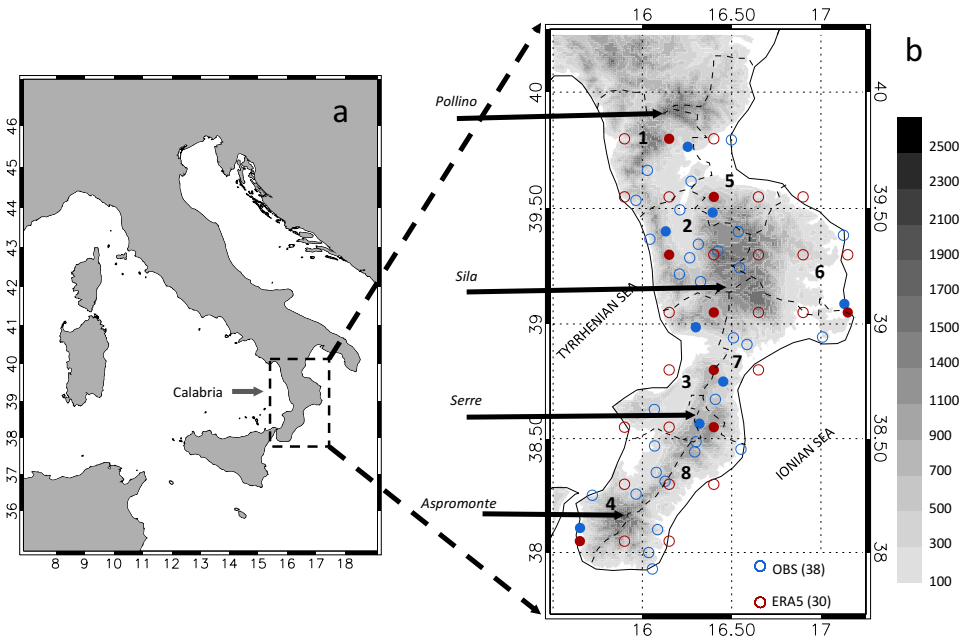

FIGURE 1.26: Spatial distribution of observations and reanalysis: observation points (38; blue circles) and ERA5 points (30; red circles). Filled circles indicate the selected points for each zone. The black numbers indicate the 8 climatic zones (delimited by dotted contours). The orography of the regions and some locations cited in the text are also shown.

starting from a larger number of them (254 raingauges and 137 thermometers). In particular, it was retained: (i) each station equipped with both rain gauges and temperature sensors; (ii) each station with possible missing data less than 3 years, even non-consecutive, considering the whole 31-year period. Using these criteria the percentages of missing data are 3.5% for temperature and 3.7% for precipitation. Starting from hourly data, we computed the daily accumulated (0-24 hours) precipitation and the daily maximum (Tmax), minimum (Tmin) and mean (Tmean) temperatures. The spatial distribution of the selected stations is shown in Figure 1.26. In the figure, eight zones in which the region has been ideally divided are also visible; the spatial extensions of these zones are comparable and they divide more or less uniformly the Calabria region in the western (1-2-3-4 zones) and eastern (5-6-7-8 zones) sides, as well as in the northern (1-5 zones) and southern sides (4-8 zones). We used this subdivision too, following that proposed by the Calabrian Regional Civil Protection (https://www.protezionecivilecalabria.it), responsible for disseminating weather-marine warnings on the region, also in order to make our results easily accessible (and usable) to the bodies responsible for the managment of weather alerts and emergencies. From each of these zones, one station was selected and taken as representative of the area (see Table 3.1) taking into account the stations with less

missing data and closest to the ERA5 gridded points; for each of these eight stations, the extreme values of daily temperature and precipitation have been computed following the Extreme Value Theory (see Section 1.1.1). In the same table, for each station we report the averaged mean temperature (T_{avg}) and average annual precipitation (ANP), considering the 31-years period, in order to provide some information about the climatic conditions of the different stations/zones.

Zone	Station name	lon-lat	lon-lat (ERA5)	Alt. (msl)	T_{avg} (°C)	ANP (mm)
1	Castrovillari	16.25 - 39.77	16.15 - 39.80	353	16.3	646
2	Montalto U.	16.13 - 39.40	16.15 - 39.30	468	15.7	1459
3	Nicastro	16.30 - 38.99	16.40 - 39.05	200	14.5	1139
4	Reggio Calabria	15.65 - 38.11	15.65 - 38.05	15	18.7	591
5	Acri	16.39 - 39.48	16.40 - 39.55	790	13.2	901
6	Crotone	17.13 - 39.09	17.15 - 39.05	5	17.9	630
7	Palermiti	16.45 - 38.75	16.40 - 38.80	480	14.6	1230
8	Serra S. Bruno	16.32 - 38.57	16.40 - 38.55	790	11.1	1630

TABLE 1.4: The eight zones and the related representative stations/ERA5 points used in the analysis. Longitude, latitude and altitude (this only for observational stations) are also reported. The positions of each station, for each zone, are identified by the blue filled circles on Figure 1.

ERA5 Reanalysis

With the aim of evaluating also the skill of the large-scale atmospheric reanalyses in reproducing daily extreme values, we used the global climate monitoring dataset ECMWF ReAnalysis (ERA5; Hersbach et al. (2020)). The ERA5 fields are available hourly on regular latitude-longitude grids at $0.25^\circ \times 0.25^\circ$ resolution. The fields taken into account are the hourly total precipitation and the 2m temperatures for the whole 31-years period; starting from these data, the daily ones are computed. Also the points of the ERA5 dataset are shown in Figure 1.26. Because of the coarse horizontal spatial resolution, the number of ERA5 points is limited (about 30 points on the whole region, clearly uniformly arranged) but comparable with the retained measuring stations.

1.4.3 Results and Discussion

EVT reliability

The purpose of this section is to evaluate the reliability of the EVT on the available datasets, in order to assess the daily extreme rainfall and temperatures over the whole region.

Diagnostic plots for the selected stations

We present the results obtained with the application of the EVT on the observational dataset. In particular, in this section we primarily comment on the application of

the theory on the selected eight stations previously defined. We have used the POT method for the precipitation and the BM method for the temperatures; in the following we will use these terms to indicate the two EVT techniques applied to the two datasets. We used two different python packages in order to apply the POT and BM methods on the available dataset. For the POT method we used the software developed by Lemos, Lima, and Duarte (2020b) while for the BM approach we used the software developed by Correoso (2019). In Figure 1.27 the diagnostic plot obtained via the application of the POT method on the rainfall data of Crotone station is reported. This station is chosen as representative, in terms of extreme events, for zone 6. The diagnostic plot is composed of 4 sub-plots: the Probability Density Function plot (PDF), the Probability Plot (P-P plot), the Quantile Plot (Q-Q Plot) and the Return Level plot. The distribution of the values above the threshold is reported in the PDF plot, while the P-P plot and the Q-Q plot are graphical methods for comparing two distributions (theoretical and empirical) and they are basically the same plots, but expressed on a different scale; if the data are adequate to model the extreme daily values of precipitations through the adopted theory, they have to lie on the diagonal of these plots. Through a Spearman's correlation coefficient we quantified this correspondence between empirical and theoretical return level obtaining for the station of Crotone the 0.94 value. The final plot is the Return Level Plot that gives a probabilistic estimation of the repetition of an extreme event.

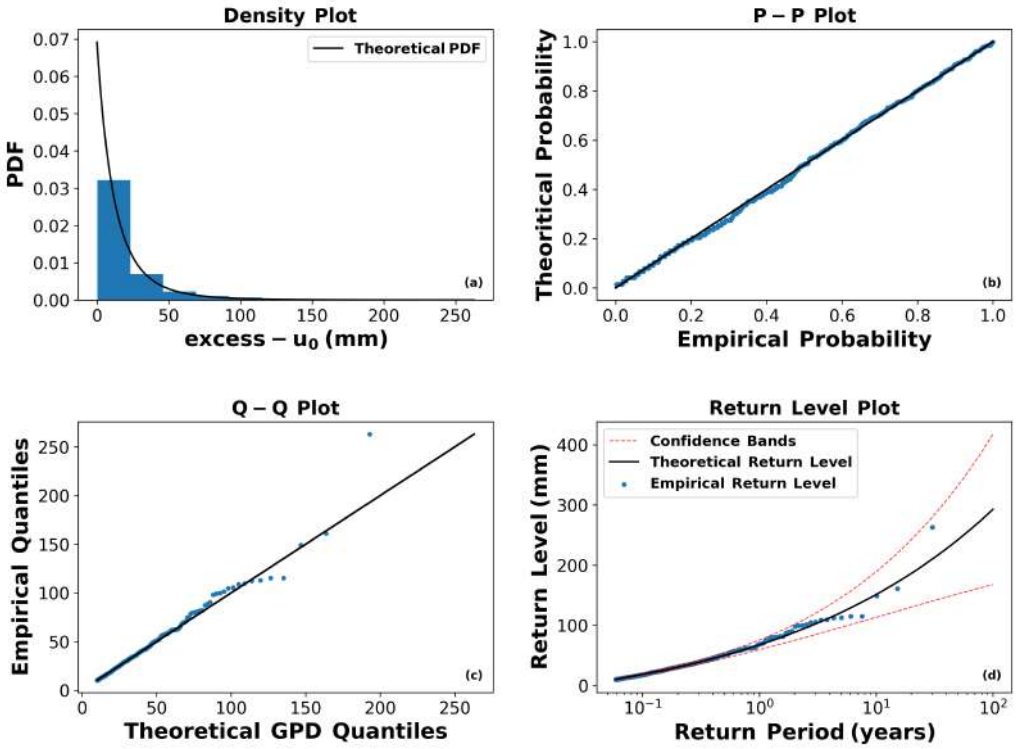

FIGURE 1.27: Diagnostic plot for the extreme rainfall data of the Crotone station: (**a**) Probability Density function, (**b**) Probability Plot, (**c**) Quantile Plot and (**d**) Return Level Plot.

Figure 1.27(a) shows the distribution of the extreme values, extreme rainfall in this

case, above threshold values. They are presented as $excess - u_0$, where u_0 is the threshold value used for the station (in this case the threshold is set to be $u_0 = 10\,mm$) and it differs from station to station. The distribution has the maximum values located between $10\,mm$ and $60\,mm$ and it is possible to observe a long tail of values that represents extreme rainfall events (less probable but more extreme).
Figures 1.27(b) and (c) permit us to assess if the adopted POT method is appropriate to describe the considered event. In these two plots most of the points lie close to the diagonal except for one. This point appears to be not well described by the POT model and this could be due to the fact that this type of event is extremely rare. A similar behaviour is also shown in the other stations in which more points do not lie close to the diagonal. It is possible to define them as "abnormal" because they are out of description for the EVT. In the panel (d) of Figure 1.27 the Return Level Plot is reported, which gives a probabilistic forecast of extreme rainfall events based on the extreme events detected by the station. All values (also the abnormal ones) are in the confidence interval of 2σ, and the POT model (black solid line) seems to describe the behaviour of the data very well, except for a few points. For these cases the EVT theory seems to either overestimate or underestimate some observed extreme values. In the case of the overestimation, the extreme data events appear below the theoretical line and we can define them as "delay" because it seems they happen after the time expected from the theory. In the case of underestimation the data are located above the theoretical line and we can define them as "advances" because they occur before what is expected from the theory. We have already seen this behaviour for some points in Section 1.3.2, in the Basilicata work, in which we reported these "advances" and "delays" in Figure 1.23. The red areas are the one interested by the "delay" phenomena, while the blue areas are the one interested by the "advances".
Before showing the same plot for the temperature data, it is usefull to apply the EMD method discussed in Section 1.1.2 to the available dataset. As already mentioned in the Section 1.1.2, the choice of the block length for the application of the BM approach could be affected by seasonal periodicity problems. To avoid these problems, we apply the EMD method to the whole dataset. We show in Figure 1.28 the application of the EMD to the Crotone station.
In Figure 1.28 we show the maximum daily temperature recorded at the Crotone station (black dots); the purple signal is the one used in the EVT analysis obtained by subtracting from the monthly maxima the IMF 1 extrapolated from the monthly mean temperature.
Figure 1.29 shows the diagnostic plot (obtained via the application of the BM method) for the extreme temperature, also in this case for the Crotone station. The plot composition is the same as Figure 1.27. The Density Plot differs from that seen for the rainfall case because we used a different approach of EVT (i.e., the BM approach). We used the GEV model, which takes into account the maximum values of the temperature for each month of the dataset. The Density Plot (Figure 1.29(a)) shows the

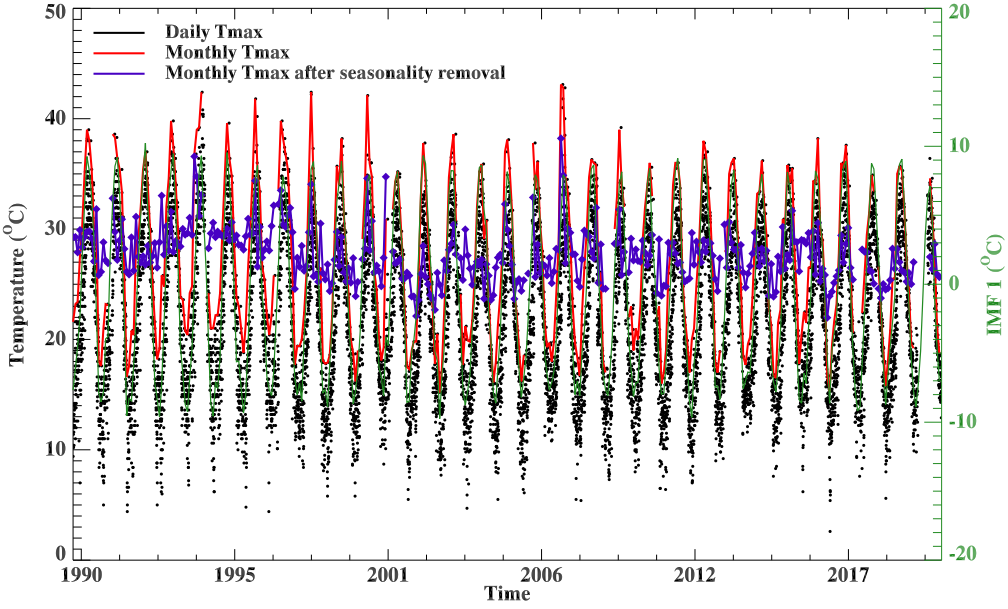

FIGURE 1.28: Maximum daily temperature recorded at the Crotone station (black dots), evolution of monthly maximum temperatures before (red line) and after (purple line) subtracting the seasonal mode obtained with the EMD decomposition. The rigth y-axis shows the IMF 1 amplitude (green line).

distribution of the maximum temperature values. The distribution does not appear symmetric, but it exhibits a pronounced tail in the right side of the figure. This indicates the presence of high extreme temperatures. Figures 1.29(b) and (c) are similar to the plot shown for the rainfall case. Most of the points lie on the diagonal except for a few of them, indicating that the adopted GEV approach well describes the dataset of extreme temperature. Again, a Spearman's correlation coefficient between empirical and theoretical return level was calculated, obtaining for the temperatures in Crotone a value of 0.95. The Return Level Plot (Figure 1.29(d)) shows a similar behaviour as the rainfall data, but in this case some values do not belong to the confidence interval of 2σ. These points are probably the "abnormal" data discussed before and the BM method fails in their description.

We computed the diagnostic-plots for all the other seven stations/zones (we chose not to show them), for both precipitation and temperature extremes. Considering the other zones, we found that the results are quite similar to zone 6 (see appendix in Prete et al. (2023)). From the analysis, it is evident that the higher values of extreme precipitation are detected in the zones located in the eastern side of the Calabria region (along the Ionian sea). These zones are characterised by more extreme rainfall events, with respect to the zones along the Tyrrhenean sea, and this is in agreement with several previous works confirming that the east side of the region is mainly affected by higher precipitation events. An inverse behaviour was found for extreme temperatures; from the results obtained with the application of the BM method, the highest extreme values appear located on the western side of the region, i.e. along the Tyrrhenian sea.

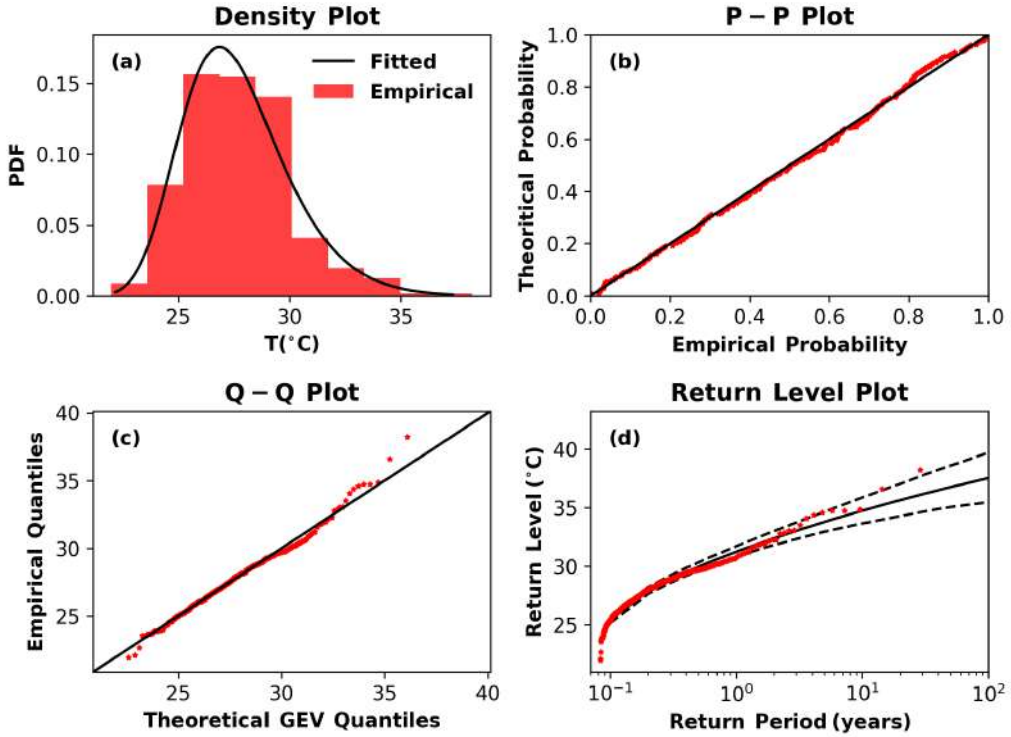

FIGURE 1.29: Diagnostic plot for the extreme temperature data of the Crotone station: (**a**) Probability Density function, (**b**) Probability Plot, (**c**) Quantile Plot and (**d**) Return Level Plot.

Return level maps for the observational dataset

In this section we discuss the application of the EVT method on the whole observed dataset. The purpose of this analysis is to qualitatively compare, in terms of return periods, the areas affected by daily precipitation and temperature extremes. Clearly, the maximum time interval for which such a comparison can be made is 31 years (i.e., the time interval in which the observations are available). The return level plots give us the probability that a certain event will be expected into a certain return period interval; this probabilistic method allows us to better identify the regions subjected to extreme phenomena.

In Figures 1.30(a) and 1.30(c) we report the maps of the empirical (i.e., considering the observed daily precipitations) return level for 10 and 30 years, respectively, while Figures 1.30(b) and 1.30(d) are the theoretical (i.e., applying the POT method on the observed daily precipitations) return level maps for 10 and 30 years, respectively. These maps, like all those in this section, are produced using the Inverse Distance interpolation method, considering all the available points (Figure 1.26).

The maps have similar characteristics, with the same features of daily extreme rainfall, as also anticipated in the diagnostic plots of Figure 1.27 (although they refer to a single station). Comparing the 10- and the 30-year return periods, a general increase in extreme rainfall values is visible. These probabilistic results, based on observations, can be used to assess the expected intensity of extreme precipitation

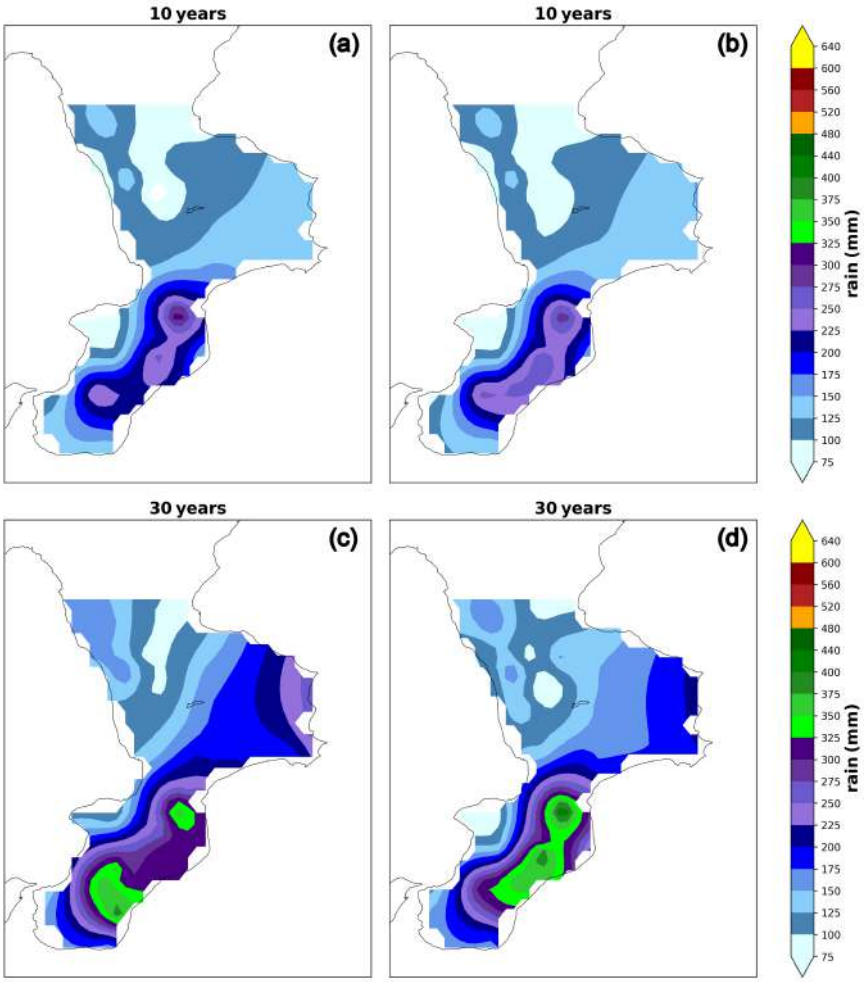

FIGURE 1.30: Comparison between daily rainfall return level maps for return periods of 10 and 30 years. Return level maps for the observed data (a,c) and from the POT model (b,d).

events, providing a useful complementary tool to climate projections and models, that hypothesise, in the coming years, an increase of such events.
For these fixed return periods, it is easy to identify a zonal gradient of extreme precipitation over Calabria, with the south-eastern part of the region most affected by such events (the Ionian areas, in particular), as opposed to the north-western part. This occurrence is found both by considering only the observational data and the application of the POT method, with values up to 300 (400) mm/day for the fixed return period of 10 (30) years. The result is not surprising since, as said in the introduction, several studies already assessed how intense rainstorms are more frequent on the east side of the region. As also confirmed by the aforementioned works (e.g. Federico et al. (2009)), the role played by the orography of the region and by the prevailing synoptic conditions associated with extreme precipitation events in southern Italy is visible in this case. In such situations, in fact, the presence of a cyclonic area located in the southern Ionian Sea (Federico et al., 2008a) prevails, which draws more unstable and humid air on the Ionian coast of Calabria. The contrast between these air masses with the terrain and the orography of the region, in particular the

Aspromonte mountain range, causes an uplift of the air masses and a consequent increase in convective instability conditions (see, for example, the case study analysed in Avolio and Federico (2018), and this results in a significant amount of precipitation windward of the orographic reliefs.
In Figures 1.31(a) and 1.31(c) we report the maximum temperature maps of the empirical (i.e., considering the observed daily maximum temperatures) return level for 10 and 30 years, respectively, while Figures 1.31(b) and 1.31(d) are the theoretical (i.e., applying the BM method on the observed daily maximum temperatures) return level maps for 10 and 30 years, respectively.

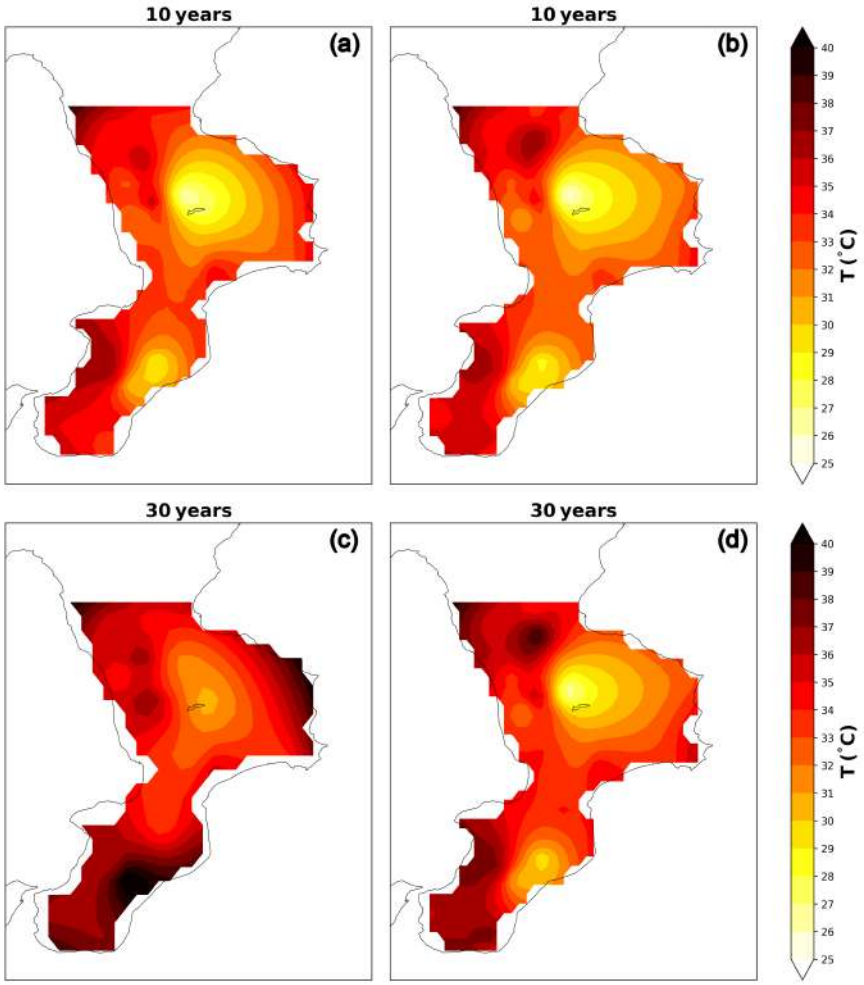

FIGURE 1.31: Comparison between daily max temperature return level maps for return periods of 10 and 30 years. Return level maps for the observed data (a,c) and from the BM model (b,d).

Also in this case the maps have similar characteristics, with the same extreme temperature features, as also anticipated in the diagnostic plots of Figure 1.29.
Considering the fixed return period of 10 years, the areas most affected by extreme daily temperatures, and therefore by possible heatwaves, are the flat areas of the region, in particular those on the Tyrrhenian side. Observing the differences between the 10- and the 30-years return periods, we can see a general increase of the daily

extreme temperature values. As for the case of daily precipitation, it is possible to use these results to obtain information on the local effects of a general global warming possibly linked to the ongoing climate change. Considering the 30 years return period, the daily extreme temperatures, besides being higher, seem to be more concentrated in the southern part of the region, although it is possible to note a little area interested by high temperature values also in the north part. The observed data (Figure 1.31(c)) suggest an intensification of extreme maximum temperature events in the south-eastern areas of Calabria, while those obtained from the application of the BM method (Figure 1.31(d)) confirm the feature seen in the 10-year return period maps, with the Tyrrhenian part most affected by these extreme thermal features.
The empirical (based on observed data) and the EVT maps are very similar; this implies that, both for daily extreme precipitation and temperature, the EVT applied on the observations describes very well their behaviour.
In considering these first results, it is important to point out the significant difference in the number of available stations over the region. In particular, the eastern-northeastern part of Calabria (zone 6 and 5, above all) is much less covered by observations (see Figure 1.26) and, therefore, also the interpolation procedure for creating the maps is inevitably conditioned by this fact.

Return level maps for the reanalysis dataset: comparison with observations

In this section we evaluate the possible use of ERA5 reanalysis data in studying extreme weather events, since regular gridded data are not affected by spatial/temporal availability problems. We consider the results obtained from observed data and from ERA5, comparing the return level maps for a fixed return period of 10 years, both for temperature and precipitation.
In Figure 1.32 we show the return level maps of extreme daily rainfall; Figure 1.32(a) is the same as 1.30(a) (here duplicated, to allow a direct comparison), while Figure 1.32(b) is the map obtained by the EVT theory application (POT method) on the reanalysis. In order to better comment on the results, we reduced the colour scale values on the maps, mainly because the maximum extreme rainfall values for the ERA5 data are significantly lower. Figure 1.33 is the same as Figure 1.32 but for the daily extreme temperatures (BM method).
A general and unquestionable underestimation is evident for the ERA5 data with respect to observations, both for precipitation and temperature. For the extreme daily rainfall, differences between observations and reanalysis even higher than 200 mm are clearly visible in several zones (mainly in the southeast). The general behaviour of the rainfall is similar, with the eastern part of the region most affected by extreme precipitation. A poor agreement is noticeable in the southeastern part of the region, the most affected by heavy rain based on observations, but where the reanalysis failed to correctly reproduce the high rainfall values. As usual, a separate comment applies to the northeastern part of Calabria where, as already said, there is a general lack of weather stations (see Figure 1.26); for this reason, we cannot obtain

useful information by the POT method application in this area. Also for the daily extreme temperature, no useful information can be drawn on the northeastern part of the region, due to the lack of stations. The areas most affected by extreme daily temperatures (based on observations) are the Tyrrhenian ones, as already seen in the previous section. The ERA5 fields fail to correctly identify this behaviour, except for the southwestern side of the region, instead showing a greater predisposition to extreme temperatures in the southeastern area (not confirmed by observations).

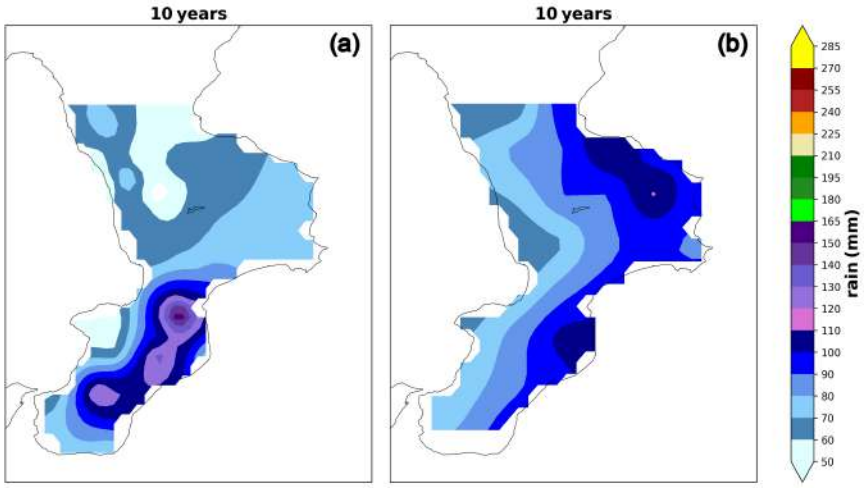

FIGURE 1.32: Comparison between daily rainfall return level maps for a return period of 10 years. Return level map for the observed data (a) and for the ERA5 data (b).

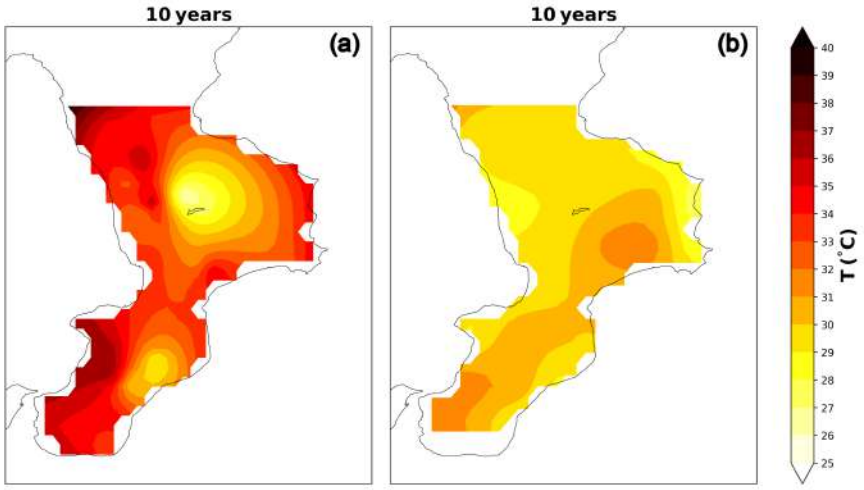

FIGURE 1.33: Comparison between daily max temperature return level maps for a return period of 10 years. Return level map for the observed data (a) and for the ERA5 data (b).

This general underestimation is not surprising, and it is in agreement with previous works ((Hu and Franzke, 2020; Velikou et al., 2022; Reder et al., 2022)) that have tried to use ERA5 fields for highly localised climatic studies.
To further highlight this aspect, also providing a more quantitative result, we show in Figure 1.34 a punctual comparison (only for the Crotone station) between the

return levels obtained using both observed data and ERA5 reanalysis; in this case, we show the return levels computed both considering the original datasets (OBS and ERA5) and the EVT results. Figure 1.34(a) refers to extreme precipitation and shows the return level of the observed data (black dotted points) and the return level of the POT method (black solid line) applied on the observations. In the same plot we present the results from ERA5 data (blue dotted points) and the return level of the POT method (blue solid line) applied on the reanalysis. Dotted lines indicate the error confidence intervals.

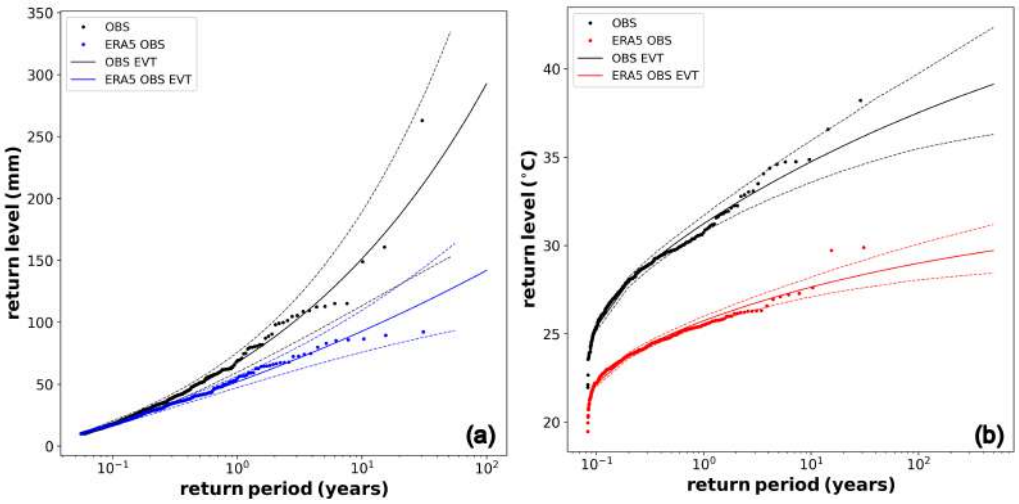

FIGURE 1.34: (a) Comparison between observed and ERA5 return levels for daily precipitations, for Crotone station. (b) Comparison between observed and ERA5 return levels for daily temperature maxima.

It is evident the discrepancy between the plots and the general ERA5 underestimation with respect to observations, although the application of the POT method provides, also on the reanalysis, valuable results (see blue dotted points vs blue solid line). Similar findings can be seen in Figure 1.34(b), for the temperature daily maxima. Here the differences, in terms of temperature values, appear more pronounced and also in this case the application of the BM method seems to work quite well.
As regards the ERA5 underestimation of the extreme values, it emerges that the reanalysis does not seem capable of well grasping the localised dynamic characteristics influencing the temperature and rainfall fields in the region. Regular gridded modelled data represent a valid and promising tool also for these types of analysis, even irreplaceable in the vast worldwide areas not sufficiently covered by observations, and the EVT technique also applied to ERA5 seems to work well. However, the fact that the reanalysis unequivocally underestimates the observed extreme values prompts us to perform our further EVT analyses only considering the observational dataset as reference.

50 and 100 years Return levels

We present in this section the 50 and 100 years return levels by applying the EVT to the whole observational dataset. This probabilistic approach allows the identification of the Calabrian areas likely most affected by daily extreme precipitation and maximum temperatures in the future. We show the return level maps obtained from the application of the POT (for rain) and the BM (for temperature) methods for each available station. The analyses were carried out for the fixed return periods of 10, 30, 50 and 100 years. Since the return level maps for 10 and 30 years were already commented at the beginning of the Section 1.4.3 (Figures 1.30 (b, d) and 1.31 (b, d)), we report in this section only the maps referring to the 50 and 100 years return periods. Figures 1.35 (a) and (b) show the return levels at 50 and 100 years, respectively, for the extreme daily rainfall. The figures clearly show two distinguished regions in which the rainfall extreme events have different features. The southeastern part of the region represents the area most affected by extreme daily precipitation, unlike the northwestern part. The behaviour, in terms of precipitation patterns, is very similar for all the return level periods. Observing Figure 1.26, we can see how the stations are well distributed over the region except for the northeastern part; in this area there are no predicted extreme precipitation values, but we cannot really quantify the role of the EVT theory, just because of the lack of observational data, as already mentioned in the previous sections. On the other hand, the fact that the most intense precipitations in Calabria occurs in the southeastern part of the region is a further confirmation of previous work results (Federico et al., 2009; Greco, De Luca, and Avolio, 2020). A sensible intensification of extreme rainfall is evident, as the return periods increase, in qualitative agreement with the increasing incidence expected by the climate projections. The Aspromonte, and the areas east of the mountain range, are the most affected zones for daily extreme precipitation. For the 50-years return period, extreme values up to 500 mm/day are predicted in this zone, and the daily extreme precipitation assumes even greater values (up to 600 mm/day) if a return period of 100 years is considered.
Figure 1.36 (a) and (b) show the return levels 50 and 100 years respectively, for the extreme daily temperatures. As already seen for the return periods of 10 and 30 years (Figure 1.31(b),(d)), also these probabilistic projections suggest that the areas most affected by extreme daily temperatures will be the Tyrrhenian flat areas. The central part of the region seems not affected by daily extreme temperatures, also because it is in the central areas that the main mountain ranges of the region are distributed, while the lack of observations in the northeastern part does not permit extracting very useful information for this area by applying the EVT. Also for temperatures, an intensification of the daily extremes is visible as the return periods increase, in agreement with the ongoing global warming.
Heatwaves with maximum daily temperatures up to 40°C are expected in the next 100 years and the southern part of Calabria is the area mainly affected; it is even

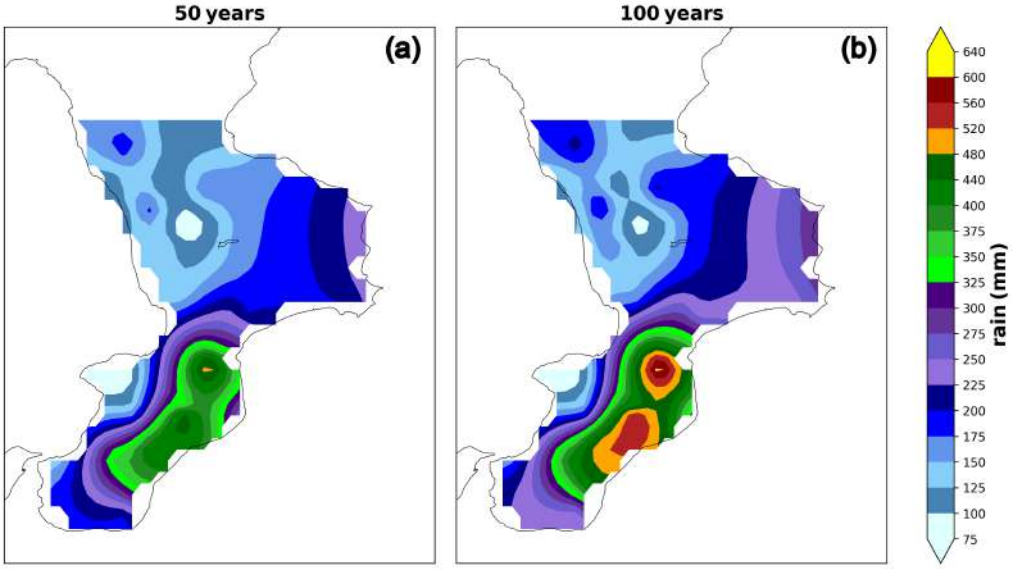

FIGURE 1.35: Return Level map of extreme rainfall for a fixed return period for all of the Calabria stations. Return level map for a return period of 50 years (a) and 100 years (b).

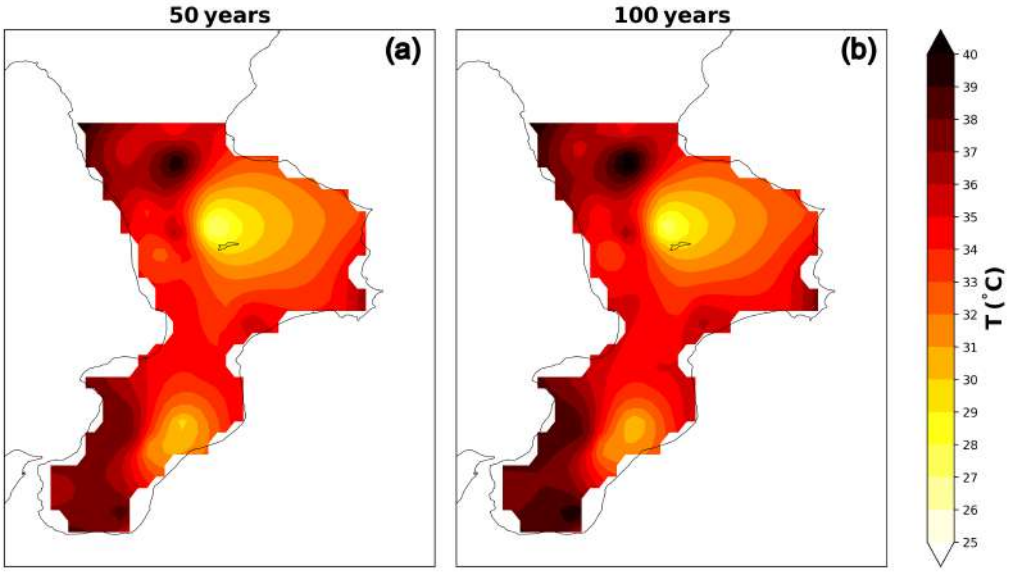

FIGURE 1.36: Return level maps of extreme temperatures for fixed return periods for all of the Calabria stations. Return level map for a return period of 50 years (a) and 100 years (b).

more interesting to note how, in the same areas, differences of maximum daily temperatures of about 2°C are visible, considering the 50 and the 100 years return periods. The maps obtained at 50 and 100 years (Figures 1.35 and 1.36) represent a great advantage of EVT theory, namely to be able to provide a forecast of the return value exceeding the time scale imposed by the dataset (in our case of 31 years). The values shown in the maps refer to the most probable RL, but each has a confidence interval highlighted by the dotted lines in the return level plot (see Figures 1.27(d) and 1.29(d)). The error for each station is impossible to be shown in a single map,

thus we decided to report two further figures showing the precise RL values and the related confidence intervals for all the stations listed in Table 3.1 (Figure 1.37 and 1.38). It is important to highlight that these results are strongly conditioned by the choice of the stations. From the box-plots it is easy to see how the representative stations of zones 7 and 8 are those more prone to an intensification of extreme daily precipitation events over the years, i.e. the areas on the southern Ionian side, where values between 350 and 400 (450 and 500) mm/day are predicted, for the return period of 50 (100) years. Considering instead temperatures, the future incidence of heat waves is more likely in the representative stations of zones 4 and 6, i.e. the southern Tyrrhenian side and the eastern part of the region respectively, where maximum daily temperatures between 36 and 37 (36 and 38) $^{\circ}C$ are predicted for the return level of 50 (100) years.

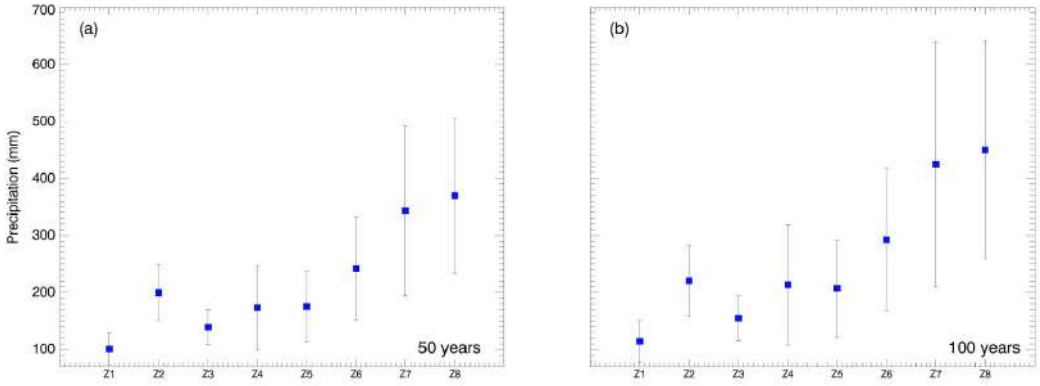

FIGURE 1.37: Return levels (daily precipitation) and respective dispersion intervals for the representative stations listed in table 1 (Z1-Z8), obtained at 50 (panel a) and 100 (panel b) years.

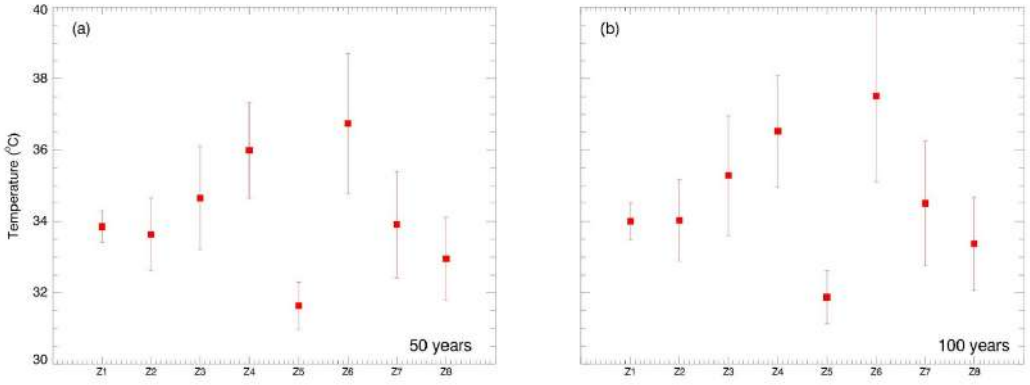

FIGURE 1.38: Return levels (daily maximum temperatures) and respective dispersion intervals for the representative stations listed in table 1 (Z1-Z8), obtained at 50 (panel a) and 100 (panel b) years.

1.5 Conclusions

In this Chapter we applied the EVT method to different datasets of three different climatic regions. We obtained different result from the application of the various EVT approaches, also because the different zones are characterized by different types of climatic phenomena.
In Section 1.2, using the EVT, we showed that Antarctic, perhaps the Earth region most vulnerable to climate changes, is affected by this phenomenon with high probability. Unfortunately, since this behaviour seems to be quite recent, only datasets of limited length are at our disposal up to now. This does not help us in making predictions with the desired accuracy, as far as the return values of maximum/minimum temperatures are concerned. However, we find that in all the cases we analysed, the maximum recorded temperature could be exceeded in a few years, indicating that the current period of global warming is an evidence that cannot be disregarded. On the other hand, if the maximum/minimum temperatures were in agreement with EVT, the maximum recorded temperatures would be exceeded again in more than a few tens of years.
A disagreement with respect to the linear relation for the highest temperatures in the quantile plots is evident in all the datasets we investigated. Some extreme temperatures, depending on the sampling, do not follow the linear behavior expected from EVT, but they appear to abnormally exceed the predictions of extreme events. To understand the goodness of the fit we used the chi-square test for the probability plot, and we found that χ^2 values are in the range [0.08215, 0.17358]. Since the goodness of fit is overall high, as evidenced from the probability plots, the anticipating probability of returns of extreme events with respect to EVT is a strong indication that accelerated climate change is at work in the Antarctic. Moreover, the disagreement of the data with respect to the theoretical linear shape in the quantile plots is a clear further signature that the maximum/minimum temperatures recorded so far could be considered as really abnormal, even with respect to the actual rate of climate changes.
We found evidences of departures from EVT for temperature maxima, while minima seem to follow EVT, thus globally indicating a rapid shift of the highest temperature PDF towards higher values. It is however interesting to remark that the departure of minimum values from EVT is evident in the return plots. Moreover, there is a clear difference between the various stations which is obviously related to the local geographic location. In particular, it is evident that the maximum value $T_M^{(min)}$ of minimum temperature registered so far has a great probability to be rapidly overcome in few years at Halley Met station, while this is not so obvious for Rothera Met station. In other words, the system seems to be particularly sensitive to local factors of the climate system which affect the dynamics (Bodart and Bingham, 2019). In particular, in our case this results in a local acceleration of the enhancement of minimum temperatures at Halley Met rather than at Rothera Met. This could be due to the effect of El Niño Southern Oscillation which influences the mass changes from region

to region (Bodart and Bingham, 2019). As mentioned before, the disagreement with EVT we evidenced can be interpreted as acceleration of warming in some regions of the Antarctic, perhaps much faster than the warming recorded through global averages (Bodart and Bingham, 2019), as results from the return plots. If confirmed, this opens new scenarios concerning local, possibly abrupt acceleration of climate change, thus strongly influencing and constraining the alert for the determination of the tipping point in the world's extremely vulnerable greatest repository of ice.
In Section 1.3 we analyzed the daily rainfall data for some stations in Basilicata, southern Italy. Unfortunately, some of them were ruled out because they presented a lack of data, and others were also excluded because the dataset did not cover a range of 30 years. We applied the extreme value theory statistics to analyze the data of each station, and in particular, we used the Generalized Pareto Distribution (GPD), which allows choosing a threshold from a sample of data and considering the value above this threshold as extreme events. We showed the results of the statistical analysis in Figure 1.19. We chose to show the plot of Potenza station because the others are similar to this, except for the return plot that seems to differ from case to case. From Figure 1.19 it is evident that the model works very well because all the points lie on the diagonal in the P-P plot. So this implies that there is a good agreement between the model and the empirical values. The most important diagnostic plot is the return plot, that enables to make predictions. We presented also a few return plots (Figures 1.19 (d), 1.22(a),1.22(b), 1.22(c)) to show the difference between the various stations. It can be seen that for many stations, the empirical values are distributed within the 95% confidence interval band and there are a few points that are outside this interval. These are the "abnormal" events and this implies that for a particular station there should be a dramatic rainfall event. Finally, using the return values of the return plots, we built the spatial map for the region. We showed the maps of empirical and theoretical return values at different return periods for each station. In both cases, it appears a pattern that shows a concentration of extreme events in the south-east region and a lower value of rainfall in the north-western region. The highest value has been recorded at San Mauro Forte station. The last plot is the theoretical return level plot for a return period of 50 years. The pattern still keeps, with the highest values on the south-eastern side and the lowest values on the north-western side. It appears evident that in the empirical plots the values are higher than the values in the theoretical one. This is a clear signal that the values of the empirical return plot are ahead of the values of the theoretical plots. This could be seen also in the return plots where the empirical values (blue dots) deviate from the theoretical trend, anticipating in terms of time the theoretical value associated with the empirical one.
All the results presented in Section 1.3 will be useful for extreme rainfall events analyses in the Basilicata region, with applications in regional land planning, landslide and flood prediction, and civil protection activities, even in a changing climate context. Moreover, the method described here, being quantitative and reproducible, can

be easily applicable in other regions with similar rainfall data.
In Section 1.4 we presented a statistical study on daily precipitation and temperature extremes in Calabria, southern Italy, applying the extreme value theory (EVT) on a long-term series (31 years) of regional observations; for the precipitation, we adopted the Peak Over Threshold method, while for the temperature the Block Maxima approach was considered. Both datasets (observations and reanalysis) present some limitations. A first one, regarding the observations, is related to the lack of stations in a specific area (northeastern part of the region), and only affects the procedure (inverse distance) adopted for generating the maps. A further limitation is related to the time series (in our case limited to 30 years) and can affect the statistical uncertainty leading to an increase of the confidence interval in the return level plot. In order to perform punctual statistical investigations, the region was divided in eight climatic zones, in agreement with the spatial subdivision adopted by the Calabrian Regional Civil Protection; from each of these zones, one station was selected and taken as representative of the area. To assess the reliability of the method, we firstly reported the diagnostic plots (i.e., the Probability Density Function, the Probability Plot, the Quantile Plot and the Return Level plot) for each selected station, both considering the empirical (directly the observed values) and the theoretical (the EVT results) data. The analysis of the diagnostic plots confirmed that the proposed methods are appropriate to describe the considered extreme weather events over the study area.
In order to qualitatively compare the areas most affected by such extremes, again considering both empirical and theoretical data, we reported the regional maps of daily precipitation and temperature extremes in terms of fixed return periods (10 and 30 years). Also in this case, a good agreement was obtained between the two datasets, confirming the reliability of the EVT applied on the long-term observations. An evident zonal gradient of extreme precipitation over Calabria was found, with the south-eastern part of the region most affected by such events, in agreement with several previous studies. The flat areas of the region, in particular the Tyrrhenian ones, are instead the most affected by extreme daily temperatures and possible heatwaves.
The possible use of reanalysis in studying the daily extremes was also investigated, comparing the results obtained considering the observations with those derived by ERA5. Although the use of modelling products represents a great opportunity, mainly in areas not covered by observations, our comparisons show how the ERA5 fields are not suitable for reproducing the occurred extreme values, showing a systematic and substantial underestimation of both daily precipitation and temperature extremes. The assessed reliability of the theory applied on the observations, allowed us to carry out a probabilistic analysis aimed at identifying the areas likely most affected by daily extreme precipitation and maximum temperatures in the future; with this aim we reported the return levels maps for the fixed periods of 50 and 100 years, for both precipitation and temperature. A general intensification of extreme rainfall

events is expected in the future years, in agreement with climate projections, with values up to 500 mm/day for the 50-year return period in the south-eastern part of Calabria. Considering the temperature, heatwaves with maximum daily values up to $40^{\circ}C$ are expected in the next 100 years, mainly in the Tyrrhenian and southern part of the region.

The unequivocal increase of the Earth's surface temperature, and the predicted exacerbation of instability and convective atmospheric conditions in the future, emphasise the importance of carrying out studies such as the one presented, devoted to the analysis of the environmental variables most connected to the risks deriving from extreme meteorological phenomena.

Chapter 2

Space Weather extreme events

Space weather extreme events are rare phenomena tipically associated to Sun's activity. Example of events that can be catalogued as "Extreme" are: Coronal Mass Ejections (CMEs) of low or high speed, solar flares of high energy, and geomagnetic storms of strong intensity. Space weather is a branch of heliophysics that studies the conditions of the Sun and of the solar wind and their effects on the functioning and reliability of technological systems in space and on Earth, with possible effects also on human health. Therefore, the study of this particular type of phenomena is important to understand and forecast how they can impact our lifes.
Extreme events of relevance for the Space weather are originated from the solar atmosphere. These events are related to the magnetic field activity. The magnetic field varies with the solar coordinates and also with time. The most important phenomena related to the magnetic field activity are the sunspots. The presence of sunspots is not always uniform, but it varies periodically and it is related to the Solar cycle. The Solar cicle is a 11-years period formally defined by considering the number of sunspots present on the Sun surface. More precisely, the solar minimum is characterized by a very low number of sunspots on the Sun surface, while the solar maximum can be identified as the time period in which a peak in the number of sunspots is observed (within the 11-year period). In Figure 2.1 an example of the solar cycle activity is shown.
Sunspots often appear within the active regions as a pair of spots with opposite magnetic polarity. An active region is a Sun's region characterized by a strong and complex magnetic field, in which it is possible to find many of Sun's phenomena as Coronal loops, CMEs and solar flares. Coronal loops are dense plasma arch-like structures confined by magnetic flux tubes, i.e. by tube-like regions that contain the magnetic field. These arch flux tubes give us an idea of the complex Sun's magnetic field structure. Solar flares are intense localized eruptions of electromagnetic radiation. They occur when charged particles are accelerated by the stored magnetic energy on the Sun's atmosphere. Solar flares are often accompained by CMEs. CMEs are large-scale eruptions of plasma and magnetic field from the Sun's atmosphere. As already mentioned in the Introduction of this thesis work, the number of these events depends on the solar activity, with an higher number of occurrence reached during the solar maximum period. When they are released from the Sun's atmosphere, they travel throughout the Heliosphere and sometimes can reach the Earth.

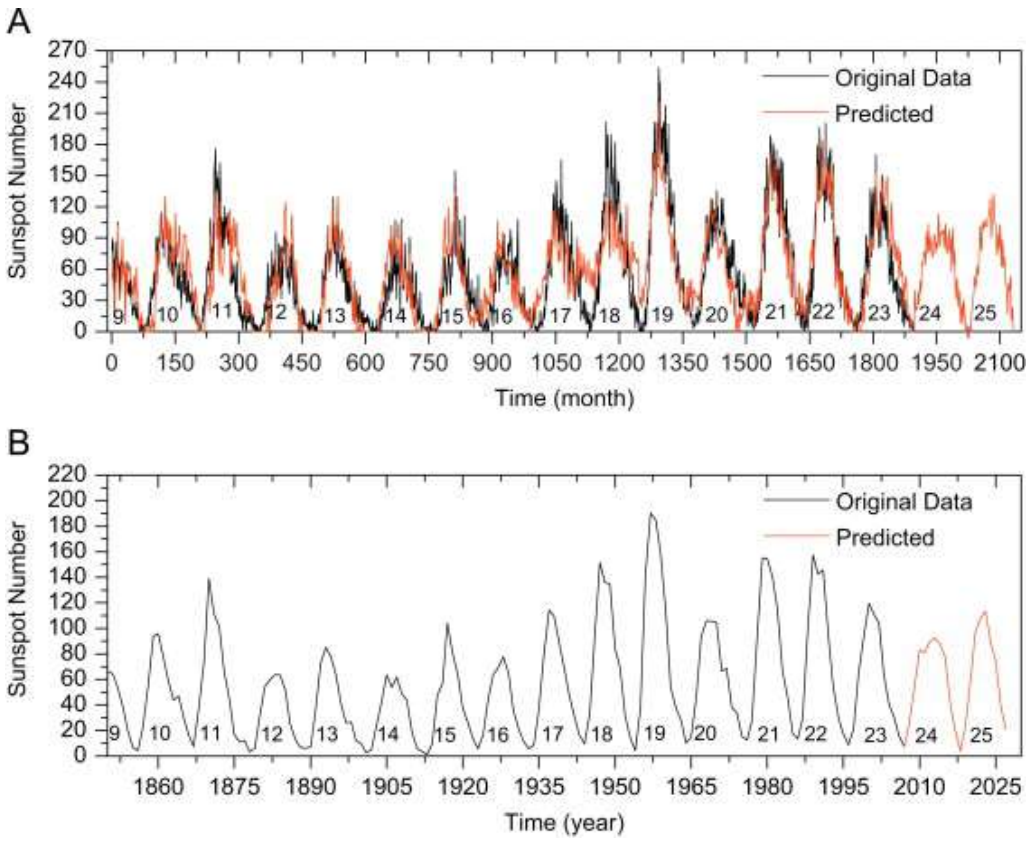

FIGURE 2.1: (A) Sunspots number as a function of time (black line), Sunspots number reconstructed and predicted (red line).(B) Annual sunspots number detected (black line) and predicted (red line). For more details see Rigozo et al. (2011)

From *in-situ* measurements, it is possible to analyze the counterpart of CMEs named Interplanetary Coronal Mass Ejections (ICMEs; Gosling et al., 1991; Kilpua et al., 2017; Song et al., 2020; Davies, E. E. et al., 2021). In the last decades, the investigation of ICMEs has increased and improved due to the availability of multi-spacecraft measurements, combining measurements from the Solar-Terrestrial Relations Observatory (STEREO; Kaiser, M. L. et al., 2008), the Advance Composition Explorer (ACE), Wind, and also using measurements from planetary missions as Cassini and MAVEN (Henry, 2002; Kilpua et al., 2009; Kilpua et al., 2013; Jakosky et al., 2015; Winslow et al., 2016; Cecconi et al., 2022), remote heliospheric observations, and numerical simulations (Taktakishvili, MacNeice, and Odstrcil, 2010; Sow Mondal et al., 2021). This allowed the scientific community to better understand the formation, propagation and interaction of ICMEs with the heliospheric environment.

From *in-situ* spacecraft data analysis to Magneto-hydrodynamic (MHD) simulations, ICMEs have been the focus of many studies. The classical signature of the passage of an ICME is identified by a sharp enhancement of the total magnetic field, corresponding to the shock passage generated by the ICME itself, e.g.Richardson, I. G. and Cane, H. V. (2010) and Kilpua, Koskinen, and Pulkkinen (2017). This region is followed by the sheath region that is the highly compressed region downstream

of the interplanetary (IP) shock, in which it is possible to observe many important plasma phenomena such as turbulence and magnetic reconnection according to the plasma β value (Gosling and McComas, 1987; Rouillard, 2011; Lapenta et al., 2020). The last part of an ICME region can be the site of a magnetic cloud (MC) (Burlaga et al., 1981; Klein and Burlaga, 1982). The presence of a MC is indicated by an enhancement of the magnetic field, with a smooth rotation of the magnetic field direction over a large angle in about one day, and by a decrease in proton temperature and plasma beta (see Figure 2 and 3 in the Introduction).

Interplanetary shocks are large-scale heliospheric structures often caused by eruptive phenomena of the Sun, and represent one of the main sources of energetic particles. Understanding the transport of supra-thermal particles such as solar energetic particles or galactic cosmic rays is of the outmost importance both for space weather predictions and for unravelling the details of acceleration particle mechanisms. Collisionless shocks are considered one of the main sources of cosmic-rays ranging from Type II radio-burst in the solar corona (Lin, 2005; Reames, 2013), to coronal-mass-ejection driven shocks expanding in the interplanetary medium (Vourlidas et al., 2003; Cliver and Ling, 2009; Grechnev et al., 2015), to the termination shock of the solar wind (Decker et al., 2005; Decker et al., 2008), to expanding blast waves at supernova remnants (Aharonian et al., 2004; Helder et al., 2012; Reynolds, Gaensler, and Bocchino, 2012), up to radio relics observed during galaxy cluster mergers (Van Weeren et al., 2016; Kang, Ryu, and Jones, 2012).

One of the mechanisms invoked for explaining the energization process of cosmic rays at shock waves is the diffusive shock acceleration (DSA) (Bell, 1978b; Lee and Fisk, 1982; Drury, 1983). It is based on the first order Fermi mechanism and on the diffusive motion of energetic particles upstream and downstream of the shock front, owing to the interaction of particles with magnetic field fluctuations. Such an interaction favours particle shock crossings, speeding up the acceleration process. If non-linear processes, such as the dynamical effect of cosmic ray pressure on the shock, wave generation by streaming particles upstream of the shock, and the magnetic field amplification, are included, a non-linear DSA can be envisaged (Drury and Voelk, 1981; Berezhko, Yelshin, and Ksenofontov, 1994; Berezhko and Völk, 2000; Amato, 2014a).

On the other hand, DSA has extensively been applied to acceleration of energetic particles at interplanetary shocks assuming a simple test-particle approach, an isotropic particle flux and a planar shock at which particles are injected with momentum p_0 (Giacalone, 2012). Thus, the solution of the transport equation, under stationary conditions and under the hypothesis that the diffusion coefficient is spatially independent, predicts an energetic particle flux that falls off exponentially moving from the shock front to far upstream, while the flux is spatially constant in the downstream side,

$$f(x,p) = Ap^3 r/(r-1)H(p-p_0) \begin{cases} exp(U_1 x/k_{xx}) & x \leq 0 \\ 1 \qquad x > 0. \end{cases} \tag{2.1}$$

Here, A is a normalization constant, r is the compression ratio of the plasma density across the shock, U_1 is the upstream plasma speed in the shock rest frame, x is the position (x=0 is chosen as the shock location), p represents the plasma-frame momentum, k_{xx} is the component of the spatial diffusion along the unit normal to the shock, and H is the Heaviside step function.
Such a behaviour has only rarely been observed for shock waves in the interplanetary medium (Giacalone, 2012; Tessein et al., 2015). Further, the shock acceleration process is influenced by the motion of charged particles upstream and downstream of the front; such a dynamic is highly dominated by the turbulent properties of the magnetic field fluctuations and depends on the particle energy itself. Indeed, Dosch and Shalchi (2010) have found a strong correlation between the maximum energies reached by particles accelerated at perpendicular shock waves and the slope of the spectrum of magnetic field turbulence, indicating that a steeper power spectrum leads to higher maximum energies.
Recently, it has been found that energetic particle motion can be faster than normal diffusive, namely superdiffusive, in the upstream region, thus questioning the validity of DSA (Perri and Zimbardo, 2007; Perri and Zimbardo, 2008; Perri and Zimbardo, 2009; Perri and Zimbardo, 2012a; Zimbardo and Perri, 2013). It is important to recall that superdiffusive transport has a great impact on shock acceleration (Ragot and Kirk, 1997; Perri and Zimbardo, 2012a; Zimbardo and Perri, 2013; Bykov, Ellison, and Osipov, 2017), since it leads to modifications of the energy spectral index and of the acceleration time (Perri and Zimbardo, 2012a; Zimbardo and Perri, 2013; Perri and Zimbardo, 2015; Perri and Zimbardo, 2015). Observations that support the occurrence of anomalous transport in astrophysical environments range from non-relativistic electrons accelerated in solar events (Lin, 1974), to the analysis of energetic particle fluxes upstream of interplanetary shocks (Perri and Zimbardo, 2008; Sugiyama and Shiota, 2011; Perri et al., 2015) that decay as power-laws far upstream (instead of an exponential fall-off as predicted by DSA), to ions accelerated at the termination of the solar wind (Perri and Zimbardo, 2009; Giacalone, 2013). Further, the analysis of X-ray synchrotron emission from relativistic electrons accelerated at supernova remnant blast waves suggests the possibility of superdiffusion within the far upstream region (Perri, Amato, and Zimbardo, 2016; Perri, 2018). Ragot and Kirk (1997) applied a continuous time random walk approach to the diffuse emission from synchrotron emitting electrons in the Coma cluster, finding a supra-diffusive, nearly ballistic, motion of energetic electrons.
Superdiffusion can be described by a mean square displacement $\langle \Delta r^2 \rangle$ growing with time t as

$$\langle \Delta r^2 \rangle = 2\mathcal{D}_\alpha \, t^\alpha, \tag{2.2}$$

where $\mathcal{D}_\alpha$ is the anomalous diffusion coefficient and α is the anomalous diffusion exponent (> 1 for superdiffusion). Notice that $\mathcal{D}_\alpha$ has dimensions $[L^2/t^\alpha]$ at variance with the standard diffusion coefficient. Perri et al. (2015) have shown that by studying the energetic particle fluxes upstream of interplanetary shock waves it is possible

to determine both α and the anomalous diffusion coefficient, thus fully characterizing the particle transport. However, the determination of these parameters from measured data can be subject to uncertainty, especially due to large amplitude fluctuations and irregularities found in the spacecraft data.
In this chapter we will discuss about extreme Space weather events, starting from a particular category of CMEs, i.e. CMEs with low speed. We will see how we can reproduce these explosive events with the help of simulations, in particular with MagnetoHydroDynamic (MHD) simulations. Then, we will show how shocks associated to these CMEs can influence the plasma parameters and also how shocks associated to Sun's events can influence the transport and the acceleration of energetic particles.

2.1 EUHFORIA modelling of a slow CME with a well-defined magnetic cloud.

Interplanetary coronal mass ejections and particularly magnetic clouds (MCs) can produce strong geomagnetic storms. Forecasting them is a recent challenge in the new era of Space Weather. The aim of this study is to understand where MCs form and how we can detect them earlier in the Sun environment.
In this Section, we focus on the magnetic structures that characterize the evolution of ICMEs at Lagrangian point L1. In particular, we analyze one event from the catalogue of magnetic clouds presented in Al-Haddad et al. (2018), in which the authors compare different techniques of ICME fitting and reconstruction in order to understand which one is the most suitable for the event selected. The aim of this paper is different. We want to understand the full chain of events from L1 all the way back to the Sun. The one-to-one linkage of *in-situ* detected ICMEs and CMEs in the corona is important and such a linkage is not easy to establish while there often exists ambiguity, especially during or near solar maximum.
We selected the event of June 27 2013, included in Al-Haddad et al. (2018). We tried to reproduce the behaviour of the ICME with the help of the 3D data-driven MHD heliospheric solar wind and CME evolution model European Heliospheric FORecasting Information Asset (EUHFORIA; Pomoell, Jens and Poedts, S., 2018; Scolini, C. et al., 2019; Poedts, Stefaan et al., 2020). We choose this particular event because it is characterized by relatively small velocities and a well-organized magnetic field structure.

2.1.1 Data

The Sun is constantly being imaged remotely in many different wavelengths, by different instruments (both ground-based and space-borne). With these images, we are able to identify coronal holes, active regions, CMEs, solar flares, and other structures and phenomena that are important for space weather. For this work, we used

the Extreme Ultraviolet (EUV) observations from the Atmospheric Imaging Assembly (AIA), aboard the Solar Dynamics Observatory (SDO; Lemen et al., 2012). With these observations, we located the position of the source regions of the CMEs that might be responsible for the selected MC. The coronal holes present on the Sun were detected using the AIA 17.1 nm channel. Signatures of the eruption were detected using the AIA 30.4 nm channel. We also analyzed data from the Helioseismic and Magnetic Imager (HMI; Schou et al., 2012) for further insight into the magnetic configuration of the active regions. Furthermore, H-α spectroheliograms from the Paris-Meudon observatory were used to analyse the filaments and prominences that were present on the solar disk at the time of the eruption. In addition, coronagraph white-light images were analyzed and used for determining the main direction of propagation of the CMEs, and (if necessary) for constraining the CME geometric and kinematic parameters in order to include them in the simulation model. These were taken from COR2-A and B, aboard the Solar TErrestrial RElations Observatory (STEREO; Howard et al., 2008), and by Large Angle Spectroscopic Observatory (LASCO), aboard SOHO.

When CMEs are expelled from the solar atmosphere, they start travelling through the heliosphere. Upon reaching and passing by measuring devices aboard different spacecrafts, the plasma parameters being measured are affected and we can analyse the main characteristics of ICMEs from these observations. For identifying the ICMEs that reached Earth's position, we used *in-situ* data obtained from the Advanced Explorer Composition (ACE) spacecraft (Stone et al., 1998; Chiu et al., 1998), located at the L1 point. The local Interplanetary Magnetic Field (IMF) direction and magnitude are measured at a time cadence of 4 minutes by the MAG instrument (Smith et al., 1998). The solar wind speed and density data are measured with a cadence of 92 seconds by the Solar Wind Electron, Proton, and Alpha Monitor experiment (SWEPAM; McComas et al., 1998). After the identification process, *in-situ* data were used in a further step as a validation of the model's output (see the following section for model description).

Investigating CMEs and ICMEs together with their effects at Earth is one of the priorities of space weather research. Numerous studies have focused on quantifying ICME effects at Earth, such as their effect on the geomagnetic indexes (Menvielle et al., 2010), effects on ionospheric conditions (Greenwald et al., 1995; Menvielle et al., 2007) or effects on galactic cosmic rays (Masías-Meza et al., 2016). In an effort for standardizing the ICMEs that are measured in the near-Earth environment, several ICME catalogues were developed. Each catalogue focuses on different effects of the CMEs and ICMEs. For this work, the SOHO LASCO CME catalogue[1] is used for identifying the corresponding solar sources. This catalogue contains a list of CMEs detected between 1996 to 2022 by the Large Angle and Spectroscopic Coronagraph (LASCO) onboard the SOlar and Heliospheric Observatory mission (SOHO; Brueckner et al., 1995). It has been generated using many studies, such as St. Cyr

[1] https://cdaw.gsfc.nasa.gov/CME_list/

et al. (e.g. 2000), Gopalswamy et al. (2004), Yashiro et al. (2004), Yashiro, Michalek, and Gopalswamy (2008), and Gopalswamy et al. (2009), and is regularly updated. It provides important CME information and characteristics such as the date and the time of the first appearance in the LASCO/C2 field of view (FOV), the central angle position, CME speed (obtained using different methods), sky-plane width, mass and kinetic energy, among others. Moreover, links to additional and complementary information about the CMEs are made available in this catalogue. It is also possible to extrapolate movies from different coronagraphs onboard different missions, such as STEREO. The catalogue also provides composite plots, that help to identify the CMEs and flares associated with specific SEP events or the CMEs responsible for certain intense geomagnetic storms.
Another very detailed catalogue, focused on ICMEs, is the Richardson and Cane list[2]. In Richardson, I. G. and Cane, H. V. (2010) the authors catalogue over 300 near-Earth events associated with CME events that occurred from 1996 onwards. The authors used measurements of the solar wind and its charge state to identify the ICMEs and summarise their properties in this list. This catalogue has been expanded continuously to cover similar events until 2022 and is still regularly updated. Richardson and Cane's list provides similar information as the SOHO LASCO CME catalogue as they combine a number of available data sets and try to assess when an ICME is probably present in the near-Earth solar wind. This list is mostly focused on the ICME characteristics as measured at 1 au and their geo-effectiveness, so disturbance time intervals plus geomagnetic indices are included. It also includes the start and end times of the ICME and the associated MC (if any).

2.1.2 Model: EUHFORIA

In order to model the selected CME event, we use the EUropean Heliospheric FOrecast Information Asset (EUHFORIA; Pomoell, Jens and Poedts, S., 2018) which is one of the current state-of-the-art heliospheric forecasting models. In fact, EUHFORIA comprises two models. First, a data-driven coronal model that uses synoptic magnetograms as input and computes the plasma characteristics using the empirical Wang-Sheeley-Arge model (WSA; Arge et al., 2003) at 0.1 au or 21.5 $R_\odot$ (solar radii). Then, the output of the coronal model is used as the inner boundary condition for the heliospheric wind and CME evolution model. This part solves the 3D time-dependent ideal MHD equations in the Heliocentric Earth EQuatorial (HEEQ) system in order to get the background solar wind at the time the CME occurred. Last, several CME models are implemented into EUHFORIA, such as the cone model (Xie, Ofman, and Lawrence, 2004), a linear force-free spheromak model(Verbeke, Pomoell, and Poedts, 2019), and the Fri3D model (Isavnin, 2016; Maharana et al., 2022). The linear force-free spheromak model will not be used in this study, as we suspect that the CME impact is a glancing blow and the spheromak model is known to be less useful is such cases. As a matter of fact, the spheromak model provides a good

[2] https://izw1.caltech.edu/ACE/ASC/DATA/level3/icmetable2.htm

approximation to the CME internal magnetic field configuration when the nose of the CME hits the observer. Flank encounters, however, are not well reproduced with a spheromak CME, and even can miss the observer, as the CME-driven shock structure that this model generates, expands less when travelling through the heliosphere in comparison to the cone model. Moreover, the focus of this study is not to reproduce the internal magnetic structure of the MC, but to highlight the importance of selecting the proper solar source. If we aimed at reproducing the magnetic structure, the Fri3D model would provide a more realistic approach, but the main drawback of this model is the substantial CPU time requirements. As we are aiming at comparing the arrival times of several CME candidates, it is not sensible and not necessary to use this model to perform multiple simulations.

For the present study, we used the simpler cone CME model, which injects at the inner boundary (at 0.1 au), a hydrodynamic pulse without an intrinsic magnetic field. Only 7 parameters are needed for a cone CME, including the time of insertion at 21.5 R_s (= 0.1 au), the latitude and longitude of the propagation direction of the cone, the angular half-width, the speed of insertion, the plasma density, and the temperature. The first five parameters for the selected CME event were obtained using the STEREO CME Analysis Tool (StereoCAT; Mays et al., 2015), developed by the Community Coordinated Modeling Center (CCMC). Temperature and density for the CME model were left unchanged from the default values of 0.8 MK and 10^{-18} kg m^{-3}. The cone model, although it does not possess an intrinsic magnetic field, has been extensively used as it is an accurate model for predicting the time of arrival of CME-driven shocks with EUHFORIA.

2.1.3 *In-situ* measurements

In Figure 2.2 we show, from top panel to bottom panel, the magnetic field strength (a), the three components of the magnetic field in the Geocentrical Solar Ecliptic (GSE) coordinate system (B_x, B_y, and B_z in panels (b), (c), and (d), respectively), as measured by ACE/MAG, and the solar wind density, bulk speed, temperature and pressure in the panels (e) through (h), as measured by ACE/SWEPAM.

The *in-situ* measurements before the arrival of the event show a very stable IMF in all three magnetic field components, and a low density together with a decreasing tendency in the solar wind speed. The temperature and pressure also registered a stable behaviour prior to the arrival of the ICME. On 2013 June 27, at around 13:00 UT, a sudden enhancement in the oscillation rate of the IMF components and a jump in all other solar wind plasma parameters was registered. This can be seen in Figure 2.2, marked by the vertical red dashed line. The solar wind velocity (panel (f)) registered an increase of $\sim$ 50 km s^{-1} at the arrival of the shock. Solar wind temperature and pressure (panels (g) and (h), respectively) showed a sharp increase and remained at elevated levels throughout the duration of the sheath region. The magnetic field components maintained this behaviour for about 12 hours. In the same period, the density gradually increased, while the velocity, temperature, and pressure had a

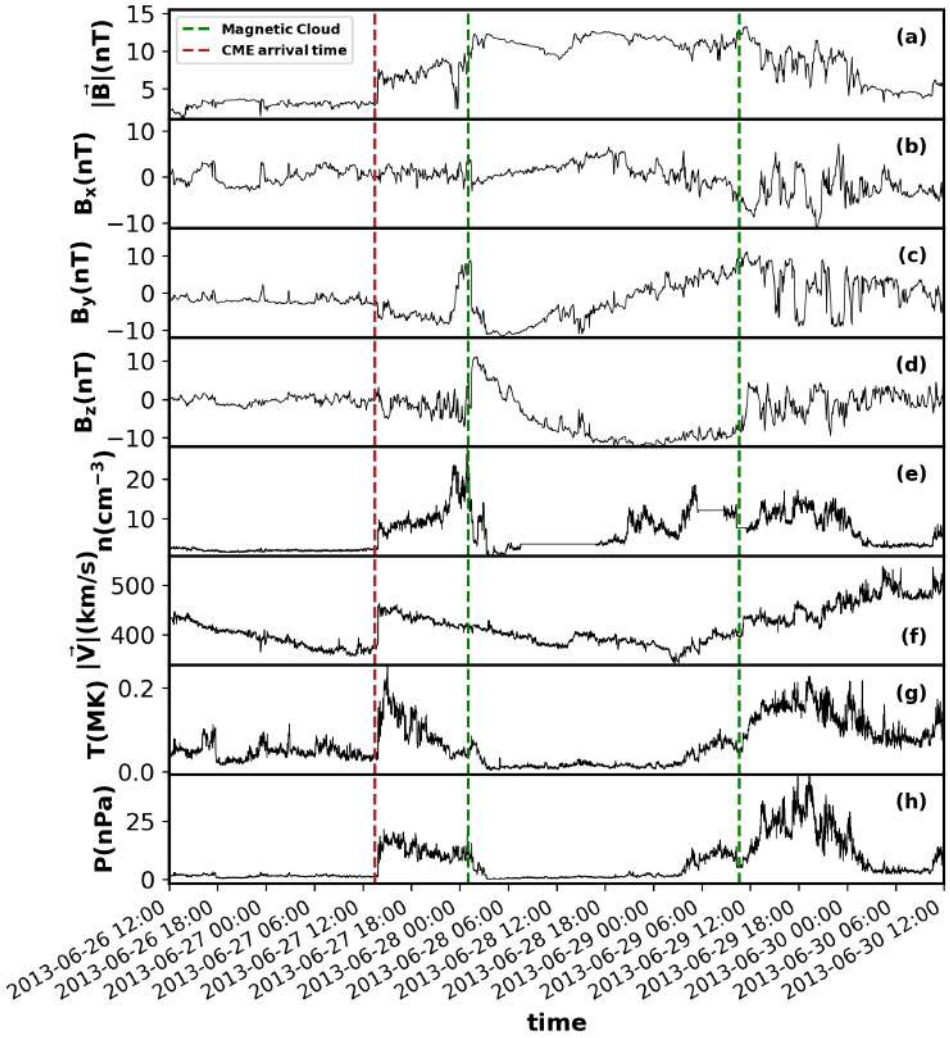

FIGURE 2.2: *In-situ* observations from ACE spacecraft at L1 between June 26 at 12:00 UT and June 30 2013 at 12:00 UT: profiles of the magnetic field magnitude (panel (a)), the 3 components (B_x, B_y, and B_z in panels (b), (c), and (d), respectively), density (panel (e)), bulk speed (panel (f)), temperature (panel (g)), and gas pressure (panel (h)). The red dashed vertical line indicates the CME-driven shock arrival, and the two vertical dashed green lines mark the start and the end of the magnetic cloud.

decreasing tendency. This corresponded to the passage of the sheath region of the ICME.

After the passage of the sheath, we observe the associated MC, with a smooth rotation in all components of the IMF, a higher strength of the magnetic field, and a lower temperature. The MC passage started at 02:23 UT on June 28 and lasted for about 33 hours, as listed in Al-Haddad et al. (2018). The starting and ending times of the MC are marked with the vertical green dashed lines in Figure 2.2. A rotation from positive to negative values in B_z was observed, while B_y showed a rotation from negative values towards positive, starting at ∼-10 nT and finishing the period

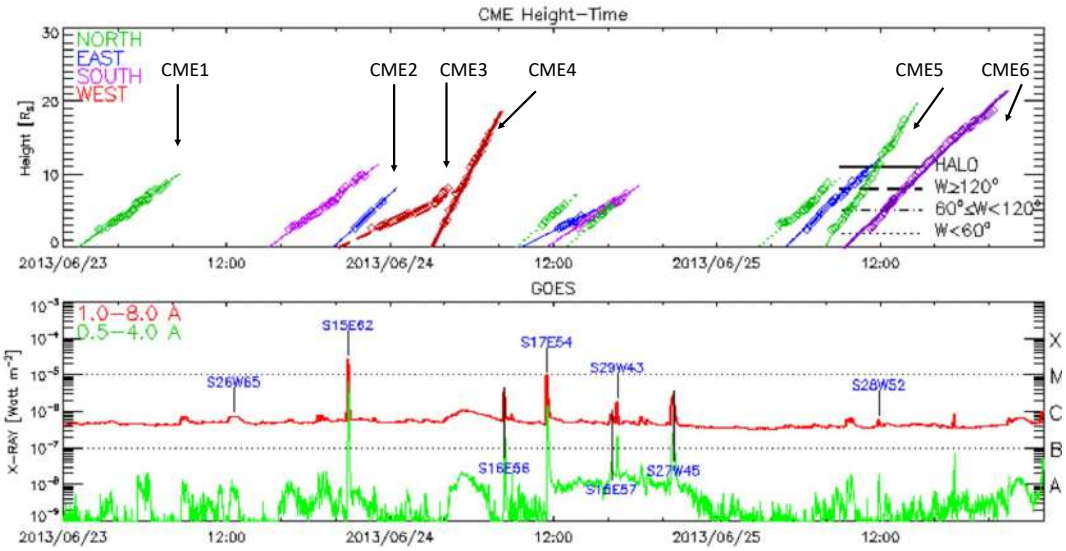

FIGURE 2.3: CME characteristics. (top panel) Height–time plots, where the six CMEs studied in this article are marked with arrows. The colours code the main CME direction (see left inset), while the type of lines codes the CME apparent angular extension (see right inset). (bottom panel) GOES X-ray flux in two wavelengths with the solar source coordinates of the identified events. Time range from June 23 00:00 UT to June 25 24:00 UT (adapted from the CDAW catalogue).

at ∼10 nT. On the other hand, B_x began the period close to 0 nT, and slightly increased until June 29 at 03:00 UT, where it started decreasing until it reached the minimum of ∼-5 nT at the end of the MC passage. The solar wind speed had a decreasing tendency until June 29 at 03:00 UT, when it reverted its trend and started increasing. The temperature and pressure remained more or less stable and at low values, until this shift in the B_x and reversal in the solar wind speed tendency. From this point on wards, they started increasing until the end of the MC.

2.1.4 Coronal Mass ejections and solar sources

In order to include the selected CMEs in the EUHFORIA simulation, we identified the possible events responsible for this MC in a time-window of 7 days before its passage at L1. Then we used the STEREO-Cat tool to obtain the parameters needed to be introduced in the simulation. We compiled the information from the different CME catalogues and used images from the different spacecrafts, described in Section 2.1.1.

Six candidate CMEs are reported in the catalogues in a time window of 3 to 5 days prior to the arrival of the MC at Earth (Table 2.1 and Figure 2.3). To compare the spacecraft data to the simulation results, we analyzed each CME and its characteristics: speed, direction of propagation, and solar source when possible.

Height-time profiles for the detected CMEs are presented in Figure 2.3. The CME events 1 through 6 from Table 2.1 are indicated. Here, the direction of propagation of the CMEs is colour-coded (legend in the top left insert of the panel). The angular

	Date(D/M/Y)	**Time(UT)**	**Width(deg.)**	**Speed(km s^{-1})**
CME 1	23/06/2013	02:36	73	261
CME 2	23/06/2013	21:24	101	339
CME 3	**23/06/2013**	**22:36**	**174**	**174**
CME 4	24/06/2013	04:00	360	709
CME 5	25/06/2013	08:24	92	562
CME 6	25/06/2013	11:12	360	349

TABLE 2.1: Six CME candidates that are possibly related to the magnetic cloud on June 28 2013 detected by the ACE spacecraft, defined by the date and time of their first appearance in LASCO C2, their angular width, their linear speed in C2 (from the CDAW catalog). The real driver is in indicated in bold.

width in the plane-of-sky is identified with the line type (see the legend in the bottom right insert of the panel). CME 1 and CME 5 have a northward propagation and both have an angular width between 60° and 120°. CME 2 is the only selected event that has an eastward propagation and an angular width between 60° and 120°. CME 6 has a southward propagation and was traced up to 22 solar radii, being a halo CME. Finally, CME 3 and CME 4 have a westward propagation, with CME 3 showing the lowest speed of all 6 events, and and angular width of over 120°, while CME 4 is registered as a halo event. The bottom panel of Figure 2.3 shows the GOES X-ray flux in two different wavelengths, with the position in the Sun of the associated solar flares. This period of time was relatively quiet, with only a few short-duration C-class X-ray flares and one M-class flare.

One may think that a full or partial halo CME can be responsible for generating the MC under study. From the SOHO LASCO CME catalogue, there are two possible candidates that were halo CMEs and erupted from the Sun within this time window of 3 to 5 days prior to the arrival of the MC at Earth. The first one of these halo CME events (CME 4) is launched from the Sun on June 24 at 04:00 UT. This event was first seen on the LASCO-C2 field of view at 04:00 UT, while in COR2-A and B it was first seen at 05:09 UT and 05:09 UT, respectively. The speed was estimated to be 709 km s^{-1}. But, when analyzing the AIA 30.4 nm images, no clear signature of this event is seen on the solar disk. When checking the direction of propagation with STA and STB, together with the position of the spacecraft that captured this event (shown in Figure 2.4), it is evident that the direction of propagation of this event is towards the backside of the Sun. This excludes this halo CME event from being responsible for the magnetic cloud of interest.

The second event we analyzed is CME 6. From the SOHO LASCO CME catalogue, this halo CME erupted on June 25, and it was seen by the LASCO-C2 detector at 11:12 UT with an estimated plane-of-sky speed of 349 km s^{-1}. CME 6 was also seen by STEREO COR2-A at 11:39 UT and STEREO COR2-B at 11:54 UT. We used the StereoCAT tool to fit this event (see Table 2.2), but we found that the longitude of propagation direction of the CME is 175°, which makes it a back-side event. The low speed of this event, together with the direction of propagation, makes this event not

compatible with an event that generates the MC of interest at L1 2 days later.
Concerning the other four candidates, and upon a more detailed inspection of the possible events responsible for the MC of interest, we concentrated on CME 1, CME 2 and CME 3 as all three events are initiated in fast succession after each other. Figure 2.3 shows the Earth position (green circle) and the STEREO-A and STEREO-B position (red and blue circle, respectively). The continuous lines associated to the position of the three points indicate the heliospheric magnetic field (HMF) lines that connect them to the Sun. These HMF lines represent the shape of the sun's extended magnetic field as it extends through the solar system. Sun's magnetic field shape is also know as Parker spiral. The dashed spiral line indicates the HMF line orginating at that position.

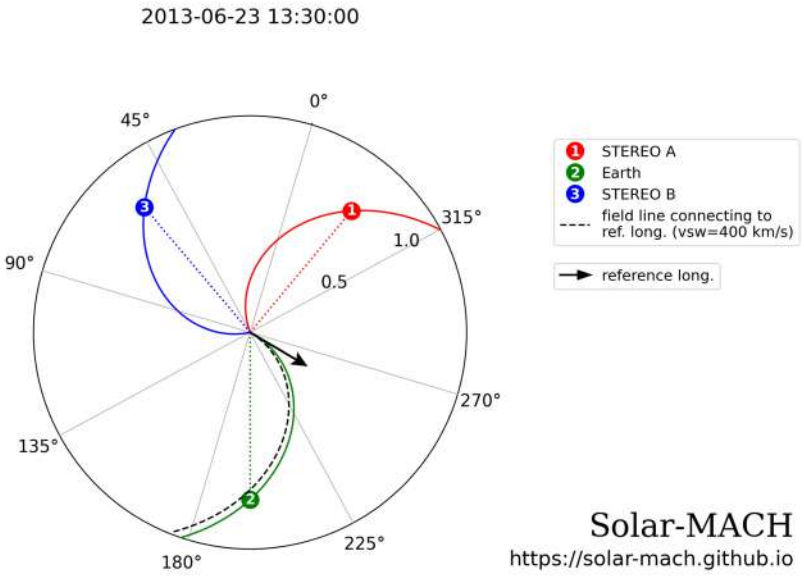

FIGURE 2.4: Spacecraft constellation position. The black arrow shows the direction of propagation in the equatorial plane for the CME. Numbered symbols indicate the observers' locations, in this case Earth position (green continuous line), STEREO-A position (red continuous line) and STEREO-B position (blue continuous line), and the spiral lines corresponding HMF lines connecting them to the Sun when considering a solar wind speed of 400 km s^{-1}.

Figure 2.5 shows the HMI magnetogram (panel a), AIA 17.1 nm (panel b) and 30.4 nm (panel c) for June 23 at 13:29 UT, prior to the eruption of CME 2 and CME 3, and 11 hours after CME 1. The light-pink arrow points at the approximate location of the source of CME 1. The white arrow points at the approximate position of AR 11778, the source of CME 2. The yellow arrow and circle point at the position of the source of CME 3, which does not correspond to any reported active region.
From the Richardson and Cane list, the magnetic cloud of interest is reported to have an associated CME, which is not seen as a halo CME. It is reported that the magnetic cloud leads to a geoeffective magnetic storm with a Dst index of -102 nT, which is already in the class of intense events. CME 1 erupts around 20 hours before CME 2 and

CME 3, but the speed at which it propagates is very slow. This results in this event still being present in all available coronagraph images (see Figure 2.6). The direction of propagation appears to have a big northward component, which makes it incompatible with a hit at Earth. Analyzing images from SDO/AIA 17.1 nm, there is a thin filament structure, positioned at approximately N35 E60 that erupts very slowly into a streamer-like structure. On the other hand, CME 2 and CME 3 are much more aligned with the ecliptic plane, making them the more suitable events to keep analyzing. The brightness of CME 1 in the images is much higher than the brightness of the other two events. This is due to the combination of the streamer and CME 1 very slow speed of eruption, which enhances the brightness in the white-light images. This entails that the analysis of the coronagraph images requires significantly more effort. From Figure 2.3 bottom panel, we see a GOES X-ray M2.9 class flare at around 22:00 UT originating at S15 E62, close to active region NOAA AR 11778, positioned at S15 E47. This is close in time with CME 2 and CME 3. CME 2 is reported to erupt close to this position with a speed of 339 km s^{-1}. The main direction of propagation is towards the southeast, and due to the position of the spacecraft and the high brightness of CME 1, it is not clearly seen in COR2-B. CME 3 erupts from a small active region (not classified as such by NOAA), positioned at N14 W14 at the time of the eruption, marked in Figure 2.5 with the yellow arrow and circle. CME 3 appears to be the best candidate (Table 2.1) for explaining the studied MC passage at L1.

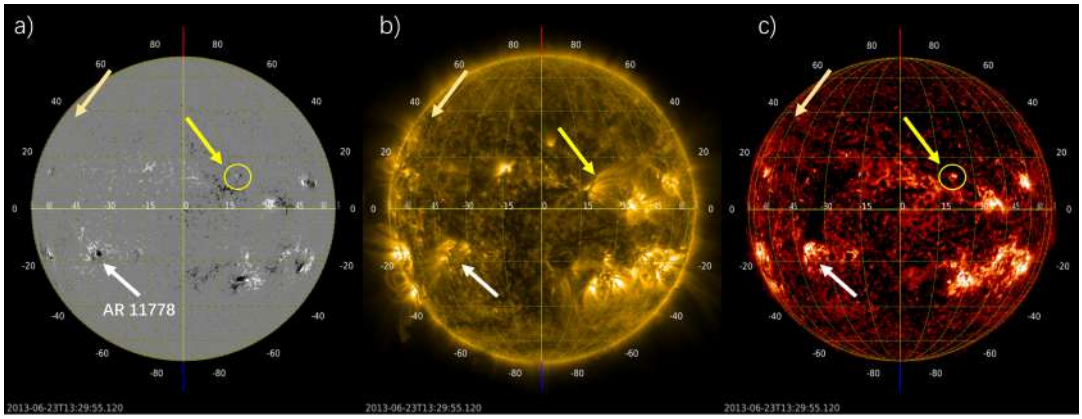

FIGURE 2.5: a) HMI magnetogram b) AIA 17.1 nm, c) AIA 30.4 nm on June 23 2013 at 13:29 UT. The light-pink arrow shows the approximate position of the source of CME 1. The white arrow shows the position of NOAA AR 11778, origin of CME 2, while the origin of CME 3 is marked with a yellow arrow and circle. CME 3 source region corresponds to a tiny emerging flux at the edge of a filament channel.

In Figure 2.6 we show the coronagraph white light observations by COR2-A and COR2-B for June 23 at 23:39 UT, aboard STEREO A and B spacecraft respectively, and the running difference images from LASCO-C2, aboard SOHO, at 23:36 UT. It is clear from the coronagraph running difference images that it is not easy to observe the CME associated with the event detected by the spacecraft positioned at L1.
From COR2-A (Figure 2.6a) it is possible to distinguish the presence of CME 1 in the northern region of the image, CME 2 in the southwestern region of the image,

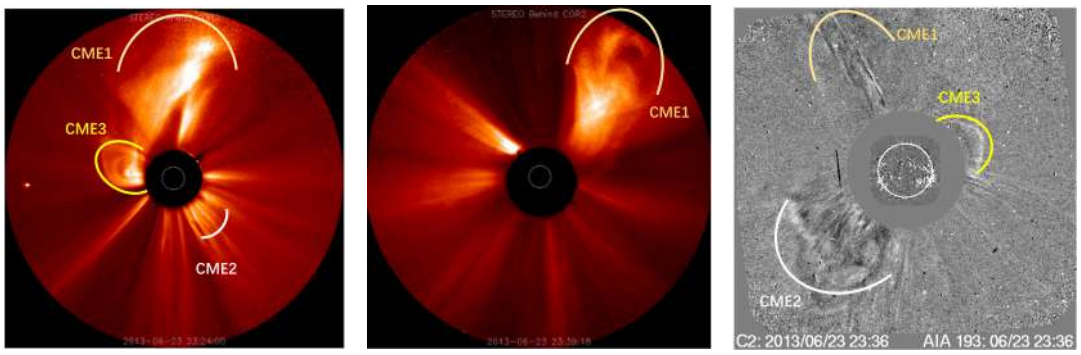

(A) (B) (C)

FIGURE 2.6: STEREO/SECCHI/COR2-A (a) and COR2-B (b) white light coronagraph observations on June 23 at 23:39 UT. SOHO/LASCO/C2 (c) running difference white light coronagraph observation at 23:36 UT for the same day. CME 1, CME 2 and CME 3 are highlighted using a light-pink, white and yellow curve (respectively). No clear signatures of CME 2 and CME 3 are present in COR2-B.

and the faint CME 3 in the eastern flank. It is not clear nor easy to see the CME 2 due to its faintness, combined with the high brightness from CME 1. In Figure 2.6b FOV, we can only observe CME 1. This is due to the faint nature of both CMEs and their direction of propagation with respect to STEREO-B. As seen from LASCO-C2 (Figure 2.6c), CME 1 is barely visible, CME 2 appears on the south-eastern side of the figure, while on the north-western side it is possible to see the presence of a faint CME (CME 3), similar to what we see in Figure 2.6a. For all cases, the detection of the main suspected CMEs is made complicated by the fast and wide CME 1, which is seen propagating northward.

2.1.5 Parameters of the CMEs

In order to reproduce the CME observed by the coronagraphs, we fit the events with the help of the StereoCAT tool[3]. StereoCAT is an online tool designed for space weather forecast and research, allowing users to obtain the CME kinematic properties. The parameters derived via this tool such as latitude (ϕ), longitude (θ), half angle (α), speed of the CME (V_{cme}) and passage time at 21 solar radii ($R_{\odot}$), can be used as input parameters for a broad range of CME propagation models. The parameters used for the CMEs are reported in Table 2.2.

The parameters of the StereoCAT fitting show that CME 3 is propagating towards Earth direction with a low velocity, which is comparable with the background solar wind speed (400 km s^{-1}) measured at Earth prior to the event (see Figure 2.2). This confirms the coordinates of the source that we identified. From our analysis and fittings, it emerged that the CME responsible for the event detected by ACE is most probably CME 3. However, in order to verify which halo and non-halo CMEs

[3]Available online at https://ccmc.gsfc.nasa.gov/analysis/stereo/

	$\phi(^\circ)$	$\theta(^\circ)$	$\alpha(^\circ)$	$\mathbf{V_{cme}(km\ s^{-1})}$	**Passes at 21R$_\odot$**
CME 1	-60	48	17	224	2013/06/23 18:30
CME 2	-62	-15	20	489	2013/06/24 06:01
CME 3	**14**	**14**	**27**	**391**	**2013/06/24 09:17**
CME 4	175	-15	56	844	2013/06/24 07:47
CME 5	-41	61	22	487	2013/06/25 15:53
CME 6	175	-21	38	620	2013/06/25 16:48

TABLE 2.2: StereoCat fitting parameters chosen for the CMEs candidate: $\phi(^\circ)$ is the heliographic longitude, $\theta(^\circ)$ is the heliographic latitude, both measured in the HEEQ system (Heliocentric Earth Equatorial), $\alpha(^\circ)$ is the angle between the legs, $V_{cme}(km\ s^{-1})$ is the CME speed propagation and "Passes at 21 $R_\odot$" indicates the time when the CME reaches 21 $R_\odot$.

(Table 2.1) can be responsible for the MC observed at Earth, we used EUHFORIA to model their propagation through the interplanetary medium (see Section 2.1.6).

2.1.6 EUHFORIA simulations

Before running the EUHFORIA simulation, a coronal model has to be computed for the day the CME started its journey in the corona (up to 0.1 au).
The coronal model of EUHFORIA that we used is data-driven part. We selected the magnetogram of June 22, 2013 at 22:36 UT, as provided by Global Oscillation Network Group and Air Force Data Assimilative Photospheric Flux Transport (GONG-ADAPT). The result for the solar wind is presented in Figure 2.7. We found a relatively good agreement with the solar wind observations for density and speed, between 25 June at 00:00 UT and 27 June at 12:00 UT, just before the arrival of the CME. Considering the list of possible CMEs shown in Table 2.1, we test a few of them to see if they could reach the Earth (see the Appendix). As anticipated by our analysis from observations and fittings, only CME 3 (as presented in Table 2.1 and being injected into the heliospheric domain with the parameters presented in Table 2.2) is capable of reaching the Earth.
We report the results of the simulations including CME 3 in Figures 2.8 and 2.9. Simulations were made using a 2° angular resolution in the longitudinal and latitudinal direction and a radial resolution of ~ 0.0039, with the domain extending up to 2 au. Figure 2.8 shows four snapshots in which it is possible to see the dynamical evolution of the CME through the heliosphere obtained from the EUHFORIA simulation. In the left panels, we show two snapshots of the number density (in units of cm^{-3}) at two different times: the first one (Figure 2.8(a)) is at the time when the CME is injected and the second one (Figure 2.8(c)) is at the time when the CME reaches the Earth. In the left plot of each panel, the plot of the plasma density in the equatorial plane is shown, while the right plot shows the same quantity in the meridional plane that contains Earth. In each snapshot, STEREO-A and STEREO-B position is shown, together with the position of the planets, as indicated in the legend located in the lower region of the snapshot. The right panels of Figure 2.8 show the radial speed in

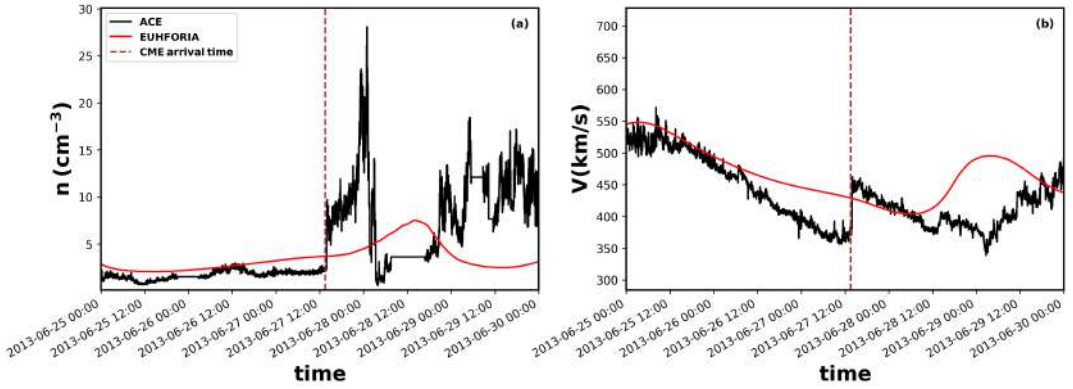

FIGURE 2.7: EUHFORIA best simulation results for the background solar wind computed at L1 (red curves) between 25 and 30 June 2013 compared with *in-situ* measurements at L1 (black curves). The dashed vertical line corresponds to the arrival of the CME at L1. Left panel: density, right panel: speed.

the simulation (in units of km s^{-1}). In particular, the two snapshots presented here (Figure 2.8(b) and 2.8(d)), are taken at the same time as the previous figures. From the plots shown, the CME travels throughout the heliosphere and hits the Earth four days after its eruption. This is related to the low speed found using the StereoCAT fitting tool, which gives us a value of the CME speed comparable with the solar wind velocity. Additional simulations for CME 1, CME 2 and CME 4 are included in Section 2.1.7.

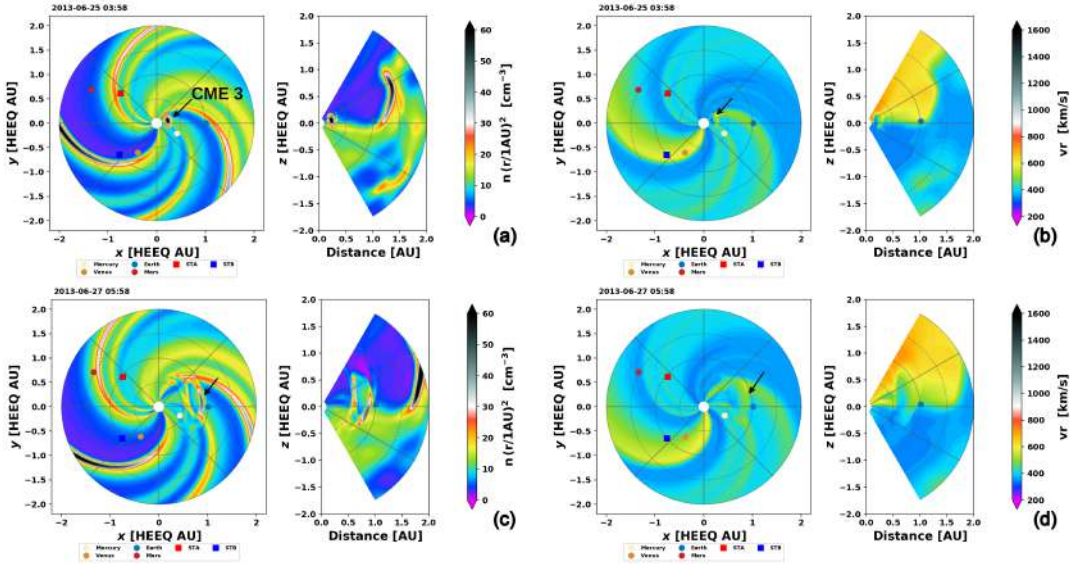

FIGURE 2.8: Overview of EUHFORIA results for the ICME modelled with a cone model: scaled plasma number density (left panels) and radial velocity (right panels). The four panels show the structure of the CME at two different times: 24 June 2013 at 09:58 UT for the top panels and 26 June 2013 at 21:58 UT for the bottom panels. At both times, both an equatorial x–z plane (left) and a meridional distance–z (or x–z) plane (right) are shown. The black arrows in each panel indicates the position of CME 3.

In Figure 2.9 we present the comparison between the EUHFORIA simulations and ACE data. From top to bottom panels, we show the solar wind density, speed, temperature, and pressure. The black line represents the measurements while the red solid line represents the EUHFORIA results. In each panel, there is a violet shaded area, which is generated using the simulated data at virtual spacecraft positioned at $\pm 5^{\circ}$ with respect to Earth in both latitude and longitude. This mesh of virtual spacecraft allows us to recover the time series at other positions, which can be helpful in the case of having some unaccounted error in the kinetic parameters when injecting the CME in the heliospheric domain.

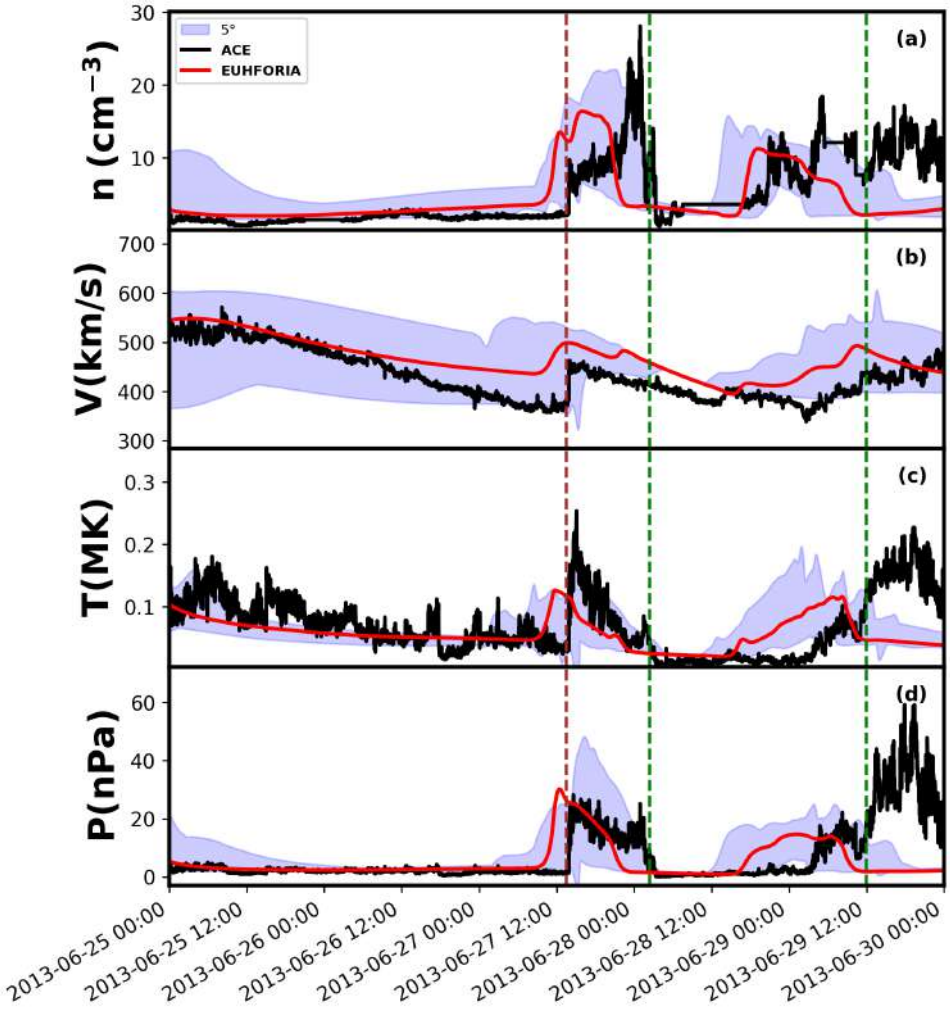

FIGURE 2.9: Comparison between simulation results and ACE spacecraft data. From the top panel to the bottom panel, we present the number density, solar wind bulk speed, temperature, and pressure of the solar wind. The spacecraft data is indicated with a solid black line, while the results from EUHFORIA simulations are indicated with a red solid line. The shaded area represents the combination of the results of the plasma parameters obtained from virtual spacecraft placed at $\pm 5^{\circ}$ in longitude and/or latitude from Earth.

When comparing *in-situ* data with simulations, we find a relatively good agreement between them. In panel (a) of Figure 2.2, we show the comparison between the

plasma density detected by the ACE spacecraft (black continuous line) and the EUHFORIA results (red continuous line). In the first region, namely the region before the shock arrival (indicated by the red vertical dashed line), the number density seems to assume low values for both *in-situ* spacecraft data and numerical simulation, showing a very good agreement. Immediately after the shock passage, there is a sudden increase of the density, for both the measurements and the simulation, with a difference in the behaviour near the beginning of the MC region. At the beginning of the MC passage, a rapid decrease is seen in both spacecraft data and the synthetic numerical simulation data. In the MC region (the region between the two vertical green dashed lines), there is a lack of data for the ACE spacecraft followed by an increase in the density values, that also continues after the end of the MC region. We observe a similar behaviour in the EUHFORIA results, with the only difference in the behaviour of the density after the ending of the MC region. The plasma density trend is also confirmed by the shaded area, which has the same behaviour as the red continuous line. In panel (b) we show the comparison between the measured and simulated velocities. Here, it seems that there is a better agreement between the simulation results and the satellite data than for the density. The curves' behaviour is basically the same, with a difference related to the higher values obtained in the simulations. This could be due to the fact that during its propagation an ICME can interact with the interstellar medium disturbances and this can lead to a decrease in the speed of its MC. The violet shaded area here has the same trend as the red line. Panels (c) and (d) show respectively the plasma temperature and the pressure. Both quantities have the same trend seen in the density panel, with the temperature that shows a more oscillating trend.

2.1.7 EUHFORIA CME1, CME2 and CME4 simulations

In this section, we show complementary results for the simulations obtained when modelling (separately) CME 1, CME 2 and CME4. The first two CMEs were initially good candidates to be the CME responsible for the MC and shock observed by ACE spacecraft, while CME4 is a backsided event. In Figure 2.10 we present the simulation results for the CME 1. As we already mentioned in Section 2.1.4, this CME has a northward propagation and from the STEREO-Cat analysis it results to have a very low speed (see Table 2.2). Indeed, it appears difficult to identify, also from EUHFORIA simulations.
In Figure 2.11 we present the results of the simulation obtained for the CME 2, i.e., the CME that preceded in time the CME 3. As it is possible to observe, the CME propagation direction is not in the Sun-Earth direction, but the CME is mostly directed in the western flank, so it does not hit Earth. This behavior is expected just from the parameters obtained from the STEREO-Cat fit. We adapted the parameters obtained from the STEREO-Cat fit, in a similar way as we did with CME 3, so that the position where EUHFORIA injects the CME corresponds to the same position in which we localized the CME on the Sun's surface.

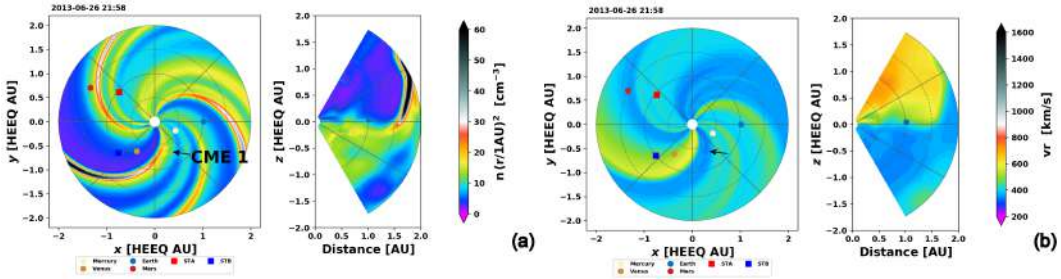

FIGURE 2.10: Overview of EUHFORIA results for the ICME modelled with a cone model: scaled plasma number density (left panel) and radial velocity (right panel). Both panels show the simulation at the same time, when the CME is approximately at 0.5 au, which corresponds to June 26 at 21:58 UT. The black arrows in each panel indicate the position of CME 1.

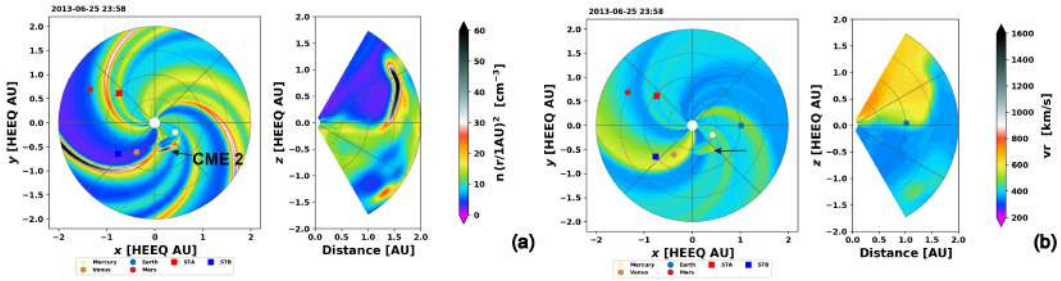

FIGURE 2.11: Overview of EUHFORIA results for the ICME modelled with a cone model: scaled plasma number density (left panel) and radial velocity (right panel). Both panels show the simulation at the same time, when the CME is approximately at 0.5 au, which corresponds to June 25 at 23:58 UT. The black arrows in each panel indicate the position of CME 2.

In Figure 2.12, we present the result of the simulation for the event seen by the SOHO/LASCO/C2 instrument on June 24 at 04:00 UT. As mentioned in Section 3.2 the CME goes in the opposite direction of the Sun-Earth direction and this allows us to discard this CME as a possible candidate for the MC seen at L1.

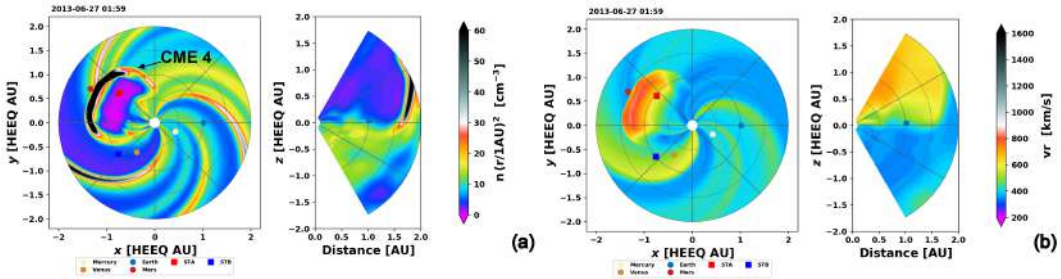

FIGURE 2.12: Overview of EUHFORIA results for the ICME modelled with a cone model: scaled plasma number density (left panel) and radial velocity (right panel). Both panels show the simulation at the same time, when the CME is approximately at 1 au, which corresponds to June 27 at 01:59 UT. The black arrows in each panel indicate the position of CME 4.

2.2 Energetic particle fluxes at heliospheric shocks: evidences of superdiffusion and comparison between analytical and numerical modeling

Energetic particles are ubiquitous in space and astrophysical environments, and understanding the acceleration and the propagation mechanisms is an open challenge for modern astrophysics. Energetic particles fluxes measured by spacecraft in the heliosphere are frequently observed to peak during interplanetary shock crossings, suggesting the shock to be the source of acceleration. It has been shown that the shape of the energetic particle fluxes, upstream and downstream of the shock, is affected by energetic particle transport properties. Here we present a comparison among a number of shock crossings observed by the ACE spacecraft, and the energetic particle fluxes derived by a test-particle numerical model in the vicinity of a planar shock. We use a complementary method to constrain α and $\mathcal{D}_\alpha$, using both spacecraft data and the energetic particle fluxes obtained by running a test-particle numerical simulation of the energetic particle dynamics around a shock (Prete, Perri, and Zimbardo, 2019).

2.2.1 Overview of the numerical method and set-up of the parameters

In this section we present the essential features of our simulation, which is described in full detail in Prete, Perri, and Zimbardo (2019). The propagation of particles accelerated at shock waves is the result of the diffusive motion due to the scattering of particles off the magnetic irregularities in the turbulent plasma, and of the ordered motion due to the plasma advection. We implement a test-particle approach, trying to mimic the process of energetic particle transport upstream and downstream of a shock front in a simple way. We set-up a one-dimensional numerical simulation in the frame of reference where the shock is at rest: the x-axis is pointing from the upstream region to the downstream region, and the shock is fixed in the origin at $x = 0$. The simulation box extends from $-L$ to L (see below), and the upstream (downstream) plasma velocity is V_1 (V_2).
The particle motion is described by a Langevin-type equation which includes the constant bulk velocity (e.g., Strauss and Effenberger, 2017), and where the random motion is described by the particle velocity v_{ran}, whose value is changed randomly after a scattering time τ:

$$dx_i = V_{\mathrm{bulk}} dt_i + v_{\mathrm{ran}} dt_i. \tag{2.3}$$

dt_i is the integration time step, and $V_{\mathrm{bulk}} = V_1$ for $x \leq 0$, while $V_{\mathrm{bulk}} = V_2$ for $x > 0$. The random velocity is determined as

$$v_{\mathrm{ran}} = (2\xi - 1)\, v, \tag{2.4}$$

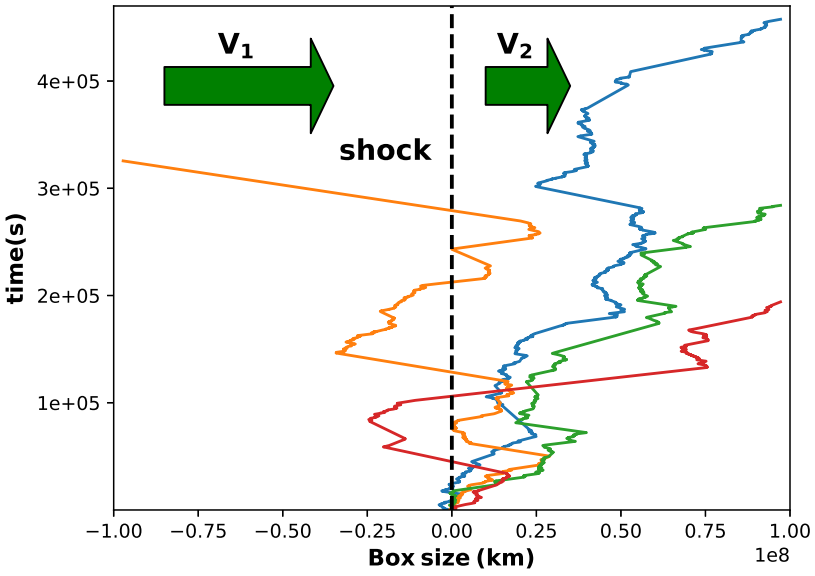

FIGURE 2.13: Simulation box set up. Upstream side on the left, downstream side on the right. A few particle trajectories, obtained from Eq. (2.3) (time is growing in the vertical direction) are shown. It can be seen that trajectories are characterized by both long and short paths.

where ξ are uncorrelated random numbers, such that $0 \leq \xi \leq 1$. Here, ξ is not changed at each time step but only after a scattering time τ (which is different from the integration time step). In order to keep the same numerical scheme for normal diffusion and superdiffusion, we put the emphasis on the scattering time: this is a constant in the case of normal diffusion while it is obtained from a power-law distribution in the case of superdiffusion. In the diffusive case, both τ and $v_{\rm ran}$ are finite, so that the resulting displacements $\Delta x = v_{\rm ran}\tau$ are finite and independent; then the Central Limit Theorem (CLT) implies that the long time behaviour is diffusive.
Conversely, in the anomalous, superdiffusive case, τ has a power-law probability distribution such that $\langle \Delta x^2 \rangle = v_{\rm ran}^2 \langle \tau^2 \rangle$ diverges, and the CLT does not apply. A new random number is generated when the particle integration time undergoes an increase corresponding to the temporary scattering time τ. Such a scattering time is variable and is extracted by a power-law distribution function corresponding to a Lévy random walk (Klafter, Blumen, and Shlesinger, 1987; Shlesinger, West, and Klafter, 1987). While various implementation schemes of a Lévy walk can be devised (see, e.g., Zaburdaev, Denisov, and Klafter, 2015), we obtain the distribution of scattering times using the method proposed by Trotta and Zimbardo (2015) and Prete, Perri, and Zimbardo (2019). The probability of free paths ℓ for a Lévy walk has a power-law form for large ℓ, (i.e. for $|\ell| > \ell_0$). Also, we choose a constant probability distribution for $|\ell| < \ell_0$. Therefore, the form of the free path probability

distribution is given by

$$\Psi(\ell,\tau) = \begin{cases} \frac{1}{2}C\delta(|\ell| - v\tau), & |\ell| < \ell_0 \\ \\ \frac{1}{2}C|\ell/\ell_0|^{-\mu}\delta(|\ell| - v\tau), & |\ell| > \ell_0\,. \end{cases} \tag{2.5}$$

As above, v is the velocity of the diffusing particles, which is kept constant in each simulation (no particle acceleration envisaged in such simlations). It can be shown that such a probability distribution of free path lengths gives rise to superdiffusion with the mean square displacement growing as

$$\langle \Delta x^2 \rangle \propto t^{\alpha} \tag{2.6}$$

for $t \to \infty$, with the exponent of superdiffusion given by $\alpha = 4 - \mu$ for $2 < \mu < 3$, while normal diffusion is recovered for $\mu > 3$ (Shlesinger, West, and Klafter, 1987; Zumofen and Klafter, 1993; Zimbardo and Perri, 2013; Zimbardo and Perri, 2018). Being fulfilled the normalization condition $\int_0^{+\infty} d\tau \int_{-\infty}^{+\infty} d\ell\ \Psi(\ell,\tau) = 1$, the scattering times are generated for $\xi > \xi_0$ as

$$\tau = \tau_0 \left[\frac{1}{\mu\,(1-\xi)}\right]^{\frac{1}{\mu-1}}, \tag{2.7}$$

while $\tau = \xi/C$ for $\xi < \xi_0$, being $\xi_0 = C\tau_0 < 1$ (see Trotta and Zimbardo (2015) and Prete, Perri, and Zimbardo (2019) for more details). Of course, when $\xi \to 1$ very long scattering times are allowed. Because of the space-time coupling of Lévy walks (see Eq. (2.5)), very long scattering times imply very long free paths. In summary, the distribution of scattering times depends on two parameters, μ and the scale time τ_0. Conversely, in the case of normal diffusion a single parameter, say $\langle\tau\rangle$, is sufficient to characterize the diffusive motion.

Energetic particles are injected at the shock, $x = 0$, and are followed until they exit a simulation box as large as $\pm 5L$ (in order to avoid the effects of what would be absorbing boundaries at $\pm L$). Typically, 10^6 particles are used in each run. The probability density $P(x,t)$ of particles being at a given position x after injection is obtained by dividing the simulation box in 200 intervals Δx_j, and counting the number of particles found in each interval at a given time. The probability density is normalized to one. Assuming a stationary situation, the steady state particle density $n(x)$ is obtained as (e.g., Kirk, Duffy, and Gallant, 1996; Perri and Zimbardo, 2008; Zimbardo and Perri, 2013)

$$n(x) = \Phi_0 \int_0^{\infty} P(x,t)dt, \tag{2.8}$$

where Φ_0 is the particle injection rate at the shock. In the numerical simulation, Φ_0 can be considered as a free parameter to be adjusted in order to match the simulation results to the observations. We set $dt_i = 1$ s, which corresponds to the inverse of the

proton gyrofrequency in a 10 nT magnetic field, $V_1 = 600$ km/s, and $V_2 = 200$ km/s, which are values appropriate to the solar wind speed in the shock frame and correspond to a compression ratio $r = V_1/V_2 = 3$. In this section, the box size L has been chosen to correspond to $L = 10^7$ km. For the purpose of illustrating the influence of the model parameters, we made simulation runs with a supra-thermal non relativistic 100 keV proton population. Thus, the particle speed is set up to $v = 4427$ km/s. We performed several runs while varying the model parameters μ and τ_0; here, we show the main features of the results, while further results are shown in Prete, Perri, and Zimbardo (2019).

Figure 2.14 shows the probability density $P(x,t)$ at time $t = 4 \times 10^4$ seconds, obtained with several different values of $\mu = 2.1$–4.5 (see legend) and a scale time $\tau_0 = 50$ seconds. We emphasize again that $2 < \mu < 3$ implies superdiffusion in such a Lévy random walk, while for $\mu > 3$ the system recovers normal diffusion. It can be seen that the value of μ directly influences the height and width of the distribution, and that the smaller μ the heavier the tails of the probability distribution. This means that, for a fixed τ_0, the small values of μ allow for a faster spreading of particles both to the left and to the right.

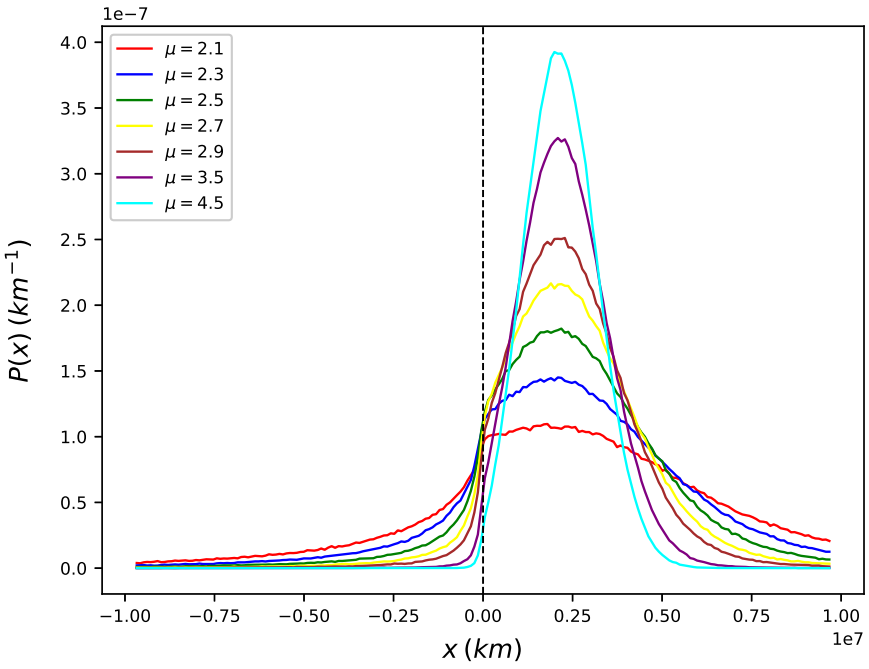

FIGURE 2.14: Probability density $P(x,t)$ at time $t = 4 \times 10^4$ s, obtained with several different values of μ (see legend) and a scale time $\tau_0 = 50$ s. The smaller μ the heavier the power-law tails of the probability distribution, while for μ= 3.5 and 4.5 the probabilities $P(x,t)$ tend to Gaussian distribution.

Figure 2.15 shows the corresponding density profiles, as obtained by Eq. (2.8), around the shock for the same values of μ shown in Figure 2.14.

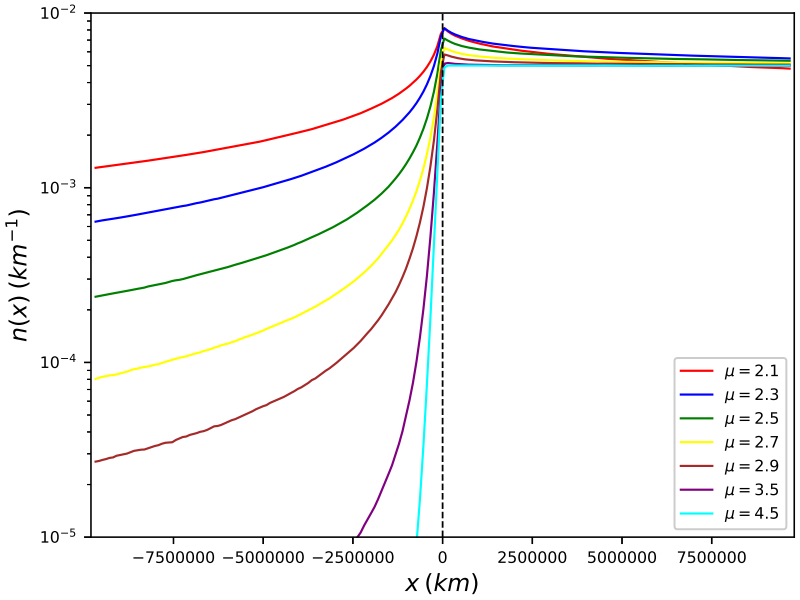

FIGURE 2.15: Energetic particle density spatial profile $n(x)$ in the case of superdiffusion, for several values of μ, as indicated in the legend, and a scale time τ_0= 50 s

Figure 2.15 clearly shows that the height of the density profile and the slope in the upstream region directly depend on μ. Also, the height of the density peak at $x = 0$ depends on μ, as predicted by Perri and Zimbardo (2012a) and Zimbardo and Perri (2013). Indeed, including superdiffusive transport within a first order Fermi process implies that the density at the shock $n(x = 0)$ is larger than that far downstream $n(x \to \infty)$, according to the ratio

$$\frac{n(x=0)}{n(x\to\infty)} = \frac{\mu - 1}{2(\mu - 2)} \tag{2.9}$$

as a consequence of the propagator scaling properties (Kirk, Duffy, and Gallant, 1996; Perri and Zimbardo, 2012a; Zimbardo and Perri, 2013). The above equation shows that when $\mu \to 3$, i.e., approaching normal diffusion, the ratio of densities approaches unity, as for normal diffusion. Conversely, for $\mu \to 2$, the ratio of densities tends to become very large. This effect can be see in Figure 2.15, since the height of the density peak at $x = 0$ grows when $\mu \to 2$, and this can be considered as a further diagnostic of superdiffusion.

To understand the influence of the scale time τ_0 on the density $n(x)$, Figure 2.16 shows the density profiles for $\mu = 2.5$ and for a number of values of τ_0 ranging from 2 s to 75 s. It can be seen that the smaller τ_0, the faster and sharper the decay of the density close upstream of the shock; therefore, τ_0 sets the value of the density jump of energetic particles on a macroscopic scale. From Figure 2.16 it appears that there is a weak dependence of the density bump at $x = 0$ on τ_0, which is not predicted by

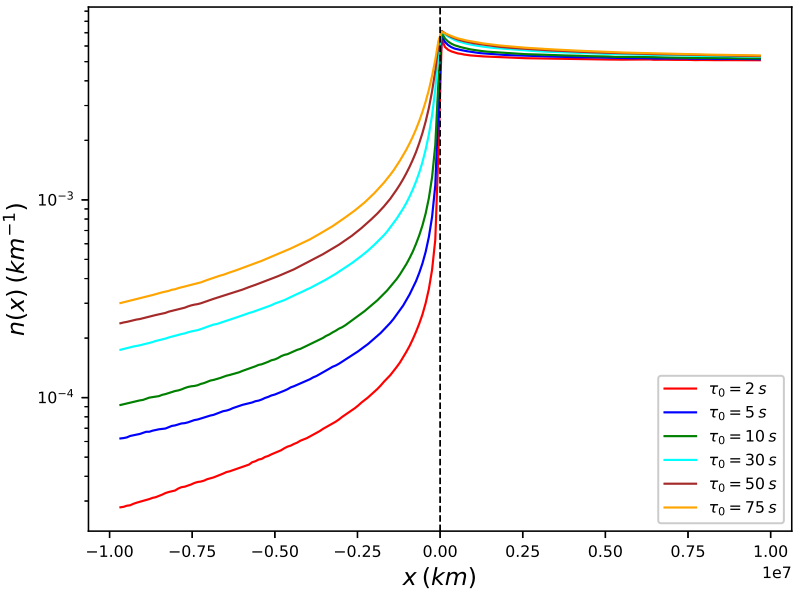

FIGURE 2.16: Energetic particle density spatial profile $n(x)$ in the case of superdiffusion with μ= 2.5 and for several values of the time scale τ_0, ranging from 2 s to 75 s.

the theory, see Eq. (2.9). However, we consider that this can be an effect related to the finite size of the intervals Δx_j along the x axis.

2.2.2 Energetic particle transport properties from particle fluxes from in-situ spacecraft measurements

Our model assumes a steady-state, one-dimensional shock, so that all the spatial variations are along the direction normal to the shock front only. All the quantities shown in the previous section have been obtained in the shock rest frame, and describe the spatial distribution of energetic particles as a function of the coordinate x, which is perpendicular to the shock.

For comparison with spacecraft observations, the upstream and downstream plasma velocities in the shock frame have to be linked to the ones in the spacecraft frame. Thus, velocities in the shock frame are related to those in the spacecraft frame by a Galilean transformation

$$V_1^{s/c} = V_{sh}^{s/c} + V_1^{sh}\,, \tag{2.10}$$

where $V_1^{s/c}$ is the upstream plasma velocity measured in the spacecraft frame, V_1^{sh} is the upstream plasma velocity in the shock frame, and $V_{sh}^{s/c}$ is the shock velocity in the spacecraft frame. Clearly, a similar transformation holds for the downstream velocities.

We make the simplified assumption that the shocks are planar and perpendicular to the radial direction. We further notice that the compression ratio can be expressed in

TABLE 2.3: Selected shock crossings by the ACE spacecraft. We have reported from the left to the right: the date, the time of the shock crossing, the angle θ_{Bn}, the Alfvénic Mach number, the compression ratio, the upstream speed in the spacecraft frame, and the downstream speed in the spacecraft frame.

date	time	$\theta_{Bn}(^\circ)$	M_A	r	$V_1^{s/c}$ (km/s)	$V_2^{s/c}$ (km/s)
26/08/98	06:20	120 ± 15	4.24	2.3 ± 0.7	455	602
08/06/00	08:41	129 ± 10	3.13	2.9 ± 0.8	521	772
23/04/02	04:15	154 ± 8	3.82	3.6 ± 1.3	410	580

the shock frame as $r = V_1^{\rm sh}/V_2^{\rm sh}$, so that the following relation can be derived (e.g., Burgess, 1995; Perri and Zimbardo, 2015)

$$V_{\rm sh}^{\rm s/c} = \frac{rV_2^{\rm s/c} - V_1^{\rm s/c}}{r-1}\,. \tag{2.11}$$

The compression ratio can be directly obtained from the observed density ratio as $r = n_2/n_1$: values for three shocks detected by the ACE spacecraft are reported in Table 2.3 . In this work, we have carefully evaluated n_1 and n_2 within selected regions around the shock front where n_1 and n_2 remain almost constant in their time profile (see Perri et al., 2015). Once the upstream and downstream speeds in the shock frame are determined from Eqs. (2.10,2.11), we can recast the numerical results for the energetic particle density as a function of time t rather than as a function of the shock distance x, i.e., for the upstream (downstream) side $t = x/V_1^{\rm sh}$ ($t = x/V_2^{\rm sh}$). We report here the comparison between ACE observations and numerical simulations for three shock crossings: 26 August 1998, 8 June 2000 and 23 April 2002. For each shock selected, we determined the compression ratio r, the Alfvénic Mach number $M_A = V_{sh}/V_A$ (being $V_A = B/\sqrt{4\pi\rho}$, the Alfvén speed), and the angle θ_{Bn} between the shock normal and the mean magnetic field direction (see Table 2.3). We analyzed the magnetic field data from the MAG instrument on board ACE at 4 minutes time cadence, while for the solar wind data we used the SWEPAM instrument at 64 vec/s resolution.
The angle θ_{Bn} was determined using the minimum variance analysis (MVA) method (Sonnerup and Cahill, 1968). To determine the plasma parameters, we selected two regions behind and ahead of each shock, whose range goes from -200 min to 200 min. From the MVA analysis, we found three different geometries for the shocks analyzed: quasi-perpendicular for the 26/08/98 event, oblique for the 08/06/00 event, and quasi-parallel for the 23/04/02 event (see Table 2.3).

2.2.3 The 26/08/1998 quasi-perpendicular shock event

In Figure 2.17 we show from top to bottom the energetic ion fluxes, measured by EPAM/LEMS-30 in the energy channels from 67–115 keV and 315–580 keV at 12 s resolution, the magnetic field magnitude, the solar wind number density, the solar wind bulk speed, and the magnetic field variance $\sigma^2 = \sum_{i=1,2,3}\sigma_i^2$ normalized to the

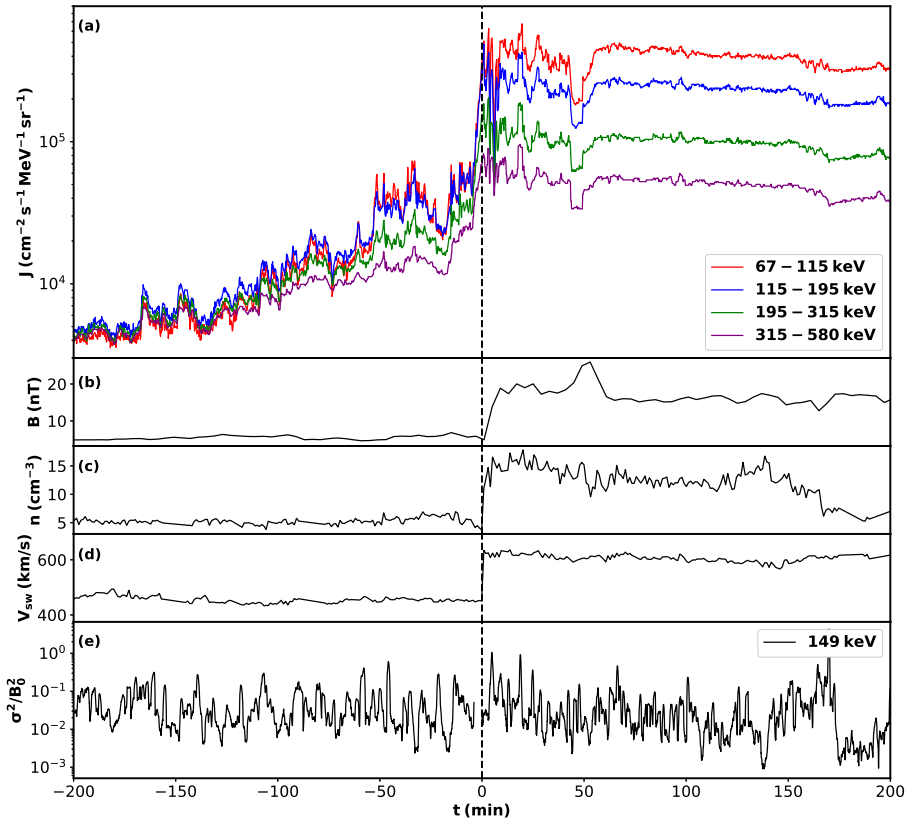

FIGURE 2.17: Shock crossing observed by ACE on 26 August 1998. From top to bottom: (a) differential flux of energetic particles measured at 12s of cadence by LEMS-30 in the energy channels from 115–195 keV to 321–580 keV, see legend; (b)the 4 minute resolution magnetic field intensity; (c) proton number density and (d) proton bulk velocity in the spacecraft frame at a resolution of 92 s; (d) magnetic variance computed over a time scale corresponding to particles with energies within the channel 115–195 keV, normalized to the average magnetic field B_0 (see Perri and Zimbardo (2012b) and Zimbardo, Prete, and Perri (2020)). The vertical dashed line indicates the time at which the satellite crossed the shock.

average magnetic field, where each component is defined as $\sigma_i^2 =< (B_i - < Bi >)^2 >_T$ and T represents the timescale for the average computation (Perri and Zimbardo, 2012b). We have excluded from the analysis the EPAM energy channel 47–65 keV, because it could be influenced by thermal particles. We have also excluded energy channels higher than $315 - 580$ keV because the signatures of shock-accelerated particles in this range are unclear and the fluxes are only slightly above the background. Magnetic variances have been computed over a time scale $\Delta t = \rho_E / V_{sw}$ corresponding to the gyroradius ρ_E of protons with energy $E = 149$ keV (namely, we have chosen the mean energy within the 115–193 keV channel). It can be seen

that the magnetic field variance does not show any significant time/spatial trend from the shock front towards far upstream; it remains almost constant, implying that there is no spatial dependence of the particle diffusion coefficient within the upstream region (Perri and Zimbardo, 2012b). The time series of the magnetic field variances computed over time scales corresponding to the Larmor radius of particles with energies within the other channels show similar behaviours (see Zimbardo, Prete, and Perri, 2020). For this shock, we found $\theta_{Bn} \sim 60^\circ \pm 15^\circ$, so that this is a quasi-perpendicular shock. In this case ions reflected at the shock do not propagate upwind, but after performing a gyromotion around the upstream magnetic field lines tend to re-enter the shock moving towards the downstream side. On the contrary, energetic particles accelerated at the shock can still propagate in the upstream region by means of diffusion or superdiffusion parallel to the average magnetic field. This happens if the particle velocity along the radial direction toward the upstream side is larger than the solar wind speed in the shock frame V_1^{sh}. Since we are considering particles with velocities that go from 4×10^3 km/s to 9×10^3 km/s and the upstream solar wind speed is typically of the order of 4–5$\times 10^2$ km/s, we have a large number of energetic particles that can propagate upstream.

The energetic particle fluxes are shown in the top panel of Figure 2.17 in log-lin axes as a function of the time from the shock front. The decay in the upstream region (from the shock towards far upstream) is not exponential, but it exhibits a long upstream tail, suggesting that the transport is superdiffusive (Perri and Zimbardo, 2007). Indeed, since the magnetic field variance displayed in the bottom panel is almost constant, this suggests a spatial independent diffusion coefficient, so that in case of normal transport Eq.(2.1) should hold. Moreover, the downstream particle fluxes are not constant as predicted from standard DSA, but they tend to decrease downwind after peaking at the shock. In Figure 2.18, we report the particle fluxes in the upstream region as a function of the time (in minutes) from the shock crossing time. Following the method developed by Perri and Zimbardo (2007), Perri and Zimbardo (2008), Perri and Zimbardo (2015), Perri et al. (2015), we have fitted the energetic particle fluxes with a power-law time decay, i.e. $J \propto t^\beta$, which is the one expected for superdiffusive transport far upstream of the shock front. In each panel, the slope β of the best-fit is indicated; this is related to the exponent α of the mean square displacement, that is $\alpha = 2 - |\beta|$, so that a value of $|\beta| < 1$ implies a superdiffusive regime with $\alpha > 1$ (see Eq.(2.6)), as found for the time profiles shown in Figure 2.18.

From the exponent of the power-law we can derive $\mu = 4 - \alpha = 2 + |\beta|$ and τ_0 (Prete, Perri, and Zimbardo, 2019). Indeed, the time scale τ_0 is related to μ by (Perri and Zimbardo, 2015; Perri et al., 2015)

$$\tau_0 = \left(\frac{v}{V_1^{sh}} \right)^{\frac{\mu}{1-\mu}} t_{break}, \tag{2.12}$$

where t_{break} can be determined by visual inspection of the particle flux profile: close

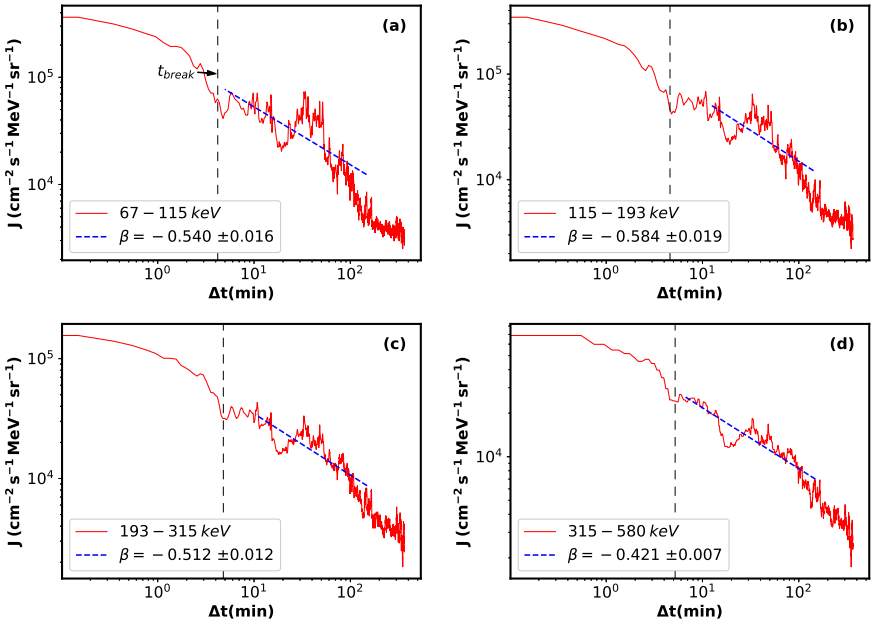

FIGURE 2.18: Power-law fits (blue dashed lines) of the energetic particle fluxes (red lines) in several energy channels for the shock crossing of 26 August 1998. The exponents of the power-law fit β as well as the energy channels are indicated in each panel. The time in the x-axis is in minutes from the shock crossing time.

to the shock front particle fluxes tend to flatten, so that the time at which the flux changes from being almost flat to a power-law decay is registered as t_{break}. In Figure 2.18 we have indicated t_{break} using a vertical dashed line. Since we are using high resolution 12 s EPAM data, there are several time fluctuations of the fluxes that make the identification of t_{break} challenging. However, using lower, 5 minute resolution EPAM data would hide any t_{break} shorter than 10 minutes.

Thus, using spacecraft data we have been able to derive the typical parameters for superdiffusion. We have then used those values as setting parameters for the test-particle simulations described in Section 2.2.1 and computed the energetic particle time/space profiles upstream and downstream of the simulated shock.

Figure 2.19 shows the comparison between the event detected by ACE and the output of our numerical run, using the parameters obtained from data analysis. The agreement between the fluxes measured by EPAM/ACE and the profiles from the model is very good, suggesting that a superdiffusive transport process upstream and downstream of the shock discontinuity can account for the observed time behaviour.

2.2.4 The 08/06/2000 oblique shock event

The shock event of 8 June 2000 is considered as oblique shock since the angle $\theta_{Bn} \sim 50° \pm 10°$.

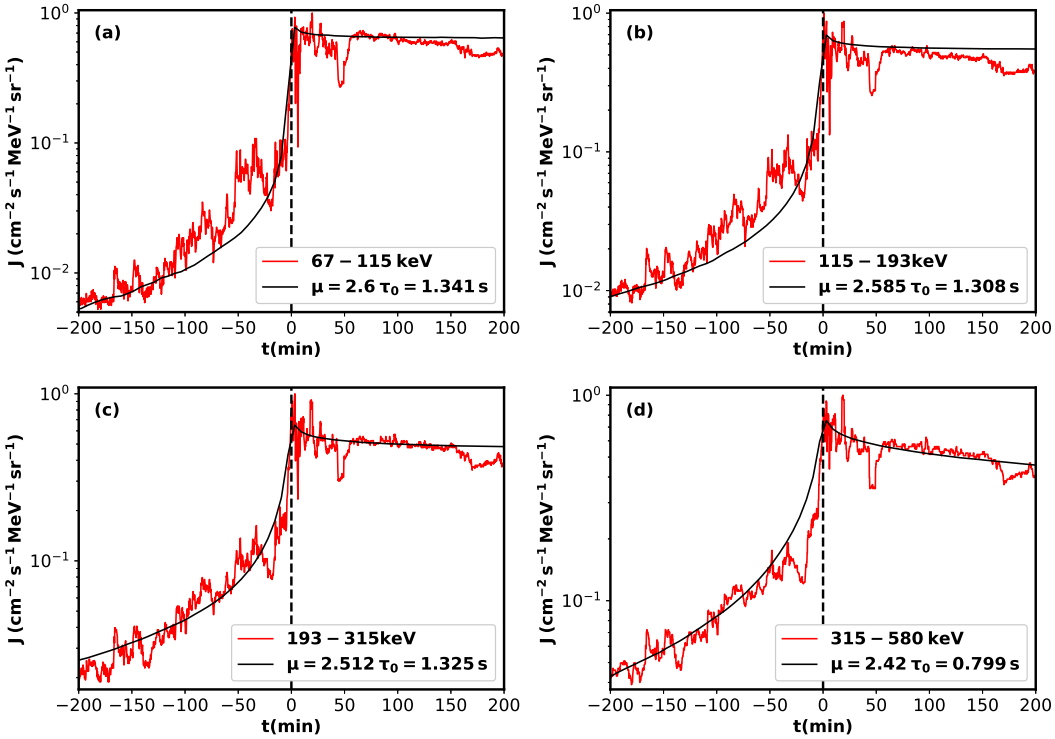

FIGURE 2.19: Comparison between EPAM/ACE measurements at 12 s resolution in the same energy channels as Figure 2.18 (red curve) and the density profiles obtained by the simulation (black curve) mimicking a superdiffusive particle process and setting the transport parameters directly from observations. The values used in the simulation are reported in the legend.

In Figure 2.20 we report ACE data in the same format as in Figure 2.17. In the top panel we notice again that the energetic particle fluxes do not show an exponential profile in the upstream region, but a long upstream power-law tail, and in the downstream region we do not have a constant profile but a gentle decrease. Once again, we can assume that the transport is superdiffusive. From panel (d) in Figure 2.20, it is possible to notice that the upstream magnetic field normalized variance tends to have a rising trend very close to the shock front, implying the possibility of a spatial dependence of the particle diffusion coefficient. However, far upstream it tends to be constant on average going further upstream, so that the long far upstream tail in the particle fluxes can be ascribed to an anomalous, superdiffusive propagation.
In Figure 2.21, we report the power-law best-fit of the energetic particle fluxes in the upstream region. The exponent of the power-law decay is found to be $|\beta| < 1$ for all the energy channels analyzed, so that the transport can be considered superdiffusive. We use these β parameters in the simulation together with the determination of τ_0 obtained from Eq. (2.12). In Figure 2.22 the comparison between the simulation results and the spacecraft particle fluxes are shown. The output energetic particle

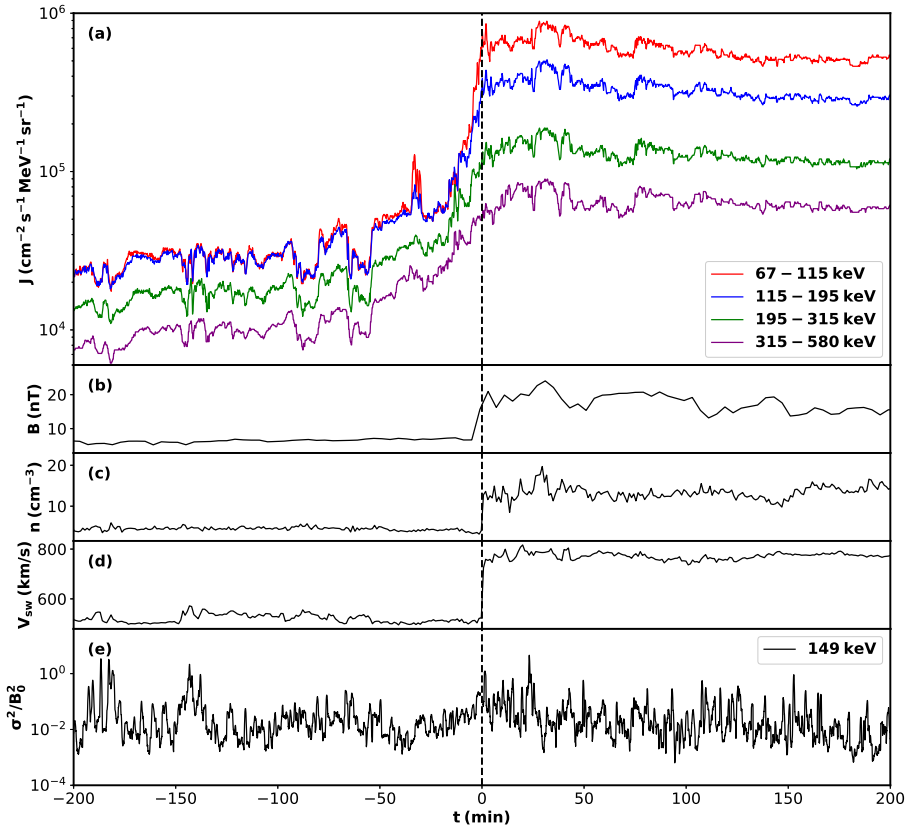

FIGURE 2.20: Same as Figure 2.17 but for the ACE shock crossing of 8 June 2000.

density profiles from the numerical code are in very good agreement with the energetic particle fluxes detected by in-situ measurements, both in the upstream and in the downstream regions.

2.2.5 The 23/04/2002 quasi-parallel shock event

The shock event of 23 April 2002 is quasi-parallel; indeed, $\theta_{Bn} \sim 25^\circ \pm 8^\circ$. In the top panel of Figure 2.23 we report energetic particle fluxes in three energy channels in log-lin axes. Again, it is possible to recognize a long upstream tail in the fluxes, which can be fitted with a power-law time decay. In the downstream region the energetic particle fluxes exhibit again a decreasing time profile. We ascribe such evidences to particle superdiffusion.

In Figure 2.24 we report the power-law best-fit of the upstream region for the three energy channels. Notice that we have also performed an exponential fit of the particle upstream fluxes but the power-law decay fits much better the data. This has been tested by computing the χ^2-test; we have found better values of the χ^2 for the

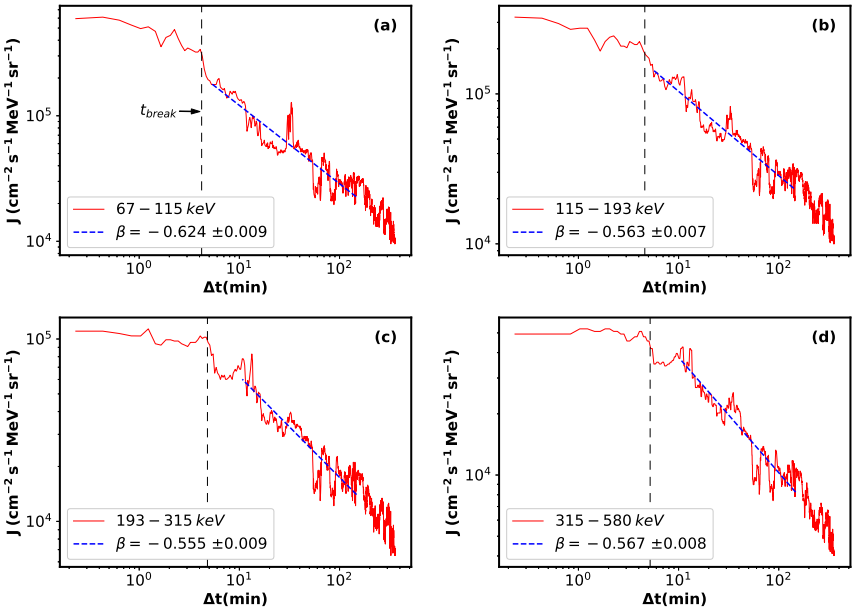

FIGURE 2.21: Same as Figure 2.18, but for the ACE shock crossing on 8 June 2000.

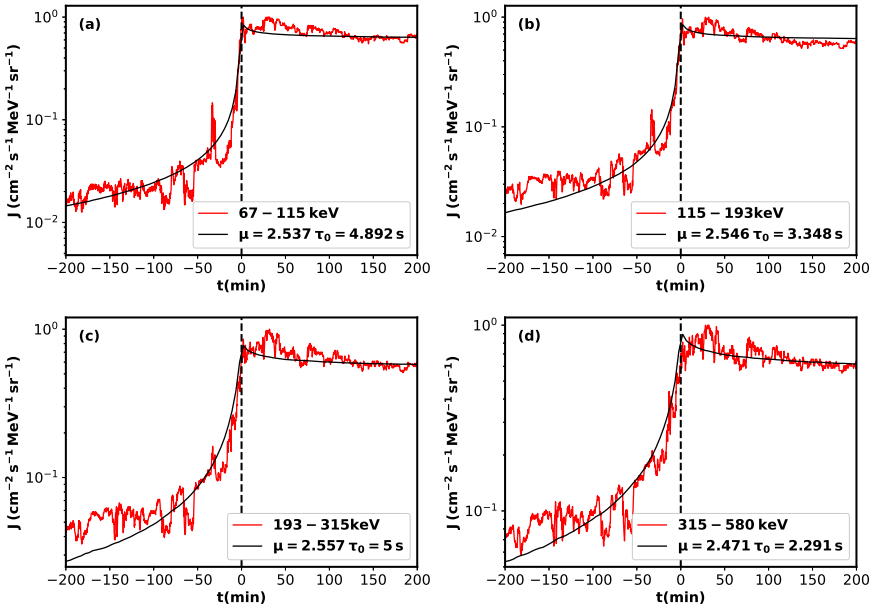

FIGURE 2.22: Comparison between ACE measurements in several energy channels (red curve) and the density profiles obtained by the simulation (black curve) in the case of superdiffusion. The values of μ and τ_0 used in the simulations are reported in the legend.

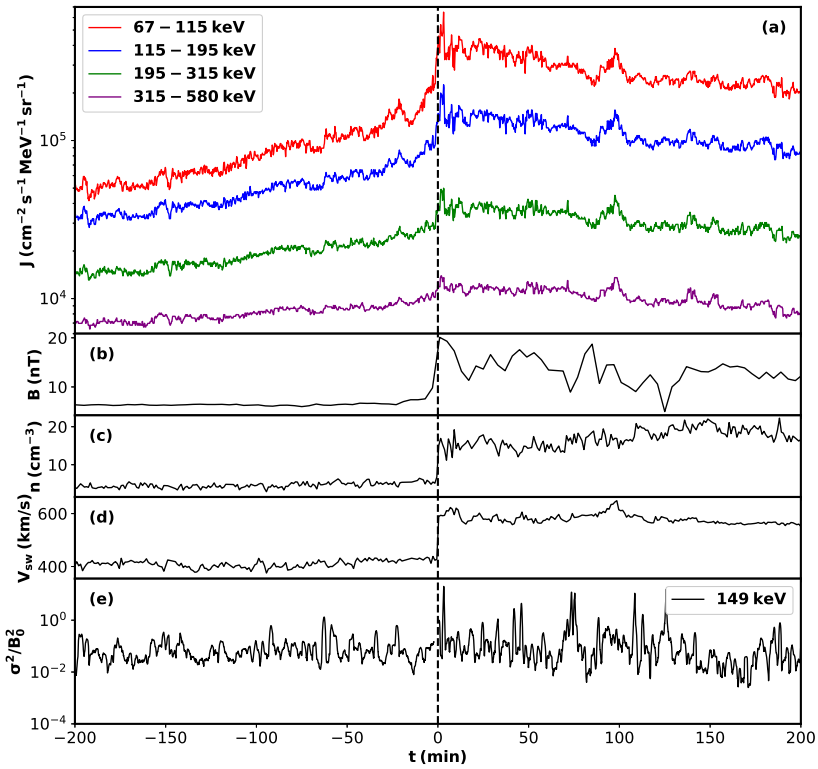

FIGURE 2.23: Same as Figure 2.17 but for ACE shock crossing of 23 April 2002.

power-law fits than for the exponential one. As we can see, the values of $|\beta|$ are less than one and in particular they assume very small values, indicating a strong superdiffusion even compared to the previous cases.

We report the comparison between the data and the simulation results in Figure 2.25, using the setting parameters for the simulations obtained from the data analysis of the shock event. The comparison is again good, however, it has to be stressed that the sudden increase of the particle fluxes close to the shock front (from about -20 to 0) cannot be captured by the numerical density profile. It is possible that this region close to the front is more affected by the plasma instabilities excited by reflected particles in a quasi-parallel shock geometry, which cannot be reproduced by a test-particle model.

2.3 Interpretation of flat energy spectra upstream of fast interplanetary shocks

Several interplanetary shock events show ion fluxes having similar amplitudes from the lower energy channels to the higher ones. We refer to them as overlapped fluxes,

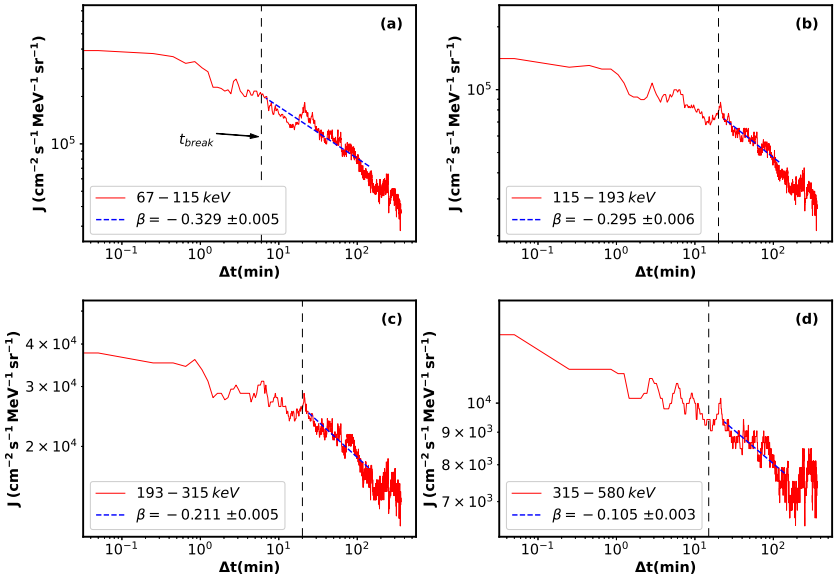

FIGURE 2.24: Same as Figure 2.18, but for the ACE shock crossing of 23 April 2002

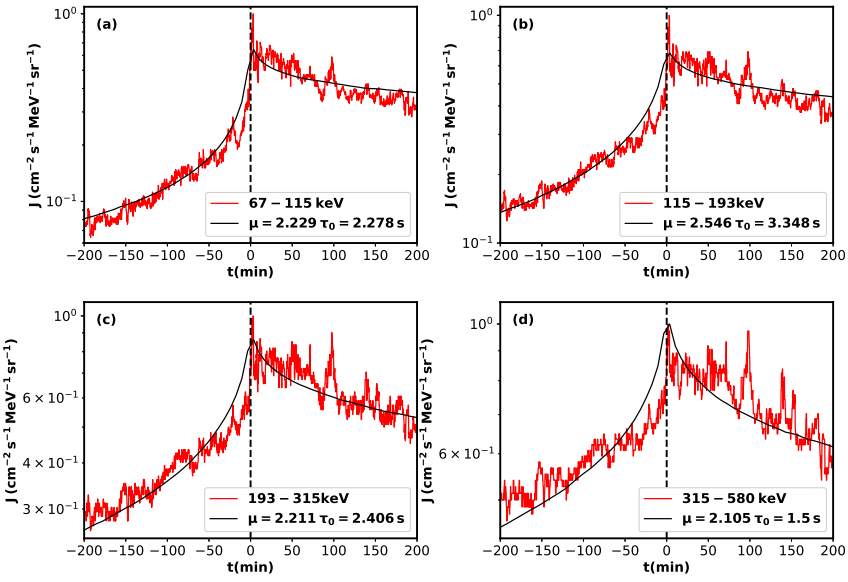

FIGURE 2.25: Comparison between ACE measurements in several energy channels (red curve) and the density profiles obtained by the simulation (black curve) in the case of superdiffusion. The values used in the simulation are reported in the legend.

characterized by flat energy spectra. Instead, close to the shock upstream, ion fluxes reach different amplitude values according to their energies and energy spectra start steepening towards high energy.

We already know, from the introduction of Section 2, that collisionless shocks represent the main sources of energetic particles and cosmic rays in astrophysical environments. Efficiency in particle acceleration at shocks can be achivied when particles remain confined near the shock, either as a result of geometry, or by scattering in turbulent magnetic fields and furthermore, particles gain energy due to the density compression at the shock front (Drury, 1983). We mentioned that collisionless shock properties depend on the angle θ_{B_n}. In the quasi-parallel configuration, reflected ions can efficiently propagate upstream, thereby forming the ion foreshock. In this region reflected ions form a beam in the velocity space which can excite different type of waves as ion cyclotron, Alfvèn waves, fast-magnetosonic, and whistlers. This makes the ion foreshock region a very turbulent region, as observed by spacecraft in the terrestrial ion foreshock (Schwartz and Burgess, 1991; Perri and Zimbardo, 2009; Wilson, 2016; Karimabadi et al., 2014). The disturbances excited by the reflected particles, can increase the level of magnetic fluctuations in such a way as to allow efficient scattering electrons (Wilson et al., 2016) and ions (Wilson et al., 2013; Turner et al., 2018), thereby trapping them near the shock for further acceleration to high energies according to the mechanism of DSA. In the quasi-perpendicular configuration particles reflected at the shock do not propagate upwind but rather re-enter the shock after gyrating in the upstream magnetic field. This allows the enhancement of the downstream magnetic fluctuations, as usually observed (Greenstadt et al., 1975). In the absence of rapid scattering upstream, DSA can be slow, as suggested by some observations (Reynoso, Hughes, and Moffett, 2013) and numerical simulations (e.g., Caprioli, Pop, and Spitkovsky, 2015; Sundberg et al., 2016; Trotta et al., 2020a; Preisser et al., 2020).

Upstream transport conditions are related to the level of magnetic fluctuations and these conditions can higly influence the suprathermal particle fluxes. For example, Lario et al. (2022) investigated the formation of an anisotropic field-aligned beam of protons upstream of an oblique shock with energies $\leq$ 30 keV together with a population of protons at higher energy propagating at small pitch-angle. The unusually long duration (and therefore spatial extent) of the field-aligned beam was interpreted as due to the absence of magnetic field fluctuations over a large distance upstream of the shock wave — a scenario where efficient scattering is not favoured.

The formation of a precursor of energetic particles, in the upstream region, is another fundamental phenomenon in which energetic particles must satisfy the condition

$$v\mu > V_1^{sh} \sec(\theta_{\mathrm{Bn}}), \tag{2.13}$$

i.e., when energetic particles have velocity parallel to the local magnetic field greater than the speed of the intersection point of a field line with the shock front along the direction of the shock front, they will form the precursor (le Roux and Webb, 2012; Lario et al., 2019). Here, V_1^{sh} represents the upstream speed in the shock reference frame and μ is the cosine of the pitch angle, i.e. the angle between the local magnetic field and the particle's velocity vector. This precursor has to be distinguished by the

ion foreshock, mostly related to the reflection of the thermal particles and from the fast/magnetosonic whistler wave precursor (Wilson et al., 2017).
It is known that high energy particles can easily propagate back upstream while low energy particles tend to be confined near the shock region, reducing their fluxes far upstream; therefore the velocity filter mentioned above can lead to a spectral flattening in the usptream region. Furthermore, the velocity filter on particles can be influenced by the presence of magnetic tubulence, that can cause pitch angle scattering and a meandering of magnetic field lines.
Here we present an analysis made on three different Interplanetary shocks and their associated ions fluxes observed by the ACE spacecraft and by Wind spacecraft. The events analyzed are the event dectectd on 25 May 2015, the one detected on 14 July 2012 and the event of 4 November 2002. We will show in this chapter just one of them, but we made the same analysis for the other two. All these events are characterized by energetic particle profiles that are overlapping far upstream and up to about 1-3 hours before the shock passage (i.e., the upstream energy spectrum is flat for a broad range of particle energies). Closer to the shocks, the fluxes at each energy separate and reach values more typical of those predicted by DSA theory. The same behaviour of ion fluxes was already highlighted by Lario et al. (2018), who noted that ion fluxes, in the energy range that goes from 50 keV to 4 MeV, showed a typical spectral flattening far upstream of different interplanetary shocks. Here, we analyze energetic particle fluxes and magnetic fluctuations close to and far upstream of the shocks. We will try to interpret observations of flat upstream energy spectra in terms of the velocity filter mechanism described above.

2.3.1 Data collection and analysis

Shock crossing

The event that we are going to show in this chapter has already been studied by Lario et al. (2018), i.e. the 25 May 2015 shock event. Ion fluxes show an overlap that extends far upstream, over six different energy channels. Energetic ion fluxes start separting at about 50 minutes before the shock arrival and downstream of the shock. The solar origin of this relatively strong event was associated with a halo, fast (plane-of-sky speed $\sim$1689 km s^{-1}) CME observed at 17:12 UT on 2005 May 13, as reported in the Coordinated Data Analysis Workshops (CDAW) Data Center SOHO LASCO CME catalog[4] and temporary associated with a M8.0 GOES class X-ray flare from the NOAA active region 10759 at N12E12 with onset at 16:13 UT on 2005 May 13 (Lario et al., 2018). The transit time for the shock to travel from the Sun to 1 AU was about 2038 minutes, corresponding to an average transit speed of $\sim$ 1223 km s^{-1} (see Table 1 in Lario et al., 2018). Using data from GOES-11, Lario et al. (2018) show that energetic particles peak at the shock even in the high energy channel of 32.5–56.4 MeV, confirming that it is a strong particle accelerator.

[4]available at cdaw.gsfc.nasa.gov/CME_list/

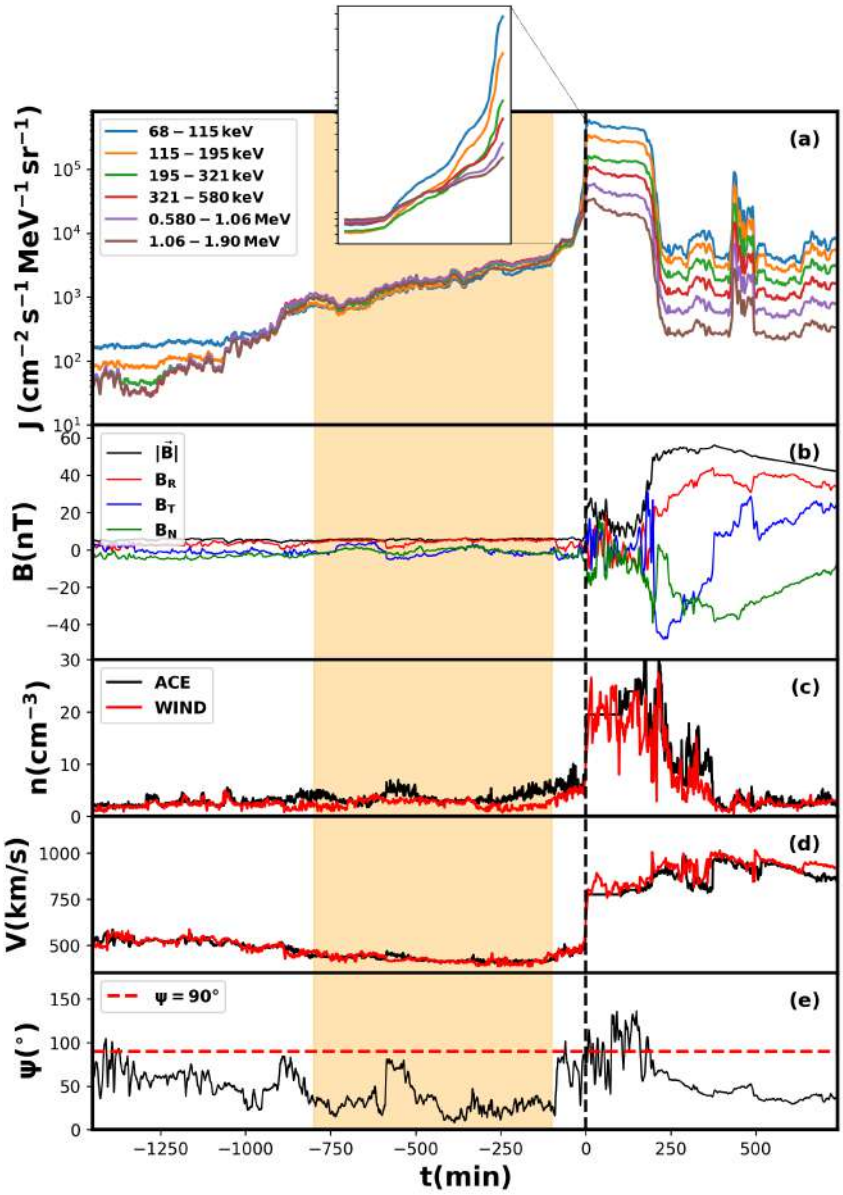

FIGURE 2.26: Overview of the shock crossing by the ACE spacecraft on 2005 May 15. From top to bottom: particle fluxes from the EPAM-LEMS120 instrument in the energy range 68-1890 keV measured at 12 s cadence, the 60 s resolution magnetic field components in the Radial-Tangential-Normal (RTN) reference frame along with the magnetic field magnitude, the proton density and the solar wind bulk speed both from ACE (at 64 s resolution) and Wind (at 92 s resolution), and the angle between the radial direction and the mean field direction computed over a running window of 5 min. The vertical dashed line indicates the shock position, the yellow shaded area shows the region where energetic particle fluxes overlap indicating a period with a relatively flat energy spectrum.

In Figure 2.26 from top panel to bottom we report (a) the 12 s resolution particle fluxes detected by the Electron, Proton, and Alpha Monitor (EPAM) instrument (Gold et al., 1998) onoboard ACE from the LEMS 120 sensor in the energy range 68

keV-1.90 MeV; (b) the total magnetic field and its component in the Radial-Tangential-Normal (RTN) coordinate system, detected by the MAG instrument onboard ACE at a time cadence of 60s; (c) and (d) the plasma proton density and the solar wind bulk speed, respectively, detected by the Solar Wind Electron, Proton, and Alpha Monitor (SWEPAM) experiment, onboard ACE with a resolution of 64s. In these panels we also chose to show the plasma proton density and the solar wind bulk speed measured by Solar Wind Experminet (SWE) (Ogilvie et al., 1995) onboard Wind measured with a resolution of 92 s (red lines), because of a gap in the SWEPAM data. In the bottom panel we show the angle ψ, i.e. the angle between the direction of the mean magnetic field and the radial direction (Sonnerup, 1969). This angle gives us information about the magnetic connectivity of the observer with the shock surface (the horizontal dashed red line indicates a 90° angle). It has been calculated by computing averages over 5-minute running windows.

The vertical black dashed line indicates the shock crossing time. We display an upstream time window of about 24 hours, also because the fluxes of different energy channels are overlapped for about $\simeq$ 16 hours (indicated by the yellow shaded area in Figure 2.26), while we show a time window of 10 hours for the downstream region. Proton fluxes in panel (a) result well separated 17 hours priors the shock arrival in the upstream region. Then, between a period that goes from 800 minutes to 80 minutes (corresponding to 16 hours) upstream of the shock, they are overlapped. At about 50 min before the shock crossing upstream, ion fluxes separate (see the inset in the top panel in Figure 2.26). It is interesting to note that in panel (b) the region corresponding to the region in which fluxes are overlapped, show a magnetic field that tends to be approximately radial (see also panel (e) in Figure 2.26 where $\psi < 30°$ for most of the time interval indicated by the shaded region), while this behavior is completely lost near the shock, i.e. in the region where the fluxes start to become separate again. This suggests that for the entire period when the upstream flat spectrum was observed, the spacecraft was well connected to the shock front.

In the downstream region, it is possible to see the presence of the magnetic cloud (MC) associated to the passage of the CME, as we already discussed in Section 2 (Burlaga et al., 1981; Klein and Burlaga, 1982). Furhermore, this is also proved by the presence of a sudden decrease of about two orders of magnitude in the particle fluxes observed after $\simeq$ 3 hours of the shock crossing downstream (Lario et al., 2018; Perri et al., 2022).

Finally, the fundamental shock parameters for the event that we are analyzing have been determined. We calculated the θ_{B_n} angle using two methods: the MVA and the Coplanarity Method(CM) (Paschmann and Daly, 2000; Koval and Szabo, 2008). Using the MVA we found that the angle is $\theta_{B_n} = 78.7 \pm 12.9$, i.e. a quasi perpendicular configuration for the shock. Since the MVA analysis, computed over a 50 minutes interval before shock crossing, can be highly unstable due to the rapid variations of the magnetic field, we have also calculated the angle via the CM. The CM technique with a systematic variation of upstream and downstream averaging windows from $\sim$ 2

to 50 minutes (as done in Trotta et al. (2022)) yields a large spread of values, indicating high levels of upstream/downstream disturbance. With this method we found an angle of about 51.3 ± 13.6, in agreement with the MVA method. We also determined, in the same time window used for the θ_{B_n} calculation, the Alfvén $M_A = 4.4$ and the sonic Mach numbers $M_S = 6.7$, the compression ration $r = 3.0 \pm 0.6$, as the ration between the downstream and the upstream proton density, the plasma beta $\beta = nk_BT/(B^2/2\mu_0) = 1.57$, where k_B and μ_0 are respectively the Boltzmann constant and the vacuum permeability, and the shock speed $V_{sh}^{s/c} = 926\,km/s$ in the spacecraft frame (Perri et al., 2015).

Magnetic field turbulence

In order to understand what are the characteristics of the environment in which our shock is propagating, turbulence properties of the magnetic field have been investigated. We did these in two upstream regions: the region in which the fluxes are overlapped (shaded area in Figure 2.26) and close to the shock region where the fluxes are well separated (from -80 minutes to -10 minutes). We did this computing the Power Spactral Density (PSD) of the magnetic field component along each direction in the RTN frame, using the Fast Fourier Transform.
In Figure 2.27 we present the power spectrum of the magnetic field in the two regions described above. In the region in which fluxes are overlapped, we found a power-law spectrum of Kolmogorov-type (black continuous line), i.e. $PSD(f) \propto f^{-5/3}$ where f is the frequency in the spacecraft frame, indicating ambient solar wind turbulence (Bruno and Carbone, 2005; Pitňa et al., 2021).
In the region where fluxes are not overlapped, i.e. the region between -80 minutes and -10 minutes, the power spectrum seems to have a different behavior $PSD(f) \propto f^{-1}$ (blue continuous line). The best power-law fits are shown in Figure 2.27, respectively with a red dashed line for the overlapped region and with a black dashed line for the near shock region. We also reported in the legend of the figure the values of the slopes for both cases. We computed the power-law fits within a range of frequencies corresponding to the Larmor radius of energetic particles, namely, $f_E = V_{up}/(2\pi\rho_E)$, where V_{up} is the upstream velocity in the spacecraft frame of reference and ρ_E is the Larmor radius of particles with a specific energy E. The frequencies are indicated by vertical dashed lines. The results found for the near shock region indicates that fluctuations are freshly-injected and the turbulence is not completely developed yet. We found similar results for the other two events.
Moreover, with the wavelet analysis of the magnetic field vector, we studied how the magnetic fluctuations are distributed in frequency and as a function of the shock distance. The square of the wavelet coefficients of the magnetic field components have been computed as (Alexandrova et al., 2008)

$$|\mathcal{W}_{\mathbf{B}}(\tau,t)|^2 = \sum_i |\mathcal{W}_i(\tau,t)|^2, \tag{2.14}$$

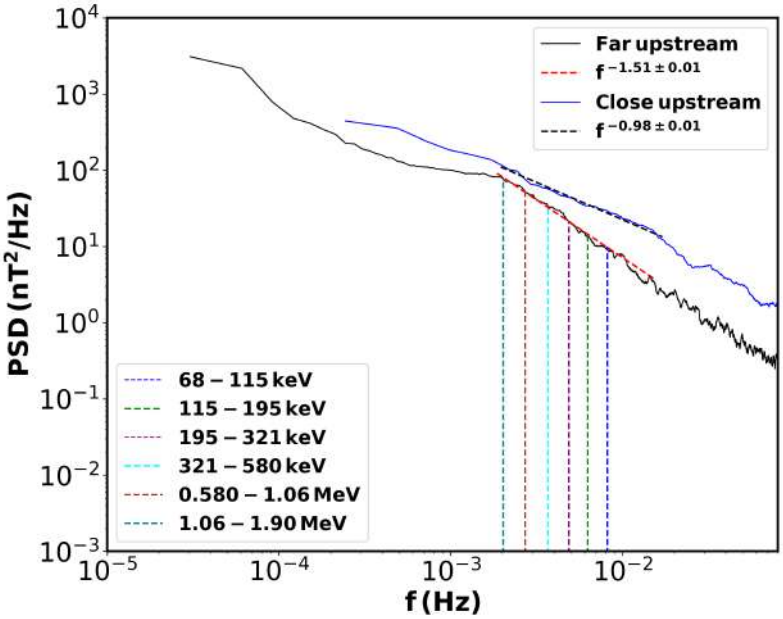

FIGURE 2.27: PSD of the magnetic field fluctuations for the 2005 May 15 event, computed in the region far upstream where the fluxes of energetic particles overlap (black line) and in the region close to the shock front upstream (blue line). The vertical dashed lines indicates the frequencies corresponding to the Larmor radius of the energetic particles (see Figure legend). The best power-law fits are also shown by the dashed lines.

where $\tau = 1/f$ is a time scale, and the sum is computed over the three components of the magnetic field, $i = R, T, N$. $\mathcal{W}_i(\tau, t)$ represent the Morlet wavelet coefficients computed over different τ and time t (Torrence and Compo, 1998), i.e., $\mathcal{W}_i(\tau, t) = \sum_{j=1}^{N} B_i(t_j)\psi^* \left[\left(t_j - t\right)/\tau\right]$, with ψ^* being the conjugate of the wavelet function. This allows us to assess the magnetic energy content in frequency and in time and localize, within the time series, the regions with high magnetic energy. In Figure 2.28 we report the result of the application of the wavelet analysis on the magnetic field components for the event of 15 May 2005.

In Figure 2.28 the white dashed vertical line indicates the shock arrival time while the two horizontal white dashed lines delimit the regions in which we have the frequencies associated to the larmor radius of energetic particles. The yellow box indicates the region where the fluxes are overlapped. From the figure it appears evident how, near the shock region, the power of the magnetic field fluctuations increases over a broad range of frequencies that includes the frequency lines. This implies that the magnetic energy stored in the fluctuations tends to increase near the shock and it is found to be high in the region just after the shock , i.e. the sheath region (see the description of this region in Section 2), in which fluctuations are highly compressed and enhanced. Recent observations of turbulence close to interplanetary shocks (Zhao et al., 2021) were found in agreement with our results near the shock region. The behavior of the magnetic power near an interplanetary shock reconciles with observations of an extended f^{-1} range in the PSD computed in this region. The

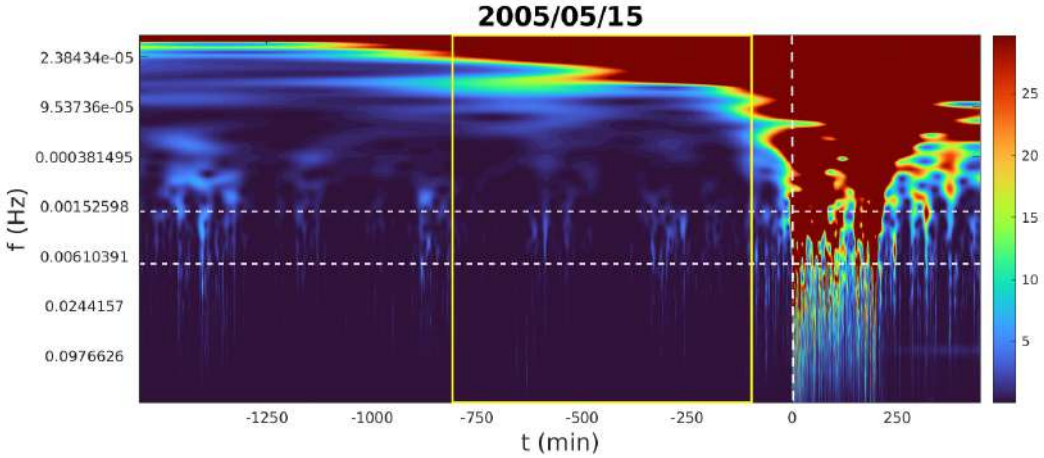

FIGURE 2.28: Power spectral density computed using the wavelet coefficients over the three magnetic field components (see text for further details). The yellow box delimits the region upstream where a flat energy spectrum has been detected, while the vertical dashed line marks the shock crossing time. The horizontal dashed lines indicate the frequency range corresponding to the Larmor radius of energetic particles from 67 keV to 2 MeV. Typical cascade patches (Greco et al., 2016) can be recognized over the entire upstream region, with an intensity increase close to the shock front. Just behind the shock the CME sheath region is characterized by a very high level of turbulence over a broad range of frequencies.

local increase of the magnetic field power and the detection of a bumped PSD close upstream might be ascribed to a self-generated, freshly-injected turbulence, due to the presence of the energetic particle fluxes. We found similar results in the other two cases.

Energetic Particle Anisotropy

In order to characterize the energetic particles motion, we investigate their propagation with respect to the local magnetic field direction using the Solid State Telescope (SST) of Wind 3DP (Lin et al., 1995). Ion fluxes are divided in 9 energy channels with average energies of 76 keV, , 130 keV, 200 keV, 336 keV, 554 keV, 1 MeV, 2 Mev, 4 MeV, 6.8 MeV. They are also binned in 8 pitch-angle values with respect to the local magnetic field direction. In Figure 2.29 we show the maximum intensity of ion fluxes as a function of pitch angle cosine μ for the event of 15 May 2005.
In order to get rid of any anisotropic feature due to the Compton-Getting effect, fluxes are in the solar wind reference frame (Compton and Getting, 1935; Forman and Morfill, 1979). In Figure 2.29 the three different types of symbols represent the three regions in which we have calculated the maximum intensity of ion fluxes: black circles indicate the maximum calculated in the overlapping region (-800 minutes, -100 minutes), red diamonds refer to the near shock region (-80 minutes, -10 minutes) and the blue stars indicate the downstream region (10 minutes, 70 minutes). Because of the presence of high magnetic field fluctuations that allow particles

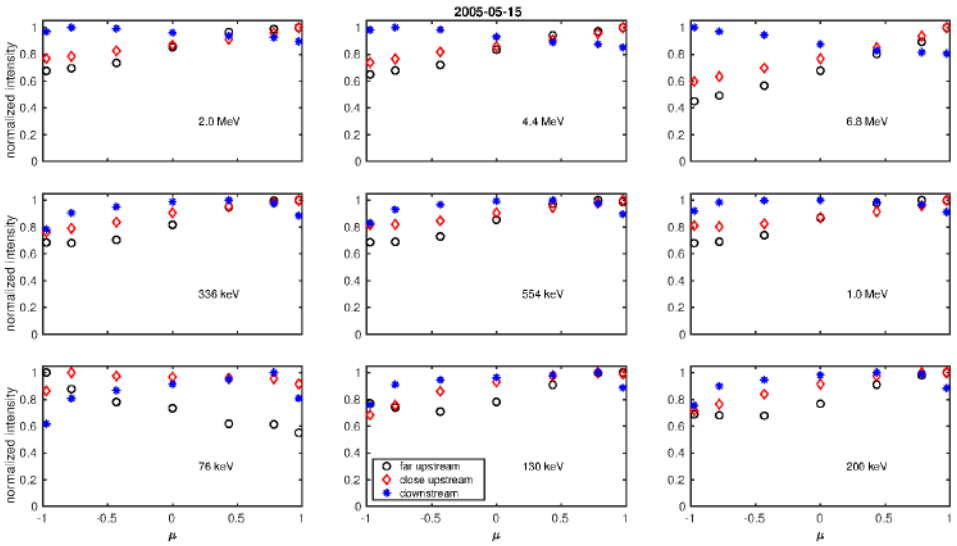

FIGURE 2.29: Mean ion fluxes, normalized to the maximum intensity in each region, as measured from the Wind/3DP/SST instrument in the solar wind frame within each pitch-angle bin during the 2005 May 15 event. Each panel refers to a given energy channel. The black circles indicate the ion fluxes measured far upstream of the shock wave within the shaded region indicated in Figure 2.26, the red diamonds refer to the close upstream region, where ion fluxes start separating, and the blue stars to the downstream sheath region.

to be efficiently scattered, all the energy channels present a distribution of ion fluxes isotropized in the downstream region. In the overlapping region, the lowest energy channel fluxes are higher at large pitch-angles, namely particles move sunward towards the shock, while the highest energy channel fluxes are lower, that means that particles travel mostly anti-sunward at small pitch-angles. As we already noted, in this region the magnetic fluctuations amplitude decreases but there is a good connection between the spacecraft and the shock due to the fact that the magnetic field is almost radial. This allows for the detection in the far upstream region of those particles that have been isotropized close upstream, considering that parallel diffusion is larger than perpendicular diffusion. In the close upstream region this anisotropy is reduced because of the presence of amplified magnetic fluctuations that, interacting with ions, permit to scatter them in all directions (Giacalone and Jokipii, 1999; Trotta et al., 2021). Here, lower energy particles tend to be isotropized in μ, while there is still anisotropy in favour of field-aligned particles at higher energies.

2.3.2 Discussion on the velocity filter condition

We used the velocity filter condition to derive the energetic particle fluxes, following the interpretation proposed by le Roux and Webb (2012). This condition does not allow particles to easily escape upstream. Firstly, we define the number of particles in a volume of phase space as (Moraal, 2013)

$$d\mathcal{N} = F(\mathbf{r}, \mathbf{p}, t) d^3r d^3p = F(\mathbf{r}, \mathbf{p}, t) d^3r p^2 dp d\Omega, \tag{2.15}$$

where $F(\mathbf{r}, \mathbf{p}, t)$ is the particle distribution function and $d\Omega = \sin\alpha d\alpha d\phi$ is the element of solid angle in momentum space. We can define a differential density in momentum, namely the number of particles in a given volume d^3r and with momentum within $\mathbf{p}$ and $\mathbf{p} + d\mathbf{p}$ as

$$U_p = p^2 \int_\Omega F(\mathbf{r}, \mathbf{p}, t) d\Omega. \tag{2.16}$$

This implies that the number of particles becomes $dN = U_p d^3r dp$. We align the polar coordinate axis with the upstream magnetic field, so that α is the pitch angle; considering that only particles with a sufficiently large parallel velocity can escape from the moving shock, we find that α can vary over a limited range of values, namely the particle velocity belongs to a limited spherical sector in phase space (see the cartoon in Figure 2.30). Then, we can calculate the differential density of *upstream propagating particles* as

$$U'_p = 2\pi p^2 \int_0^{\alpha_{max}} F(\mathbf{r}, \mathbf{p}, t) \sin\alpha d\alpha. \tag{2.17}$$

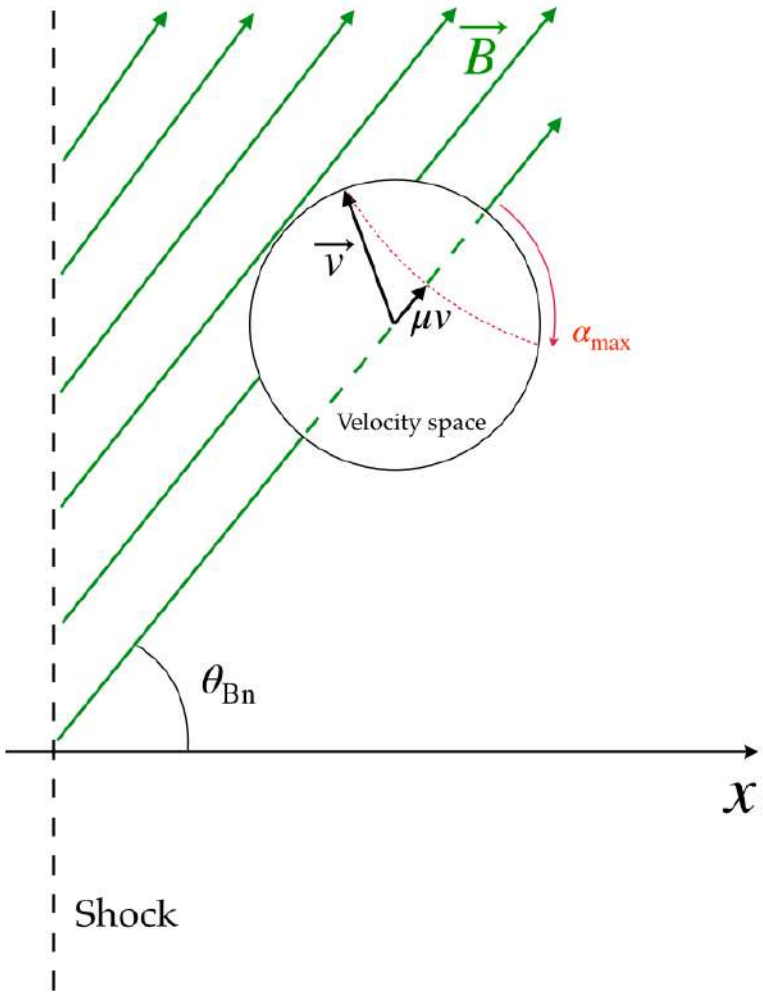

FIGURE 2.30: Cartoon of the spherical sector around the magnetic field direction with radius given by the particle velocity **v**.

Since close to the shock, due to the presence of enhanced magnetic field fluctuations, ions undergo a lot of scattering, we can make the assumption of nearly isotropic particle distribution function. With this assumption, it is possible to insert the omni-directional distribution function $f(\mathbf{r}, p, t)$ in Eq.(2.17). Using the pitch-angle cosine $\mu = \cos\alpha$, defining a minimum pitch-angle cosine μ_{min} corresponding to α_{max}, and being $d\mu = -\sin\alpha d\alpha$, one can readily find that

$$U'_p = 2\pi p^2 f(\mathbf{r}, p, t)(1 - \mu_{min}) = 2\pi p^2 f(\mathbf{r}, p, t)\left(1 - \frac{V_1^{sh}\sec\theta_{\mathrm{Bn}}}{v}\right). \tag{2.18}$$

Eq.(2.18) introduces a correction to the isotropic (in pitch-angle) flux of particles related to the condition for particles escaping from the shock (Eq. 2.13). From Eq.(2.18) we found a relation between the differential density and the flux, $J = U'_p \propto p^2 f(p)$ (Moraal, 2013), that is in agreement with what we expected from the DSA prediction, in which $f(p) \propto p^{-3r/(r-1)}$, where $r = n_2/n_1$ is the compression ratio of the shock.
To better understand the effect of the velocity filter on the particle energy spectrum observed in the usptream region of an interplanetary shock, we determined the flux J in the energy range from 70 KeV to 40 MeV using Eq.(2.18). We present in Figure 2.31 the results obtained applying the velocity filter method.

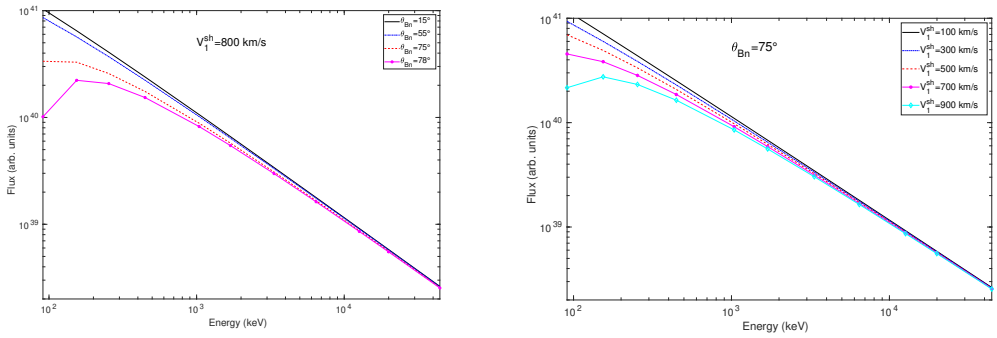

FIGURE 2.31: Left panel: Particle energy spectrum computed fixing the upstream plasma speed in the shock reference frame at $V_1^{sh} = 800$ km/s and by varying the θ_{Bn} angle. The velocity filter acts for quasi-perpendicular shocks at low energies. Such a flux reduction produces a flat energy spectrum. Right panel: Particle energy spectrum computed fixing $\theta_{\mathrm{Bn}} = 75°$ and by varying V_1^{sh}. The velocity filter acts for high speed plasma flows at low energies.

In the left panel of Figure 2.31, we fixed the plasma speed in the shock rest frame and we varied θ_{B_n} from quasi-parallel to quasi-perpendicular configuration. At low energies, fluxes are reduced in a quasi-perpendicular configuration. This promotes observations of flat spectra upstream of the shocks. This reduction involves the energy channels that go from 400 to 600 keV, that usually are the channels where the upstream energetic particle fluxes are found to be overlapped.
In the right panel of Figure 2.31, we have fixed the θ_{B_n} value and we varied the upstream plasma speed in the shock frame of reference. In this case we can observe a

reduction of the low energy flux when the speed is increasing. This happens because the particle escape condition tends to be marginally fulfilled for high V_1^{sh} values.

2.4 Conclusions

In this Chapter we studied different Space weather phenomena related to the Sun's activity. To this purpose, we analyzed spacecraft data and coupled them with numerical simulations. We tried to reproduce the evolution of a CME with the help of a MHD code to compare these results with what it is seen by the spacecraft at the Lagrangian point L_1. We also studied how the shocks, that can be sometimes associated to the evolution of a CME, can influence the transport and the acceleration of charged particles. In this case we used a test-particle numerical code in order to have a comparison with satellite analysis.
In Section 2.1, we focused on the study of a particular case of a magnetic cloud, observed at L1 on June 28 2013 at 02:23 UT. This period of time is close to the maximum of solar cycle 24. It is well known that during solar maximum, the frequency of CMEs increases in comparison to the solar minimum. Therefore, there were six possible candidates in a time window of 5 days prior to the MC: two halo CMEs (CME 4 on the 24 June at 04:00 UT and CME 6 on the 25 June at 11:12 UT) and four partial halos and low-speed CMEs.
They were all analyzed and two of them were excluded for being responsible for the MC, due to the direction of propagation of these CMEs, towards the back side of the Sun *i.e.*, CME 4 and CME 6, while CME 1 and CME 5 were also excluded because they propagate in the northward direction and never reached the Earth. Finally, CME 2 and CME 3 were found to be the most probable events responsible for the MC measured at L1 on June 28. Both events erupted on June 23, at 21:24 UT and 22:36 UT, respectively. We analyzed HMI magnetograms, AIA 30.4 nm and 17.1 nm images just before 22:00 UT and detected some brightenings which helped us to determine the position of the source. We identified the possible source of CME 2 in the active region NOAA AR 11778 in the South-East solar disk and CME 3 source in a tiny bright point close to a filament channel at longitude of 15°. The tiny brightening corresponds to an emerging flux at the edge of a filament channel. It is a favourable location for reconnection between emerging flux and open field, and for CME ejection. We used the StereoCAT tool for obtaining the CME parameters required by the cone CME model in EUHFORIA and we did a 3D-MHD modelling of the event, to further confirm that the CME coming from the northwest (CME 3) was finally responsible for the MC. The EUHFORIA simulations show that this CME is the only one capable of generating the MC passage measured at L1, as the arrival time, velocity and density increase have been perfectly recovered.
EUHFORIA is a very useful tool to confirm the CME responsible for the observed MC passage. Further improvements to the simulations could be made as we used the simple Cone model in this case. This model does not take into account the internal

magnetic structure of the CMEs and, therefore, is not capable of reproducing the evolution of the different magnetic field components during the propagation of the ICME. As a future work, we will include a different model of EUHFORIA in order to better reproduce the MC.

In the present case, the two fast halos which fit with the propagation time did not do it in the Sun-Earth direction and did not arrive at Earth. Statistical analysis only based on fast halo CMEs as candidates in a 3-5 day time window prior to a MC is ambiguous, especially during solar maximum periods. It confirms the conclusion obtained by Schmieder et al. (2020), where 12 X-ray flares with 12 associated halo CMEs were analysed. There the authors concluded that none of these 12 halo CMEs were really geoeffective. One of them with a source at the central meridian and a fast speed has been tested by EUHFORIA and due to lateral over-expansion could not be geoeffective (Verbeke et al., 2022). Additional conditions are needed for the geoeffectiveness (Rodriguez et al., 2008; Echer et al., 2008; Rodriguez et al., 2009; Bein et al., 2011; Echer, Tsurutani, and Gonzalez, 2013; Bocchialini et al., 2018). In fact, it is proved that C-class flares accompanied by partial filament eruptions and slow-speed CMEs can be geoeffective (Chandra et al., 2010; Bocchialini et al., 2018). Studies by Zuccarello et al. (2018), Linan et al. (2018), and Linan et al. (2020) show the importance of considering the solar source of the CME with its complexity and its excess in magnetic helicity.

We are planning to study all the magnetic clouds in the heliosphere listed by Al-Haddad et al. (2018) in order to detect and analyze their solar sources. It would be also helpful, in order to better study and reproduce the evolution of the CME ejected from the Sun, the use of a more realistic CME model, other than the Cone model used in this work. This will help to reproduce the evolution of the magnetic field associated with the CME.

In Section 2.2, we have studied the propagation of energetic particles during three shock crossings detected by the ACE spacecraft. Following the methodology described in Perri and Zimbardo (2007) and Perri and Zimbardo (2008), the particle fluxes in the upstream side have been fitted via a power-law decay, which is the profile expected within the framework of superdiffusion for a spatially independent diffusion coefficient (Perri and Zimbardo, 2012b). The slopes of the power-law found imply a mean-square displacement for energetic particles that is growing faster than normal diffusive. Then, the observed fluxes have been compared with the ones obtained by running a test particle code (see Prete, Perri, and Zimbardo (2019)) where the shock is treated as a planar infinite discontinuity and energetic particles propagate around the shock region with a probability distribution of path lengths that is a power-law (i.e., Equation (2.5)). Also the parameters relevant to the particle motion in the simulations, i.e., β, μ, and τ_0, have been derived from the analysis of the ion fluxes measured in-situ. Notice that our simplified numerical model does not explicitly take into account the shock geometry, since there is no magnetic field present and the random motion of particles is simulated using a Langevin equation along

the x direction, which is normal to the shock.
From the data analysis, the evaluation of the parameter τ_0 is subject to a large uncertainty, because of the high level of fluctuations in the high-resolution energetic particle fluxes. Therefore, the determination of τ_0 in some cases has been fine-tuned by comparing the output density profile upstream and downstream from the shock derived from the numerical simulation and the one observed by the ACE spacecraft. The comparisons between simulated particle density profiles and the observed ones are satisfactory, since the numerical results reproduce both the upstream and the downstream profiles as a function of the distance from the shock. In case of normal diffusion, the expected downstream profile of energetic particle is flat, but this is never observed. In all the events studied, the comparison with test-particle simulations with particle superdiffusion is satisfactory. Here, for the first time, we are able to reproduce the downstream side by assuming a Lévy walk for energetic particles. In addition, the values of the fundamental parameters μ and τ_0 used in the numerical simulations are the same for the upstream and downstream sides. In principle, we could use different values of μ and τ_0 in the upstream and the downstream regions, since the transport properties could be different in the two sides. For a comparison, using a self-consistent particle-in-cell simulation, Trotta et al. (2020b) have found that transport is superdiffusive both upstream and downstream of the shock, but the exponent of superdiffusion α is larger in the upstream region. That result is probably due to the enhanced level of downstream magnetic fluctuations generated in the simulation. In this connection, we notice that for the three events considered here the level of magnetic fluctuations in resonance with energetic particles does not appreciably change from the upstream to the downstream side (see the lower panels in Figures 5, 8, 11). Since pitch-angle scattering depends on the resonant magnetic fluctuations, even in the case of superdiffusion (Zimbardo and Perri, 2020), the same transport regime can be expected everywhere. We argue that this is the reason why our numerical simulation can reproduce the energetic particle time profiles both in the upstream region and in the downstream region with the same simulation parameters μ and τ_0.
Finally, in Section 2.3 we studied a peculiar behavior of the energetic particle fluxes, namely the low energy ion fluxes are overlapped in a given region far upstream of an interplanetary shock detected by ACE and Wind spacecraft. As a consequence, we observed flat energy spectra for particles. In the event analyzed the spacecraft was well connected to the shock front, so it has been possible to observe fluxes of particles previously accelerated at the shock. From the PSD analysis, we found an increasing of magnetic energy stored in fluctuations very close to the shock that suggests the presence of newly injected fresh turbulence, probably due to the presence of streaming energetic particles, that favours their scattering and diffusion near the shock front. Using the Wind/3DP/SST instrument, we have also analyzed the energetic ion fluxes in different pitch-angle bins, from which we found an isotropic ditribution in pitch-angle in the downstream region and for lower energy particles

close upstream, where the level of magnetic fluctuations is enhanced. High energy particles tend to be more anisotropic close upstream and far upstream, suggesting that they can escape more easily back upstream, and this supports the formation of a flat energy spectrum. This scenario is also in agreement with the numerical results by Ng, Reames, and Tylka (2003).
We tried to explain these observations with the velocity filter method suggested by Lario et al. (2018). This method asserts that a velocity filter may depend on both particles speed and pitch-angle. This will favor the propagation back upstream of faster particles, while low energy particles remain more confined close to the shock. This will cause an overlap of the ion fluxes over different energy channels far upstream and then a flattening of energy spectrum. We derived the differential density of upstream propagating particles and we found that, for a fixed value of θ_{B_n}, particles with higher velocities and large μ tend to fulfill the velocity filter condition and be can easily detected far upstream, while lower energy particles cannot match that condition and tend to be confined close to the shock front. This implies that their fluxes are depleted far upstream leading to flat spectra. Such a mechanism would lead to particle anisotropy, and the degree of anisotropy should depend on both the velocity filter and the scattering undergone by energetic particles. Moreover, we showed the energetic particle fluxes both as a function of the shock normal angle θ_{B_n} and as a function of the shock speed. We found that when the shock configuration is more perpendicular, the velocity filter becomes more relevant. The flattening that we found using the velocity filter method is in good agreement with spacecraft data (we analyzed three events and we found similar results between them, see Perri et al. (2023)), since the energy channels where a significant depletion of the flux is observed correspond to those in which overlapped ion fluxes are detected in the observations (i.e., from 70 keV up to $\sim$ 600 keV). Since these flat spectra are observed several hours prior the shock arrival and particles can be accelerated by a shock that has different properties such as the shock normal angle θ_{B_n}, we can assume that the CME associated to the shock event is propagating too far from the Sun-Earth line. Furthermore, because of the typical shape of the Parker spiral magnetic field, spacecraft at L_1 are connected with the westward part of the CME driven shock, which can be considered to be more "perpendicular" than the shock near to Sun-Earth line. This makes the velocity filter effect efficient. It is also interesting to note that the spectral flattening is maintained for a large range of distances between the approaching shock and Earth, something which suggests that the energetic particle transport properties might be nearly independent of the particle energy.

Chapter 3

Supernovae Explosion as an extreme event

Another class of extreme phenomena that can be included in the extreme events category are the Supernovae explosions. As already mentioned in the Introduction of this thesis, these catastrophic events are associated to a massive star collapse or to a merge between a binary system of stars composed at least of a white dwarf. After the explosion, the material ejected by the Supernova expands throughout the interstellar medium (ISM) forming what is called Supernova Remnant (SNR). It is widely believed that SNR powerfull shocks are the sources of Galactic cosmic rays, whose energy can reach 10^{15} eV, and also a source of X-ray and strong radio emissions. These high Mach number shocks, can accelerate energetic particles at relativistic energies through the diffusive shock acceleration (DSA) mechanism, in which particles can cross the shock back and forth due to the scattering with magnetic irregularities and after each crossing they gain energy (Krymskii, 1977; Blandford and Ostriker, 1978; Bell, 1978; Bell, 1978a; Drury, 1983). In these high energy processes, a key role is played by the magnetic field. It is already known that the ISM is turbulent with a Kolmogorov-like power spectrum (Lee and Jokipii, 1976; Armstrong, Cordes, and Rickett, 1981; Armstrong, Rickett, and Spangler, 1995). The observations have revealed that the Galactic magnetic field assumes value of few μG and it is formed by two components, a uniform one and a fluctuating one, that are in equipartition between them (Beck et al., 1996; Minter and Spangler, 1996; Han, Ferriere, and Manchester, 2004). Several studies have been computed on the interaction between a turbulent magnetic field and a shock wave. When a turbulent magnetic field interacts with a shock wave, it can distort its surface, leading to the formation of the shock ripples (Ofman and Gedalin, 2013) and to an increase of the fluctuation level in the downstream region of the shock (Neugebauer and Giacalone, 2005; Lu, Hu, and Zank, 2009; Trotta et al., 2021). Magnetic field can also be amplified by the presence of energetic particles, that streaming back ahead of the shock (Amato, 2014b), can excite magnetohydrodynamic (MHD) turbulence, allowing an enhancement of the magnetic field far above its original value, and as a consequence this will produce a highly turbulent field (Bell, 2004). The presence of the turbulence in the upstream

region is often used to explain the irregular emissions seen in SNRs and also to explain the particular shape that the edges of the shock assume when it interacts with the ISM (Anderson and Rudnick, 1996; Balsara, Benjamin, and Cox, 2001; Guo et al., 2012; Reynoso, Hughes, and Moffett, 2013; Yu et al., 2015).
Particle acceleration in SNRs shock is testified by the presence of syncrotron emission from relativistic electrons detected at their shock front. One of the common SNRs that show this kind of emission is SN1006. SN1006 is a Type Ia supernova, i.e. the result from the explosion of a white dwarf in an accretion binary system. In these systems, white dwarfs increase their mass from a companion that can be any type of star. The companion pushes the white dwarf over the Chandrasekhar limit into core collapse and this results in a total distruption of the star. There is no stellar remnant in this case, such as neutron star or black hole (Weiler and Sramek, 1988). SN1006 has a bilateral morphology consisting of two bright limbs located in the north-eastern part (NE) and in the south-western part (SW), that present knots and filaments along the boundary of the remnant (Koyama et al., 1995; Bamba et al., 2003; Rothenflug et al., 2004; Reynoso, Hughes, and Moffett, 2013). The NE and the SW regions mainly emit in the radio and X-ray bands, that correspond to the syncrotron emission from high-energy electrons, and γ-ray band that could be associated to high-energy protons. Synchroton emission is responsible for both the thermal emission (in the radio band) and for the non-thermal emission (in the z-ray band). Another confirmation of the presence of non-thermal emission is related to the difference in the spectral indices found in several papers (Koyama et al., 1995; Ellison, Berezhko, and Baring, 2000). From the analysis made on the spectra of the bright regions it emerged that X-ray spectra were much steeper (α = 1.9) than the radio spectra (α = 0.6). This is predicted by non-thermal emission models since this is a measure of the high energy cut-off in the electron distribution. In the case TeV γ-ray emission, the possible candidate associated to the production of such high energy photons are protons that interacting with hadrons present in the ISM, lead to the productions of π^0 and to their subsequent decay. But there is still no complete picture regarding the production of high energy γ-rays, also because these can be produced in the inverse Compton mechanism from ultrarelativistic electrons (Giuffrida et al., 2022). The NW (north-western), the SE (south-eastern) and the center region are dominated by thermal emission (Koyama et al., 1995).
In this work we will try to reproduce the evolution of SN1006 with the help of the MHD PLUTO code (Mignone et al., 2007; Mignone et al., 2011b). We will simulate the expansion of the blast wave in a turbulent environment, following the idea of Guo et al. (2012). We will develop the expansion of the SN in three different turbulence conditions, trying to understand what is the most appropriate to reproduce real observations. Finally, we will make a comparison with Chandra data.

3.1 Numerical model

3.1.1 Numerical code

In order to better understand and reproduce the dynamical evolution of a SNR blast wave propagating through a magnetized environment medium we used the time-dependent ideal MHD equations of mass, momentum and energy conservation in a Cartesian coordinate system. We chose to use the PLUTO code (Mignone et al., 2007; Mignone et al., 2011b). PLUTO is a Godunov-type code that provides modular computational framework for the solution of gasdynamics equation under different regimes. It is designed to integrate a general system of conservation laws

$$\frac{\partial \mathbf{U}}{\partial t} = -\nabla \cdot \mathbf{T}(\mathbf{U}) + \mathbf{S}(\mathbf{U}), \tag{3.1}$$

where $\mathbf{U}$ represents a state vector of conservative quantities, $\mathbf{T}(\mathbf{U})$ denotes a tensor of rank 2, whose rows are the fluxes of each component of $\mathbf{U}$, and $\mathbf{S}(\mathbf{U})$ is a source term. PLUTO is composed by 4 indipendent modules: the hydrodynamic (HD) module that solves the Euler equations of gas dynamics; the magnetohydrodynamic (MHD) module that solves the ideal/resistive MHD equations; the relativistic (RHD) module that solves the energy-momentum conservation laws of a special relativistic perfect gas, and the relativistic MHD (RMHD) module that solves the relativistic magnetized ideal plasma equations. To mimic the expansion of a SNR shock in the ISM, we used the MHD module. The MHD equations are

$$\begin{cases} \frac{\partial \rho}{\partial t} + \boldsymbol{\nabla} \cdot (\rho \boldsymbol{v}) = 0 \\ \frac{\partial (\rho v)}{\partial t} + \boldsymbol{\nabla} \cdot (\rho \boldsymbol{v}\boldsymbol{v} - \boldsymbol{B}\boldsymbol{B}) + \boldsymbol{\nabla} P_t = \boldsymbol{\nabla} \cdot \boldsymbol{\tau} + \rho \boldsymbol{g} \\ \frac{\partial \varepsilon}{\partial t} + \boldsymbol{\nabla} \cdot \left[(\varepsilon + P_t)\boldsymbol{v} - (\boldsymbol{v} \cdot \boldsymbol{B})\boldsymbol{B} \right] = \boldsymbol{\nabla} \cdot \Pi_\varepsilon - \Lambda + \rho \boldsymbol{v} \cdot \boldsymbol{g} \\ \frac{\partial \boldsymbol{B}}{\partial t} - \boldsymbol{\nabla} \times (\boldsymbol{v} \times \boldsymbol{B}) = -\boldsymbol{\nabla} \times (\eta \boldsymbol{J}). \end{cases} \tag{3.2}$$

Here ρ is the plasma density, $\boldsymbol{v}$ is the fluid velocity, $\boldsymbol{B}$ is the magnetic field, P_t is the total gas pressure, i.e the the sum of the thermal and the magnetic pressure ($P_t = P + B^2/2$), $\boldsymbol{g}$ is the gravitational term, $\boldsymbol{\nabla} \cdot \boldsymbol{\tau}$ is the thermal conductivity term, ε is the total energy density, $\boldsymbol{\nabla} \cdot \Pi_\varepsilon$ is the radiative cooling term, Λ is a term that takes into account the optical thin losses and $\eta \boldsymbol{J}$ is the resistive term. At this stage we do not take into account the effects related to thermal conduction, radiative cooling, non linear effects due to acceleration of charged particle and to the amplification of the magnetic field due to accelerated particles. So the (ideal) MHD equations become

$$\begin{cases} \frac{\partial \rho}{\partial t} + \boldsymbol{\nabla} \cdot (\rho \boldsymbol{v}) = 0 \\ \frac{\partial (\rho v)}{\partial t} + \boldsymbol{\nabla} \cdot (\rho \boldsymbol{v}\boldsymbol{v} - \boldsymbol{B}\boldsymbol{B}) + \boldsymbol{\nabla} P_t = 0 \\ \frac{\partial \varepsilon}{\partial t} + \boldsymbol{\nabla} \cdot \left[(\varepsilon + P_t)\boldsymbol{v} - (\boldsymbol{v} \cdot \boldsymbol{B})\boldsymbol{B} \right] = 0 \\ \frac{\partial \boldsymbol{B}}{\partial t} - \boldsymbol{\nabla} \times (\boldsymbol{v} \times \boldsymbol{B}) = 0. \end{cases} \tag{3.3}$$

We couple this set of equations with an ideal equation of state. This allowed us to write the total energy density in this way

$$\varepsilon = \frac{P}{\gamma - 1} + \frac{1}{2}\rho v^2 + \frac{B^2}{2},$$

where γ is the adiabatic index. The solutions of the ideal MHD equations must satisfy the divergence free condition, i.e. $\boldsymbol{\nabla} \cdot \boldsymbol{B} = 0$. This condition is not naturally preserved in numerical schemes without a proper dicretization technique. PLUTO uses three different techniques in order to fulfill the condition $\boldsymbol{\nabla} \cdot \boldsymbol{B} = 0$: the eight wave formulation (Powell, 1994; Powell et al., 1999), the hyperbolic divergence cleaning (Mignone and Tzeferacos, 2010; Mignone, Tzeferacos, and Bodo, 2010) and the constrained transport (CT) (Balsara and Spicer, 1999; Londrillo and Del Zanna, 2004). In the eight waves formalism the magnetic field has a cell-centered representation and additional terms (source terms) are added to the ideal MHD equations and, depending on the Riemann solver used, the source terms can be discretized in different ways. In the hyperbolic divergence cleaning the divergence free condition is enforced by solving a modified system of conservation laws, in which the induction equation is coupled with a generalized Lagrange multiplier (GLM). This technique is useful because no source terms are introduced, so the equations keep a conservative form, all variables retain a cell-centered representation and it is possible to use different Rienmann solvers. The CT formalism uses two sets of magnetic field: a face-centered and a cell-centered. In the first one the field components are located at different spatial points in the control volume, while in the second one the staggered magnetic field is treated as an area-weighted average on the zone face and the Stoke's theorem is used to update it. In this work we decided to advance the magnetic field and to preserve the divergence-free condition using the CT formalism, but we tried to reproduce the same simulations with the other two schemes. We obtained the same results.

3.1.2 Numerical setup

In order to reproduce the evolution of a SNR throughout the ISM we model the simulations in two-dimensional Cartesian coordinates (x,y) with a uniform grid. The computational domain extends between -15 pc and 15 pc in both directions with 4096^2 grid points. We set all the other quantities following the work of Orlando et al. (2012) and (Guo et al., 2012). Since we are simulating the evolution of a type-Ia SN (SN1006), we assumed an initial cylindrical remnant of radius $R_{SN,0} = 0.4$ pc and lenght in the z-direction of $L_z = 0.8$ pc, that corresponds to an age of $t_0 = 10$ years, whose progenitor is a star with mass of 1.4 $M_\odot$. We set the internal energy within the cylinder area equal to $E_{inj} = 1.5 \times 10^{51}$ erg. This allows us to define an internal initial number density of about $n_{inj} = 13.3\,\mathrm{cm}^{-3}$. The environment in which our remnant is evolving is set with a uniform density $n = 1\ \mathrm{cm}^{-3}$ (Morlino et al., 2010; Perri, Amato, and Zimbardo, 2016) and a uniform temperature $T = 10^4$ K .

The shock associated to the SNR remnants is supposed to expand with a velocity $V_{sh} \simeq 4400$ km/s and the adiabatic index is chosen as $\gamma = 5/3$ for a monoatomic non-relativistic ideal gas. We chose to follow the SNR expansion up to 10 pc; at this stage we are in the Sedov-Taylor phase (see Introduction for more details) in which the energy is conserved.
We set a background mean magnetic field of $B_0 = 3\mu G$, and we varied its direction spanning different case studies. The components of the mean magnetic field in spherical coordinates are:

$$\begin{cases} B_x = B_0 cos(\phi) sin(\tilde{\theta}) \\ B_y = B_0 sin(\phi) sin(\tilde{\theta}) \\ B_z = B_0 cos(\tilde{\theta}). \end{cases}$$

In this chapter we show different simulation results obtained varying the values of ϕ and $\tilde{\theta}$, but in order to make a comparisn with SN1006 we will choose $\phi = 150^\circ$ and $\tilde{\theta} = 90^\circ$. These values were obtained from the observations made by Reynoso, Hughes, and Moffett (2013), where they found that the mean magnetic field is oriented at 60° with respect to the Galactic plane normal. In Figure 3.1 we report the results obtained by Reynoso, Hughes, and Moffett (2013).

3.1.3 Homogeneous turbulence

In order to mimic a turbulent background plasma in which the SNR blast wave propagates, we initialize the in-plane magnetic field as done in classical simulations of plasma turbulence Servidio et al. (2012). We start from the $z-$component of the vector potential, described in the Fourier space by:

$$A_z(x, y) = \sum_{k_x, k_y} \widetilde{A}(k) e^{i(\boldsymbol{k}\cdot\boldsymbol{x} + \phi_k)}, \tag{3.4}$$

where $\boldsymbol{k} = (k_x, k_y)$ is the $k-$vector, $k = |\boldsymbol{k}|$, and ϕ_k are random phases. In the above, $\widetilde{A}(k) = [1 + (k/k_0)^\alpha]^{-1}$ sets the initial shape of the spectrum, peaked at $k = k_0 = 4$, and with a power-law $\alpha = -7.5/3$. This initial condition consists of a plasma perturbed by a 2D spectrum of Fourier modes, with energy distributed via random phases. By performing the curl of Eq. (3.4), we then obtain the magnetic field whose power spectral density follows a Kolmogorov-like decay with slope $p_0 \sim -5/3$, according to large scale observations of astrophysical plasma turbulence. To avoid numerical disturbance from aliasing effects, we filter both the magnetic field components in the Fourier space by using a smoothing technique described in Meringolo, Servidio, and Veltri (2021), suppressing the high-energy modes at $k > k^*$. In Figure 3.2(A) we show the initial power spectra for the potential and for the total magnetic field. In Figure 3.2(B) we report the initial x- and y-components of the magnetic field obtained from the A_z potential vector.

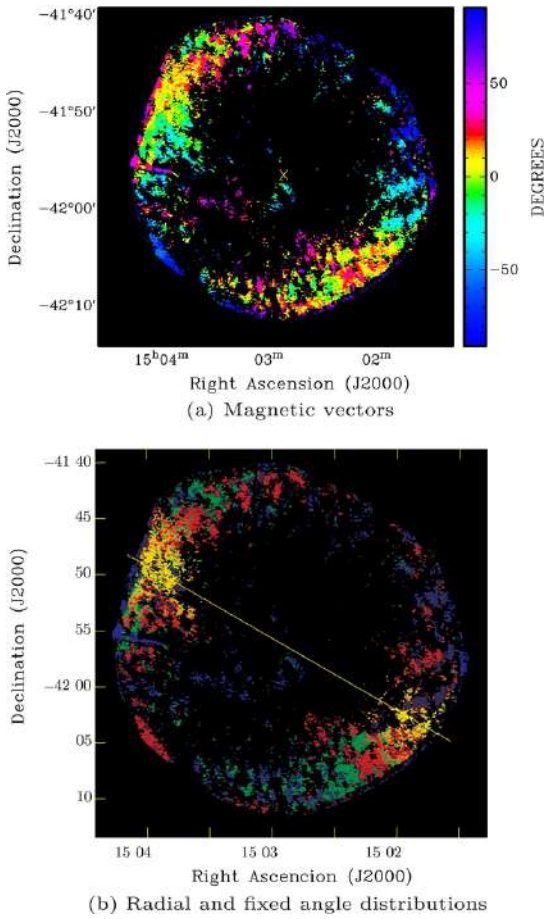

FIGURE 3.1: (a) Magnetic field orientation with respect to the polar angle. (b) Magnetic field orientation with respect to the polar angle and the Galactic plane. The yellow continuous line represents the Galactic plane direction. For more details see Reynoso, Hughes, and Moffett (2013).

3.2 Simulation Results

We show the results obtained via the MHD-PLUTO simulations in this section. In Table 3.1 we report all the explorative runs we have performed. In particular, we concentrate on the results coming from Run 3 (in bold in Table 3.1), where the level of magnetic field turbulence is set such as $\delta B/B = 1$ (Guo et al., 2012).

3.2.1 Run 3

In Figure 3.3 we show the results obtained from Run 3. The figure presents six different maps at the simulation final time $t = 1000$ years. The first map shows the spatial distribution of the number density. At the beginning of the simulation, the ejecta is characterized by high values of density and pressure. This allows them to drive a strong shock in the turbulent background environment, heating and compressing the ambient medium. Since the shocked circumstellar medium pushes back the ejecta, a reverse shock is produced.

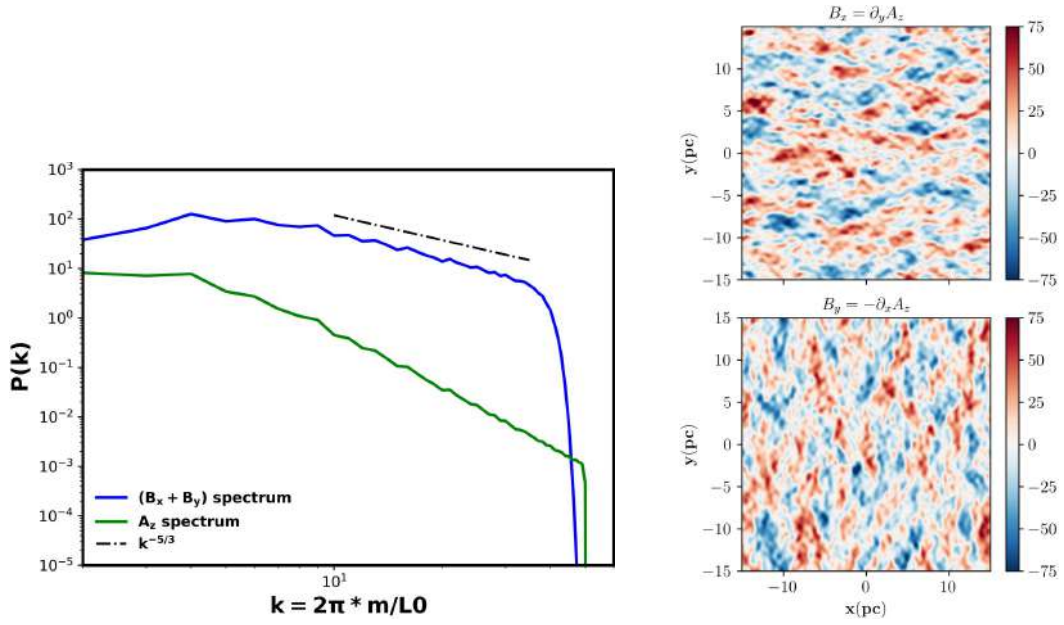

(A) (B)

FIGURE 3.2: (A) Power spectra of the potential vector (green solid line) and of the total magnetic field (blue solid line). (B) Initial magnetic field obtained computing the curl of the A_z potential vector.

Run	$\mathbf{M_{ej}}(\mathbf{M_\odot})$	$\delta\mathbf{B}/\mathbf{B}$	$\mathbf{B_{avg}}(\mu\mathbf{G})$	$\mathbf{B_{max}}(\mu\mathbf{G})$	$\mathbf{n_{avg}}(\mathbf{cm^{-3}})$	$\mathbf{n_{max}}(\mathbf{cm^{-3}})$
1	1.4	0.1	48.2	5010.7	0.2	1.98
2	1.4	0.5	49.9	5303.6	0.2	1.98
3	**1.4**	**1**	**57.0**	**5652.8**	**0.18**	**1.99**
4	3	1	46.1	4555.4	0.3	3.6
5	5	1	43.3	3296.2	0.4	4.9

TABLE 3.1: Five different runs made varying the level of fluctuations and the mass of the ejecta. The first two columns show the number associated to the particular run; in the second and in the third column the values of the mass of the ejecta and of the turbulence level are displayed; in the last 4 columns the mean and the maximum magnetic field values, the mean and the maximum density values, calculated over the whole simulation box at the final time, are reported.

It is possible to observe in Figure 3.3 the presence of the forward shock (FS) and of the reverse shock (RS). The FS extends up to 12 pc, while the RS extends up to 9 pc. Between them it is possible to find the contact discontinuity (CD) zone, in which the Rayleigh-Taylor instability is triggered. Outside the inner ejecta the density fluctuations are visible and they are oriented along the direction of the mean magnetic field. Pressure and temperature maps present a similar behavior. The spatial distribution of the velocity components shows two hemispheres of opposite speed, with the maximum velocities oriented, respectively, along the x-direction for the V_x-component and along the y-direction for the V_y-component. Finally, the magnetic field shows a noticeable amplification and compression in the direction perpendicular to the direction of the mean magnetic field. In this case the magnetic field fluctuations outside the SNR tend to distort the shape of the FS and as a result it is possible to observe

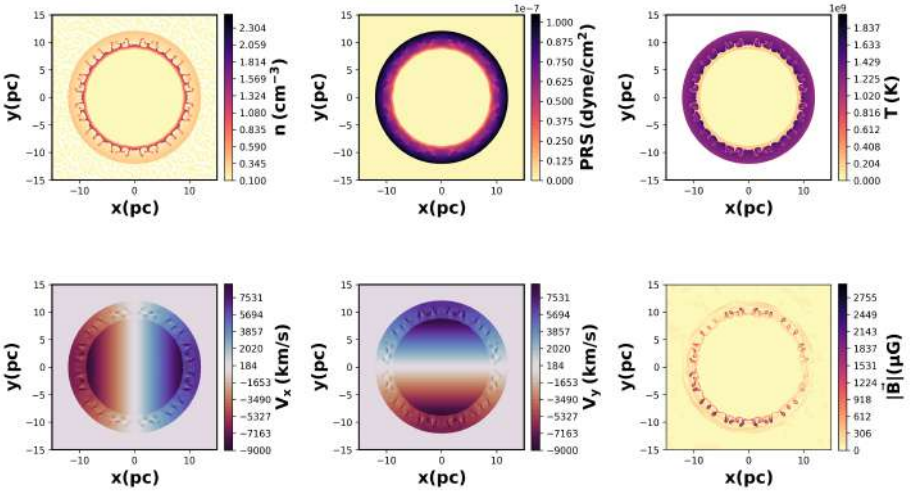

FIGURE 3.3: Spatial distribution of the number density, pressure, temperature, x- and y-components of the velocity, and the magnetic field magnitude from the 2D simulation with an age of 1000 years.

knots and filaments in this region.

Figure 3.4 shows the time evolution of 4 quantities: maximum value reached by the magnetic field over the whole simulation domain (Figure 3.4(a)), the total kinetic energy (Figure 3.4(b)), the magnetic field energy (Figure 3.4(c)), and the thermal energy (Figure 3.4(d)). The energies are averaged over the whole simulation domain.

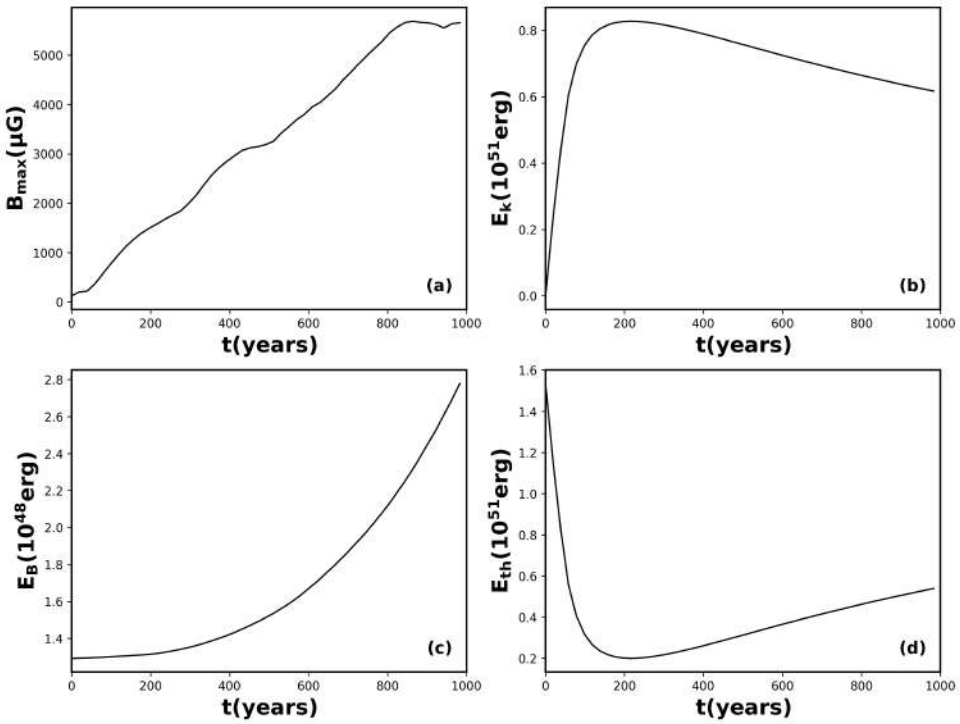

FIGURE 3.4: (a) Time evolution of the maximum value of the magnetic field in the domain, (b) total kinetic energy, (c) magnetic energy averaged and (d) thermal energy, all averaged over the whole simulation domain.

The maximum value of $|\vec{B}|$ shows a constant increase until $\simeq$ 400 years in which it reaches 3000 μG. After a brief period during which a little plateau appears (around 500 years), it rapidly increases until 800 years and reaches a maximum value of 5652.8 μG. After 800 years it sets at a constant value until the end of the simulation. The behavior of the maximum value of the magnetic field is reflected on the magnetic energy that continuously increases, reaching a maximum value of 2.8×10^{48} erg. These results are in agreement with the ones found by (Giacalone and Jokipii, 2007; Guo et al., 2012). Figures 3.4 (b) and (d) show the kinetic energy and the thermal energy. They have an opposite trend, at the beginning of the simulation. The kinetic energy increases rapidly until 200 years due to the the high density and pressure whose drive a strong shock in the interstellar turbulent medium, while the thermal energy decreases rapidly with the same trend. The kinetic energy, during this rapid increase, reaches a maximum value of 0.8×10^{51} erg that corresponds to a conversion of about 54 % of the thermal energy. After that, the ejecta slow down interacting with the turbulent interstellar medium, so the kinetic energy decreases slowly, and consequently the thermal energy increases.
In Figure 3.5 we show the time evolution of the SNR radius (a) and the shock speed (b) of the FS. Since the ejecta is expanding in a dense and turbulent environment, the shock velocity constantly decreases. The shock speed decreases from about 8000 km/s to 3000 km/s, in agreement with the theoretical eveolution of the FS speed in the Sedov-Taylor phase, i.e. $V_{sh} \propto t^{-3/5}$ (Helder et al., 2012). The radius of the FS also increases as a power-law predicted by the theory $r \propto t^{2/5}$ (Chevalier, 1982; Helder et al., 2012; Guo et al., 2012).

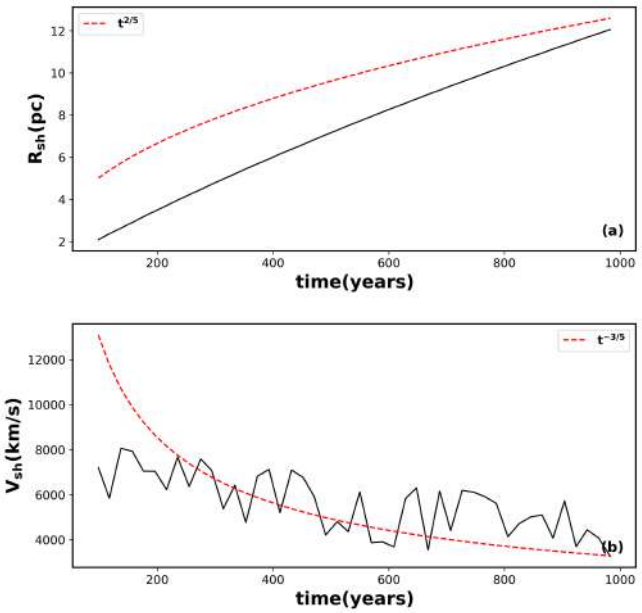

FIGURE 3.5: Time evolution of the FS radius (a) and of the shock speed (b).

We present in Figures 3.6, 3.7, 3.8 a cut made on the y axis at 0 pc. Each of these plots are taken at the final time of the simulation. It is clear in every figure the presence of

the FS (at 12 pc) and of a RS (at 9pc), with the region between these two (CD zone) characterized by an oscillating behavior related to the Rayleigh-Taylor instability. The central part of the plots appears constant, with values equal to 0, except in the velocity case.

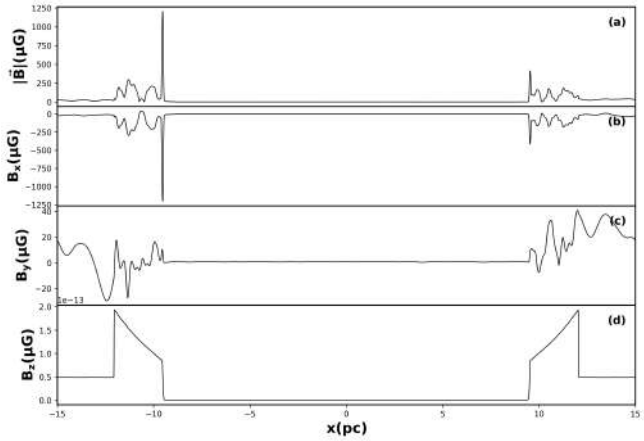

FIGURE 3.6: (a) Magnetic field amplitude, (b) x-component, (c) y-component, (d) z-component of the magnetic field. All the quantities are expressed in μG.

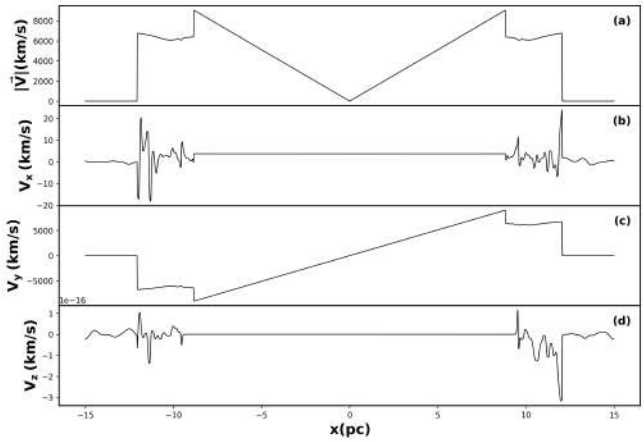

FIGURE 3.7: (a) Velocity amplitude, (b) x-component, (c) y-component, (d) z-component of the velocity field. All the quantities are expressed in km/s.

This is due to the fact that the mass of the inner ejecta is swept-up outside the inner core constantly, and at the end of the simulation the inner core of the ejecta is completely emptied. In the case of the velocity, firstly the speed of the ejecta increses rapidly at early times, and due to the interaction with the turbulent and dense environment, it starts to decelerate. We chose to show the z-component of the magnetic and of the velocity field just to be sure that these components do not influence the results. We show in Figure 3.9 a zoom of the spatial distributions of the number density and of the magnetic field amplitude. As discussed in the case of Figure 3.3, it is possible to see the structures formed by the triggered Rayleigh-Taylor instabilities in both figures and the deformation of the FS with the shock surface in the magnetic

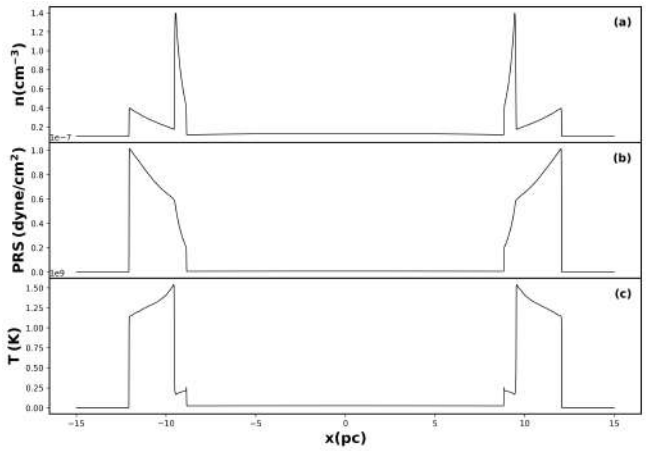

FIGURE 3.8: (a) Number density (in units of cm^{-3}), (b) pressure (in unit of (dyne/cm^2), (c) temperature (in K).

field maps due to the interaction of the ejecta with the turbulent environment. We cannot see the same for the density, probably because the level of the density fluctuations is not high enough to distort the shock surface or because the value chosen for the ISM density is too small. A future investigation on this aspect is planned.

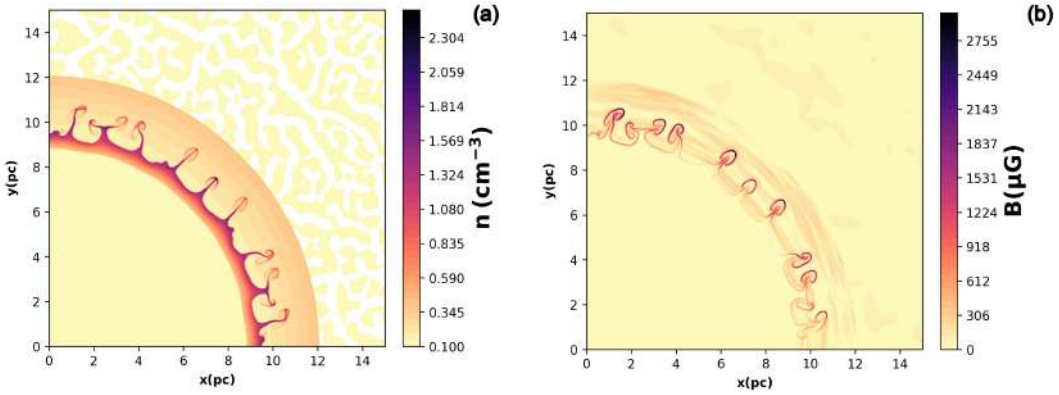

FIGURE 3.9: Zoom of the spatial distributions for the number density (a) and for the magnetic field amplitude (b).

We calculate the compression ratio in the region in which the shock assumes a quasi-perpendicular geometry using the ratio between the downstream magnetic field B_d and the upstream magnetic field B_{up}. In order to see if we are in agreement with the Rankine-Hugoniot theoretical conditions of a shock wave in a magnetized plasma medium, we compare this value with the ratio between the downstream (n_d) and the upstream (n_{up}) density. We found a value of $B_d/B_{up} = 3.8$ that is similar to the value found in the case of $n_d/n_{up} = 4.0$.

Finally, we tried to study the level of anysotropy related to the presence of a strong magnetic field. Shebalin, Matthaeus, and Montgomery (1983) found that starting from an initial isotropic spectrum, the anisotropy develops also with modest level of the mean magnetic field. Different levels of anisotropies can also be found in different regions of the solar wind (Bandyopadhyay and McComas, 2021). In order

to study the plasma anisotropy (Matthaeus, Goldstein, and Roberts, 1990; Horbury, Forman, and Oughton, 2008; Wicks et al., 2010), we applied a Heavyside mask (ring shaped) on the density and magnetic field maps, in such a way we consider only the region beetween the RS and the FS. We calculate the autocorrelation function $C_2(\vec{\ell})$ on the ring mask

$$C_2(\vec{\ell}) = f(\vec{\ell} + \vec{r}) \cdots f(\vec{r}) \tag{3.5}$$

where f is a generic field, $\vec{\ell}$ are the increments and $\vec{r}$ is the position. In Figures 3.10 and 3.11 we report the result of the application of the autocorrelation function in both cases, for the density map and for the magnetic field map.

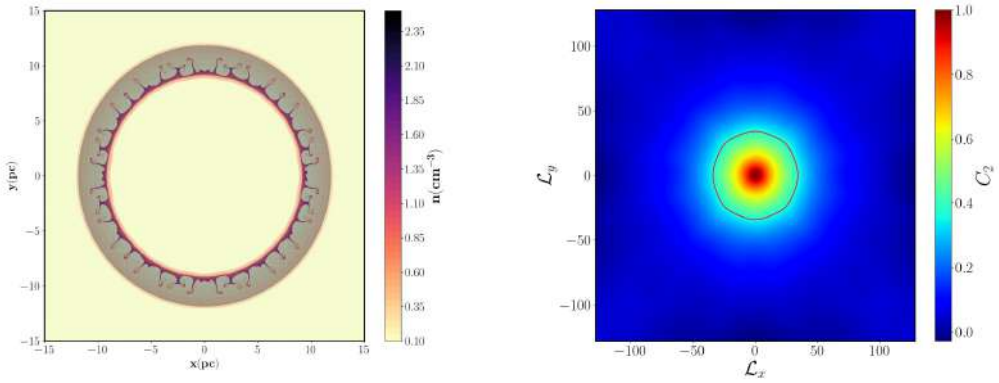

(A) (B)

FIGURE 3.10: (A) Density map distribution with the ring-shaped mask. (B) Autocorrelation function map applied on the ring-shaped region. The red solid line represents the autocorrelation length, namely the isocontour of $C_2 = 1/e$.

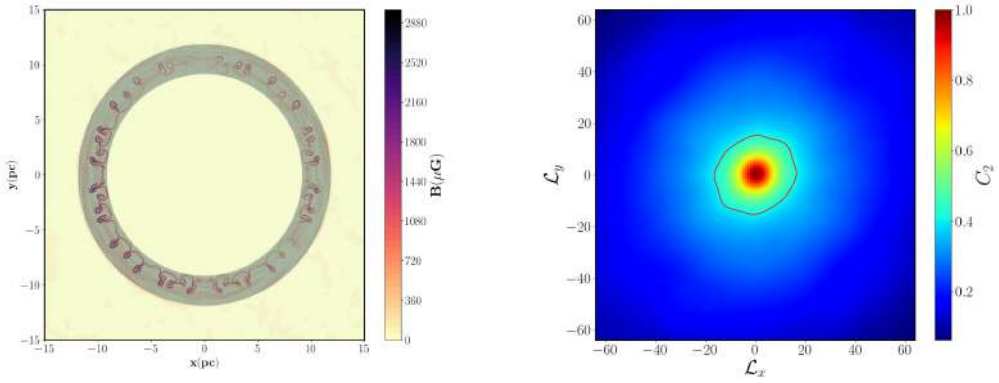

(A) (B)

FIGURE 3.11: (A) Magnetic field map distribution with the ring-shaped mask. (B) Autocorrelation function map applied on the ring-shaped region. The red solid line represents the autocorrelation length, namely the isocontour of $C_2 = 1/e$.

From Figure 3.10 the autocorrelation map appears to be isotropic, with no anisotropies in any particular direction. The same thing cannot be said for the case of the magnetic field map. In this case it is possible to observe that in the region perpendicular to the mean magnetic field we have the highest values of correlation length while in the region parallel to the mean magnetic field it is possible to observe the lowest value of the correlation length.

3.2.2 Simulations with different background turbulence

In this Section we compare the results from Run1, Run2 and Run3 (see Table 3.1).

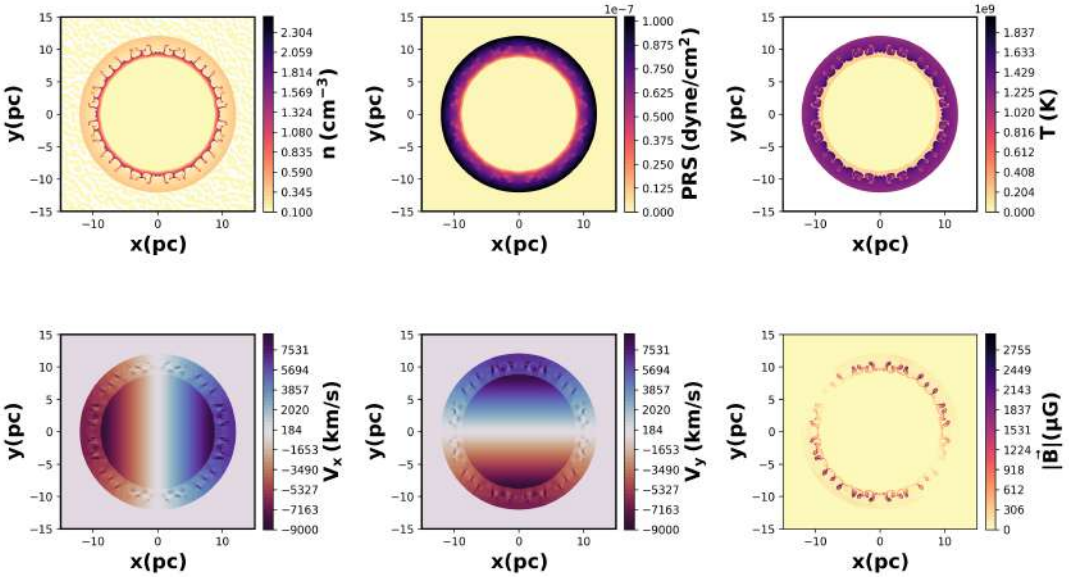

FIGURE 3.12: Spatial distribution of the number density, pressure, temperature, x- and y-components of the velocity, and the magnetic field magnitude from the 2D simulation with an age of 1000 years in Run 1.

The two figures (Figure 3.12 and 3.13) do not differ a lot from Figure 3.3, except for the magnetic field magnitude. Indeed, varying the amplitude of the turbulent fluctuations in the ISM causes a change in the magnetic field amplification at the shock front, as well as the local distortion of the front with a subsequent appearence of knots and filaments. This is also reflected in the cut shown in Figures 3.14, 3.15, 3.16.

As already noted, the behavior among the simulations is similar with fluctuations that become larger in amplitude as the $\delta B/B$ value increases. This is seen in both the magnetic and the velocity field, while the number density, the pressure and the temperature present an identical behavior.

In Figure 3.17 a comparison among the averaged energies and the maximum magnetic fields strenght over the three simulations is displayed. From the comparison, we see an increase of the magnetic energy and the maximum value of $|\vec{B}|$ as the amplitude of the magnetic field fluctuations increases (panels (a) and (c)) in Figure 3.17.

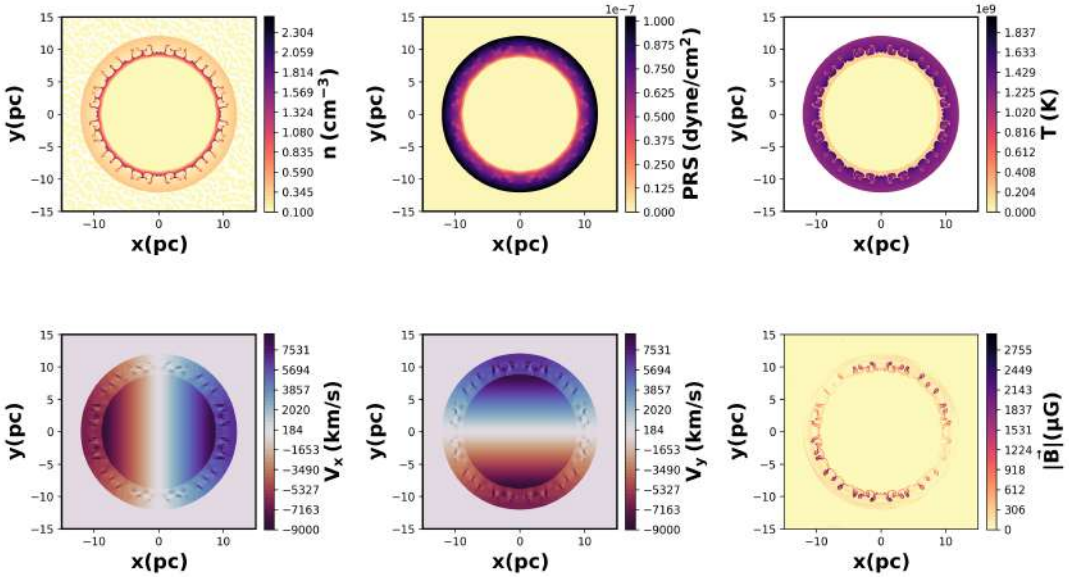

FIGURE 3.13: Spatial distribution of the number density, pressure, temperature, x- and y-components of the velocity, and the magnetic field magnitude from the 2D simulation with an age of 1000 years in Run 2.

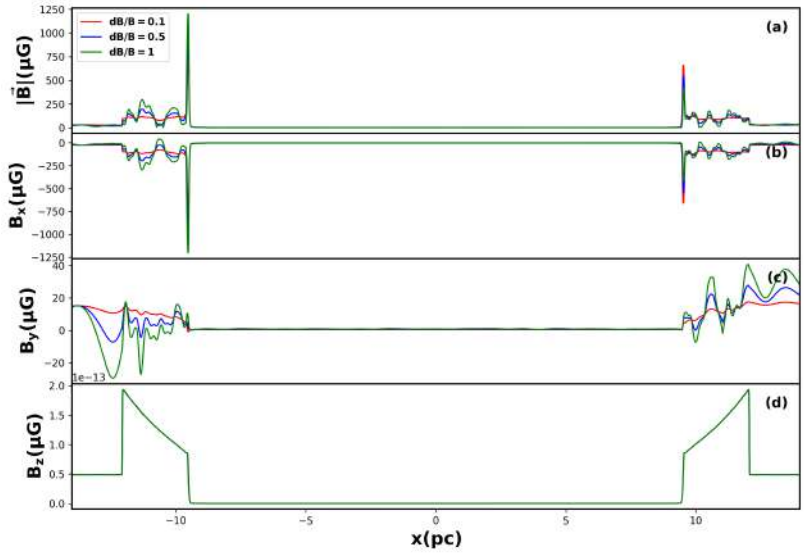

FIGURE 3.14: Same as Figure 3.6. The red, blue and green lines refer to Run 1, Run 2 and Run 3, respectively.

The kinetic and the thermal energies remain similar in the three sets of simulations. This is due to the lower increase in the density fluctuations level. We determined the mean value of the density fluctuations that corresponds to $\delta n \simeq 10^{-5}$ cm^{-3}. In the simulations, we set the turbulent environment just with the magnetic field fluctuations and this cannot allow to generate intense density fluctuations. As next step of this work, we will try to expand our SNR inside an ambient in which both types of irregularities will be present, following the idea of Giacalone and Jokipii (2007).

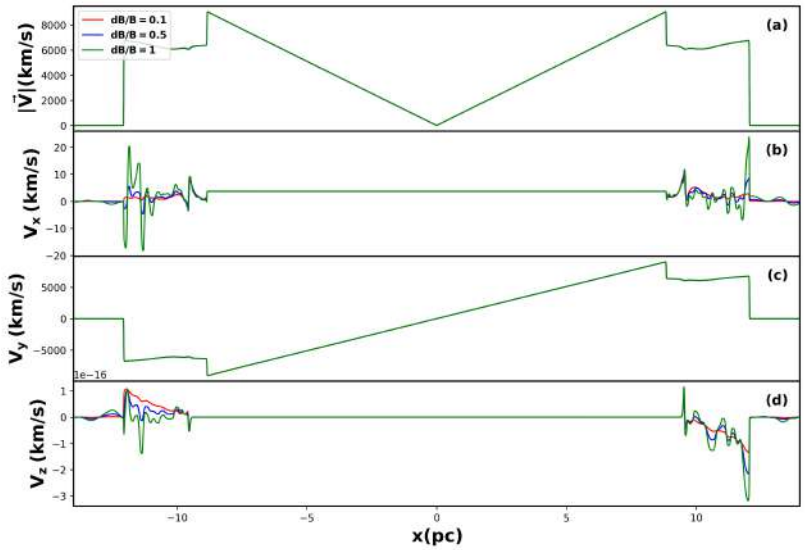

FIGURE 3.15: Same as Figure 3.7. The red, blue and green lines refer to Run 1, Run 2 and Run 3, respectively.

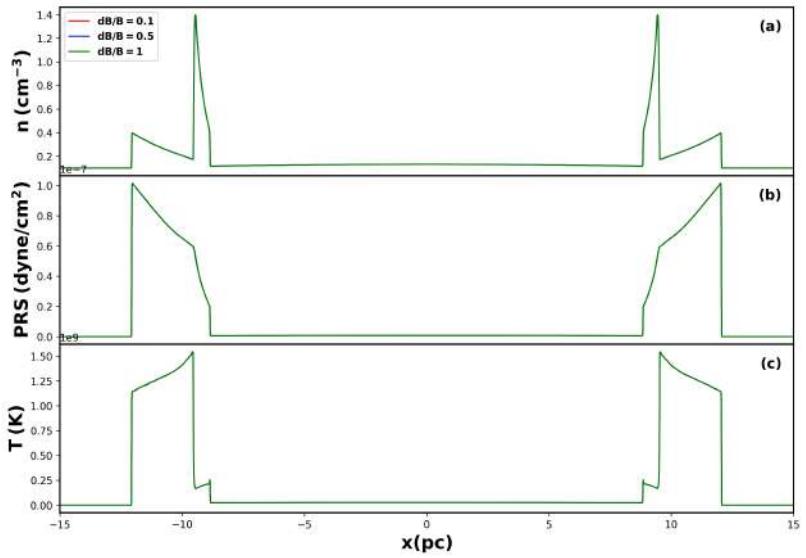

FIGURE 3.16: Same as Figure 3.8. The red, blue and green lines refer to Run 1, Run 2 and Run 3, respectively.

3.2.3 Simulations with different mass of the ejecta

We also tried to vary the values of the mass of the ejecta in order to study its effect on the evolution of a SNR. We did a comparison among Run 3, Run 4 and Run 5 (see Table 3.1). In Figures 3.18 and 3.19 we report the spatial maps of the number density, pressure, temperature, the velocity components and the magnetic field amplitude. In these two cases the difference with Figure 3.3 are evident. It is possible to observe immediately that the inner core of the number density spatial map is not empty but the value inside the core is high. This means that varying the mass of the ejecta it becomes more difficult to swept-up the mass in the same time as in the case of $M_{ej} = 1.4 M_{\odot}$. In the CD region the expanding mass interacts with the turbulent and

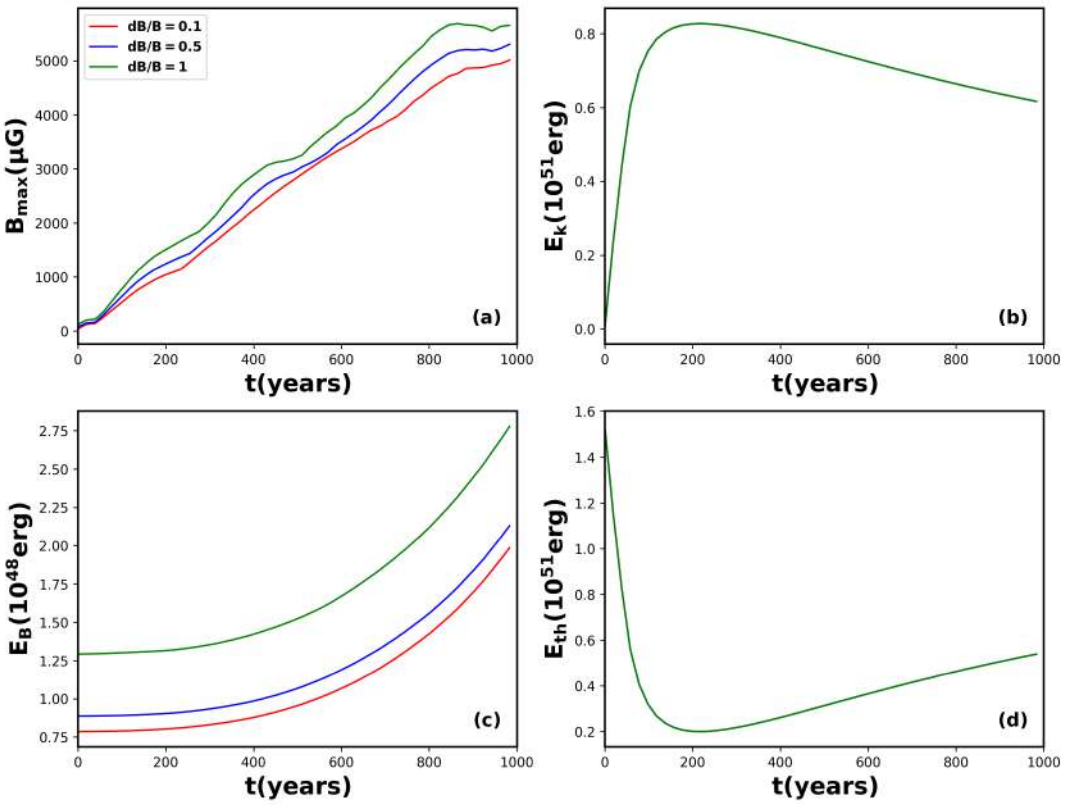

FIGURE 3.17: Same quantities as in Figure 3.4. The red, blue and green lines indicate Run 1, Run 2 and Run 3, respectively.

dense ISM environment but it also interacts with an inner dense core. This inhibits the formation of the Raylegh-Taylor structures in the region, as in the previous case. As a consequence, the radius of the FS in Run 4 and Run 5 is smaller than in Run 3. Also, we observe a magnetic field amplification close to the expanding shock but lower than in Run 3. Again, the level of fluctuations is high enough to distort the shock surface and to create knots and filaments.

As we made for the other runs in the previous Section, we compare the cut made on the plasma quantities for Run 3, Run 4 and Run 5 in Figures 3.20, 3.21, 3.22. In these cases the cuts are not made along the y-axis, but within a region in which we have the maximum amplification of the magnetic field.

We notice that the position of the FS and the RS decreases as the mass of the ejecta increases. In the case of magnetic and velocity fields (Figure 3.20 and 3.21) the values associated to Run 3 are the highest, as already explained at the beginning of the section. The values of density, pressure and temperature in the inner core (Figure 3.22) are observed to be larger in Run 5 than in the other simulations, because the mass is swept up out over a longer time scale. We finally calculated the averaged energies and the magnetic field strength for Run 4 and Run 5 and we made a comparison with Run 3. The comparison is presented in Figure 3.23.

As expected, the magnetic energy and the maximum value reached by the magnetic field within the simulation domain decrease as the mass of the ejecta increases. On

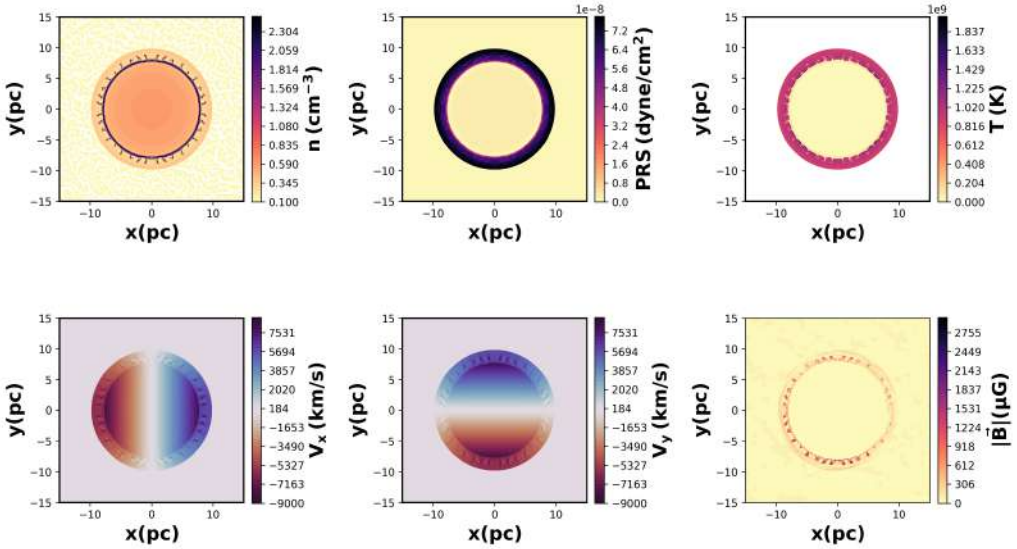

FIGURE 3.18: Spatial distribution of the number density, pressure, temperature, x- and y-components of the velocity, and the magnetic field magnitude from the 2D simulation with an age of 1000 years in Run 4.

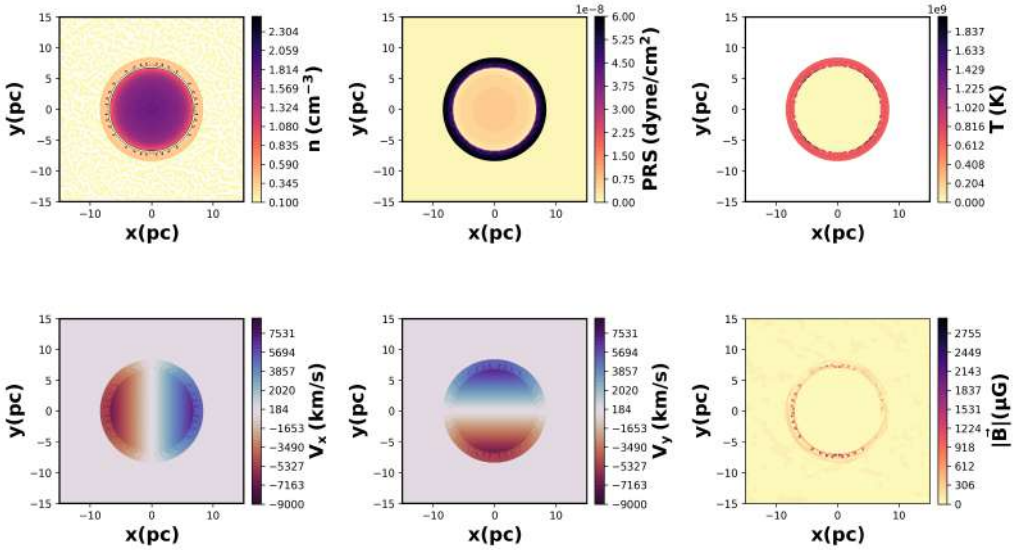

FIGURE 3.19: Spatial distribution of the number density, pressure, temperature, x- and y-components of the velocity, and the magnetic field magnitude from the 2D simulation with an age of 1000 years in Run 5.

the other hand, the kinetic energy increases slower in Run 4 and 5 and, consequently, the thermal energy decreases slower, being the expansion time longer for high values of the mass of the ejecta.

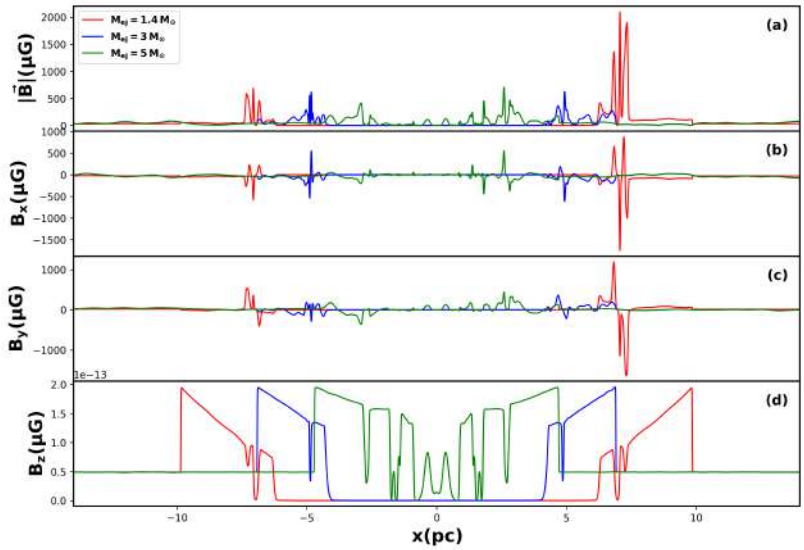

FIGURE 3.20: Same as Figure 3.6. The red, blue and green lines refer to Run 4, Run 5 and Run 6, respectively.

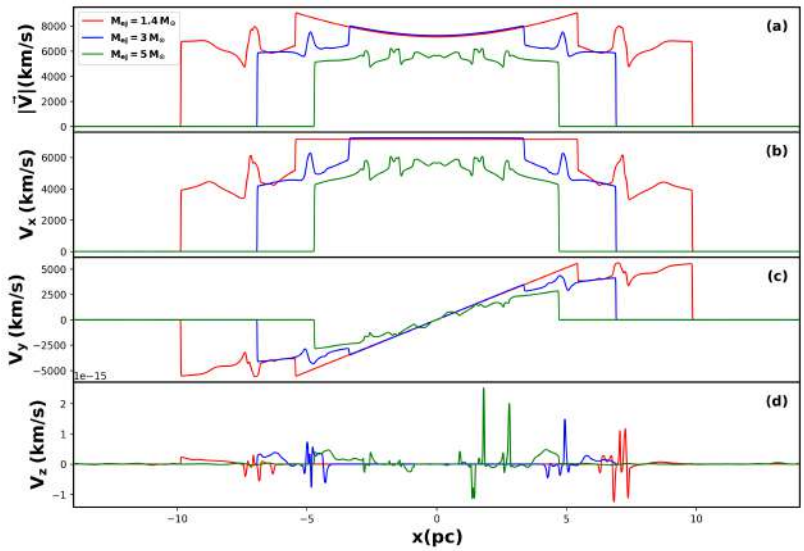

FIGURE 3.21: Same as Figure 3.7. The red, blue and green lines refer to Run 4, Run 5 and Run 6, respectively.

3.3 Comparison with Chandra observations

In this section we try to make a visual comparison between the observations from the Chandra spacecraft and numerical simulations. The X-ray data from Chandra are retrieved from `https://chandra.harvard.edu/photo/openFITS/xray_data.html`. Data are provided by the Advanced CCD Imaging Spectrometer (ACIS) instrument onboard of Chandra, that gives information about the energy, the position and the arrival time of the X-ray photons. In Figure 3.24 the X-ray image of the SNR SN1006 in the energy channel 1.34-3.0 keV is shown.

The X-ray emission is brighter at the edge of the supernova blast wave and it is mainly a non thermal synchrotron emission from relativistic electron gyrating in an

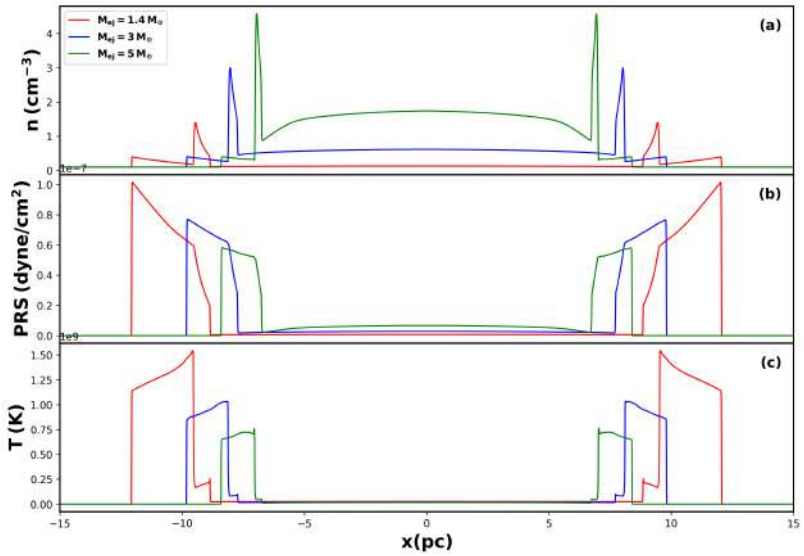

FIGURE 3.22: Same as Figure 3.8. The red, blue and green lines refer to Run 4, Run 5 and Run 6, respectively.

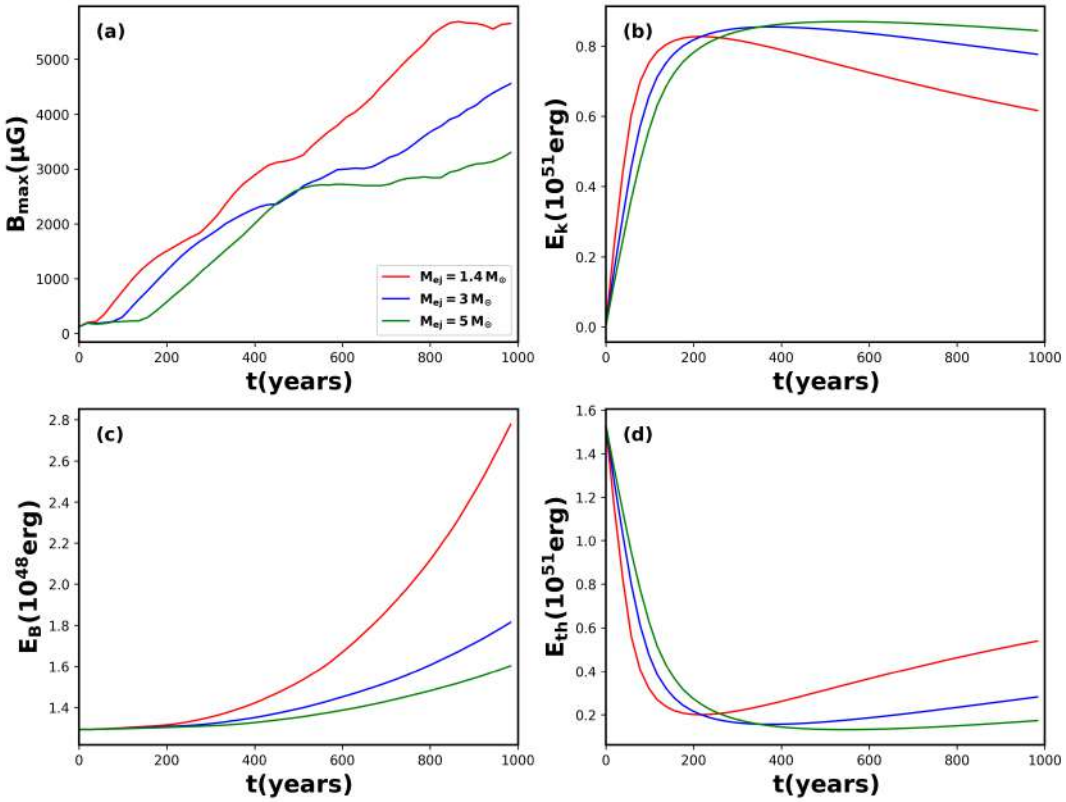

FIGURE 3.23: Same quantities as in Figure 3.4. The red, blue and green lines indicate Run 3, Run 4 and Run 5, respectively.

amplified magnetic field. It has been assessed that the brightest cups correspond to regions in which the shock normal direction is parallel to the direction of the magnetic field. In order to make a visual comparison between Chandra data and the PLUTO results we made a cut in a similar way as we did in Section 3.2. Figure 3.25 shows the cut made for Chandra data on the y-axis at 0 pc.

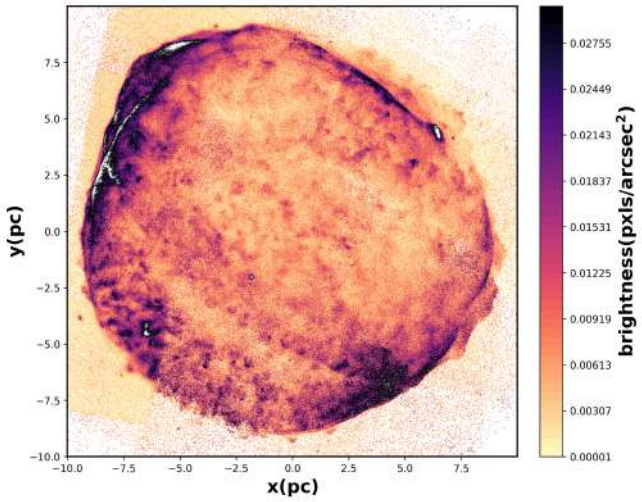

FIGURE 3.24: Chandra X-ray images in the energy channel 1.34-3.0 keV.

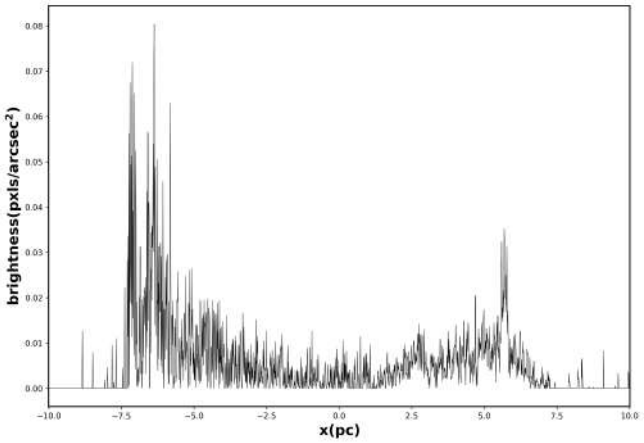

FIGURE 3.25: Brightness cut made on the y-axis at 0 pc .

The brightness cut looks qualitatively similar to the cut made for Run 3 (Figure 3.8(a)), with the highest values of brightness in correspondence of the FS. The differences that appear in the two cuts are also due to the shape of SN1006, that, unlike the SNR obtained from the numerical simulations, having a spherical shape, is more like an ellipsoid with a non uniform brightness. In the case of numerical simulations, the density was distributed uniformly around the region between the FS and the RS, with the exception made by the Rayleigh-Taylor structures. Furthermore, we considered in the simulation an explosion in which the ejecta just interacts with a turbulent and dense environment and we do not take into account the contribution of energetic particles, which play a key role in the evolution of a SNR.
We also tried to study the degree of anisotropy in this case. We applied a ring shaped mask in a similar way as described in Section 3.2.1, but in this case on the brightness field. The results are ported in Figure 3.26.
In this case we found a similar result to what we obtained from Figure 3.11. It seems that the highest values of the correlation length are located in the region in which

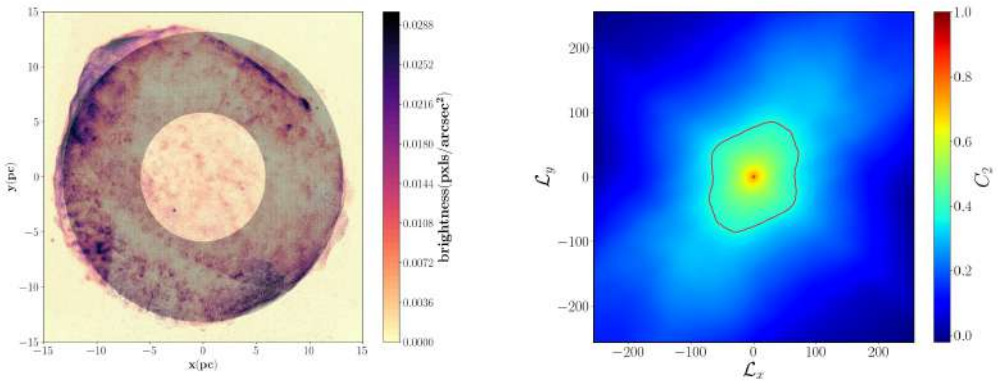

(A) (B)

FIGURE 3.26: (A) Brightness map distribution with the ring-shaped mask. (B) Autocorrelation function map applied on the ring-shaped region. The red solid line represents the autocorrelation lenght, namely the isocontour of $C_2 = 1/e$.

the shock normal is perpendicular to the mean magnetic field direction, while the shortest ones are located in the region in which the shock normal is parallel to the mean magnetic field direction. A further investigation will be done in the future, also because the results presented here are preliminary. We need to better study the brightness map and we have to extrapolate from it the density and also the magnetic field configurations.

3.4 Conclusions

In this Chapter we developed a preliminary work on the evolution of a SNR with the help of the MHD PLUTO code. Following previous works made by (Balsara, Benjamin, and Cox, 2001; Guo et al., 2012; Orlando et al., 2012; Fang and Zhang, 2012; Yu et al., 2015), we run a numerical simulation in which a SNR can expand in a turbulent and dense environment. We set 5 types of simulations, varying first the amplitude of the magnetic field fluctuations of the ISM and then varying the mass of the ejecta of the SNR. We analyzed in detail the simulation called Run 3, in which a SNR with $M_{ej} = 1.4 M_{\odot}$ is evolving inside an ISM with a level of fluctuations $\delta B/B = 1$. At the final time of the evolution of the SNR, i.e. 1000 years, that corresponds to the Sedov-Taylor phase for a SNR, we see the developing of the Rayleigh-Taylor instability in the CD region, i.e. the region between the FS and the RS. The presence of an high turbulent ambient allows the magnetic field to be amplified in particular in the regions perpendicular to the mean magnetic field direction. As a consequence, in the magnetic field map it is possible to observe the distortion of the shock surface resulting in the emergence of knots and filaments. From the calculation of the averaged energies we found that the magnetic field energy tends to increase with the simulation time, and the maximum value of the magnetic field gets enhanced by at least three orders of magnitude with respect to the initial one.

Almost the 54 % of the initial thermal energy is converted in kinetic energy of the expansion. In order to study the level of anisotropy due to the presence of a strong magnetic field, we applied a ring mask on the region between the RS and the FS on density and magnetic field maps. We found an isotropic configuration in the case of density map, while in the case of the magnetic field map we found a particular degree of anisotropy, especially in the region in which the FS normal is perpendicular to the direction of the mean magnetic field.
We have then made a comparison among three different simulations, in which we have changed the amplitude of the magnetic field fluctuations. While no significant variations are observed in the plasma quantities, the magnetic energy tends to increase as the $\delta B/B$ increases. Thus, we obtain a noticeable amplification of the magnetic field at the shock (mostly within the perpendicular region) as the ISM turbulence increases.
When we compared the simulations made with different mass values of the ejecta, slight changes appear. The radius of the SNR over a time corresponding to about 1000 years is smaller when the mass of the ejecta is higher, since it needs more time to swept away all the mass initially concentrated in the cilindrical inner core. Also, the Rayleigh-Taylor instability is inhibited within the CD. The magnetic field maps show again the effect of distortion of shock surfaces, also because we are in the presence of a high level of magnetic turbulence. When we tried to make a comparison between cuts we found in all cases a systematic behavior, namely that the values of each quantity is always lower when the ejecta mass is higher. The only exception is represented by the number density that in the case of $M_{ej} = 5M_{\odot}$ resulted the highest in the inner core of the SNR. The behavior just described has an impact also on the averaged energies. Indeed, the magnetic energy shows a similar trend among the runs, but the values of the magnetic energy are smaller when the ejecta mass is higher. The maximum value of $|\vec{B}|$ behaves in the same manner. Further, the kinetic energy increases with a slower rate as the mass of the ejecta increases and the thermal energy decreases slower as well. Since the mass of the ejecta swept-up by the inner core is higher for Run 5, it requires a greater kinetic energy in order to wipe out all the mass. This will result in a higher percentage of conversion of thermal energy into kinetic energy than in Run 3 and 4.
Finally, we tried to make a visual comparison between Chandra data of the SNR SN1006 and numerical simulations. From the brightness map it is clear that SN1006 has two main emission regions, located in the north-eastern side and in the south-western part. These regions are characterized by the emission of synchrotron radiation from the relativistic electrons that spiral along the magnetic field lines. We need to specify that in the case of the PLUTO simulations we do not take into account the cosmic ray feedback to the plasma. We actually plan to use the PIC version of the PLUTO code (Mignone et al., 2018a; Vaidya et al., 2018) to take into account the cosmic ray current in the plasma. From the cuts made at a fixed value of y and along x, within the X-ray brightest regions we observe a behavior of the Chandra

surface brightness similar to the trend of the plasma density captured in the simulations, which shows a peak close to the FS. We also tried to calculate the degree of anisotropy in the case of the Chandra observations. We found similar results to what we obtained from the autocorrelation map of the magnetic field in the simulation case. The highest values of the correlation length are located in the region in which the FS is perpendicular to the mean magnetic field direction. Since this is just a preliminary study, we aim at including other physical factors, such as the cosmic ray contribution in the energy conversion, in order to make the comparison with observations more quantitative.

Conclusions

In this thesis work different types of extreme events were analyzed. Since this category of events can be defined in different astrophysical and geophysical environments, it has been possible to study them with different approaches.
In the first Chapter, we presented the analysis of extreme temperature and rainfall in three different geographic areas. In particular, we applied the statistical analysis called EVT on the datasets available. We focused on three localized regions: the Antarctica, the Basilicata region and the Calabria region. In the case of Antarctica, we just focused on two stations in the region called "Antarctica peninsula", and we analyzed the extreme temperatures (maxima and minima) detected at the stations. The results obtained show a shift toward higher temperatures for both cases, thus indicating a local increase of temperatures. This behavior is not reproduced in all of the stations located of the Antarctica, because it is a local result. Other stations can show an inverse trend than what we saw for these two, as well as other can present similar results. In particular, the results obtained for the Antarctica peninsula can be influenced by other phenomena such as El Niño Southern oscillation. In the other two cases, namely the analysis for the extreme rainfall detected at the Basilicata stations and the analysis of both, extreme temperature and extreme rainfall, detetcted at the Calabria stations, we did a similar work. We chose to apply two different techniques in order to analyze the extreme data available. This choice was motivated by the nature of the signal that is quite different between temperature and rainfall. We found similar results in the case of extreme rainfall, for both regions. These results show a concentration of extreme events in the south-east of both regions (areas bordering the Ionian Sea), while in the case of extreme temperature analyzed just for the Calabria region, it is evident an opposite trend of extreme events with Tyrrhenian areas most affected by extreme daily temperatures and possible heatwaves. For the Calabria case, we also tried to do a reanalysis study with the help of the global climate monitoring dataset ERA5. Despite this tool allowed us to cover areas of the region in which there were no stations, from the comparison with the stations' data we found that ERA5 fields are not suitable for reproducing extreme values, because they show a systematic and substantial underestimation of both, daily precipitations and extreme temperatures. The analysis made with the EVT could help scientific community to better understand what are the regions most affected by warming and consequent loss of ice-mass (in the case of the Antarctica) and also, in more regional studies (as what we did for the Basilicata and Calabria regions), allowing the application of the statistical results obtained in regional land

planning, landslides and flood prediction and civil protection activities.
In the second part of the thesis, we focused on space weather extreme events. In particular we analyzed CMEs of slow velocities and the shock associated to them with the help of the 3D-MHD numerical code EUHFORIA. We used a catalogue of CMEs seen by the Coronagraph on-board STEREO spacecraft in order to model our CME in the simulation. We extrapolated the parameters needed to model the evolution of the CME candidate with the support of a specific tool (StereoCat). We also made a comparison with the ACE spacecraft data and we found a very good agreement between satellite data and numerical results. Interplanetary shocks, often associated to the CME evolution, have also been analyzed in this chapter. Since energetic particles are accelerated at IP shocks, we studied the transport properties related to their motion. In particular we concentrated on the superdiffusive mechanism, that allows particles to diffuse faster than the most invoked mechanism, i.e. DSA. We studied three different shock events detected by the ACE spacecraft and also in this case we resorted to using numerical simulations. We used a test-particle numerical code in order to reproduce the behavior of particle fluxes at IP shocks. From the comparison between numerical simulations and spacecraft data we found a good agreement between them, and this indicates that the most adapt transport regimes to describe the particle fluxes behavior, for these three specific shocks, is the superdiffusive one. In the final part of the chapter we analyzed a particular shock event in which the lower energy ion fluxes are overlapped in the upstream region. We tried to explain these observations with the velocity filter method. This method assumes that the velocity filter can depend on the particle speed and on the pitch-angle. In this way faster particles can propagate upstream while lower particles will remain more confined close to the shock. As a consequence, ion fluxes over different energy channels tend to overlap far upstream and the energy spectrum related to those particles will turn out flat. The analysis made in this chapter will be very useful in terms of extreme weather forecasting. Indeed, the use of numerical simulations can help to understand what are the impacts of abrupt eruptions, as CMEs, and what could be their effects on the Earth environment.
In the last part of the thesis we studied another category of phenomena included in the class of extreme events, the Supernova explosion. We studied it with the help of MHD numerical simulations. We set the environment in which the SNR expands as dense and turbulent, following the results obatained from spacecraft data analysis. We firstly fixed the ejecta mass equal to the Chandrasekhar mass limit, and we studied the results of the simulation in this case. We found that the effect of the presence of turbulence leads to the distortion of the shock surface with a consequent development of knots and filaments in these regions. The presence of a dense core leads, during the evolution, to the formation of structures related to the Rayleigh-Taylor instability. We calculated the rate of conversion of thermal energy, i.e. the initial energy of the explosion of the Supernova, into kinetic energy and we found that the 54 % of the thermal energy is converted into kinetic energy. We also tried

to analyze the degree of anisotropy due to the presence of a strong magnetic field. We found a high degree of anisotropy in the perpendicular direction of the mean magnetic field. In the second part of the Chapter, we developed different numerical simulations varying the turbulence level and the ejecta mass. From the comparison between the simulations with different level of magnetic field fluctuations, we found similar results, with the only exception related to the magnetic energy that results higher when we increase the turbulence level. When we compared the numerical simulations made varying the ejecta mass we found that the ejecta cannot be able to reach the same SNR radius reached in the original simulation. The inner core in this case is denser and the ejecta has to swept up a higher amount of mass that requires more time than the original case. Consequently, we found that the amount of energy needed to the inner core of a SNR to wipe out the mass is higher than the case of the lowest value of the ejecta mass, and this coresponds to a greater conversion of thermal energy into kinetic energy. Finally, we try to make a visual comparison between Chandra data of the SNR SN1006 and the numerical simulations. The map from spacecraft data shows two brighter regions located in the north-eastern and in the south-western region related to the synchrotron emission of electrons that spiral around the magnetic field lines. The cut made on the map shows a behavior similar to what we found from the numerical simulations. The same has been found in the case of the measure of the anisotropy degree. We found a similar behavior to what we have seen in the case of numerical simulations, with the highest values of the correlation length in the direction perpendicular to the mean magnetic field. We need to say that the work presented here it is just a preliminary work. We are developing 3D simulations, in order to better represent the evolution of a SNR and we will include the particle's contribution in order to try to reproduce a more realistic simulation.

Bibliography

Aharonian, F. A. et al. (Nov. 2004). "High-energy particle acceleration in the shell of a supernova remnant". In: *Nature* 432.7013, pp. 75–77. DOI: 10.1038/nature02960. arXiv: astro-ph/0411533 [astro-ph].

Al-Haddad, Nada et al. (Apr. 2018). "Fitting and Reconstruction of Thirteen Simple Coronal Mass Ejections". In: *Solar Physics* 293.5, p. 73. ISSN: 1573-093X. DOI: 10.1007/s11207-018-1288-3. URL: https://doi.org/10.1007/s11207-018-1288-3.

Alexandrova, O. et al. (Feb. 2008). "Small-Scale Energy Cascade of the Solar Wind Turbulence". In: *Astrophys. J.* 674.2, pp. 1153–1157.

Alpert, P. et al. (2002). "The paradoxical increase of Mediterranean extreme daily rainfall in spite of decrease in total values". In: *Geophysical Research Letters* 29.11, pp. 31–1–31–4. DOI: https://doi.org/10.1029/2001GL013554. eprint: https://agupubs.onlinelibrary.wiley.com/doi/pdf/10.1029/2001GL013554. URL: https://agupubs.onlinelibrary.wiley.com/doi/abs/10.1029/2001GL013554.

Amano, T. and M. Hoshino (May 2007). "Electron Injection at High Mach Number Quasi-perpendicular Shocks: Surfing and Drift Acceleration". In: *The Astrophysical Journal* 661.1, pp. 190–202. DOI: 10.1086/513599. arXiv: astro-ph/0612204 [astro-ph].

Amano, Takanobu and Masahiro Hoshino (Jan. 2009). "Electron Shock Surfing Acceleration in Multidimensions: Two-Dimensional Particle-in-Cell Simulation of Collisionless Perpendicular Shock". In: *The Astrophysical Journal* 690.1, pp. 244–251. DOI: 10.1088/0004-637X/690/1/244. arXiv: 0805.1098 [astro-ph].

Amato, Elena (2014a). "The origin of galactic cosmic rays". In: *International Journal of Modern Physics D* 23.07, p. 1430013.

— (2014b). "The origin of galactic cosmic rays". In: *International Journal of Modern Physics D* 23.07, p. 1430013.

Anderson, M. C. and L. Rudnick (Jan. 1996). "Sites of Relativistic Particle Acceleration in Supernova Remnant Cassiopeia A". In: *The Astrophysical Journal* 456, p. 234. DOI: 10.1086/176644.

Anisimov, O.A. et al. (2007). "Climate Change 2022: Impacts, Adaptation and Vulnerability". In: Cambridge, pp. 653–685.

Arge, Charles N. et al. (Sept. 2003). "Improved Method for Specifying Solar Wind Speed Near the Sun". In: *Solar Wind Ten*. Ed. by Marco Velli et al. Vol. 679. American Institute of Physics Conference Series, pp. 190–193. DOI: 10.1063/1.1618574.

Armstrong, J. W., J. M. Cordes, and B. J. Rickett (June 1981). "Density power spectrum in the local interstellar medium". In: 291.5816, pp. 561–564. DOI: 10.1038/291561a0.

Armstrong, J. W., B. J. Rickett, and S. R. Spangler (Apr. 1995). "Electron Density Power Spectrum in the Local Interstellar Medium". In: *The Astrophysical Journal* 443, p. 209. DOI: 10.1086/175515.

Artha, A A and A Sofro (2019). "Rainfall Prediction in East Java Using Spatial Extreme Value Theory". In: *Journal of Physics: Conference Series* 1417.1, p. 012010. DOI: 10.1088/1742-6596/1417/1/012010. URL: https://dx.doi.org/10.1088/1742-6596/1417/1/012010.

Avolio, E. et al. (2019). "Brief communication: Preliminary hydro-meteorological analysis of the flash flood of 20 August 2018 in Raganello Gorge, southern Italy". In: *Natural Hazards and Earth System Sciences* 19.8, pp. 1619–1627. DOI: 10.5194/nhess-19-1619-2019. URL: https://nhess.copernicus.org/articles/19/1619/2019/.

Avolio, Elenio and Stefano Federico (Mar. 2018). "WRF simulations for a heavy rainfall event in southern Italy: Verification and sensitivity tests". In: *Atmospheric Research* 209, pp. 14–35. DOI: 10.1016/j.atmosres.2018.03.009.

Balsara, Dinshaw, Robert A Benjamin, and Donald P Cox (2001). "The evolution of adiabatic supernova remnants in a turbulent, magnetized medium". In: *The Astrophysical Journal* 563.2, p. 800.

Balsara, Dinshaw S and Daniel S Spicer (1999). "A staggered mesh algorithm using high order Godunov fluxes to ensure solenoidal magnetic fields in magnetohydrodynamic simulations". In: *Journal of Computational Physics* 149.2, pp. 270–292.

Bamba, Aya et al. (2003). "Small-scale structure of the SN 1006 shock with Chandra observations". In: *The Astrophysical Journal* 589.2, p. 827.

Bandyopadhyay, Riddhi and David J McComas (2021). "Geometry of Magnetic Fluctuations near the Sun from the Parker Solar Probe". In: *The Astrophysical Journal* 923.2, p. 193.

Barbon, R., F. Ciatti, and L. Rosino (Feb. 1979). "Photometric properties of type II supernovae." In: *Astronomy and Astrophysics* 72, pp. 287–292.

Battista, Bradley Matthew et al. (2007). "Application of the empirical mode decomposition and Hilbert-Huang transform to seismic reflection data". In: *Geophysics* 72.2, H29–H37.

Beck, Rainer et al. (Jan. 1996). "Galactic Magnetism: Recent Developments and Perspectives". In: *Annual review of astronomy and astrophysics* 34, pp. 155–206. DOI: 10.1146/annurev.astro.34.1.155.

Bein, B. M. et al. (2011). "IMPULSIVE ACCELERATION OF CORONAL MASS EJECTIONS. I. STATISTICS AND CORONAL MASS EJECTION SOURCE REGION CHARACTERISTICS". In: *The Astrophysical Journal* 738.2, p. 191. DOI: 10.1088/0004-637X/738/2/191. URL: https://dx.doi.org/10.1088/0004-637X/738/2/191.

Bell, A. R. (Feb. 1978a). "The acceleration of cosmic rays in shock fronts - II." In: *Monthly Notices of the Royal Astronomical Society: Letters* 182, pp. 443–455. DOI: 10.1093/mnras/182.3.443.

— (Jan. 1978b). "The acceleration of cosmic rays in shock fronts. I". In: *Monthly Notices Royal Astron. Soc.* 182, pp. 147–156. DOI: 10.1093/mnras/182.2.147.

Bell, A. R. (Feb. 1978). "The acceleration of cosmic rays in shock fronts – I". In: *Monthly Notices of the Royal Astronomical Society* 182.2, pp. 147–156. ISSN: 0035-8711. DOI: 10.1093/mnras/182.2.147. eprint: https://academic.oup.com/mnras/article-pdf/182/2/147/3710138/mnras182-0147.pdf. URL: https://doi.org/10.1093/mnras/182.2.147.

Bell, AR (2004). "Turbulent amplification of magnetic field and diffusive shock acceleration of cosmic rays". In: *Monthly Notices of the Royal Astronomical Society* 353.2, pp. 550–558.

Berezhko, E. G. and H. J. Völk (May 2000). "Kinetic theory of cosmic ray and gamma-ray production in supernova remnants expanding into wind bubbles". In: *Astronomy & Astrophysics* 357, pp. 283–300. arXiv: astro-ph/0002411 [astro-ph].

Berezhko, E. G., V. K. Yelshin, and L. T. Ksenofontov (May 1994). "Numerical investigation of cosmic ray acceleration in supernova remnants". In: *Astroparticle Physics* 2.2, pp. 215–227. DOI: 10.1016/0927-6505(94)90043-4.

Besselaar, EJM Van den, AMG Klein Tank, and TA Buishand (2013). "Trends in European precipitation extremes over 1951–2010". In: *International Journal of Climatology* 33.12, pp. 2682–2689.

Bhatia, Udit and Auroop Ratan Ganguly (2019). "Precipitation extremes and depth-duration-frequency under internal climate variability". In: *Scientific reports* 9.1, p. 9112.

Blandford, R. D. and J. P. Ostriker (Apr. 1978). "Particle acceleration by astrophysical shocks." In: *The Astrophysical Journal Letters* 221, pp. L29–L32. DOI: 10.1086/182658.

Bocchialini, K. et al. (May 2018). "Statistical Analysis of Solar Events Associated with Storm Sudden Commencements over One Year of Solar Maximum During Cycle 23: Propagation from the Sun to the Earth and Effects". In: *Solar Physics* 293.5, 75, p. 75. DOI: 10.1007/s11207-018-1278-5. arXiv: 1803.07593 [astro-ph.SR].

Bodart, Julien A and R.J. Bingham (Dec. 2019). "The Impact of the Extreme 2015-16 El Niño on the Mass Balance of the Antarctic Ice Sheet". In: *Geophysical Research Letters* 46. DOI: 10.1029/2019GL084466.

Bonaccorso, Brunella and Giuseppe T. Aronica (2016). "Estimating Temporal Changes in Extreme Rainfall in Sicily Region (Italy)". In: *Water Resources Management* 30, 5651–5670. DOI: https://doi.org/10.1007/s11269-016-1442-3. URL: https://link.springer.com/article/10.1007/s11269-016-1442-3.

Brown, Simon J, J Caesar, and Christopher AT Ferro (2008). "Global changes in extreme daily temperature since 1950". In: *Journal of Geophysical Research: Atmospheres* 113.D5.

Brueckner, G.E. et al. (Dec. 1995). "The large angle spectroscopic coronagraph (LASCO)". In: *Solar Physics* 162, pp. 357–402. DOI: 10.1007/BF00733434.

Brunetti, Michele et al. (2001). "Trends in the daily intensity of precipitation in Italy from 1951 to 1996". In: *International Journal of Climatology* 21.3, pp. 299–316. DOI: https://doi.org/10.1002/joc.613. eprint: https://rmets.onlinelibrary.wiley.com/doi/pdf/10.1002/joc.613. URL: https://rmets.onlinelibrary.wiley.com/doi/abs/10.1002/joc.613.

Brunetti, Michele et al. (2004a). "Changes in daily precipitation frequency and distribution in Italy over the last 120 years". In: *Journal of Geophysical Research: Atmospheres* 109.D5. DOI: https://doi.org/10.1029/2003JD004296. URL: https://agupubs.onlinelibrary.wiley.com/doi/abs/10.1029/2003JD004296.

Brunetti, Michele et al. (2004b). "Temperature, precipitation and extreme events during the last century in Italy". In: *Global and Planetary Change* 40.1. Global Climate Changes during the Late Quaternary, pp. 141–149. ISSN: 0921-8181. DOI: https://doi.org/10.1016/S0921-8181(03)00104-8. URL: https://www.sciencedirect.com/science/article/pii/S0921818103001048.

Bruno, Roberto and Vincenzo Carbone (2005). "The Solar Wind as a Turbulence Laboratory". In: *Living Reviews in Solar Physics* 2.1, p. 4. ISSN: 1614-4961. DOI: 10.12942/lrsp-2005-4. URL: https://doi.org/10.12942/lrsp-2005-4.

Burgess, D. (Apr. 1995). *Introduction to Space Physics*. Edited by Margaret G. Kivelson and Christopher T. Russell, pp. 586. ISBN 0521451043. Cambridge, UK: Cambridge University Press, April 1995., p. 586.

Burke, Eleanor J, Richard HJ Perry, and Simon J Brown (2010). "An extreme value analysis of UK drought and projections of change in the future". In: *Journal of Hydrology* 388.1-2, pp. 131–143.

Burlaga, L. et al. (1981). "Magnetic loop behind an interplanetary shock: Voyager, Helios, and IMP 8 observations". In: *Journal of Geophysical Research: Space Physics* 86.A8, pp. 6673–6684. DOI: https://doi.org/10.1029/JA086iA08p06673. eprint: https://agupubs.onlinelibrary.wiley.com/doi/pdf/10.1029/JA086iA08p06673. URL: https://agupubs.onlinelibrary.wiley.com/doi/abs/10.1029/JA086iA08p06673.

Bykov, Andrei M., Donald C. Ellison, and Sergei M. Osipov (2017). "Nonlinear Monte Carlo model of superdiffusive shock acceleration with magnetic field amplification". In: *Phys. Rev. E* 95 (3), p. 033207. DOI: 10.1103/PhysRevE.95.033207. URL: https://link.aps.org/doi/10.1103/PhysRevE.95.033207.

Callahan, Christopher W. and Justin S. Mankin (2022). "Globally unequal effect of extreme heat on economic growth". In: *Science Advances* 8.43, eadd3726. DOI: 10.1126/sciadv.add3726. eprint: https://www.science.org/doi/pdf/10.1126/sciadv.add3726. URL: https://www.science.org/doi/abs/10.1126/sciadv.add3726.

Caloiero, T. et al. (July 2014). "Spatial and temporal characterization of climate at regional scale using homogeneous monthly precipitation and air temperature

data: an application in Calabria (southern Italy)". In: *Hydrology Research* 46.4, pp. 629–646. ISSN: 0029-1277. DOI: 10.2166/nh.2014.022. eprint: https://iwaponline.com/hr/article-pdf/46/4/629/369951/nh0460629.pdf. URL: https://doi.org/10.2166/nh.2014.022.

Caloiero, T. et al. (2017). "Trend analysis of monthly mean values and extreme indices of daily temperature in a region of southern Italy". In: *International Journal of Climatology* 37.S1, pp. 284–297. DOI: https://doi.org/10.1002/joc.5003. eprint: https://rmets.onlinelibrary.wiley.com/doi/pdf/10.1002/joc.5003. URL: https://rmets.onlinelibrary.wiley.com/doi/abs/10.1002/joc.5003.

Canfield, Ronand V et al. (1980). "Use of extreme value theory in estimating flood peaks from mixed populations". In.

Cannon, Alex J (2010). "A flexible nonlinear modelling framework for nonstationary generalized extreme value analysis in hydroclimatology". In: *Hydrological Processes: An International Journal* 24.6, pp. 673–685.

Capparelli, V., A. Vecchio, and V. Carbone (2011). "Long-range persistence of temperature records induced by long-term climatic phenomena". In: *Phys. Rev. E* 84 (4), p. 046103. DOI: 10.1103/PhysRevE.84.046103. URL: https://link.aps.org/doi/10.1103/PhysRevE.84.046103.

Capparelli, Vincenzo et al. (2013). "A spatiotemporal analysis of US station temperature trends over the last century". In: *Journal of Geophysical Research: Atmospheres* 118.14, pp. 7427–7434.

Caprioli, D. and A. Spitkovsky (2014). "SIMULATIONS OF ION ACCELERATION AT NON-RELATIVISTIC SHOCKS. I. ACCELERATION EFFICIENCY". In: *The Astrophysical Journal* 783.2, p. 91. DOI: 10.1088/0004-637X/783/2/91. URL: https://dx.doi.org/10.1088/0004-637X/783/2/91.

Caprioli, Damiano, Ana-Roxana Pop, and Anatoly Spitkovsky (Jan. 2015). "Simulations and Theory of Ion Injection at Non-relativistic Collisionless Shocks". In: *The Astrophysical Journal Letters* 798.2, L28, p. L28. DOI: 10.1088/2041-8205/798/2/L28. arXiv: 1409.8291 [astro-ph.HE].

Cecconi, B. et al. (2022). "Effect of an Interplanetary Coronal Mass Ejection on Saturn's Radio Emission". In: *Frontiers in Astronomy and Space Sciences* 9. ISSN: 2296-987X. DOI: 10.3389/fspas.2022.800279. URL: https://www.frontiersin.org/articles/10.3389/fspas.2022.800279.

Chandra, R. et al. (Jan. 2010). "How Can a Negative Magnetic Helicity Active Region Generate a Positive Helicity Magnetic Cloud?" In: *Solar Physics* 261.1, pp. 127–148. DOI: 10.1007/s11207-009-9470-2. arXiv: 0910.0968 [astro-ph.SR].

Chavez, Mario, Michael Ghil, and Jaime Urrutia-Fucugauchi (2015). "Extreme events: Observations, modeling, and economics". In: vol. 214. John Wiley & Sons.

Cheung, William W. L. et al. (2021). "Marine high temperature extremes amplify the impacts of climate change on fish and fisheries". In: *Science Advances* 7.40, eabh0895. DOI: 10.1126/sciadv.abh0895. eprint: https://www.science.org/

doi/pdf/10.1126/sciadv.abh0895. URL: https://www.science.org/doi/abs/10.1126/sciadv.abh0895.

Chevalier, R. A. (July 1982). "Self-similar solutions for the interaction of stellar ejecta with an external medium." In: *The Astrophysical Journal* 258, pp. 790–797. DOI: 10.1086/160126.

Chiu, M.C. et al. (1998). "ACE Spacecraft". In: *Space Science Reviews* 86.1. DOI: 10.1023/A:1005002013459. URL: https://doi.org/10.1023/A:1005002013459.

Cliver, E. W. and A. G. Ling (Jan. 2009). "Low-Frequency Type III Bursts and Solar Energetic Particle Events". In: *Astrophys. J.* 690.1, pp. 598–609. DOI: 10.1088/0004-637X/690/1/598.

Cliver, Edward W. et al. (2022). "Extreme solar events". In: *Living Reviews in Solar Physics* 19, p. 2. DOI: 10.1007/s41116-022-00033-8. URL: https://doi.org/10.1007/s41116-022-00033-8.

Coles, Stuart et al. (2001a). *An introduction to statistical modeling of extreme values*. Vol. 208. Springer.

— (2001b). *An introduction to statistical modeling of extreme values*. Vol. 208. Springer.

Compton, Arthur H. and Ivan A. Getting (June 1935). "An Apparent Effect of Galactic Rotation on the Intensity of Cosmic Rays". In: *Physical Review* 47.11, pp. 817–821.

Cooley, Daniel (Nov. 2009). "Extreme value analysis and the study of climate change: A commentary on Wigley 1988". In: *Climatic Change* 97, pp. 77–83. DOI: 10.1007/s10584-009-9627-x.

Correoso, Kiko (Nov. 2019). "skextremes Documentation". In: URL: https://readthedocs.org/projects/scikit-extremes/downloads/pdf/latest/.

Craigmile, Peter F and Peter Guttorp (2013). "Can a regional climate model reproduce observed extreme temperatures?" In: *Statistica* 73.1, pp. 103–122.

Cramer, Wolfgang et al. (2018). "Climate change and interconnected risks to sustainable development in the Mediterranean". In: *Nature Climate Change* 8. DOI: 10.1038/s41558-018-0299-2. URL: https://doi.org/10.1038/s41558-018-0299-2.

Dahan, Ely and Haim Mendelson (Jan. 2001). "An Extreme-Value Model of Concept Testing". In: *Management Science* 47, pp. 102–116. DOI: 10.1287/mnsc.47.1.102.10666.

Davies, E. E. et al. (2021). "In situ multi-spacecraft and remote imaging observations of the first CME detected by Solar Orbiter and BepiColombo". In: *A&A* 656, A2. DOI: 10.1051/0004-6361/202040113. URL: https://doi.org/10.1051/0004-6361/202040113.

Dawson, T.H. (2000). "Maximum Wave Crests in Heavy Seas." In: *Journal of Offshore Mechanics and arctic Engineering-Transactions of the AMSE* 122, pp. 222–224. URL: https://doi.org/10.1115/1.1287039.

Decker, R. B. et al. (Sept. 2005). "Voyager 1 in the Foreshock, Termination Shock, and Heliosheath". In: *Science* 309.5743, pp. 2020–2024. DOI: 10.1126/science.1117569.

— (July 2008). "Mediation of the solar wind termination shock by non-thermal ions". In: *Nature* 454.7200, pp. 67–70. DOI: 10.1038/nature07030.

Dosch, A. and A. Shalchi (2010). "Diffusive shock acceleration at interplanetary perpendicular shock waves: Influence of the large scale structure of turbulence on the maximum particle energy". In: *Advances in Space Research* 46.9, pp. 1208–1217. ISSN: 0273-1177. DOI: https://doi.org/10.1016/j.asr.2010.07.001. URL: https://www.sciencedirect.com/science/article/pii/S0273117710004588.

Drury, L. O. (Aug. 1983). "An introduction to the theory of diffusive shock acceleration of energetic particles in tenuous plasmas". In: *Reports on Progress in Physics* 46, pp. 973–1027. DOI: 10.1088/0034-4885/46/8/002.

Drury, L. O'C. and J. H. Voelk (Aug. 1981). "Hydromagnetic shock structure in the presence of cosmic rays". In: *The Astrophysical Journal* 248, pp. 344–351. DOI: 10.1086/159159.

Dunne J.F., Ghanbari M. (2001). "Efficient Extreme Value Prediction for Nonlinear Beam Vibrations Using Measured Random Response Histories." In: *Nonlinear Dynamics* 24, pp. 71–101. URL: https://doi.org/10.1023/A:1026531505091.

Echer, E., B. T. Tsurutani, and W. D. Gonzalez (2013). "Interplanetary origins of moderate (-100 nT < Dst $\leq$ -50 nT) geomagnetic storms during solar cycle 23 (1996–2008)". In: *Journal of Geophysical Research: Space Physics* 118.1, pp. 385–392. DOI: https://doi.org/10.1029/2012JA018086. eprint: https://agupubs.onlinelibrary.wiley.com/doi/pdf/10.1029/2012JA018086. URL: https://agupubs.onlinelibrary.wiley.com/doi/abs/10.1029/2012JA018086.

Echer, E. et al. (2008). "Interplanetary conditions causing intense geomagnetic storms (Dst ≤ -100 nT) during solar cycle 23 (1996–2006)". In: *Journal of Geophysical Research: Space Physics* 113.A5. DOI: https://doi.org/10.1029/2007JA012744. eprint: https://agupubs.onlinelibrary.wiley.com/doi/pdf/10.1029/2007JA012744. URL: https://agupubs.onlinelibrary.wiley.com/doi/abs/10.1029/2007JA012744.

Echeverria, JC et al. (2001). "Application of empirical mode decomposition to heart rate variability analysis". In: *Medical and Biological Engineering and Computing* 39.4, pp. 471–479.

Ellison, Donald C, Evgeny G Berezhko, and Matthew G Baring (2000). "Nonlinear shock acceleration and photon emission in supernova remnants". In: *The Astrophysical Journal* 540.1, p. 292.

Elvidge, Sean (2020). "Estimating the Occurrence of Geomagnetic Activity Using the Hilbert-Huang Transform and Extreme Value Theory". In: *Space Weather* 18.8. e2020SW002513 2020SW002513, e2020SW002513. DOI: https://doi.org/10.1029/2020SW002513. eprint: https://agupubs.onlinelibrary.wiley.com/doi/

pdf/10.1029/2020SW002513. URL: https://agupubs.onlinelibrary.wiley.com/doi/abs/10.1029/2020SW002513.

Elvidge, Sean and Matthew Angling (Apr. 2018). "Using Extreme Value Theory for Determining the Probability of Carrington-Like Solar Flares". In: *Space Weather* 16, pp. 417–421. DOI: 10.1002/2017SW001727.

Fang, Jun and Li Zhang (2012). "Two-dimensional magnetohydrodynamics simulations of young Type Ia supernova remnants". In: *Monthly Notices of the Royal Astronomical Society* 424.4, pp. 2811–2820.

Federico, S., C. Bellecci, and M. Colacino (2003). "Quantitative precipitation forecast of the Soverato flood: The role of orography and surface fluxes". English. In: *Nuovo cimento della Societa italiana di fisica. C, Geophysics and space physics*. ISSN: 1124-1896.

Federico, S. et al. (2008a). "Atmospheric patterns for heavy rain events in Calabria". In: *Natural Hazards and Earth System Sciences* 8.5, pp. 1173–1186. DOI: 10.5194/nhess-8-1173-2008. URL: https://nhess.copernicus.org/articles/8/1173/2008/.

Federico, S. et al. (2008b). "Numerical analysis of an intense rainstorm occurred in southern Italy". In: *Natural Hazards and Earth System Sciences* 8.1, pp. 19–35. DOI: 10.5194/nhess-8-19-2008. URL: https://nhess.copernicus.org/articles/8/19/2008/.

Federico, S. et al. (2010). "Brief communication "Calabria daily rainfall from 1970 to 2006"". In: *Natural Hazards and Earth System Sciences* 10.4, pp. 717–722. DOI: 10.5194/nhess-10-717-2010. URL: https://nhess.copernicus.org/articles/10/717/2010/.

Federico, Stefano et al. (Dec. 2009). "Preliminary results of a 30-year daily rainfall data base in southern Italy". In: *Atmospheric Research* 94, pp. 641–651. DOI: 10.1016/j.atmosres.2009.03.008.

Filippenko, Alexei V. (Dec. 1988). "Supernova 1987K: Type II in Youth, Type Ib in Old Age". In: *Astronomical Journal* 96, p. 1941. DOI: 10.1086/114940.

Fischer, E. and R. Knutti (2016). "Observed heavy precipitation increase confirms theory and early models". In: *Nature Climate Change* 6, 986–991. DOI: https://doi.org/10.1038/nclimate3110.

Fischer, Erich, Sebastian Sippel, and Reto Knutti (Aug. 2021). "Increasing probability of record-shattering climate extremes". In: *Nature Climate Change* 11. DOI: 10.1038/s41558-021-01092-9.

Fisher, R. A. and L. H. C. Tippett (1928). "Limiting forms of the frequency distribution of the largest or smallest member of a sample". In: *Mathematical Proceedings of the Cambridge Philosophical Society* 24.2, 180–190. DOI: 10.1017/S0305004100015681.

Forman, M. A. and G. E. Morfill (1979). "Time-Dependent Acceleration of Solar Wind Plasma to Mev Energies at Corotating Interplanetary Shocks". In: *International Cosmic Ray Conference* 5, p. 328.

Fowler, HJ et al. (2005). "New estimates of future changes in extreme rainfall across the UK using regional climate model integrations. 1. Assessment of control climate". In: *Journal of Hydrology* 300.1-4, pp. 212–233.

Fuller, W. A. (1976). "Introduction to Statistical Time Series". In: vol. 373. John Wiley and Sons.

Genthon, Christophe et al. (Dec. 2011). "Atmospheric Temperature Measurement Biases on the Antarctic Plateau". In: *Journal of Atmospheric and Oceanic Technology* 28, pp. 1598–1605. DOI: 10.1175/JTECH-D-11-00095.1.

Giacalone, J. (Dec. 2012). "Energetic Charged Particles Associated with Strong Interplanetary Shocks". In: *Astrophysical Journal* 761, 28, p. 28. DOI: 10.1088/0004-637X/761/1/28.

Giacalone, J. and J. R. Jokipii (July 1999). "The Transport of Cosmic Rays across a Turbulent Magnetic Field". In: *The Astrophysical Journal* 520, pp. 204–214. DOI: 10.1086/307452.

Giacalone, J. and J. R. Jokipii (2007). "Magnetic Field Amplification by Shocks in Turbulent Fluids". In: *The Astrophysical Journal* 663.1, p. L41. DOI: 10.1086/519994. URL: https://dx.doi.org/10.1086/519994.

Giacalone, J. et al. (1992). "Hybrid simulations of protons strongly accelerated by a parallel collisionless shock". In: *Geophysical Research Letters* 19.5, pp. 433–436. DOI: https://doi.org/10.1029/92GL00379. eprint: https://agupubs.onlinelibrary.wiley.com/doi/pdf/10.1029/92GL00379. URL: https://agupubs.onlinelibrary.wiley.com/doi/abs/10.1029/92GL00379.

Giacalone, Joe (2013). "Cosmic-ray transport and interaction with shocks". In: *Space Science Reviews* 176.1-4, pp. 73–88.

Giacalone, Joe and Donald C. Ellison (2000). "Three-dimensional numerical simulations of particle injection and acceleration at quasi-perpendicular shocks". In: *Journal of Geophysical Research: Space Physics* 105.A6, pp. 12541–12556. DOI: https://doi.org/10.1029/1999JA000018. eprint: https://agupubs.onlinelibrary.wiley.com/doi/pdf/10.1029/1999JA000018. URL: https://agupubs.onlinelibrary.wiley.com/doi/abs/10.1029/1999JA000018.

Giorgi, F., F. Raffaele, and E. Coppola (2019). "The response of precipitation characteristics to global warming from climate projections". In: *Earth System Dynamics* 10.1, pp. 73–89. DOI: 10.5194/esd-10-73-2019. URL: https://esd.copernicus.org/articles/10/73/2019/.

Giorgi, F. et al. (Jan. 2001). "Regional Climate Information – Evaluation and Projections". In.

Giuffrida, Roberta et al. (2022). "The supernova remnant SN 1006 as a Galactic particle accelerator". In: *Nature Communications* 13.1, p. 5098.

Gnedenko, B. (1943). "Sur La Distribution Limite Du Terme Maximum D'Une Serie Aleatoire". In: *Annals of Mathematics* 44.3, pp. 423–453. ISSN: 0003486X. URL: http://www.jstor.org/stable/1968974.

Gold, R. E. et al. (July 1998). "Electron, Proton, and Alpha Monitor on the Advanced Composition Explorer spacecraft". In: *Space Science Reviews* 86, pp. 541–562.

Gopalswamy, N. et al. (Jan. 2004). "Variability of solar eruptions during cycle 23". In: *Advances in Space Research* 34.2, pp. 391–396. DOI: 10.1016/j.asr.2003.10.054.

Gopalswamy, Nat (2022). "The Sun and Space Weather". In: *Atmosphere* 13.11. ISSN: 2073-4433. DOI: 10.3390/atmos13111781. URL: https://www.mdpi.com/2073-4433/13/11/1781.

Gopalswamy, Nat et al. (Apr. 2009). "The SOHO/LASCO CME catalog". In: *Earth Moon and Planets* 104, pp. 295–313. DOI: 10.1007/s11038-008-9282-7.

Gosling, J. T. and D. J. McComas (1987). "Field line draping about fast coronal mass ejecta: A source of strong out-of-the-ecliptic interplanetary magnetic fields". In: *Geophysical Research Letters* 14.4, pp. 355–358. DOI: https://doi.org/10.1029/GL014i004p00355. eprint: https://agupubs.onlinelibrary.wiley.com/doi/pdf/10.1029/GL014i004p00355. URL: https://agupubs.onlinelibrary.wiley.com/doi/abs/10.1029/GL014i004p00355.

Gosling, J. T. et al. (1991). "Geomagnetic activity associated with earth passage of interplanetary shock disturbances and coronal mass ejections". In: *Journal of Geophysical Research: Space Physics* 96.A5, pp. 7831–7839. DOI: https://doi.org/10.1029/91JA00316. eprint: https://agupubs.onlinelibrary.wiley.com/doi/pdf/10.1029/91JA00316. URL: https://agupubs.onlinelibrary.wiley.com/doi/abs/10.1029/91JA00316.

Grechnev, V. V. et al. (Jan. 2015). "Responsibility of a Filament Eruption for the Initiation of a Flare, CME, and Blast Wave, and its Possible Transformation into a Bow Shock". In: *Sol. Phys.* 290.1, pp. 129–158. DOI: 10.1007/s11207-014-0621-8. arXiv: 1410.8696 [astro-ph.SR].

Greco, A. et al. (June 2016). "The Complex Structure of Magnetic Field Discontinuities in the Turbulent Solar Wind". In: *Astrophys. J. Lett.* 823.2, L39, p. L39.

Greco, Aldo, Davide Luciano De Luca, and Elenio Avolio (2020). "Heavy Precipitation Systems in Calabria Region (Southern Italy): High-Resolution Observed Rainfall and Large-Scale Atmospheric Pattern Analysis". In: *Water* 12.5. ISSN: 2073-4441. DOI: 10.3390/w12051468. URL: https://www.mdpi.com/2073-4441/12/5/1468.

Greenstadt, E. W. et al. (Feb. 1975). "Structure of the quasi-perpendicular laminar bow shock". In: *J. Geophys. Res.* 80.4, p. 502.

Greenwald, R. A. et al. (1995). "Super dual auroral radar network radar imaging of dayside high-latitude convection under northward interplanetary magnetic field: Toward resolving the distorted two-cell versus multicell controversy". In: *Journal of Geophysical Research: Space Physics* 100.A10, pp. 19661–19674. DOI: https://doi.org/10.1029/95JA01215. eprint: https://agupubs.onlinelibrary.wiley.com/doi/pdf/10.1029/95JA01215. URL: https://agupubs.onlinelibrary.wiley.com/doi/abs/10.1029/95JA01215.

Gumbel, E. J. (1958). *Statistics of Extremes*. Columbia University Press. DOI: doi:10.7312/gumb92958. URL: https://doi.org/10.7312/gumb92958.

Guo, Fan et al. (2012). "On the amplification of magnetic field by a supernova blast shock wave in a turbulent medium". In: *The Astrophysical Journal* 747.2, p. 98.

Han, J. L., K. Ferriere, and R. N. Manchester (Aug. 2004). "The Spatial Energy Spectrum of Magnetic Fields in Our Galaxy". In: *The Astrophysical Journal* 610.2, pp. 820–826. DOI: 10.1086/421760. arXiv: astro-ph/0404221 [astro-ph].

Hanson, CE et al. (2007). "Modelling the impact of climate extremes: an overview of the MICE project". In: *Climatic change* 81, pp. 163–177.

Harrington, Luke J et al. (2016). "Poorest countries experience earlier anthropogenic emergence of daily temperature extremes". In: *Environmental Research Letters* 11.5, p. 055007. DOI: 10.1088/1748-9326/11/5/055007. URL: https://dx.doi.org/10.1088/1748-9326/11/5/055007.

Harris, Raymond (Feb. 2001). "The accuracy of design values predicted from extreme value analysis". In: *Journal of Wind Engineering and Industrial Aerodynamics - J WIND ENG IND AERODYN* 89, pp. 153–164. DOI: 10.1016/S0167-6105(00)00060-X.

Hawcroft, Matt et al. (2018). "Significantly increased extreme precipitation expected in Europe and North America from extratropical cyclones". In: *Environmental Research Letters* 13, p. 124006. DOI: https://doi.org/10.1088/1748-9326/aaed59.

Helder, E. A. et al. (2012). "Observational Signatures of Particle Acceleration in Supernova Remnants". In: *Space Science Reviews* 173.1-4, pp. 369–431. DOI: 10.1007/s11214-012-9919-8.

Henry, Curt (July 2002). "An Introduction to the Design of the Cassini Spacecraft". In: *Space Science Reviews* 104, pp. 129–153. DOI: 10.1023/A:1023696808894.

Hersbach, Hans et al. (2020). "The ERA5 global reanalysis". In: *Quarterly Journal of the Royal Meteorological Society* 146.730, pp. 1999–2049. DOI: https://doi.org/10.1002/qj.3803. eprint: https://rmets.onlinelibrary.wiley.com/doi/pdf/10.1002/qj.3803. URL: https://rmets.onlinelibrary.wiley.com/doi/abs/10.1002/qj.3803.

Horbury, Timothy S, Miriam Forman, and Sean Oughton (2008). "Anisotropic scaling of magnetohydrodynamic turbulence". In: *Physical Review Letters* 101.17, p. 175005.

Howard, R. A. et al. (Apr. 2008). "Sun Earth Connection Coronal and Heliospheric Investigation (SECCHI)". In: *Space Science Review* 136.1-4, pp. 67–115. DOI: 10.1007/s11214-008-9341-4.

Hu, Guannan and Christian L. E. Franzke (2020). "Evaluation of Daily Precipitation Extremes in Reanalysis and Gridded Observation-Based Data Sets Over Germany". In: *Geophysical Research Letters* 47.18. e2020GL089624 10.1029/2020GL089624, e2020GL089624. DOI: https://doi.org/10.1029/2020GL089624. eprint: https://agupubs.onlinelibrary.wiley.com/doi/pdf/10.1029/2020GL089624.

URL: https://agupubs.onlinelibrary.wiley.com/doi/abs/10.1029/2020GL089624.

Huang, Norden E et al. (1998). "The empirical mode decomposition and the Hilbert spectrum for nonlinear and non-stationary time series analysis". In: *Proceedings of the Royal Society of London. Series A: mathematical, physical and engineering sciences* 454.1971, pp. 903–995.

Huang, Whitney K et al. (2016). "Estimating changes in temperature extremes from millennial-scale climate simulations using generalized extreme value (GEV) distributions". In: *Advances in Statistical Climatology, Meteorology and Oceanography* 2.1, pp. 79–103.

Huo, Ran et al. (2021). "Extreme Precipitation Changes in Europe from the Last Millennium to the End of the Twenty-First Century". In: *Journal of Climate* 34.2, pp. 567 –588. DOI: 10.1175/JCLI-D-19-0879.1.

IPCC (2012). "Managing the risks of extreme events and disasters to advance climate change adaptation. A Special Report of Working Groups I and II of the Intergovernmental Panel on Climate Change." In: Cambridge, UK and New York, USA: Cambridge University Press.

— (2022). "Climate Change 2022: Impacts, Adaptation and Vulnerability". In: Summary for Policymakers. Cambridge, UK and New York, USA: Cambridge University Press, pp. 3–33. ISBN: 9781009325844.

Isavnin, A. (Dec. 2016). "FRiED: A Novel Three-dimensional Model of Coronal Mass Ejections". In: *The Astrophysical Journal* 833.2, 267, p. 267. DOI: 10.3847/1538-4357/833/2/267. arXiv: 1703.01659 [physics.space-ph].

Iyamuremye, Emmanuel, Samson Wanyonyi, and Drinold Mbete (Mar. 2019). "Analysis and Modelling of Extreme Rainfall: A Case Study for Dodoma, Tanzania". In: *Asian Journal of Mathematics & Statistics* 3, pp. 1–29. DOI: 10.9734/ajpas/2019/v3i230086.

Jakosky, Bruce et al. (Jan. 2015). "The Mars Atmosphere and Volatile Evolution (MAVEN) Mission". In: *Space Science Reviews*.

Jenkinson, AF (1969). "Statistics of extremes". In: *Estimation of maximum floods, WMO* 233, pp. 183–228.

Jenkinson, Arthur F (1955). "The frequency distribution of the annual maximum (or minimum) values of meteorological elements". In: *Quarterly Journal of the Royal Meteorological Society* 81.348, pp. 158–171.

Jones, Megan et al. (July 2019). "Sixty Years of Widespread Warming in the Southern Mid- and High-Latitudes (1957-2016)". In: *Journal of Climate* 32. DOI: 10.1175/JCLI-D-18-0565.1.

Kaiser, M. L. et al. (2008). "The STEREO Mission: An Introduction". In: *Space Science Reviews* 136, p. 5. DOI: 10.1007/s11214-007-9277-0. URL: https://doi.org/10.1007/s11214-007-9277-0.

Kang, H., D. Ryu, and T. W. Jones (Sept. 2012). "Diffusive Shock Acceleration Simulations of Radio Relics". In: *Astrophysical Journal* 756, 97, p. 97. DOI: 10.1088/0004-637X/756/1/97. arXiv: 1205.1895 [astro-ph.HE].

Karimabadi, H. et al. (June 2014). "The link between shocks, turbulence, and magnetic reconnection in collisionless plasmas". In: *Physics of Plasmas* 21.6, 062308, p. 062308.

Katz, R W and B G Brown (1992). "Extreme events in a changing climate: variability is more important than averages". In: *Climatic Change* 21:3. DOI: 10.1007/BF00139728.

Katz, Richard W (2010). "Statistics of extremes in climate change". In: *Climatic change* 100.1, pp. 71–76.

Kawas, Marie Louise and Rosana G Moreira (2001). "Characterization of product quality attributes of tortilla chips during the frying process". In: *Journal of Food Engineering* 47.2, pp. 97–107. ISSN: 0260-8774. DOI: https://doi.org/10.1016/S0260-8774(00)00104-7. URL: https://www.sciencedirect.com/science/article/pii/S0260877400001047.

Kilpua, E. K. J., Hannu E. J. Koskinen, and Tuija I. Pulkkinen (2017). "Coronal mass ejections and their sheath regions in interplanetary space". In: *Living Reviews in Solar Physics* 14, pp. 1614–4961. DOI: 10.1007/s41116-017-0009-6. URL: https://doi.org/10.1007/s41116-017-0009-6.

Kilpua, E. K. J. et al. (Feb. 2009). "Multispacecraft Observations of Magnetic Clouds and Their Solar Origins between 19 and 23 May 2007". In: *Solar Physics* 254.2, pp. 325–344. DOI: 10.1007/s11207-008-9300-y.

Kilpua, E. K. J. et al. (July 2013). "On the relationship between interplanetary coronal mass ejections and magnetic clouds". In: *Annales Geophysicae* 31.7, pp. 1251–1265. DOI: 10.5194/angeo-31-1251-2013.

Kilpua, E. K. J. et al. (2017). "Geoeffective Properties of Solar Transients and Stream Interaction Regions". In: *Space Science Reviews* 212, pp. 1572–9672. DOI: 10.1007/s11214-017-0411-3. URL: https://doi.org/10.1007/s11214-017-0411-3.

King, AD et al. (2015). "The timing of anthropogenic emergence in simulated climate extremes". In: 10.9. ISSN: 1748-9318. URL: http://handle.unsw.edu.au/1959.4/unsworks_36611.

Kirk, J. G., P. Duffy, and Y. A. Gallant (Oct. 1996). "Stochastic particle acceleration at shocks in the presence of braided magnetic fields." In: *Astron. Astrophys.* 314, pp. 1010–1016. eprint: astro-ph/9604056.

Klafter, J., A. Blumen, and M. F. Shlesinger (Apr. 1987). "Stochastic pathway to anomalous diffusion". In: *Physical Review A* 35, pp. 3081–3085. DOI: 10.1103/PhysRevA.35.3081.

Klein, L. W. and L. F. Burlaga (1982). "Interplanetary magnetic clouds At 1 AU". In: *Journal of Geophysical Research: Space Physics* 87.A2, pp. 613–624. DOI: https://doi.org/10.1029/JA087iA02p00613. eprint: https://agupubs.onlinelibrary.

wiley.com/doi/pdf/10.1029/JA087iA02p00613. URL: https://agupubs.onlinelibrary.wiley.com/doi/abs/10.1029/JA087iA02p00613.

Koval, A. and A. Szabo (2008). "Modified "Rankine-Hugoniot" shock fitting technique: Simultaneous solution for shock normal and speed". In: *Journal of Geophysical Research: Space Physics* 113.A10. DOI: https://doi.org/10.1029/2008JA013337. eprint: https://agupubs.onlinelibrary.wiley.com/doi/pdf/10.1029/2008JA013337. URL: https://agupubs.onlinelibrary.wiley.com/doi/abs/10.1029/2008JA013337.

Koyama, Katsuji et al. (1995). "Evidence for shock acceleration of high-energy electrons in the supernova remnant SN1006". In: *Nature* 378.6554, pp. 255–258.

Krause, Oliver et al. (2008). "The Cassiopeia A Supernova Was of Type IIb". In: *Science* 320.5880, pp. 1195–1197. DOI: 10.1126/science.1155788. URL: https://doi.org/10.1126\%2Fscience.1155788.

Krymskii, G. F. (June 1977). "A regular mechanism for the acceleration of charged particles on the front of a shock wave". In: *Akademiia Nauk SSSR Doklady* 234, pp. 1306–1308.

Lapenta, G. et al. (Jan. 2020). "Local Regimes of Turbulence in 3D Magnetic Reconnection". In: *The Astrophysical Journal* 888.2, 104, p. 104. DOI: 10.3847/1538-4357/ab5a86. arXiv: 1910.12067 [astro-ph.SR].

Lario, D. et al. (Oct. 2018). "Flat Proton Spectra in Large Solar Energetic Particle Events". In: *Journal of Physics Conference Series*. Vol. 1100. Journal of Physics Conference Series, 012014, p. 012014. DOI: 10.1088/1742-6596/1100/1/012014.

Lario, D. et al. (July 2019). "Evolution of the Suprathermal Proton Population at Interplanetary Shocks". In: *The Astronomical Journal* 158.1, 12, p. 12. DOI: 10.3847/1538-3881/ab1e49.

Lario, D. et al. (Feb. 2022). "The Extended Field-aligned Suprathermal Proton Beam and Long-lasting Trapped Energetic Particle Population Observed Upstream of a Transient Interplanetary Shock". In: *Astrophys. J.* 925.2, 198, p. 198.

Larrodera, C., L. Nikitina, and C. Cid (2021). "Estimation of the Solar Wind Extreme Events". In: *Space Weather* 19.12. e2021SW002902 2021SW002902, e2021SW002902. DOI: https://doi.org/10.1029/2021SW002902. eprint: https://agupubs.onlinelibrary.wiley.com/doi/pdf/10.1029/2021SW002902. URL: https://agupubs.onlinelibrary.wiley.com/doi/abs/10.1029/2021SW002902.

Lavenda, B.H. and E. Cipollone (2000). "Extreme Value Statistics and Thermodynamics of Earthquakes: Aftershock Sequences." In: *Annali di geofisica* 43, pp. 967–982.

le Roux, J. A. and G. M. Webb (Feb. 2012). "A Focused Transport Approach to the Time-dependent Shock Acceleration of Solar Energetic Particles at a Fast Traveling Shock". In: *The Astrophysical Journal* 746.1, 104, p. 104.

Lee, L. C. and J. R. Jokipii (June 1976). "The irregularity spectrum in interstellar space." In: *The Astrophysical Journal* 206, pp. 735–743. DOI: 10.1086/154434.

Lee, M. A. and L. A. Fisk (Mar. 1982). "Shock acceleration of energetic particles in the heliosphere". In: *Space Science Reviews* 32.205, p. 228. ISSN: 1572-9672. DOI: 10.1007/BF00225185. URL: https://doi.org/10.1007/BF00225185.

Lee, M. A. and L. A. Fisk (Mar. 1982). "Shock acceleration of energetic particles in the heliosphere". In: *Space Sci. Rev.* 32, pp. 205–228. DOI: 10.1007/BF00225185.

Lemen, James R. et al. (Jan. 2012). "The Atmospheric Imaging Assembly (AIA) on the Solar Dynamics Observatory (SDO)". In: *Solar Physics* 275.1-2, pp. 17–40. DOI: 10.1007/s11207-011-9776-8.

Lemos, Iago, A.M.G. Lima, and Marcus Duarte (Feb. 2020a). "thresholdmodeling: A Python package for modeling excesses over a threshold using the Peak-Over-Threshold Method and the Generalized Pareto Distribution". In: *Journal of Open Source Software* 5, p. 2013. DOI: 10.21105/joss.02013.

— (Feb. 2020b). "thresholdmodeling: A Python package for modeling excesses over a threshold using the Peak-Over-Threshold Method and the Generalized Pareto Distribution". In: *Journal of Open Source Software* 5, p. 2013. DOI: 10.21105/joss.02013.

Li, Hui and Yang Chen (2012). "γ-rays from molecular clouds illuminated by accumulated diffusive protons–II. Interacting supernova remnants". In: *Monthly Notices of the Royal Astronomical Society* 421.2, pp. 935–942. DOI: 10.1111/j.1365-2966.2012.20270.x. URL: https://doi.org/10.1111\%2Fj.1365-2966.2012.20270.x.

Lim, Young-Kwon and Siegfried D Schubert (2011). "The impact of ENSO and the Arctic Oscillation on winter temperature extremes in the southeast United States". In: *Geophysical research letters* 38.15.

Lin, R. P. (Jan. 2005). "Relationship of solar flare accelerated particles to solar energetic particles (SEPs) observed in the interplanetary medium". In: *Advances in Space Research* 35.10, pp. 1857–1863. DOI: 10.1016/j.asr.2005.02.087.

Lin, R. P. et al. (Feb. 1995). "A Three-Dimensional Plasma and Energetic Particle Investigation for the Wind Spacecraft". In: *Space Science Reviews* 71.1-4, pp. 125–153. DOI: 10.1007/BF00751328.

Lin, RP (1974). "Non-relativistic solar electrons". In: *Space Science Reviews* 16.1-2, pp. 189–256.

Linan, L. et al. (Sept. 2018). "Time Variations of the Nonpotential and Volume-threading Magnetic Helicities". In: *The Astrophysical Journal* 865.1, 52, p. 52. DOI: 10.3847/1538-4357/aadae7. arXiv: 1809.03765 [astro-ph.SR].

Linan, L. et al. (Apr. 2020). "Energy and helicity fluxes in line-tied eruptive simulations". In: *Astronomy and Astrophysics* 636, A41, A41. DOI: 10.1051/0004-6361/202037548. arXiv: 2003.01698 [astro-ph.SR].

Lionello, P., P. Malanotte-Rizzoli, and R. Boscolo (2006). *Mediterranean Climate Variability*. Elsevier. ISBN: 9780080460796. URL: https://www.elsevier.com/books/mediterranean-climate-variability/lionello/978-0-444-52170-5.

Lionello, Piero and Luca Scarascia (2018). "The relation between climate change in the Mediterranean region and global warming". In: *Regional Environmental Change* 18. DOI: 10.1007/s10113-018-1290-1. URL: https://doi.org/10.1007/s10113-018-1290-1.

Londrillo, P. and L. Del Zanna (Mar. 2004). "On the divergence-free condition in Godunov-type schemes for ideal magnetohydrodynamics: the upwind constrained transport method". In: *Journal of Computational Physics* 195.1, pp. 17–48. DOI: 10.1016/j.jcp.2003.09.016. arXiv: astro-ph/0310183 [astro-ph].

Longden, Thomas et al. (Jan. 2022). "Energy insecurity during temperature extremes in remote Australia". In: *Nature Energy* 7, pp. 1–12. DOI: 10.1038/s41560-021-00942-2.

Lu, Quanming, Qiang Hu, and Gary P Zank (2009). "The interaction of Alfvén waves with perpendicular shocks". In: *The Astrophysical Journal* 706.1, p. 687.

Maharana, Anwesha et al. (Sept. 2022). "Implementation and validation of the FRi3D flux rope model in EUHFORIA". In: *Advances in Space Research* 70.6, pp. 1641–1662. DOI: 10.1016/j.asr.2022.05.056. arXiv: 2207.06707 [astro-ph.SR].

Mahlstein, Irina et al. (July 2011). "Early onset of significant local warming in low latitude countries". In: *Environmental Research Letters* 6, p. 034009. DOI: 10.1088/1748-9326/6/3/034009.

Marty, Christoph and Juliette Blanchet (2012). "Long-term changes in annual maximum snow depth and snowfall in Switzerland based on extreme value statistics". In: *Climatic Change* 111, pp. 705–721.

Masías-Meza, J. J. et al. (Aug. 2016). "Superposed epoch study of ICME sub-structures near Earth and their effects on Galactic cosmic rays". In: *Astronomy & Astrophysics* 592, A118. DOI: 10.1051/0004-6361/201628571. URL: https://doi.org/10.1051/0004-6361/201628571.

Matthaeus, William H, Melvyn L Goldstein, and D Aaron Roberts (1990). "Evidence for the presence of quasi-two-dimensional nearly incompressible fluctuations in the solar wind". In: *Journal of Geophysical Research: Space Physics* 95.A12, pp. 20673–20683.

Mays, M. L. et al. (June 2015). "Ensemble Modeling of CMEs Using the WSA-ENLIL+Cone Model". In: *Solar Physics* 290.6, pp. 1775–1814. DOI: 10.1007/s11207-015-0692-1. arXiv: 1504.04402 [astro-ph.SR].

McComas, D. J. et al. (July 1998). "Solar Wind Electron Proton Alpha Monitor (SWEPAM) for the Advanced Composition Explorer". In: *Space Science Review* 86, pp. 563–612.

McNulty, P.J. et al. (2000). "First failure predictions for EPROMs of the type flown on the MPTB satellite". In: *IEEE Transactions on Nuclear Science* 47.6, pp. 2237–2243. DOI: 10.1109/23.903759.

Meehl, Gerald A. and Claudia Tebaldi (2004). "More Intense, More Frequent, and Longer Lasting Heat Waves in the 21st Century". In: *Science* 305.5686, pp. 994–997. DOI: 10.1126/science.1098704. eprint: https://www.science.org/doi/

pdf/10.1126/science.1098704. URL: https://www.science.org/doi/abs/10.1126/science.1098704.

Menvielle, M. et al. (2007). "A new method for studying the thermospheric density variability derived from CHAMP/STAR accelerometer data for magnetically active conditions". In: *Annales Geophysicae* 25.9, pp. 1949–1958. DOI: 10.5194/angeo-25-1949-2007. URL: https://angeo.copernicus.org/articles/25/1949/2007/.

Menvielle, Michel et al. (Dec. 2010). "Geomagnetic Indices". In: vol. 5, pp. 183–228. ISBN: 978-90-481-9857-3. DOI: 10.1007/978-90-481-9858-0_8.

Meringolo, Claudio, Sergio Servidio, and Pierluigi Veltri (2021). "A spectral method algorithm for numerical simulations of gravitational fields". In: *Classical and Quantum Gravity* 38.7, p. 075027.

Mignone, A. et al. (May 2007). "PLUTO: A Numerical Code for Computational Astrophysics". In: *The Astrophysical Journal Supplement Series* 170.1, pp. 228–242. DOI: 10.1086/513316. arXiv: astro-ph/0701854 [astro-ph].

Mignone, A. et al. (2011a). "THE PLUTO CODE FOR ADAPTIVE MESH COMPUTATIONS IN ASTROPHYSICAL FLUID DYNAMICS". In: *The Astrophysical Journal Supplement Series* 198.1, p. 7. DOI: 10.1088/0067-0049/198/1/7. URL: https://dx.doi.org/10.1088/0067-0049/198/1/7.

Mignone, A et al. (2018a). "A particle module for the pluto code. I. An implementation of the MHD–PIC equations". In: *The Astrophysical Journal* 859.1, p. 13.

Mignone, A. et al. (2018b). "A Particle Module for the PLUTO Code. I. An Implementation of the MHD–PIC Equations". In: *The Astrophysical Journal* 859.1, p. 13. DOI: 10.3847/1538-4357/aabccd. URL: https://dx.doi.org/10.3847/1538-4357/aabccd.

Mignone, Andrea and Petros Tzeferacos (2010). "A second-order unsplit Godunov scheme for cell-centered MHD: The CTU-GLM scheme". In: *Journal of Computational Physics* 229.6, pp. 2117–2138.

Mignone, Andrea, Petros Tzeferacos, and Gianluigi Bodo (2010). "High-order conservative finite difference GLM–MHD schemes for cell-centered MHD". In: *Journal of Computational Physics* 229.17, pp. 5896–5920.

Mignone, Andrea et al. (2007). "PLUTO: a numerical code for computational astrophysics". In: *The Astrophysical Journal Supplement Series* 170.1, p. 228.

Mignone, Andrea et al. (2011b). "The PLUTO code for adaptive mesh computations in astrophysical fluid dynamics". In: *The Astrophysical Journal Supplement Series* 198.1, p. 7.

Minkowski, R. (Aug. 1941). "Spectra of Supernovae". In: *Astronomical Society of the Pacifi* 53.314, p. 224. DOI: 10.1086/125315.

Minter, Anthony H. and Steven R. Spangler (Feb. 1996). "Observation of Turbulent Fluctuations in the Interstellar Plasma Density and Magnetic Field on Spatial Scales of 0.01 to 100 Parsecs". In: *The Astrophysical Journal* 458, p. 194. DOI: 10.1086/176803.

Mishra, Ashok K and Vijay P Singh (2010). "Changes in extreme precipitation in Texas". In: *Journal of Geophysical Research: Atmospheres* 115.D14.

Moghaddasi, M., Sedigheh Anvari, and Tayybeh Mohammadi (June 2022). "Comparison of extreme value theory approaches in temperature frequency analysis (case study: Arak plain in Iran)". In: *Arabian Journal of Geosciences* 15. DOI: 10.1007/s12517-022-10409-7.

Molina, M. O., E. Sánchez, and C. Gutiérrez (2020). "Future heat waves over the Mediterranean from an Euro-CORDEX regional climate model ensemble". In: *Scientific Reports* 10.8801, pp. 2045–2322. DOI: 10.1038/s41598-020-65663-0. URL: https://doi.org/10.1038/s41598-020-65663-0.

Moraal, H. (June 2013). "Cosmic-Ray Modulation Equations". In: *Space Sci. Rev.* 176.1-4, pp. 299–319.

Morlino, G. et al. (June 2010). "Spatial structure of X-ray filaments in SN 1006". In: *Monthly Notices of the Royal Astronomical Society: Letters* 405.1, pp. L21–L25. DOI: 10.1111/j.1745-3933.2010.00851.x. arXiv: 0912.2972 [astro-ph.HE].

Morrison, Julia E and James A Smith (2002). "Stochastic modeling of flood peaks using the generalized extreme value distribution". In: *Water resources research* 38.12, pp. 41–1.

Murali, Gopal et al. (2023). "Future temperature extremes threaten land vertebrates". In: *Nature*, pp. 1476–4687. DOI: 10.1038/s41586-022-05606-z. URL: https://doi.org/10.1038/s41586-022-05606-z.

Myhre, G. et al. (2019). "Frequency of extreme precipitation increases extensively with event rareness under global warming". In: *Scientific Reports* 9, p. 16063. DOI: https://doi.org/10.1038/s41598-019-52277-4.

Nakamura, Masao et al. (Dec. 2015). "Statistical analysis of extreme auroral electrojet indices Extremely Severe Space Weather and Geomagnetically Induced Currents in Regions with Locally Heterogeneous Ground Resistivity 2. Aeronomy". In: *Earth, Planets and Space* 67. DOI: 10.1186/s40623-015-0321-0.

Naveau, Philippe et al. (2005). "Statistical methods for the analysis of climate extremes". In: *Comptes Rendus Geoscience* 337.10, pp. 1013–1022. ISSN: 1631-0713. DOI: https://doi.org/10.1016/j.crte.2005.04.015. URL: https://www.sciencedirect.com/science/article/pii/S1631071305001112.

Neugebauer, M. and J. Giacalone (2005). "Multispacecraft observations of interplanetary shocks: Nonplanarity and energetic particles". In: *Journal of Geophysical Research: Space Physics* 110.A12. DOI: https://doi.org/10.1029/2005JA011380. eprint: https://agupubs.onlinelibrary.wiley.com/doi/pdf/10.1029/2005JA011380. URL: https://agupubs.onlinelibrary.wiley.com/doi/abs/10.1029/2005JA011380.

Ng, C. K., D. V. Reames, and A. J. Tylka (July 2003). "Modeling Shock-accelerated Solar Energetic Particles Coupled to Interplanetary Alfvén Waves". In: *The Astrophysical Journal* 591.1, pp. 461–485. DOI: 10.1086/375293.

Nicolas, Julien and David Bromwich (Aug. 2014). "New Reconstruction of Antarctic Near-Surface Temperatures: Multidecadal Trends and Reliability of Global Reanalyses". In: *Journal of Climate* 27, pp. 8070–8093. DOI: 10.1175/JCLI-D-13-00733.1.

Ofman, L and M Gedalin (2013). "Rippled quasi-perpendicular collisionless shocks: Local and global normals". In: *Journal of Geophysical Research: Space Physics* 118.10, pp. 5999–6006.

Ogilvie, K. W. et al. (Feb. 1995). "SWE, A Comprehensive Plasma Instrument for the Wind Spacecraft". In: *Space Science Reviews* 71.1-4, pp. 55–77.

Onwuegbuche F. Kenyatta A., Affognon S. B. Enock E. and Akinade M. (2019). "Application of Extreme Value Theory in Predicting Climate Change Induced Extreme Rainfall in Kenya". In: *International Journal of Statistics and Probability* 8. DOI: 10.5539/ijsp.v8n4p85.

Orlando, S et al. (2012). "Role of ejecta clumping and back-reaction of accelerated cosmic rays in the evolution of type Ia supernova remnants". In: *The Astrophysical Journal* 749.2, p. 156.

Pangaluru, Kishore et al. (Nov. 2018a). "Estimating changes of temperatures and precipitation extremes in India using the Generalized Extreme Value (GEV) distribution". In: *Hydrology and Earth System Sciences Discussions*, pp. 1–33. DOI: 10.5194/hess-2018-522.

Pangaluru, Kishore et al. (2018b). "Estimating changes of temperatures and precipitation extremes in India using the Generalized Extreme Value (GEV) distribution". In: *Hydrology and Earth System Sciences Discussions*, pp. 1–33.

Papalexiou, Simon Michael and Demetris Koutsoyiannis (2013). "Battle of extreme value distributions: A global survey on extreme daily rainfall". In: *Water Resources Research* 49.1, pp. 187–201.

Parsons, Annette et al. (2011). "Wang-Sheeley-Arge–Enlil Cone Model Transitions to Operations". In: *Space Weather* 9.3. DOI: https://doi.org/10.1029/2011SW000663. eprint: https://agupubs.onlinelibrary.wiley.com/doi/pdf/10.1029/2011SW000663. URL: https://agupubs.onlinelibrary.wiley.com/doi/abs/10.1029/2011SW000663.

Paschmann, G. and P. W. Daly (2000). In: ed. by ISSI Scientific Report.

Perri, S. (Jan. 2018). "Superdiffusion of relativistic electrons at supernova remnant shocks". In: *Plasma Physics and Controlled Fusion* 60.1, 014005, p. 014005. DOI: 10.1088/1361-6587/aa8602.

Perri, S., E. Amato, and G. Zimbardo (Nov. 2016). "Transport of relativistic electrons at shocks in shell-type supernova remnants: diffusive and superdiffusive regimes". In: *Astron. Astrophys.* 596, A34, A34. DOI: 10.1051/0004-6361/201628767.

Perri, S and G Zimbardo (2007). "Evidence of superdiffusive transport of electrons accelerated at interplanetary shocks". In: *The Astrophysical Journal Letters* 671.2, pp. L177–L180.

Perri, S. and G. Zimbardo (Mar. 2008). "Superdiffusive transport of electrons accelerated at corotating interaction regions". In: *Journal of Geophysical Research (Space Physics)* 113, A03107, A03107. DOI: 10.1029/2007JA012695.

Perri, S and G Zimbardo (2012a). "Superdiffusive shock acceleration". In: *The Astrophysical Journal* 750.2, p. 87.

Perri, S. and G. Zimbardo (Sept. 2015). "Evidence for superdiffusive shock acceleration at interplanetary shock waves". In: *Journal of Physics Conference Series*. Vol. 642. Journal of Physics Conference Series, 012020, p. 012020. DOI: 10.1088/1742-6596/642/1/012020.

Perri, S and G Zimbardo (2015). "Short Acceleration Times from Superdiffusive Shock Acceleration in the Heliosphere". In: *The Astrophysical Journal* 815.1, p. 75.

Perri, S. et al. (June 2015). "Parameter estimation of superdiffusive motion of energetic particles upstream of heliospheric shocks". In: *Astron. Astrophys.* 578, A2, A2. DOI: 10.1051/0004-6361/201425295. arXiv: 1505.07980 [astro-ph.SR].

Perri, Silvia, Elena Amato, and Gaetano Zimbardo (2016). "Transport of relativistic electrons at shocks in shell-type supernova remnants: diffusive and superdiffusive regimes". In: *Astronomy & Astrophysics* 596, A34.

Perri, Silvia and Gaetano Zimbardo (2009). "Ion superdiffusion at the solar wind termination shock". In: *The Astrophysical Journal Letters* 693.2, pp. L118–L121.

— (2012b). "Magnetic variances and pitch-angle scattering times upstream of interplanetary shocks". In: *The Astrophysical Journal* 754.1, p. 8.

Perri, Silvia et al. (June 2022). "Recent Developments in Particle Acceleration at Shocks: Theory and Observations". In: *Space Sci. Rev.* 218.4, 26, p. 26.

Perri, Silvia et al. (2023). "Interpretation of flat energy spectra upstream of fast interplanetary shocks". In: DOI: 10.48550/ARXIV.2301.05454. URL: https://arxiv.org/abs/2301.05454.

Pitňa, A. et al. (Apr. 2021). "Turbulence Upstream and Downstream of Interplanetary Shocks". In: *Frontiers in Physics* 8, 654, p. 654.

Poedts, Stefaan et al. (2020). "EUropean Heliospheric FORecasting Information Asset 2.0". In: *J. Space Weather Space Clim.* 10, p. 57. DOI: 10.1051/swsc/2020055. URL: https://doi.org/10.1051/swsc/2020055.

Pomoell, Jens and Poedts, S. (2018). "EUHFORIA: European heliospheric forecasting information asset". In: *J. Space Weather Space Clim.* 8, A35. DOI: 10.1051/swsc/2018020. URL: https://doi.org/10.1051/swsc/2018020.

Powell, Kenneth G. et al. (Sept. 1999). "A Solution-Adaptive Upwind Scheme for Ideal Magnetohydrodynamics". In: *Journal of Computational Physics* 154.2, pp. 284–309. DOI: 10.1006/jcph.1999.6299.

Powell, KG (1994). "An approximate Riemann solver for MHD (that actually works in more than one dimension)". In: *ICASE Report*, pp. 94–24.

Power, Scott B. and François P. D. Delage (June 2019). "Setting and smashing extreme temperature records over the coming century". In: *Nature Climate Change* 9.7, pp. 529–534. DOI: 10.1038/s41558-019-0498-5.

Preisser, L. et al. (Apr. 2020). "Influence of He^{++} and Shock Geometry on Interplanetary Shocks in the Solar Wind: 2D Hybrid Simulations". In: *Journal of Geophysical Research (Space Physics)* 125.4, e27442, e27442. DOI: 10.1029/2019JA027442.

Prescott, P. and A.T. Walden (1983). "Maximum likeiihood estimation of the parameters of the three-parameter generalized extreme-value distribution from censored samples". In: *Journal of Statistical Computation and Simulation* 16.3-4, pp. 241–250. DOI: 10.1080/00949658308810625. eprint: https://doi.org/10.1080/00949658308810625. URL: https://doi.org/10.1080/00949658308810625.

Prete, Giuseppe, Silvia Perri, and Gaetano Zimbardo (2019). "Influence of the transport regime on the energetic particle density profiles upstream and downstream of interplanetary shocks". In: *Advances in Space Research* 63.8, pp. 2659 –2671. ISSN: 0273-1177. DOI: https://doi.org/10.1016/j.asr.2019.01.002. URL: http://www.sciencedirect.com/science/article/pii/S0273117719300109.

Prete, Giuseppe et al. (2023). "Daily Precipitation and Temperature Extremes in Southern Italy (Calabria Region)". In: *Atmosphere* 14.3. ISSN: 2073-4433. DOI: 10.3390/atmos14030553. URL: https://www.mdpi.com/2073-4433/14/3/553.

Ragot, B. R. and J. G. Kirk (1997). "Anomalous transport of cosmic ray electrons". In: DOI: 10.48550/ARXIV.ASTRO-PH/9708041. URL: https://arxiv.org/abs/astro-ph/9708041.

Ragot, B. R. and J. G. Kirk (Nov. 1997). "Anomalous transport of cosmic ray electrons." In: *Astron. Astrophys.* 327, pp. 432–440. eprint: astro-ph/9708041.

Raymond, J. C. (Jan. 1979). "Shock waves in the interstellar medium." In: *The Astrophysical Journal Supplement Series* 39, pp. 1–27. DOI: 10.1086/190562.

Reames, Donald V. (June 2013). "The Two Sources of Solar Energetic Particles". In: *Space Sci. Rev.* 175.1-4, pp. 53–92.

Reder, A. et al. (2022). "Characterizing extreme values of precipitation at very high resolution: An experiment over twenty European cities". In: *Weather and Climate Extremes* 35, p. 100407. ISSN: 2212-0947. DOI: https://doi.org/10.1016/j.wace.2022.100407. URL: https://www.sciencedirect.com/science/article/pii/S2212094722000019.

Reis, Carlos et al. (Apr. 2022). "Modeling of the air temperature using the Extreme Value Theory for selected biomes in Mato Grosso do Sul (Brazil)". In: *Stochastic Environmental Research and Risk Assessment* 36. DOI: 10.1007/s00477-022-02206-1.

Reynolds, S. P., B. M. Gaensler, and F. Bocchino (May 2012). "Magnetic Fields in Supernova Remnants and Pulsar-Wind Nebulae". In: *Space Sci. Rev.* 166, pp. 231–261. DOI: 10.1007/s11214-011-9775-y. arXiv: 1104.4047.

Reynoso, Estela M., John P. Hughes, and David A. Moffett (Apr. 2013). "On the Radio Polarization Signature of Efficient and Inefficient Particle Acceleration in Supernova Remnant SN 1006". In: *The Astronomical Journal* 145.4, 104, p. 104. DOI: 10.1088/0004-6256/145/4/104. arXiv: 1302.4678 [astro-ph.GA].

Reynoso, Estela M, John P Hughes, and David A Moffett (2013). "On the radio polarization signature of efficient and inefficient particle acceleration in supernova remnant SN 1006". In: *The Astronomical Journal* 145.4, p. 104.

Richardson, I. G. and Cane, H. V. (2010). "Near-Earth Interplanetary Coronal Mass Ejections During Solar Cycle 23 (1996–2009): Catalog and Summary of Properties". In: *Solar Physics* 264, pp. 1573–093X. DOI: 10.1007/s11207-010-9568-6. URL: https://doi.org/10.1007/s11207-010-9568-6.

Rigozo, N.R. et al. (2011). "Prediction of sunspot number amplitude and solar cycle length for cycles 24 and 25". In: *Journal of Atmospheric and Solar-Terrestrial Physics* 73.11. Influence of Solar Activity on Interplanetary and Geophysical Phenomena, pp. 1294–1299. ISSN: 1364-6826. DOI: https://doi.org/10.1016/j.jastp.2010.09.005. URL: https://www.sciencedirect.com/science/article/pii/S1364682610002658.

Rivoire, Pauline et al. (2022). "High return level estimates of daily ERA-5 precipitation in Europe estimated using regionalized extreme value distributions". In: *Weather and Climate Extremes* 38, p. 100500. ISSN: 2212-0947. DOI: https://doi.org/10.1016/j.wace.2022.100500. URL: https://www.sciencedirect.com/science/article/pii/S2212094722000792.

Rodriguez, L. et al. (Feb. 2008). "Magnetic clouds seen at different locations in the heliosphere". In: *Annales Geophysicae* 26.2, pp. 213–229. DOI: 10.5194/angeo-26-213-2008.

Rodriguez, L. et al. (June 2009). "Three frontside full halo coronal mass ejections with a nontypical geomagnetic response". In: *Space Weather* 7.6, S06003, S06003. DOI: 10.1029/2008SW000453.

Román-Palacios, Cristian and John J. Wiens (2020). "Recent responses to climate change reveal the drivers of species extinction and survival". In: *Proceedings of the National Academy of Sciences* 117.8, pp. 4211–4217. DOI: 10.1073/pnas.1913007117. eprint: https://www.pnas.org/doi/pdf/10.1073/pnas.1913007117. URL: https://www.pnas.org/doi/abs/10.1073/pnas.1913007117.

Rothenflug, R et al. (2004). "Geometry of the non-thermal emission in SN 1006-Azimuthal variations of cosmic-ray acceleration". In: *Astronomy & Astrophysics* 425.1, pp. 121–131.

Rouillard, A.P. (2011). "Relating white light and in situ observations of coronal mass ejections: A review". In: *Journal of Atmospheric and Solar-Terrestrial Physics* 73.10. Three dimensional aspects of CMEs, their source regions and interplanetary manifestations, pp. 1201–1213. ISSN: 1364-6826. DOI: https://doi.org/10.1016/j.jastp.2010.08.015. URL: https://www.sciencedirect.com/science/article/pii/S1364682610002488.

Ruggiero, Peter, Paul D Komar, and Jonathan C Allan (2010). "Increasing wave heights and extreme value projections: The wave climate of the US Pacific Northwest". In: *Coastal Engineering* 57.5, pp. 539–552.

Rypkema, Diana and Shripad Tuljapurkar (2021). "Modeling extreme climatic events using the generalized extreme value (GEV) distribution". In: *Handbook of Statistics*. Vol. 44. Elsevier, pp. 39–71.

Salisbury, J. I. and M. Wimbush (2002). "Using modern time series analysis techniques to predict ENSO events from the SOI time series". In: *Nonlinear Processes in Geophysics* 9.3/4, pp. 341–345. DOI: 10.5194/npg-9-341-2002. URL: https://npg.copernicus.org/articles/9/341/2002/.

Schmieder, B. et al. (May 2020). "Low Geo-Effectiveness of Fast Halo CMEs Related to the 12 X-Class Flares in 2002". In: *Journal of Geophysical Research (Space Physics)* 125.6, e27529, e27529. DOI: 10.1029/2019JA027529. arXiv: 2003.10777 [astro-ph.SR].

Schou, J. et al. (Jan. 2012). "Design and Ground Calibration of the Helioseismic and Magnetic Imager (HMI) Instrument on the Solar Dynamics Observatory (SDO)". In: *Solar Physics* 275.1-2, pp. 229–259. DOI: 10.1007/s11207-011-9842-2.

Schwartz, Steven J. and David Burgess (Mar. 1991). "Quasi-parallel shocks: A patchwork of three-dimensional structures". In: *Geophysical Reasearch Letters* 18.3, pp. 373–376. DOI: 10.1029/91GL00138.

Scoccimarro, Enrico et al. (2015). "Projected Changes in Intense Precipitation over Europe at the Daily and Subdaily Time Scales". In: *Journal of Climate* 28.15, pp. 193–6203. DOI: 10.1175/JCLI-D-14-00779.1.

Scolini, C. et al. (2019). "Observation-based modelling of magnetised coronal mass ejections with EUHFORIA". In: *A&A* 626, A122. DOI: 10.1051/0004-6361/201935053. URL: https://doi.org/10.1051/0004-6361/201935053.

Seneviratne, S.I. et al. (2012). "Changes in climate extremes and their impacts on the natural physical environment". In: *Managing the Risks of Extreme Events and Disasters to Advance Climate Change Adaptation. A Special Report of Working Groups I and II of the Intergovernmental Panel on Climate Change (IPCC)*. Ed. by C.B. Field et al. Cambridge, UK, and New York, NY, USA: Cambridge University Press, pp. 109–230.

Servidio, S et al. (2012). "Local kinetic effects in two-dimensional plasma turbulence". In: *Physical review letters* 108.4, p. 045001.

Shebalin, John V, William H Matthaeus, and David Montgomery (1983). "Anisotropy in MHD turbulence due to a mean magnetic field". In: *Journal of plasma physics* 29.3, pp. 525–547.

Shen, L., L. J. Mickley, and E. Gilleland (Apr. 2016). "Impact of increasing heat waves on U.S. ozone episodes in the 2050s: Results from a multimodel analysis using extreme value theory". In: *Geophysical Reasearch Letters* 43.8, pp. 4017–4025. DOI: 10.1002/2016GL068432.

Shlesinger, M. F., B. J. West, and J. Klafter (Mar. 1987). "Levy dynamics of enhanced diffusion - Application to turbulence". In: *Physical Review Letters* 58, pp. 1100–1103. DOI: 10.1103/PhysRevLett.58.1100.

Skansi, María et al. (Mar. 2017). "Evaluating Highest-Temperature Extremes in the Antarctic". In: *Eos* 98. DOI: 10.1029/2017EO068325.

Smith, C. W. et al. (July 1998). "The ACE Magnetic Fields Experiment". In: *Space Science Review* 86, pp. 613–632.

Song, H. Q. et al. (2020). "Do All Interplanetary Coronal Mass Ejections Have a Magnetic Flux Rope Structure Near 1 au?" In: *The Astrophysical Journal Letters* 901.2, p. L21. DOI: 10.3847/2041-8213/abb6ec. URL: https://doi.org/10.3847/2041-8213/abb6ec.

Sonnerup, B. U. Ö. (1969). "Acceleration of particles reflected at a shock front". In: *Journal of Geophysical Research* 74, p. 1301. DOI: 10.1029/JA074i005p01301.

Sonnerup, B. U. Ö. and Jr. Cahill L. J. (1968). "Explorer 12 observations of the magnetopause current layer". In: *J. Geophys. Res.* 73.5, p. 1757.

Soroye, Peter, Tim Newbold, and Jeremy Kerr (Feb. 2020). "Climate change contributes to widespread declines among bumble bees across continents". In: *Science* 367, pp. 685–688. DOI: 10.1126/science.aax8591.

Sow Mondal, Shanwlee et al. (Dec. 2021). "Acceleration of Solar Energetic Particles by the Shock of Interplanetary Coronal Mass Ejection". In: *The Atrophysical Journal* 923.1, 80, p. 80. DOI: 10.3847/1538-4357/ac2c7a. arXiv: 2110.01828 [astro-ph.SR].

St. Cyr, O. et al. (Aug. 2000). "Properties of coronal mass ejections: SOHO LASCO observations from January 1996 to June 1998". In: *jgr* 105, pp. 18169–18186. DOI: 10.1029/1999JA000381.

Stewart, Mathew, W. Christopher Carleton, and Huw S. Groucutt (2022). "Extreme events in biological, societal, and earth sciences: A systematic review of the literature". In: *Frontiers in Earth Science* 10. ISSN: 2296-6463. DOI: 10.3389/feart.2022.786829. URL: https://www.frontiersin.org/articles/10.3389/feart.2022.786829.

Stine, Alexander R, P Huybers, and Inez Y Fung (2009). "Changes in the phase of the annual cycle of surface temperature". In: *Nature* 457.7228, pp. 435–440.

Stone, E. C. et al. (1998). "The Advanced Composition Explorer". In: *Space Science Reviews* 86.1. DOI: 10.1023/A:1005082526237. URL: https://doi.org/10.1023/A:1005082526237.

Strauss, R. D. T. and F. Effenberger (Oct. 2017). "A Hitch-hiker's Guide to Stochastic Differential Equations. Solution Methods for Energetic Particle Transport in Space Physics and Astrophysics". In: *Space Sci. Rev.* 212, pp. 151–192.

Sugiyama, T. and D. Shiota (Apr. 2011). "Sign for Super-diffusive Transport of Energetic Ions Associated with a Coronal-mass-ejection-driven Interplanetary Shock". In: *Astrophysical Journal Letters* 731, L34, p. L34. DOI: 10.1088/2041-8205/731/2/L34.

Sundberg, Torbjörn et al. (Mar. 2016). "Ion Acceleration at the Quasi-parallel Bow Shock: Decoding the Signature of Injection". In: *The Astrophysical Journal* 820.1, 21, p. 21. DOI: 10.3847/0004-637X/820/1/21. arXiv: 1511.02077 [astro-ph.HE].

Tabari, Hossein (2021). "Extreme value analysis dilemma for climate change impact assessment on global flood and extreme precipitation". In: *Journal of Hydrology* 593, p. 125932.

Taktakishvili, A., P. MacNeice, and D. Odstrcil (June 2010). "Model uncertainties in predictions of arrival of coronal mass ejections at Earth orbit". In: *Space Weather* 8.6. DOI: https://doi.org/10.1029/2009SW000543. eprint: https://agupubs.onlinelibrary.wiley.com/doi/pdf/10.1029/2009SW000543. URL: https://agupubs.onlinelibrary.wiley.com/doi/abs/10.1029/2009SW000543.

Tessein, Jeffrey A. et al. (Oct. 2015). "Effect of Coherent Structures on Energetic Particle Intensity in the Solar Wind at 1 AU". In: *The Astrophysical Journal* 812.1, 68, p. 68. DOI: 10.1088/0004-637X/812/1/68.

Thomson, David J (1995). "The seasons, global temperature, and precession". In: *Science* 268.5207, pp. 59–68.

Till, Aaron et al. (2019). "Fish die-offs are concurrent with thermal extremes in north temperate lakes". In: *Nature Climate Change* 9, pp. 1758–6798. DOI: 10.1038/s41558-019-0520-y.

Torrence, Christopher and Gilbert P. Compo (1998). "A Practical Guide to Wavelet Analysis". In: *Bulletin of the American Meteorological Society* 79.1, pp. 61–78.

Trotta, D. et al. (Jan. 2020a). "Particle transport in hybrid PIC shock simulations: A comparison of diagnostics". In: *Mont. Not. Roy. Astr. Soc.* 491.1, pp. 580–595.

— (Jan. 2020b). "Particle transport in hybrid PIC shock simulations: A comparison of diagnostics". In: *Monthly Notices of the Royal Astronomical Society* 491 (1), 580–595. DOI: https://doi.org/10.1093/mnras/stz2760.

Trotta, D. et al. (2022). "Single-spacecraft techniques for shock parameters estimation: A systematic approach". In: *Frontiers in Astronomy and Space Sciences* 9. ISSN: 2296-987X. DOI: 10.3389/fspas.2022.1005672. URL: https://www.frontiersin.org/articles/10.3389/fspas.2022.1005672.

Trotta, Domenico et al. (May 2021). "Phase space transport in the interaction between shocks and plasma turbulence". In: *Proceedings of the National Academy of Science* 118.21, e2026764118, e2026764118.

Trotta, Domenico et al. (2021). "Phase space transport in the interaction between shocks and plasma turbulence". In: *Proceedings of the National Academy of Sciences* 118.21, e2026764118.

Trotta, E. M. and G. Zimbardo (Jan. 2015). "A numerical study of Lévy random walks: Mean square displacement and power-law propagators". In: *Journal of Plasma Physics* 81.1, 325810108, p. 325810108. DOI: 10.1017/S0022377814000592.

Tsubouchi, Ken and Yoshiharu Omura (Dec. 2007). "Long-term occurrence probabilities of intense geomagnetic storm events". In: *Space Weather-the International Journal of Research and Applications - SPACE WEATHER* 5. DOI: 10.1029/2007SW000329.

Turner, D. L. et al. (Sept. 2018). "Autogenous and efficient acceleration of energetic ions upstream of Earth's bow shock". In: 561.7722, pp. 206–210.

Turner, John et al. (July 2016). "Absence of 21st century warming on Antarctic Peninsula consistent with natural variability". In: *Nature* 535, pp. 411–415. DOI: 10.1038/nature18645.

Turner, John et al. (2020). "Antarctic temperature variability and change from station data". In: *International Journal of Climatology* 40.6, pp. 2986–3007. DOI: https://doi.org/10.1002/joc.6378. eprint: https://rmets.onlinelibrary.wiley.com/doi/pdf/10.1002/joc.6378. URL: https://rmets.onlinelibrary.wiley.com/doi/abs/10.1002/joc.6378.

UNDRR (2020). *The human cost of disasters: An overview of the last 20 years (2000-2019)*. United Nations. URL: https://www.undrr.org/publication/human-cost-disasters-2000-2019.

Vaidya, Bhargav et al. (2018). "A particle module for the PLUTO Code. II. Hybrid framework for modeling nonthermal emission from relativistic magnetized flows". In: *The Astrophysical Journal* 865.2, p. 144.

Van Weeren, R. J. et al. (Feb. 2016). "LOFAR, VLA, and Chandra Observations of the Toothbrush Galaxy Cluster". In: *Astrophysical Journal* 818, 204, p. 204. DOI: 10.3847/0004-637X/818/2/204. arXiv: 1601.06029 [astro-ph.HE].

Vasseur, David et al. (Jan. 2014). "Increased temperature variation poses a greater risk to species than climate warming". In: *Proceedings. Biological sciences / The Royal Society* 281, p. 20132612. DOI: 10.1098/rspb.2013.2612.

Vaughan, David et al. (Oct. 2003). "Recent Rapid Regional Climate Warming on the Antarctic Peninsula". In: *Climatic Change* 60, pp. 243–274. DOI: 10.1023/A:1026021217991.

Vecchio, A., V. Capparelli, and V. Carbone (2010). "The complex dynamics of the seasonal component of USA's surface temperature". In: *Atmospheric Chemistry and Physics* 10.19, pp. 9657–9665. DOI: 10.5194/acp-10-9657-2010. URL: https://acp.copernicus.org/articles/10/9657/2010/.

Vecchio, A and V Carbone (2010). "Amplitude-frequency fluctuations of the seasonal cycle, temperature anomalies, and long-range persistence of climate records". In: *Physical Review E* 82.6, p. 066101.

Vecchio, A et al. (2012). "Has the Mediterranean Sea felt the March 11th, 2011, Mw 9.0 Tohoku-Oki earthquake?" In: *EPL (Europhysics Letters)* 98.5, p. 59001.

Velikou, Kondylia et al. (2022). "Reliability of the ERA5 in Replicating Mean and Extreme Temperatures across Europe". In: *Water* 14.4. ISSN: 2073-4441. DOI: 10.3390/w14040543. URL: https://www.mdpi.com/2073-4441/14/4/543.

Verbeke, C., J. Pomoell, and S. Poedts (July 2019). "The evolution of coronal mass ejections in the inner heliosphere: Implementing the spheromak model with EUHFORIA". In: *Astronomy and Astrophysics* 627, A111, A111. DOI: 10.1051/0004-6361/201834702.

Verbeke, Christine et al. (Sept. 2022). "Over-expansion of coronal mass ejections modelled using 3D MHD EUHFORIA simulations". In: *Advances in Space Research* 70.6, pp. 1663–1683. DOI: 10.1016/j.asr.2022.06.013. arXiv: 2207.03168 [astro-ph.SR].

Vourlidas, A. et al. (2003). "Direct Detection of a Coronal Mass Ejection-Associated Shock in Large Angle and Spectrometric Coronagraph Experiment White-Light Images". In: *Astrophys. J.* 598.2, pp. 1392–1402.

Wallace, Craig J and Timothy J Osborn (2002). "Recent and future modulation of the annual cycle". In: *Climate Research* 22.1, pp. 1–11.

Wang, Xiaolan L et al. (2013). "Historical changes in Australian temperature extremes as inferred from extreme value distribution analysis". In: *Geophysical Research Letters* 40.3, pp. 573–578.

Watts, J. (2013). "Antarctic temperature rises above 20C for first time on record". In: The Guardian.

Webb, D. F. and Howard, T. A. (2012). "Coronal Mass Ejections: Observations". In: *Living Reviews in Solar Physics* 9, pp. 1614–4961.

Weiler, Kurt W and Richard A Sramek (1988). "Supernovae and supernova remnants". In: *Annual review of astronomy and astrophysics* 26.1, pp. 295–341.

Wicks, RT et al. (2010). "Power and spectral index anisotropy of the entire inertial range of turbulence in the fast solar wind". In: *Monthly Notices of the Royal Astronomical Society: Letters* 407.1, pp. L31–L35.

Wigley, TML (1988). "Future CFC concentrations under the Montreal Protocol and their greenhouse-effect implications". In: *Nature* 335.6188, pp. 333–335.

Wijsen, Nicolas et al. (2021). "A Self-consistent Simulation of Proton Acceleration and Transport Near a High-speed Solar Wind Stream". In: *The Astrophysical Journal Letters* 908.2, p. L26. DOI: 10.3847/2041-8213/abe1cb. URL: https://dx.doi.org/10.3847/2041-8213/abe1cb.

Wijsen, N. et al. (2022). "Observation-based modelling of the energetic storm particle event of 14 July 2012". In: *A&A* 659, A187. DOI: 10.1051/0004-6361/202142698. URL: https://doi.org/10.1051/0004-6361/202142698.

Wilson L. B., III et al. (Sept. 2017). "Revisiting the structure of low-Mach number, low-beta, quasi-perpendicular shocks". In: *Journal of Geophysical Research (Space Physics)* 122.9, pp. 9115–9133. DOI: 10.1002/2017JA024352.

Wilson, L. B. (Feb. 2016). "Low Frequency Waves at and Upstream of Collisionless Shocks". In: *Washington DC American Geophysical Union Geophysical Monograph Series* 216, pp. 269–291.

Wilson, L. B. et al. (Mar. 2013). "Shocklets, SLAMS, and field-aligned ion beams in the terrestrial foreshock". In: *Journal of Geophysical Research (Space Physics)* 118.3, pp. 957–966. DOI: 10.1029/2012JA018186. arXiv: 1207.5561 [physics.space-ph].

Wilson, L. B. et al. (Nov. 2016). "Relativistic Electrons Produced by Foreshock Disturbances Observed Upstream of Earth's Bow Shock". In: *Physical review letters* 117.21, 215101, p. 215101.

Winslow, Reka M. et al. (2016). "Longitudinal conjunction between MESSENGER and STEREO A: Development of ICME complexity through stream interactions". In: *Journal of Geophysical Research: Space Physics* 121.7, pp. 6092–6106. DOI: https://doi.org/10.1002/2015JA022307. eprint: https://agupubs.onlinelibrary.wiley.com/doi/pdf/10.1002/2015JA022307. URL: https://agupubs.onlinelibrary.wiley.com/doi/abs/10.1002/2015JA022307.

Xie, Hong, Leon Ofman, and Gareth Lawrence (Mar. 2004). "Cone model for halo CMEs: Application to space weather forecasting". In: *Journal of Geophysical Research (Space Physics)* 109.A3, A03109, A03109. DOI: 10.1029/2003JA010226.

Yashiro, S., G. Michalek, and N. Gopalswamy (2008). "A comparison of coronal mass ejections identified by manual and automatic methods". In: *Annales Geophysicae* 26.10, pp. 3103–3112. DOI: 10.5194/angeo-26-3103-2008. URL: https://angeo.copernicus.org/articles/26/3103/2008/.

Yashiro, S. et al. (2004). "A catalog of white light coronal mass ejections observed by the SOHO spacecraft". In: *Journal of Geophysical Research: Space Physics* 109.A7. DOI: https://doi.org/10.1029/2003JA010282. eprint: https://agupubs.onlinelibrary.wiley.com/doi/pdf/10.1029/2003JA010282. URL: https://agupubs.onlinelibrary.wiley.com/doi/abs/10.1029/2003JA010282.

Young, IR et al. (2012). "Investigation of trends in extreme value wave height and wind speed". In: *Journal of Geophysical Research: Oceans* 117.C11.

Yu, Dejie, Junsheng Cheng, and Yu Yang (2005). "Application of EMD method and Hilbert spectrum to the fault diagnosis of roller bearings". In: *Mechanical systems and signal processing* 19.2, pp. 259–270.

Yu, Huan et al. (2015). "Three-dimensional magnetohydrodynamic studies of the non-thermal X-ray morphologies of SN 1006". In: *Astronomy & Astrophysics* 579, A35.

Zaburdaev, V., S. Denisov, and J. Klafter (Apr. 2015). "Lévy walks". In: *Reviews of Modern Physics* 87, pp. 483–530. DOI: 10.1103/RevModPhys.87.483. arXiv: 1410.5100 [cond-mat.stat-mech].

Zhao, L. L. et al. (Dec. 2021). "Turbulence and wave transmission at an ICME-driven shock observed by the Solar Orbiter and Wind". In: *Astronomy & Astrophysics* 656, A3, A3.

Zimbardo, G. and S. Perri (Aug. 2018). "Understanding the radio spectral indices of galaxy cluster relics by superdiffusive shock acceleration". In: *Monthly Notices Royal Astron. Soc.* 478, pp. 4922–4930. DOI: 10.1093/mnras/sty1438.

Zimbardo, Gaetano and Silvia Perri (2013). "From Lévy walks to superdiffusive shock acceleration". In: *The Astrophysical Journal* 778.1, p. 35.

Zimbardo, Gaetano and Silvia Perri (Nov. 2020). "Non-Markovian Pitch-angle Scattering as the Origin of Particle Superdiffusion Parallel to the Magnetic Field". In: *The Astrophysical Journal* 903.2, 105, p. 105. DOI: 10.3847/1538-4357/abb951.

Zimbardo, Gaetano, Giuseppe Prete, and Silvia Perri (2020). "Collisionless Shocks as a Diagnostic Tool for Understanding Energetic Particle Transport in Space Plasmas". In: *Frontiers in Astronomy and Space Sciences* 7, p. 16. ISSN: 2296-987X. DOI: 10.3389/fspas.2020.00016. URL: https://www.frontiersin.org/article/10.3389/fspas.2020.00016.

Zittis, George, Adriana Bruggeman, and Jos Lelieveld (2021). "Revisiting future extreme precipitation trends in the Mediterranean". In: *Weather and Climate Extremes* 34, p. 100380. ISSN: 2212-0947. DOI: https://doi.org/10.1016/j.wace.2021.100380. URL: https://www.sciencedirect.com/science/article/pii/S2212094721000700.

Zittis, George et al. (2019). "A multi-model, multi-scenario, and multi-domain analysis of regional climate projections for the Mediterranean". In: *Regional Environmental Change* 19. ISSN: 1436-378X. DOI: 10.1007/s10113-019-01565-w. URL: https://doi.org/10.1007/s10113-019-01565-w.

Zuccarello, F. P. et al. (Aug. 2018). "Threshold of Non-potential Magnetic Helicity Ratios at the Onset of Solar Eruptions". In: *The Astrophysical Journal* 863.1, 41, p. 41. DOI: 10.3847/1538-4357/aacdfc. arXiv: 1807.00532 [astro-ph.SR].

Zumofen, G. and J. Klafter (1993). "Scale-invariant motion in intermittent chaotic systems". In: *Phys. Rev. E* 47 (2), pp. 851–863. DOI: 10.1103/PhysRevE.47.851. URL: https://link.aps.org/doi/10.1103/PhysRevE.47.851.

Zumofen, G. and J. Klafter (Feb. 1993). "Scale-invariant motion in intermittent chaotic systems". In: *Phys. Rev. E* 47, pp. 851–863. DOI: 10.1103/PhysRevE.47.851.